Journal of Nanomaterials

Functional Graded Nanomaterials

Lead Guest Editor: Senthilkumar N
Guest Editors: Deepanraj B and Ao Xia

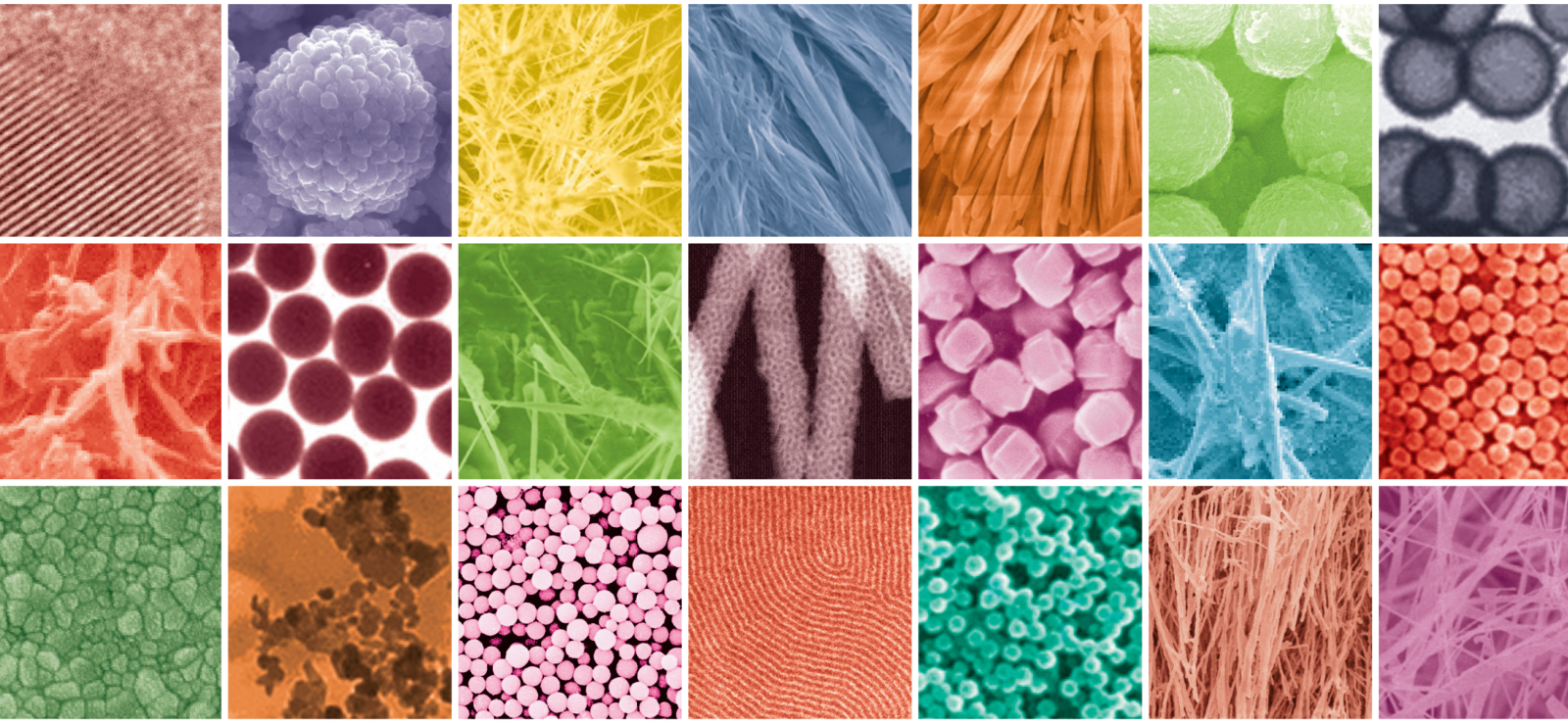

Functional Graded Nanomaterials

Journal of Nanomaterials

Functional Graded Nanomaterials

Lead Guest Editor: Senthilkumar N
Guest Editors: Deepanraj B and Ao Xia

Contents

Nanoclay-Incorporated Polycaprolactone Matrix via Electrospinning Techniques-Enriched Spectroscopic Responses
D. Devina Merin, R. Anith Jose, T. S. Arulananth, Antony Allwyn Sundarraj, T. M. Inbamalar, and Meseret Getnet Meharie
Research Article (8 pages), Article ID 1194158, Volume 2023 (2023)

Comparative Performance Study of Difference Differential Amplifier Using 7 nm and 14 nm FinFET Technologies and Carbon Nanotube FET
Anand Kumar, M. Janakirani, M. Anand, Sudeep Sharma, Chettiyar Vani Vivekanand, and Ankit Chakravarti
Research Article (15 pages), Article ID 8200856, Volume 2022 (2022)

Friction and Wear Response of Friction Stir Processed Cu/ZrO_2 Surface Nano-Composite
Harikishor Kumar, Rabindra Prasad, Parshant Kumar, and Solomon Aynalem Hailu
Research Article (12 pages), Article ID 6767941, Volume 2022 (2022)

Optimization of Dual Coating Using Electroless Ni-P-Nano-TiO_2 and Plasma Yttria-Stabilized Zirconia on Piston Crown and Cylinder Liner in CI Engine
V. S. Shaisundaram, V. Balambica, D. Sendil Kumar, S. Nithish, M. Chandrasekaran, Mohanraj Shanmugam, and Dabala Misgana Likassa
Research Article (8 pages), Article ID 4934926, Volume 2022 (2022)

Characterization Analysis of Silver Nanoparticles Synthesized from *Chaetoceros calcitrans*
R. Anith Jose, D. Devina Merin, T. S. Arulananth, and Nagaraju Shaik
Research Article (15 pages), Article ID 4056551, Volume 2022 (2022)

Influence of Future Material Nano-ZrO_2 and Graphene on the Mechanical Properties of Al Composites
MD. Umar, R. Muraliraja, V. S. Shaisundaram, and Shiferaw Garoma Wayessa
Research Article (7 pages), Article ID 1454037, Volume 2022 (2022)

Glass Fibre Reinforced Epoxy Composites Modified with Graphene Nanofillers: Electrical Characterization
Lokasani Bhanuprakash, Soney Varghese, and Sitesh Kumar Singh
Research Article (8 pages), Article ID 4611251, Volume 2022 (2022)

[Retracted] Spatial-Temporal Variation Characteristics of Soil Moisture and Nutrients Based on Nanomaterials in the Root Zone of Haloxylon ammodendron Seedlings
Ze Wang, Haibin Gu, An Yan, Pingan Jiang, Hao Ma, Jiandong Sheng, and Wentai Zhang
Research Article (15 pages), Article ID 9202493, Volume 2022 (2022)

Hindawi
Journal of Nanomaterials
Volume 2023, Article ID 9825217, 1 page
https://doi.org/10.1155/2023/9825217

Retraction

Retracted: Spatial-Temporal Variation Characteristics of Soil Moisture and Nutrients Based on Nanomaterials in the Root Zone of Haloxylon ammodendron Seedlings

Journal of Nanomaterials

Received 20 June 2023; Accepted 20 June 2023; Published 21 June 2023

This article has been retracted by Hindawi following an investigation undertaken by the publisher [1]. This investigation has uncovered evidence of one or more of the following indicators of systematic manipulation of the publication process:

1. Discrepancies in scope
2. Discrepancies in the description of the research reported
3. Discrepancies between the availability of data and the research described
4. Inappropriate citations
5. Incoherent, meaningless and/or irrelevant content included in the article
6. Peer-review manipulation

The presence of these indicators undermines our confidence in the integrity of the article's content and we cannot, therefore, vouch for its reliability. Please note that this notice is intended solely to alert readers that the content of this article is unreliable. We have not investigated whether authors were aware of or involved in the systematic manipulation of the publication process.

Wiley and Hindawi regrets that the usual quality checks did not identify these issues before publication and have since put additional measures in place to safeguard research integrity.

We wish to credit our own Research Integrity and Research Publishing teams and anonymous and named external researchers and research integrity experts for contributing to this investigation.

The corresponding author, as the representative of all authors, has been given the opportunity to register their agreement or disagreement to this retraction. We have kept a record of any response received.

References

[1] Z. Wang, H. Gu, A. Yan et al., "Spatial-Temporal Variation Characteristics of Soil Moisture and Nutrients Based on Nanomaterials in the Root Zone of Haloxylon ammodendron Seedlings," *Journal of Nanomaterials*, vol. 2022, Article ID 9202493, 15 pages, 2022.

Hindawi
Journal of Nanomaterials
Volume 2023, Article ID 6553200, 9 pages
https://doi.org/10.1155/2023/6553200

Research Article

Enhancing the Mechanical Properties of AZ31D Alloy by Reinforcing Nanosilicon Carbide/Graphite

Itha Veeranjaneyulu,[1,2] **Vemulapalli Chittaranjan Das**,[3] **and Srikanth Karumuri**[4]

[1]*Department of Mechanical Engineering, Acharya Nagarjuna University, Guntur, India*
[2]*Department of Mechanical Engineering, Aditya Engineering College, Surampalem, India*
[3]*Department of Mechanical Engineering, R.V.R. and J.C. College of Engineering, Guntur, India*
[4]*Department of Mechanical Engineering, Mizan Tepi University, Teppi, Ethiopia*

Correspondence should be addressed to Itha Veeranjaneyulu; anjimech@gmail.com and Srikanth Karumuri; srikanth.karumuri@mtu.edu.et

Received 7 September 2022; Revised 9 November 2022; Accepted 25 April 2023; Published 22 May 2023

Academic Editor: N. Senthilkumar

Magnesium-based alloys were more prevalent in automobile applications owing to their mechanical properties, low mass, and density. However, its poor mechanical properties are restricting its applications. Therefore, the present study focuses on improving the mechanical properties of AZ31D alloy by reinforcing silicon carbide (SiC) and graphite (Gr) nanoparticles with weight fractions of 2%, 4%, and 6% using stir-casting technique. The microstructure analysis was performed using a scanning electron microscope. The elemental analysis was confirmed using energy-dispersive spectroscopy, and X-ray diffraction was used to study various phases in the nanocomposites. Further, the mechanical properties, such as microhardness, ultimate tensile strength, yield strength, and compression strength of the nanocomposites, were significantly improved by 53%, 59%, 62%, and 82%, respectively, as compared with base alloy.

1. Introduction

Nowadays, substantial research outcomes concentrate on the advancement of product demand for designing materials with low specific gravities, lightweight materials, and with high strengths [1]. It was brought on by technical advancements, particularly in the aviation designing field. Magnesium alloys (specific gravity: 1.7 g/cm^3) appear to meet these standards. The exploration of magnesium (Mg) was a substitute for iron, polymers, and aluminum [2, 3]. Due to its low weight, Mg and its alloys have become popular materials for usage in products, including computer parts, recreational goods, aircraft components, home appliances, and vehicles, in recent years. Zinc and aluminum are alloyed with Mg material to enhance their mechanical properties and form group Mg–Al–Zn [4]. AZ31 is widely used in Mg–Al alloys. This structural material has a lot of potential for the aviation sector because of its less density and strong mechanical characteristics [5, 6]. However, the improvement in properties for AZ31 alloys is still challenging. Therefore, the nanocomposites play a vital role to enhance the mechanical, corrosion, and wear properties. Different methods were used to fabricate the nanocomposites [7–9]. Among different methods, stir casting is easy and economical compared to other methods to fabricate the metal matrix composites (MMC's) [10].

Several researchers have fabricated MMC's using stir-casting technique by mixing the various reinforcements. Khandelwal et al. [11] studied various weight proportions of $(Al_2O_3)_{np}$ on AZ31 and concluded that there was improvement in the tensile properties of nanocomposites. Torabi Parizi et al. [12] fabricated AZ80/calcium/aluminum oxide nanocomposite through stir-casting method. The results reveal that stir composite had more agglomerated particles than rheo composite and that stir composite had higher mechanical characteristics. Singh et al. [13] studied friction stir welding joint made of AZ61 alloy and reported that the microhardness of AZ61 is more in the thermo-mechanically impacted zone but lower in the stir zone. Rogal et al. [14] fabricated AZ91 nanocomposites by injection technology. The nanocomposites had hardness and compressive strength that were raised by 29% and 18%,

Figure 1: Stir-casting set up.

respectively. Subramani et al. [15] studied the microstructure of AZ31 alloy and the effect of SiC_{np} in composites. Further, the authors reported significant changes in mechanical properties with lamellar structure. The mechanical characteristics of metal matrix nanocomposite were investigated by Nourbakhsh et al. [16], and the findings revealed that the nanocomposites exhibited better qualities than base alloys. The effectiveness of composite materials reinforced with nanoscale and microscale graphene was studied by Vahedi et al. [17]. The results are shown that the particles are uniformly distributed and improved the mechanical properties. Huang et al. [18] investigated WS_2 reinforcement with different matrix materials and concluded that they reduced the secondary phases and enhanced the properties of 0.2 wt% WS_2. Huang et al. [19] studied Al_2O_3 and Sic nanoparticles in hybrid composites. The results have improved the ultimate tensile strength (UTS), yield strength (YS), and hardness. Silicon carbide particles were utilized as support in the magnesium network, which improves hardness, and strength in composites. By strengthening different particles, some researchers have been investigating unique techniques to enhance the properties of aluminum zinc series alloys [20, 21]. However, still enhancing the mechanical properties is challenging.

The novel feature of the work is the use of stir casting to reinforce SiC/Gr particles in AZ31D nanocomposites, improving their mechanical properties. As far as we are aware, stir casting has rarely been used in the manufacturing of nanocomposites. The mechanical properties of reinforced nanocomposites and evaluations of the microstructure were investigated using different techniques. All these results were compared with the AZ31D magnesium alloy. Overall, the present results are potential for the biomedicine and aviation industry.

2. Materials and Methods

2.1. Materials and Fabrication of Composites. In the experiment, AZ31D was employed as the matrix material, and silicon carbide and graphite particles with an average sizes of 75 and 53 nm, respectively, were used as reinforcements. Figure 1 illustrates the manufacturing of nanocomposites using the stir-casting technique. Figure 2 depicts the schematic view of the stir-casting setup. Table 1 provides the AZ31D alloy's chemical composition. AZ31D alloy makes into small pieces, poured in a muffle furnace, and set in a graphite crucible to overcome the chemical reactions while matrix material is in the liquid state. The raw materials and crucibles are heated to eliminate different gases and defects in castings. The crucible is preheated to 400°C in the muffle furnace and stacked with the material by increasing the

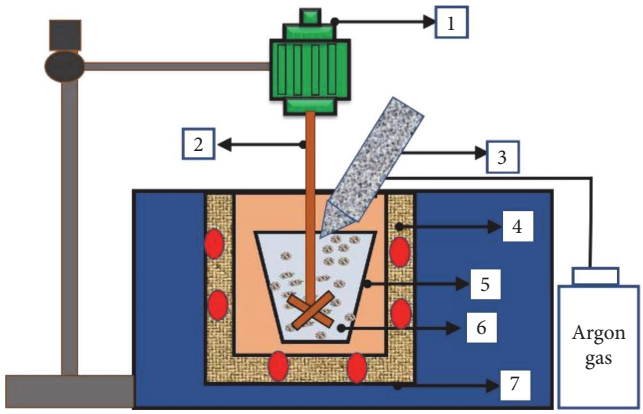

(1) DC motor
(2) Stirrer
(3) Reinforcement
(4) Insulation
(5) Graphite crucible
(6) Molten metal
(7) Induction furnace

Figure 2: Schematic view of stir-casting method.

Table 1: Elements of AZ31D in wt%.

Elements	Al	Zn	Mn	Cu	Fe	Si	Mg
wt%	3	0.98	0.01	0.02	0.001	0.01	Rest

Table 2: Designation of specimens.

S. no.	Specimens	Compositions
1	S1	AZ31D
2	S2	AZ31D + 2% SiC + 2% graphite
3	S3	AZ31D + 4% SiC + 4% graphite
4	S4	AZ31D + 6% SiC + 6% graphite

temperature to 650°C. To prevent atmospheric oxidation, argon gas was used to create a vacuum environment in the furnace [22].

The flux 1 wt% of the matrix is used to prevent oxidation. The vortex made by a traditional stirrer worked at a speed of 700 rpm, and the stirring time is 15 min, which was run by an electronic variance. The prewarmed (200°C) reinforcements are included in the pool's center created by the moving process.

After increased sustenance, the liquid metal was filled in the preheated die. The specimens are quenched at room temperature for homogenization. Homogenization was carried out 24 hr to relieve stress. The designation of specimens is presented in Table 2.

2.2. Density and Porosity Measurement. The density of alloy and nanocomposites were evaluated using an experimental kit according to the ASTM: B962-13 standard [23] and it referred to Equation (1). The rule of the mixture method was applied to calculate the samples theoretical density using Equation (2). The percentage porosity of specimens was calculated using Equation (3) [24].

$$\text{Measured density (g/cc)} = \frac{\text{Weight of specimen in air}}{\text{Loss of weight in water}}, \tag{1}$$

$$\text{Theoretical density } (\rho_t) = \rho_m w_m + \rho_r w_r, \tag{2}$$

$$\text{Porosity } (\%) = \left(1 - \frac{\text{Measured density}}{\text{Theoretical density}}\right) \times 100, \tag{3}$$

where ρ_m = matrix density, ρ_r = reinforcement density, w_m = weight fractions of matrix, w_r = weight fractions of reinforcement.

2.3. Microstructure Characterization. The specimens were polished using different grades (500–2,000) of polishing paper by a disc polishing machine. Later, the samples were etched using a solution for 10–20 s. The microstructure of the base alloy and nanocomposites were investigated using a scanning electron microscope (SEM) (TESCAN and Model: VEGA3 SBH). Energy-dispersive spectroscopy (EDS) was used to know the existence of elements in the fabrication of the samples. X-ray diffraction (XRD) (Shimadzu, XRD-7000, and Japan) analysis was performed on the specimens to know the existence of different phases.

2.4. Mechanical Properties. Microhardness of the S1, S2, S3, and S4 were measured using Vickers's microhardness tester. During the testing, a load of 100 g for 10 s was applied to the specimen through a square-based diamond indenter, and the hardness readings were taken in a standard manner. The specimen was prepared (shown in Figure 3) as per the ASTM: E384 standard [25]. The experiment was repeated three times for each specimen and noted the average of three values.

Tensile and compressive properties are evaluated using UTM (INSTRON-E1025) with a strain rate of 3 mm/min. The specimen was prepared as per ASTM: E8 standard [26], and compression testing specimens were prepared as per ASTM: E9 standard [27], as shown in Figure 4. To get standardized values, the experiment was run three times for each specimen.

3. Results and Discussion

3.1. Microstructure Analysis. Figure 5 shows the microstructure analysis of AZ31D alloy and nanocomposites. Figure 4(a) represents α-Mg dendritic structure and the secondary phases surrounding grain boundaries [28]. Figure 5(b)–5(d) were shown the SEM images of nanocomposites with reinforcing of 2%, 4%, and 6% in weight fraction of SiC/Gr.

During the stirring process, it was noticed that SiC/Gr particles were evenly dispersed into the Mg matrix. There were no agglomerations occurred in the nanocomposites. Furthermore, the presence of reinforcements allowed for grain refining. A stronger mixing effect is produced by nanoparticles than by micron particles. Dendritic structures show a consistent distribution of particles with minimal porosity

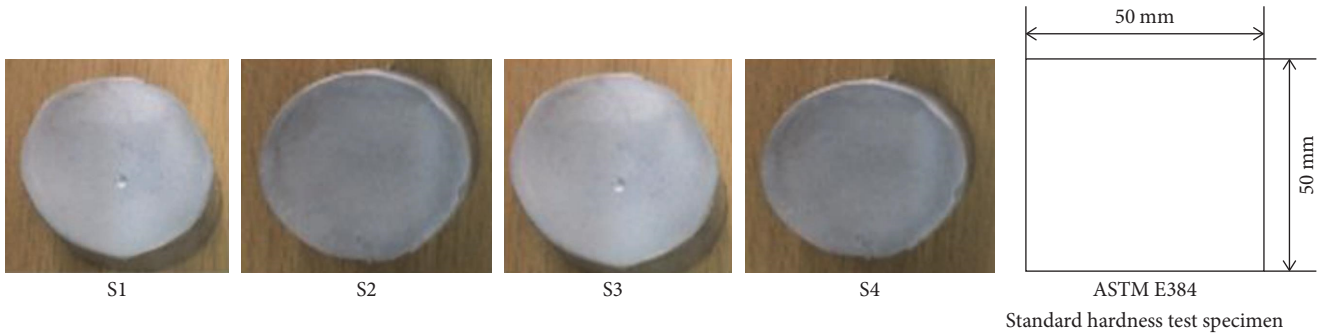

Figure 3: Specimens for microhardness test.

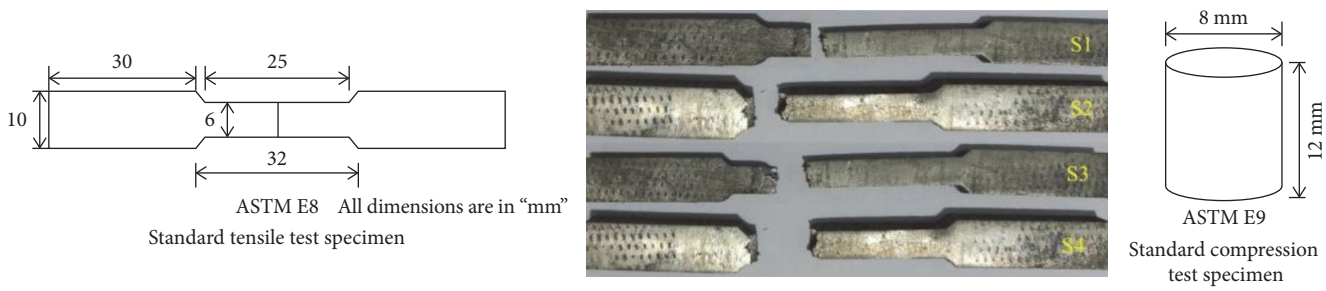

Figure 4: ASTM standards of tensile and compression test.

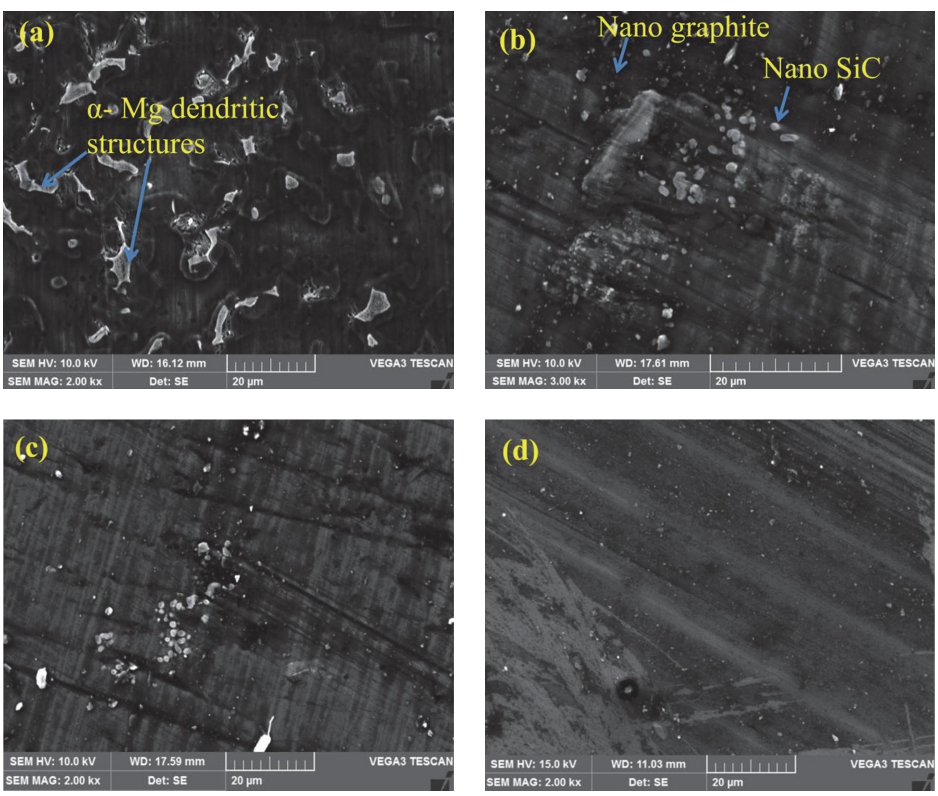

Figure 5: SEM images of (a) S1, (b) S2, (c) S3, and (d) S4 specimens.

and strong bonding between the AZ31D base alloy matrix and reinforcement. The reason for the little reduction in strength of the S4 nanocomposite was the porosity of the sample was increased compared to other nanocomposites.

EDS analysis revealed the presence of elements in AZ31D base alloy and nanocomposites, shown in Figure 6. Figure 6(a) shows the presence of aluminum (Al), zinc (Zn), and magnesium (Mg) elements in the AZ31D alloy.

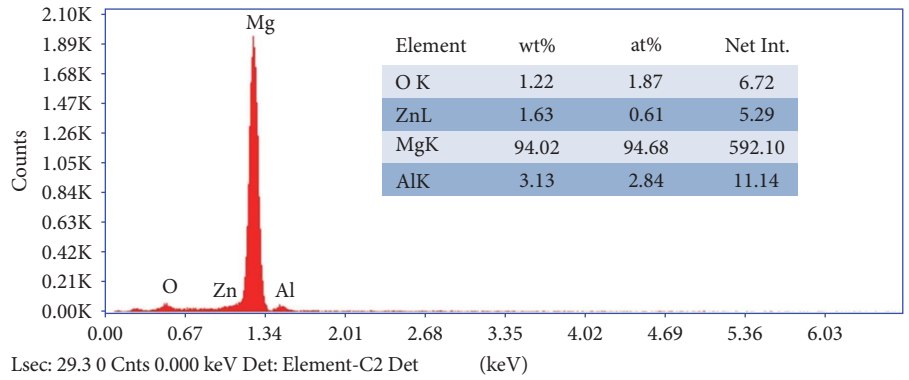

Element	wt%	at%	Net Int.
O K	1.22	1.87	6.72
ZnL	1.63	0.61	5.29
MgK	94.02	94.68	592.10
AlK	3.13	2.84	11.14

(a)

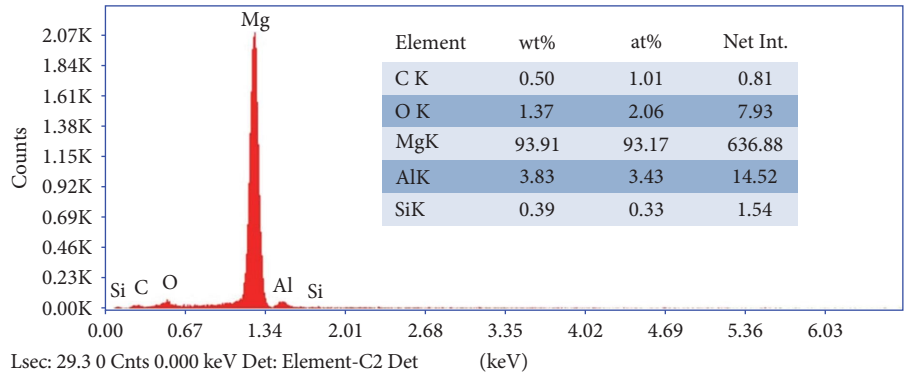

Element	wt%	at%	Net Int.
C K	0.50	1.01	0.81
O K	1.37	2.06	7.93
MgK	93.91	93.17	636.88
AlK	3.83	3.43	14.52
SiK	0.39	0.33	1.54

(b)

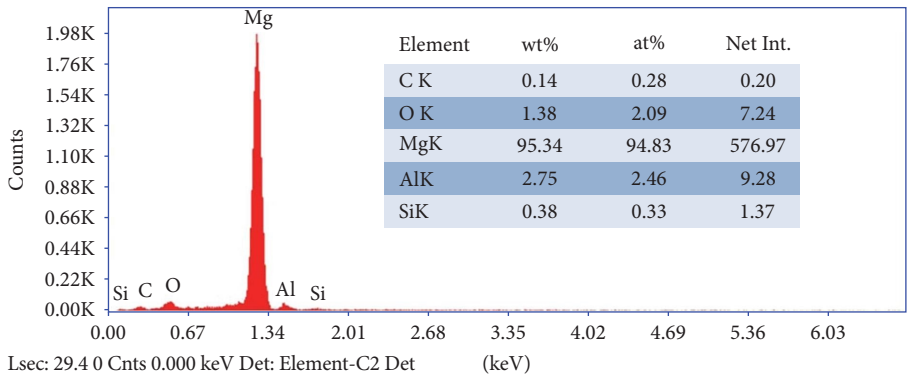

Element	wt%	at%	Net Int.
C K	0.14	0.28	0.20
O K	1.38	2.09	7.24
MgK	95.34	94.83	576.97
AlK	2.75	2.46	9.28
SiK	0.38	0.33	1.37

(c)

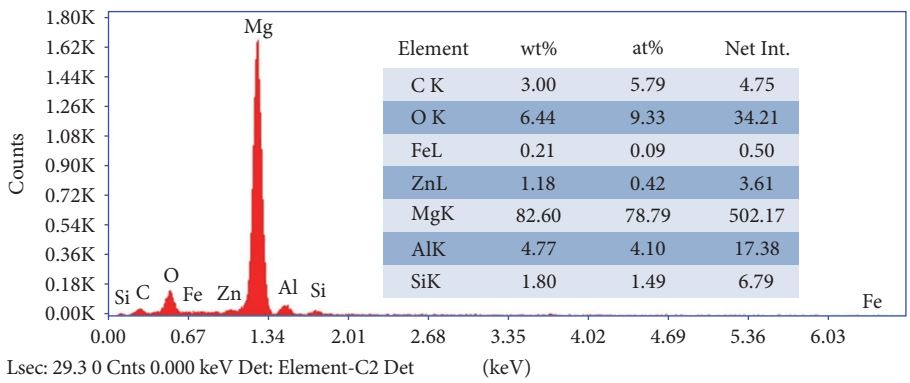

Element	wt%	at%	Net Int.
C K	3.00	5.79	4.75
O K	6.44	9.33	34.21
FeL	0.21	0.09	0.50
ZnL	1.18	0.42	3.61
MgK	82.60	78.79	502.17
AlK	4.77	4.10	17.38
SiK	1.80	1.49	6.79

(d)

Figure 6: EDS analysis of (a) S1, (b) S2, (c) S3, and (d) S4 specimens.

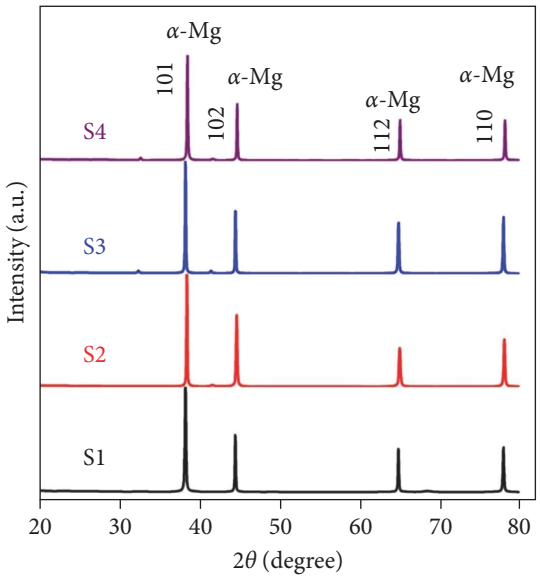

Figure 7: XRD spectrum of S1, S2, S3, and S4 specimens.

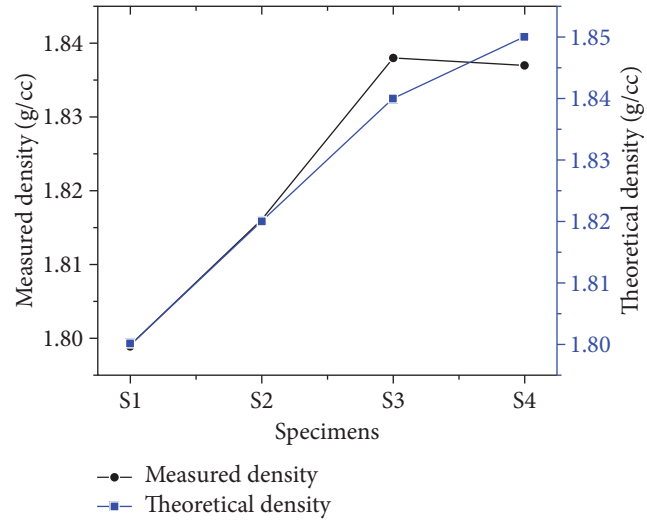

Figure 8: Variation of density for specimens.

Table 3: Density and porosity results.

Specimens	Theoretical density (g/cc)	Measured density (g/cc)	Porosity (%)
S1	1.8	1.799	0.05
S2	1.82	1.816	0.22
S3	1.84	1.838	0.11
S4	1.85	1.837	0.7

Table 4: Mechanical properties of AZ31D magnesium alloy and nanocomposites.

Specimens	Microhardness	UTS (MPa)	YS (MPa)	CS (MPa)
S1	71.89	102.3	65.09	173.42
S2	93.36	142.32	86.56	256.35
S3	98.89	162.94	105.25	315.56
S4	110	160.21	103.42	308.47

Figure 6(b)–6(d) shows the peaks of Al, Zn, Si, C, and Mg of the nanocomposite. The formation of magnesium oxide during the solidification process resulted in the peak of oxygen [29]. The impingement of the argon gas during the casting process prevents oxidation.

The XRD spectrums of the four specimens are illustrated in Figure 7. This analysis was used to identify the different phases and it indicates that α-Mg is the primary element that exists in the nanocomposite. The primary diffraction peaks (2θ) identified for α-Mg are 38.05°, 44.81°, 65.12°, and 78.23° [30], and the planes assigned for α-Mg peaks were (101), (102), (112), and (110). The peak intensity varies with varying weight fractions of SiC/Gr. Peak intensity increases with an increase in SiC/Gr wt% in AZ31D alloy. The base material is mainly composed of Mg in matrix form; the large peaks correspond to the parent AZ31D alloy.

3.2. Density and Porosity. The densities of the four specimens are illustrated in Table 3. The density of nanocomposites increased with decreased porosity as the increase particulates [24]. Here, the measured density was lower values as compared with the theoretical density due to the dispersion of atoms in the nanocomposite, as is represented in Figure 8. The S3 specimen exhibited less porosity than other nanocomposites. Therefore, it helps to improve the mechanical properties.

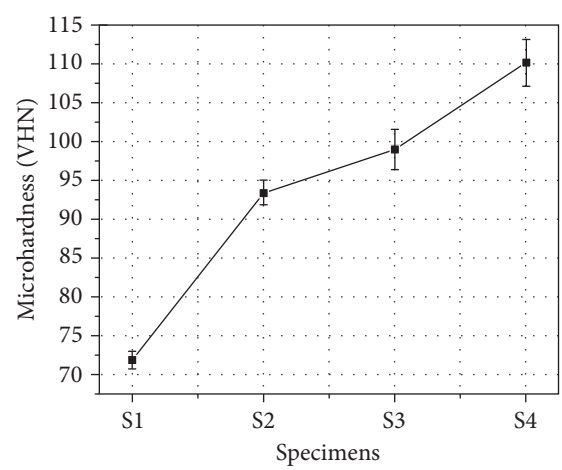

Figure 9: Microhardness of specimens.

3.3. Mechanical Properties. The mechanical properties of AZ31D alloy and nanocomposites are shown in Table 4. The microhardness of AZ31D alloy and nanocomposites are shown in Figure 9. The microhardness of the nanocomposite of the S4 specimen consists of a higher hardness value (110 VHN) as compared to AZ31D magnesium alloy (71.89 VHN). It shows clearly that the microhardness of nanocomposites exhibits 53% higher than the base alloy. The increase in hardness is

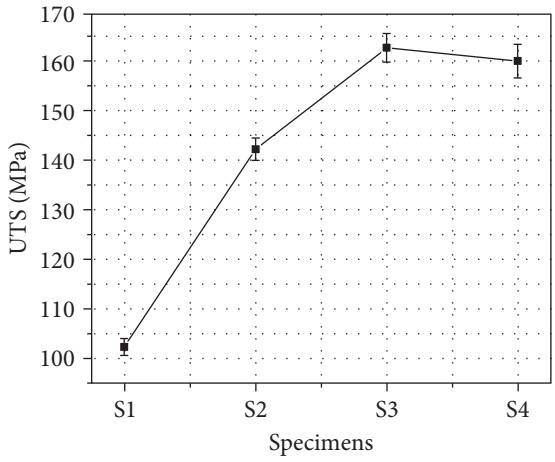

Figure 10: Ultimate tensile strength (UTS) of specimens.

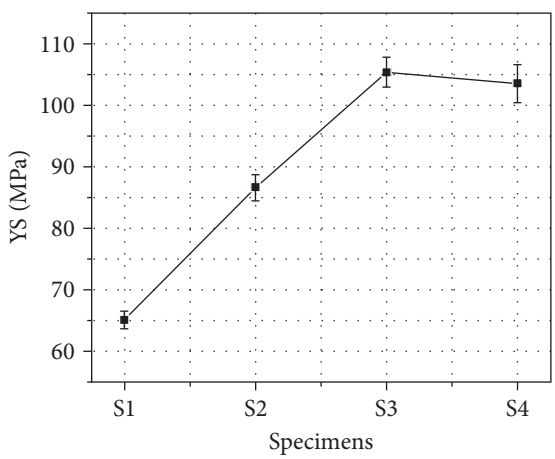

Figure 11: Yield strength (YS) of specimens.

attributed due to the addition of reinforcement particles in the matrix. The grain refinements of nanocomposites were improved due to the uniform distribution of the reinforcement particles, and it was confirmed by the SEM images. During solidification, the functioning of grain boundary anchors and nucleation locations for new grains will occur [22]. The result of an increase in microhardness was limiting the mobility of the dislocations [31].

UTS, YS, and compression strength (CS) of nanocomposites are shown in Table 4. The tight interfacial connection between the matrix and reinforcement is crucial for improving the tensile properties. Figures 10–12 show a little reduction in the strength of the S4 nanocomposite compared to the S3 nanocomposite. It was due to the formation of fewer voids and cracks in the microstructural image of the S4 nanocomposite. Another reason was the reinforcements overstrained the lattice. The grain size of the reinforcements bonding between the reinforcements and matrix may affect the composite's strength [24, 29]. The increased weight fractions of reinforcement will lead to enhance in the mechanical properties of S2 and S3 nanocomposites. Overall, the UTS

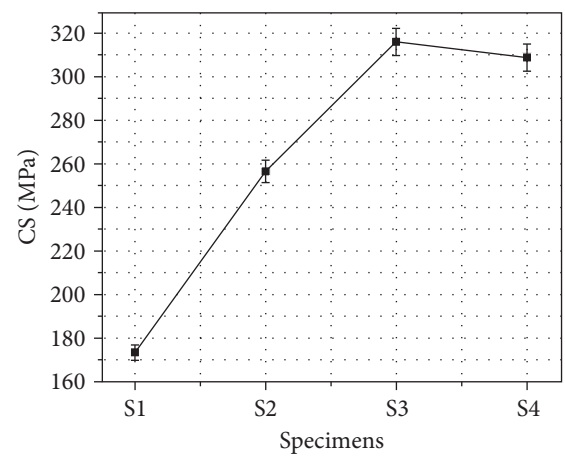

Figure 12: Compressive strength (CS) of specimens.

and YS were enhanced by 59% and 62%, respectively, as compared with the base alloy.

The nanocomposite's compressive strength varies depending on the particle size and how well the reinforcement bonds to the matrix [28, 32]. The superior strength is attained due to microstructural modifications. The reinforcement and matrix have a sufficient surface-to-surface bond, and the applied stress changes the matrix's interactions with the reinforced particles. The compressive strength of the alloy is 173.42 MPa, whereas improved compressive property was observed for the S3 nanocomposite because of the surface–surface bonding between reinforcement and matrix. Finally, by addition of SiC/Gr particles make more compressive strength, whereas the flexibility may reduce. Overall, the CS of nanocomposite was enhanced by 82% as compared with base alloy.

4. Conclusion

The results of the present investigation can be summarized as follows:

(i) AZ31D magnesium alloy and AZ31D-SiC-Gr nanocomposites with (2, 4, and 6 wt%) have been successfully fabricated using the stir-casting technique.

(ii) The microstructure analysis of AZ31D magnesium alloy and nanocomposites was performed. SEM images revealed the distribution of reinforcements in the matrix material, dendritic structure, grain boundaries, and defects in nanocomposites.

(iii) EDS analysis examined all the elements (Al, Zn, C, Si, and Mg) and their wt% and at% of the nanocomposites. XRD analysis provided complete information about phases of constitutes in the nanocomposites and indicated α-Mg was the primary element in the nanocomposite.

(iv) Microhardness of the nanocomposites was enhanced due to the presence of reinforcements. Finally, it was concluded that the nanocomposites were stabilized, and the load transformed equally to the entire nanocomposite.

(v) The porosity of the S3 specimen was exhibited less as compared with other nanocomposites. Therefore, the S3 specimen has shown better mechanical properties than other specimens.

(vi) UTS, YS, and CS were significantly enhanced by 59%, 62%, and 82%, respectively, due to the presence of SiC/Gr particles in the matrix. Perfect interfacial bonding and little clustering of reinforcement particles were attributed to improvement in tensile properties.

Based on the microstructure analysis and experimental investigations, concluded that the S3 nanocomposite has exhibited less porosity and better mechanical properties as compared to all other nanocomposites. The result of the present study was promising for the biomedicine and aviation industry.

Data Availability

The data used to support the findings of this study are available from the corresponding author upon request.

Conflicts of Interest

The authors declare that they have no conflicts of interest.

References

[1] P. Samal, P. R. Vundavilli, A. Meher, and M. M. Mahapatra, "Recent progress in aluminum metal matrix composites: a review on processing, mechanical and wear properties," *Journal of Manufacturing Processes*, vol. 59, pp. 131–152, 2020.

[2] M. Gupta and W. L. E. Wong, "Magnesium-based nanocomposites: lightweight materials of the future," *Materials Characterization*, vol. 105, pp. 30–46, 2015.

[3] R. Vara Prasad Kaviti, D. Jeyasimman, G. Parande, M. Gupta, R. Narayanasamy, and P. G. Koppad, "Improving the friction and wear characteristics of AZ31 alloy with the addition of Al_2O_3 nanoparticles," *Materials Research Express*, vol. 6, no. 12, Article ID 126505, 2019.

[4] S. You, Y. Huang, K. U. Kainer, and N. Hort, "Recent research and developments on wrought magnesium alloys," *Journal of Magnesium and Alloys*, vol. 5, no. 3, pp. 239–253, 2017.

[5] A. Dziubińska, A. Gontarz, K. Horzelska, and P. Pieśko, "The microstructure and mechanical properties of AZ31 magnesium alloy aircraft brackets produced by a new forging technology," *Procedia Manufacturing*, vol. 2, pp. 337–341, 2015.

[6] E. Suneesh and M. Sivapragash, "Comprehensive studies on processing and characterization of hybrid magnesium composites," *Materials and Manufacturing Process*, vol. 33, no. 12, pp. 1324–1345, 2018.

[7] S. K. Sharma and K. K. Saxena, "Effects on microstructure and mechanical properties of AZ31 reinforced with CNT by powder metallurgy: an overview," *Materials Today: Proceedings*, vol. 56, Part 4, pp. 2038–2042, 2022.

[8] A. K. Singh, S. Soni, and R. S. Rana, "A critical review on synthesis of aluminum metallic composites through stir casting: challenges and opportunities," *Advanced Engineering Materials*, vol. 22, no. 10, Article ID 2000322, 2020.

[9] I. Dinaharan, S. Zhang, G. Chen, and Q. Shi, "Development of titanium particulate reinforced AZ31 magnesium matrix composites via friction stir processing," *Journal of Alloys and Compounds*, vol. 820, Article ID 153071, 2020.

[10] A. Kumar, R. S. Rana, and R. Purohit, "Microstructure evolution, mechanical properties, and fractography of AA7068/Si_3N_4 nanocomposite fabricated thorough ultrasonic-assisted stir casting advanced with bottom pouring technique," *Materials Research Express*, vol. 9, no. 1, Article ID 015009, 2022.

[11] A. Khandelwal, K. Mani, N. Srivastava, R. Gupta, and G. P. Chaudhari, "Mechanical behavior of AZ31/Al_2O_3 magnesium alloy nanocomposites prepared using ultrasound assisted stir casting," *Composites: Part B: Engineering*, vol. 123, pp. 64–73, 2017.

[12] M. Torabi Parizi, A. Habibolahzadeh, and G. R. Ebrahimi, "Optimizing and investigating influence of manufacturing techniques on the microstructure and mechanical properties of AZ80-0.5Ca-1.5Al_2O_3 nanocomposite," *Materials Chemistry and Physics*, vol. 199, pp. 485–496, 2017.

[13] K. Singh, G. Singh, and H. Singh, "Investigation of microstructure and mechanical properties of friction stir welded AZ61 magnesium alloy joint," *Journal of Magnesium and Alloys*, vol. 6, no. 3, pp. 292–298, 2018.

[14] L. Rogal, B. Baran, P. Bobrowski, A. Tarasek, P. Ozga, and L. Litynska-Dobrzyńska, "Effect of nano-SiC on microstructure and mechanical properties of AZ91 magnesium alloy processed by thixomolding," *Solid State Phenomena*, vol. 285, pp. 133–138, 2019.

[15] M. Subramani, S.-J. Huang, and K. Borodianskiy, "Effect of SiC nanoparticles on AZ31 magnesium alloy," *Materials*, vol. 15, no. 3, Article ID 1004, 2022.

[16] S. H. Nourbakhsh, M. A. Shahrokhian, M. Hasanzadeh, and A. Atrian, "Investigation of mechanical and microstructural properties of AZ31/SiC nanocomposite fabricated by squeeze stir casting," *Materials Research Express*, vol. 5, no. 8, Article ID 086514, 2018.

[17] F. Vahedi, A. Zarei-Hanzaki, A. Salandari-Rabori, H. R. Abedi, A. Razaghian, and P. Minarik, "Microstructural evolution and mechanical properties of thermomechanically processed AZ31 magnesium alloy reinforced by micro-graphite and nano-graphene particles," *Journal of Alloys and Compounds*, vol. 815, Article ID 152231, 2020.

[18] S.-J. Huang, C.-C. Lin, J.-Y. Huang, and R. Tenne, "Mechanical behavior enhancement of AZ31/WS_2 and AZ61/WS_2 magnesium metal matrix nanocomposites," *Advances in Mechanical Engineering*, vol. 10, no. 2, pp. 1–14, 2018.

[19] S.-J. Huang, M. Subramani, and C.-C. Chiang, "Effect of hybrid reinforcement on microstructure and mechanical properties of AZ61 magnesium alloy processed by stir casting method," *Composites Communications*, vol. 25, Article ID 100772, 2021.

[20] M. Subramani, S.-J. Huang, and K. Borodianskiy, "Effect of WS_2 nanotubes on the mechanical and wear behaviors of AZ31 stir casted magnesium metal matrix composites," *Journal of Composites Science*, vol. 6, no. 7, Article ID 182, 2022.

[21] N. Anand and S. Senthil Kumaran, "Development and influence of tribomechanical properties on magnesium based hybrid metal matrix composites—a review," *Materials Research Express*, vol. 7, Article ID 036520, 2020.

[22] J. Pradeep Kumar, D. S. Robinson Smart, S. Manova, and N. Ummal Salmaan, "Effect of TaC/Ti/Si_3N_4 hard ceramics on mechanical and microstructural behaviour of AA7075 processed through stir casting process," *Advances in Materials Science and Engineering*, vol. 2022, Article ID 6804011, 13 pages, 2022.

[23] ASTM Standard B962-13, *Standard Test Methods for Density of Compacted or Sintered Powder Metallurgy (PM) Products*

Using Archimedes' Principle, ASTM International, West Conshohocken, PA, USA, 2013.

[24] A. H. Khan, S. A. A. Shah, F. Umar et al., "Investigating the microstructural and mechanical properties of novel ternary reinforced AA7075 hybrid metal matrix composite," *Materials*, vol. 15, no. 15, Article ID 5303, 2022.

[25] ASTM Standard E384, *Standard Test Method for Knoop and Vickers Hardness of Materials*, ASTM International, West Conshohocken, PA, USA, 2013.

[26] ASTM Standard E8, *Standard Test Methods for Tension Testing of Metallic Materials*, ASTM International, West Conshohocken, PA, USA, 2013.

[27] ASTM Standard E9, *Standard Test Methods for Compression Testing of Metallic Materials*, ASTM International, West Conshohocken, PA, USA, 2013.

[28] B. Saleh, J. Jiang, R. Fathi, Q. Xu, L. Wang, and A. Ma, "Study of the microstructure and mechanical characteristics of AZ91–SiCp composites fabricated by stir casting," *Archives of Civil and Mechanical Engineering*, vol. 20, Article ID 71, 2020.

[29] S. Sharma, J. Singh, M. K. Gupta et al., "Investigation on mechanical, tribological and microstructural properties of Al–Mg–Si–T6/SiC/muscovite-hybrid metal–matrix composites for high strength applications," *Journal of Materials Research and Technology*, vol. 12, pp. 1564–1581, 2021.

[30] U. Rokkala, S. Bontha, M. R. Ramesh, V. K. Balla, A. Srinivasan, and S. V. Kailas, "Tailoring surface characteristics of bioabsorbable Mg–Zn–Dy alloy using friction stir processing for improved wettability and degradation behavior," *Journal of Materials Research and Technology*, vol. 12, pp. 1530–1542, 2021.

[31] V. K. Soni and A. K. Sinha, "Effect of alloying elements, phases and heat treatments on properties of high-entropy alloys: a review," *Transactions of the Indian Institute of Metals*, vol. 76, pp. 897–914, 2023.

[32] K. C. K. Kumar, B. R. Kumar, and N. M. Rao, "Microstructural, mechanical characterization, and fractography of AZ31/SiC reinforced composites by stir casting method," *Silicon*, vol. 14, pp. 5017–5027, 2022.

Hindawi
Journal of Nanomaterials
Volume 2023, Article ID 1055071, 13 pages
https://doi.org/10.1155/2023/1055071

Research Article

Fabrication and Experimental Estimation of Mechanical Properties of Kevlar-Glass/Epoxy Interwoven Composite Laminate

J. Jensin Joshua,[1] **Dalbir Singh**,[1] **Sai Hemanth Kumar Vennelakanti**,[1] **P. Sivaprakasam**,[2] **D. Raja Joseph**,[1] **and P. S. Venkatanarayanan**[1]

[1]*School of Aeronautical Sciences, Hindustan Institute of Technology and Science, Chennai, India*
[2]*Department of Mechanical Engineering, College of Electrical and Mechanical Engineering, Addis Ababa Science and Technology University, Addis Ababa, Ethiopia*

Correspondence should be addressed to P. Sivaprakasam; shiva@aastu.edu.et

Received 1 August 2022; Revised 4 December 2022; Accepted 12 April 2023; Published 16 May 2023

Academic Editor: N. Senthilkumar

Hybrid composites made of natural and synthetic fibers are stronger, lighter, cheaper, biodegradable, and greener than conventional metals, and they are replacing conventional metals. The primary objective of the study was to examine the mechanical properties of interwoven hybrid composite laminates. Kevlar and glass fiber are used as reinforcement for this work. The fibers are woven together using various weaving techniques. 1×1, 3×3, and 5×5 weaving patterns are considered to explore the properties of the laminates. The composites are woven using a conventional handloom method. As a matrix, LY556 resin and HY951 hardener are combined at a ratio of $10:1$. The composites are cured using compression molding. The cured composites are assessed for their tensile strength, flexural strength, compressive strength, interlaminar shear strength, impact strength, and fracture toughness. The highest tensile, compressive, and flexural strength were found in the 1×1 pattern, shear strength and fracture toughness were found in the 5×5 pattern, which finds applications in aerospace and defense sectors, and 3×3 dominated in impact strength; as a result, it can be used in bulletproof applications. At last, a scanning electron microscope (SEM) was used to visualize the matrix-reinforcement bonding. The microscopic images show the ripped-out fibers because of the tensile test. The shards in SEM are evident that impact force breaks the matrix elements in a brittle manner.

1. Introduction

Composites are made of two or more constituent materials. At the macroscopic level, matrix materials use reinforcement fibers to form composite structures. The composites are classified into three types based on the underlying material: ceramic, polymeric, and metallic composites. Polymeric composites are made up of two types of polymeric base materials: thermosets and thermoplastics. Reinforcing fibers are also used in short, long, and continuous forms, and their primary function is to withstand forces applied to the material and cause force transmission from one fiber to another [1].

Composite materials have proven their worth by being widely used in mechanical industries such as aerospace, marine, and automobiles. Because of their better strength, composite materials have largely supplanted metals in many industries [2]. In the aircraft sector, the use of these materials reduces structural weight and, as a result, fuel consumption. Furthermore, composite materials are more durable and resistant to fatigue, impact, and corrosion [3, 4]. Polymer-based composites, which are formed of a polymer resin as the basis and fiber reinforcements, are one of the most popular composites [2].

Due to their enhanced qualities, such as ease of manufacturing and low cost, these materials are widely produced and employed. The adhesion of the matrix and fiber is a key factor in defining the final attributes of the composite material, particularly its mechanical properties, which determines how effective the reinforcement is [5]. Epoxy resin is extensively employed in the fabrication of polymer-based

composites due to its appealing mechanical properties, optimal adhesion, strong chemical resistance, and wide diversity. Because fibers like Kevlar, basalt, carbon, and glass each have their advantages and limitations in terms of mechanical characteristics and reactivity to different impacts, hybridization appears to be one of the greatest approaches for improving the overall qualities of composites [3, 6, 7].

Kevlar is an aromatic polyamide family organic fabric. The strongly aligned chains of molecules in Kevlar fibers generate a considerable anisotropy in their mechanical characteristics. Because there is no appreciable difference in mechanical properties between orientations perpendicular to the fiber axis, Kevlar fibers are commonly considered transversely isotropic, as are many other high-performance fibers. The distinctive qualities and chemical composition of fully aromatic polyamides (aramids) set them apart from other commercial, man-made fibers, particularly Kevlar. Kevlar has a one-of-a-kind combination of strength, modulus [8, 9], toughness, and thermal stability. It was created for high-stress industrial and advanced technology applications. Many different varieties of Kevlar® are now manufactured to accommodate a wide range of end purposes.

Kevlar is a material that has long been used in bulletproof [10] vests and military helmets due to its strength and excellent impact reaction (Kevlar). Kevlar fibers have high tensile strength and elastic flexibility, as well as high impact and fire resistance, and low density [3]. However, Kevlar has low chemical resistance and a weak reactivity to pressure. Although Kevlar has excellent longitudinal properties, its transverse properties are undesirable. It is beneficial to hybridize it with other fibers such as glass and carbon [3], basalt (basalt paper), and ceramics to increase these properties.

The most often used synthetic fiber for reinforcing thermoplastic and thermoset polymers is glass fiber. Glass fiber possesses a wide range of distinctive properties, such as strong bending resistance, tensile and compressive strength, non-flammability, resistance to high temperatures and humidity, resistance to chemical and biological effects, and a relatively low density. Furthermore, glass fiber is used as a constituent in various defensive elements to boost laminate strength. Because of its convenience and simplicity of access in comparison to other synthetic fibers, glass fiber is the most well-known synthetic fiber used in these hybrid composites [11, 12].

Although significantly more expensive than glass fibers, Kevlar fiber has a unique combination of high stiffness, strength, low density, and high elongation at fracture, resulting in outstanding impact resistance. Hybrid composites are produced by joining the upside of one fiber with the upside of another. For example, high modulus fibers, such as graphite, have an extremely high solidarity to weight proportion, although their effect quality is typically regarded as reasonably low in comparison [11, 13]. As a result, hybrid composites based on these Kevlar/glass fibers can be designed to achieve a reasonable balance of tensile, flexural, and impact properties [14].

Hybrid composite refers to composites comprising more than one type of fiber material. Hybrid composites are appealing structural materials because they allow designers to tailor composites and achieve properties that are not possible in binary systems. It is a more cost-effective way of using expensive fibers, such as graphite and boron, and hybrids can achieve a balance of stiffness and strength, as well as increased elongation to failure [15, 16].

The mechanical strength and stiffness of a composite can be altered depending on its type and orientation and the proportions of its constituent materials. When considering a fabric, the properties of the fibers and yarns fundamentally dictate the fabric properties [17]. But geometric criteria, such as the fabric weave structure, knitted or non-woven construction, cover factor, and yarn crimp in woven fabrics, must also be addressed, as the matrix-to-fiber connection and the underlying matrix mechanical characteristics change depending on those [18, 19]. It has been suggested that combining high-strength and high-stiffness fibers might result in fibers with improved properties [20, 21]. The mechanical and wear properties of composites can be improved through hybridization [22].

Some of the mechanical and thermal properties of the Kevlar/glass fiber interwoven hybrid composites by varying proportions of cyanate ester/benzoxazine resin blend are studied by Zegaoui et al. [23]. This research investigates the mechanical properties of a hybrid Kevlar/glass-epoxy interwoven composite laminates such as tensile, flexural, compressive, interlaminar shear, impact strengths, and the mode one fracture toughness to offer a complete comparison of these properties.

2. Materials and Methods

In this research, two different fibers consisting of Kevlar 49 and C-Glass were chosen as the reinforcement for the hybrid composite because of their higher mechanical properties compared to other variants. A GSM determines the weight and cost of the fabric to fabricate a laminate with less cost and reduced weight with good properties 240 GSM fabric fibers are selected for the study. Epoxy LY556 and hardener HY951 are used as the matrix material because of their advanced impact characteristics. The epoxy and the hardener were mixed in a 10 : 1 weight ratio. Table 1 displays the mechanical characteristics of the reinforcement and matrix components.

2.1. Weaving. The two fundamental weaving parts that convert thread or yarn into fabric are the warp and the weft. The transverse weft (often called the woof) is dragged through and inserted over and under the lengthwise or longitudinal warp strands, which are held motionless in tension on a frame or loom. The Kevlar and glass threads are woven together to create the composite lamina. Three different laminates are made by altering the Kevlar and glass fiber weaving pattern. Plain, twill, and satin weaves are the three main types. Plain weave is a 1×1 weave in which each warp strand passes over and beneath each weft strand. 3×3 twill weaves: the weft thread is passed over two or more warp threads to make a twill weave, which is then repeated one other warp thread over to create a diagonal line [24].

Table 1: Properties of reinforcement and matrix.

S. no	Density (g/cc)	Tensile strength (MPa)	Elastic modulus (GPa)	Elongation at break (%)
Kevlar 49	1.44	3,620	76	2.8
C glass	2.52	3,310	68.9	4.8
LY556	1.14	73.3	3.47	4.5
HY951	1.19	52	2.8	11

Table 2: Weaving pattern.

	S. no	Plain	Twill	Satin
Vertical	Kevlar	1	3	5
Horizontal	Glass	1	1	1

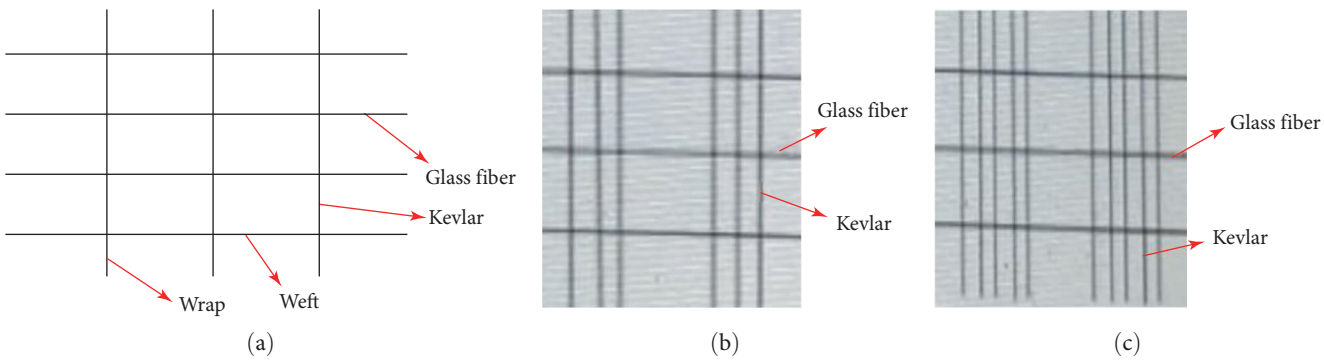

Figure 1: Weaving patterns: (a) 1 × 1 weave; (b) 3 × 3 weave; (c) 5 × 5 weave.

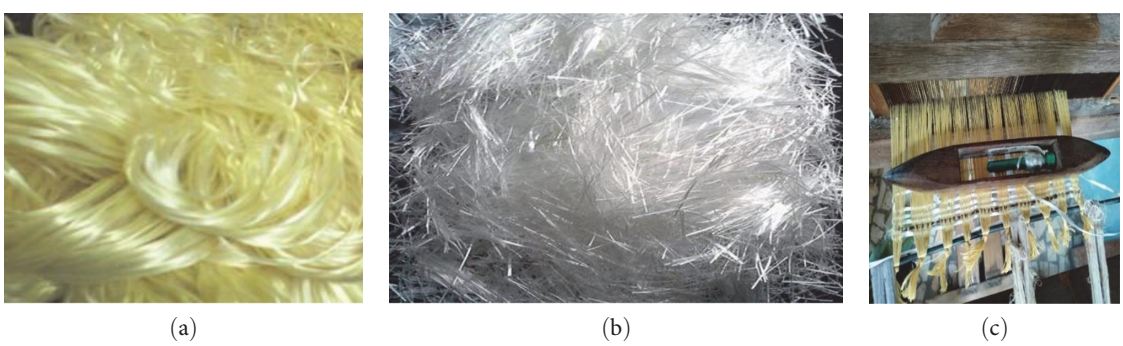

Figure 2: Reinforcement fibers: (a) reinforcement fiber (Kevlar); (b) reinforcement fiber (glass fiber); (c) weaving of fibers.

Harness satin 5 × 5 weave: each fill strand in this weave floats over five warp strands before tucking beneath one warp strand. This is more malleable than a twill weave and adapts well to intricate curves. Weaving pattern arrangements are given in Table 2, and the Weaving patterns are shown in Figure 1 1 × 1 (Figure 1(a)), 3 × 3 (Figure 1(b)), 5 × 5 (Figure 1(c)).

2.2. Compression Molding. Each laminate is made of seven laminae that are interwoven with reinforcement fibers in one of three possible designs using the traditional handloom process (Kanchipuram). The laminate was then put into a mold for compression molding [25] at room temperature at 5 bar pressure, and it was cured for 5 hr. Through compression molding, 250 mm × 250 mm in-plane Kevlar and Glass fiber-reinforced composite laminates of 2.8 mm thickness were manufactured. The plates from the fabrication process are cut using a high-speed hacksaw to the test specifications. The Figure 2 show reinforcement fibers (Kevlar Figure 2(a), glass fiber 2(b)).

2.3. Testing. The mechanical characteristics of the hybrid composite laminates were evaluated. The test specimens were prepared in accordance with ASTM guidelines. According to ASTM D3039, D790-03, D3410, D256, and D5528-1, the tensile, flexural, compression, impact, and mode one fracture tests were carried out [8, 26]. As the fixture is not available for the interlaminar shear test under ASTM

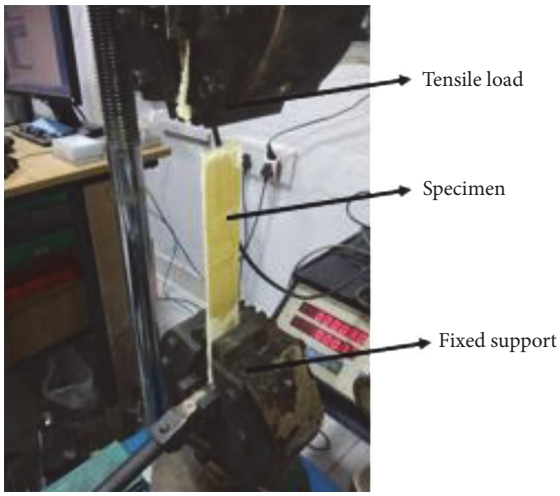

Figure 3: Tensile test setup.

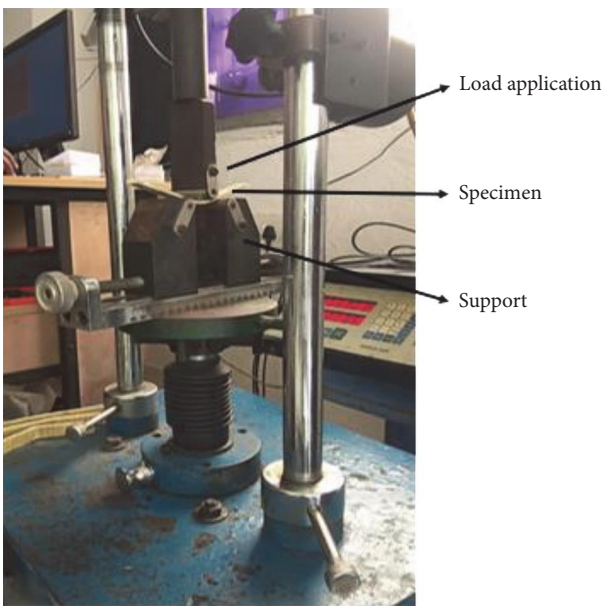

Figure 4: Flexural test setup.

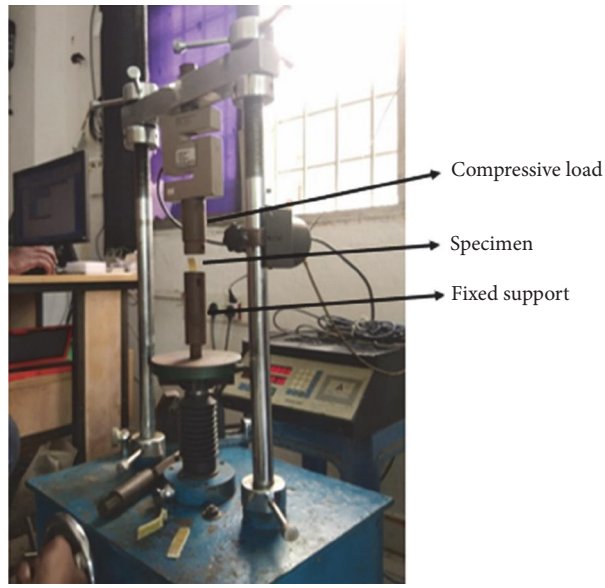

Figure 5: Compression test setup.

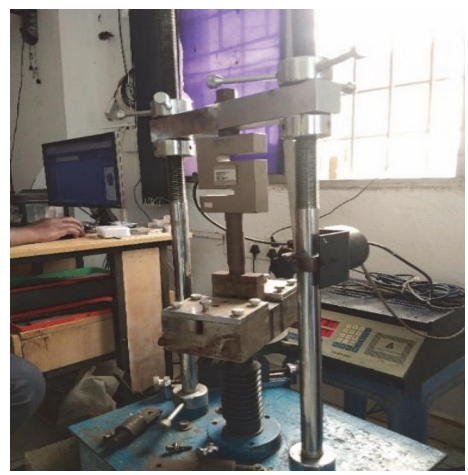

Figure 6: Interlaminar shear test setup.

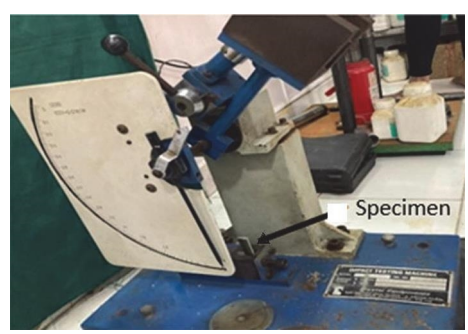

Figure 7: Izod impact test setup.

standards, a rectangular-shaped specimen (length × width × thickness 25 mm × 9.5 mm × 2.8 mm) where length is more significant than six times, width greater than two times the thickness of the specimen suitable for the available fixture was used for testing [27].

As the hardness test comes under physical characterization instead of the hardness test mode-1 fracture test was performed in this research. Tensile tests were conducted using a universal testing machine (UTM) with a tensile grip attached to it, as seen in Figure 3. The UTM has been used to conduct flexural, compression, and interlaminar shear tests, as shown in Figures 4–6.

Figure 7 depicts an Izod impact testing device; the sample mounted to take the impact was indicated with an arrow mark. Five samples per weaving pattern were considered for tensile, flexural, compression, and shear tests. Four samples per weaving pattern were taken for the mode-1 fracture test. One sample for each weaving pattern was taken for the Izod impact test, as the error is less within the same weaving pattern and used [11, 28].

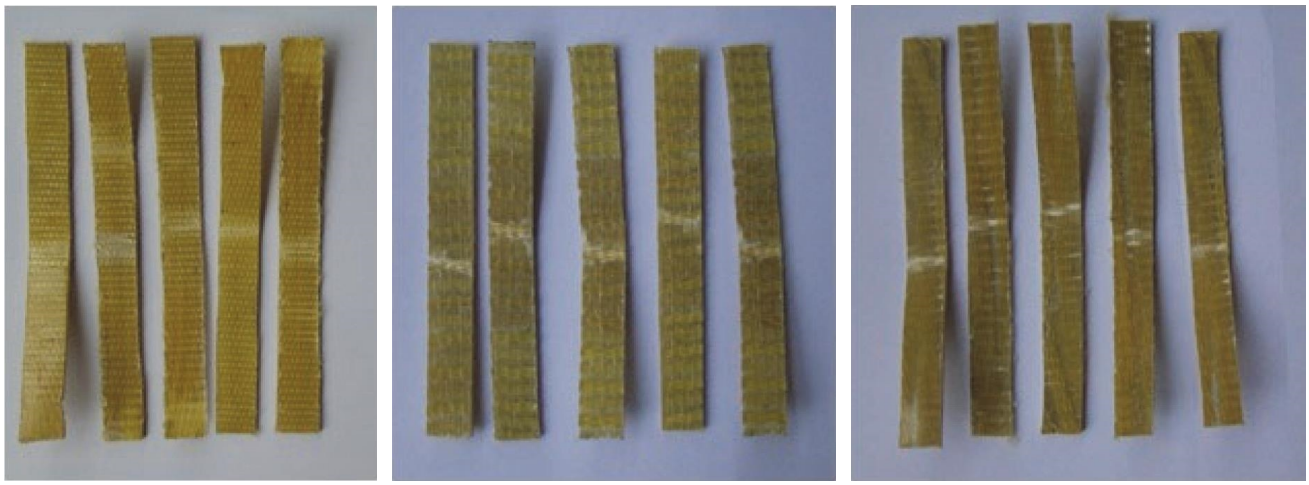

1 × 1 3 × 3 5 × 5

Figure 8: Specimens after flexural test.

Table 3: Tensile test results.

Orientation	Cross sectional length (l) (mm)	Cross sectional breadth (b) (mm)	Cross sectional area (A) ($l \times b$) (mm^2)	Load (P) (N)	Tensile strength ($\sigma_t = P/A$) (MPa)	Average tensile strength (MPa)
	3.9	27	105.3	7,000	66.48	
	3.8	26	98.8	7,370	74.60	
1 × 1	3.6	27.5	99	7,690	77.68	74.80
	3.7	26.5	98.05	7,520	76.70	
	3.7	27	99.9	7,850	78.58	
	3.7	27	99.9	6,740	67.47	
	3.8	27.2	103.36	7,350	71.11	
3 × 3	3.9	26.9	104.91	6,690	63.77	68.71
	3.8	26.5	100.7	7,180	71.30	
	3.6	27.5	99	6,920	69.90	
	3.7	29	107.3	6,660	62.07	
	3.8	28	106.4	6,580	61.84	
5 × 5	3.6	28.6	102.96	7,410	71.97	66.45
	3.9	27.5	107.25	6,940	64.71	
	3.7	27	99.9	7,160	71.67	

The 15 specimens undergone flexural tests are shown in Figure 8. Scanning electron microscopy (SEM) was used to examine the cracked surfaces of the tested specimens (VEGA3 TESCAN). SEM examination was done on the shattered surface of the specimens put through the mechanical testing. This was done to evaluate the material's quality and identify the type of failure that occurred when the appropriate test's load was applied.

3. Results and Discussion

3.1. Tensile Test. The tensile test determines the maximum load (tensile strength) that a material can withstand without breaking [29]. Five samples of each type (1 × 1, 3 × 3, and 5 × 5) were used in the tensile testing, yielding 15 readings. Five values of every composite are averaged to provide an average value for each laminate suggested by Felipe et al. [13]. The results are presented in Table 3. The three hybrid composite laminates employed in the current study's tensile strengths comparison are shown in Figure 9.

The 1 × 1 pattern laminate produced the maximum tensile strength of these three distinct composites, measuring 74.80 MPa. The 5 × 5 pattern had the weakest tensile strength of all, measuring 66.45 MPa. The 3 × 3 pattern achieved a tensile strength of 68.71 MPa. The mechanical properties of the latter are comparable to those of pure laminates, according to the theory behind the characteristics of hybrid composite laminates. The same is true for the current study [9, 30].

One of the test specimens is shown in Figure 10. The specimens cracked at the gauge region and between the tensile grips, as seen in Figure 10. These cracks appear when

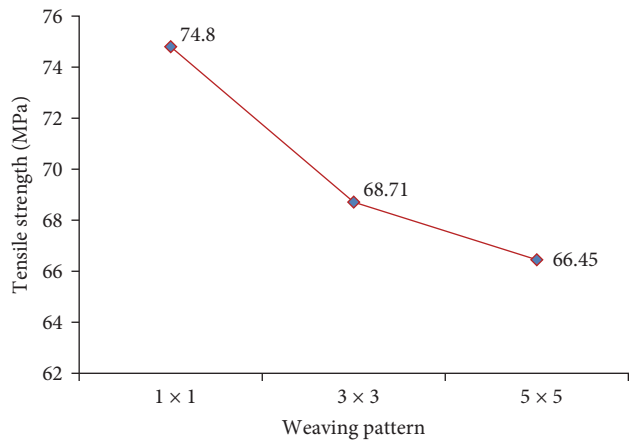

Figure 9: Tensile strength vs. specimens orientation.

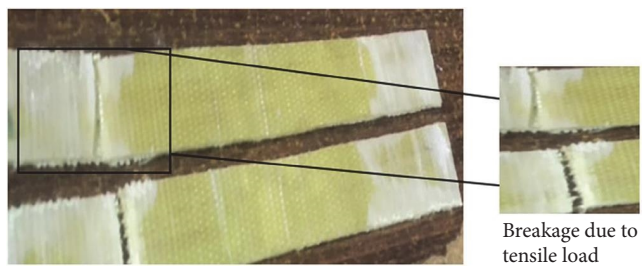

Figure 10: Test specimens after tensile test.

Table 4: Flexural test results.

Orientation	Gauge length $L = 4 \times b$ (mm)	Breadth (b) (mm)	Thickness (t) (mm)	Load (P) (N)	Flexural strength ($F = 3PL/2bt^2$) (MPa)	Average flexural strength (MPa)
	55.2	13.8	3.2	1,390	814.45	
	55.2	13.4	2.8	1,310	1,032.48	
1 × 1	56	14.1	3.1	1,430	886.49	905.68
	56.4	14	3.2	1,380	814.37	
	55.8	13.6	2.9	1,340	980.61	
	56	14	3.3	1,480	815.43	
	55.2	13.8	3.2	1,410	826.17	
3 × 3	54	13.5	3.1	1,390	867.85	860.86
	55.7	14.2	2.9	1,430	1,000.46	
	56.3	13.6	3.2	1,310	794.39	
	52.8	13.2	3.2	1,440	843.75	
	55.6	13.9	3.1	1,310	817.90	
5 × 5	54.8	13.7	3	1,390	926.67	859.79
	55.3	14.3	3.3	1,410	751.05	
	53.8	13.6	2.9	1,360	959.57	

tensile testing occurs at the gauge region under constant stress. Additionally, it is clear from Figure 10 that the complete specimen always fails to be brittle, which is proper under the same stress and strain behavior.

The plain weave specimen is less pliable and holds wrap and weft well. The number of crossover points is more in plain fabric and less porous. As a result, it can withstand more tensile load than any other pattern [30]. The tensile strength of the 1 × 1 pattern is 8.1% higher than the 3 × 3 pattern and 11.2% higher than the 5 × 5 pattern.

3.2. Flexural Test. The flexural test results are given in Table 4. Figure 11 compares the flexural strengths of three hybrid composite laminates used in this study.

The photographs of the test specimens following the flexural testing are displayed in Figure 12. It can be seen

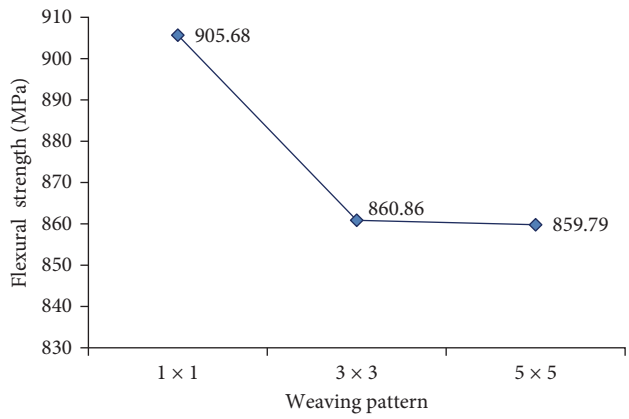

Figure 11: Flexural strength vs. specimens orientation.

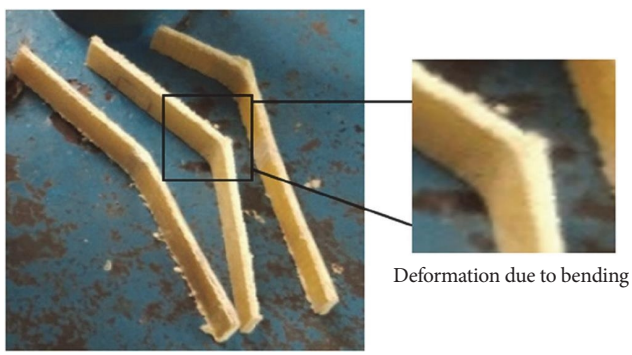

Figure 12: Test specimens after flexural test.

Table 5: Compression test results.

Orientation	Cross sectional length (l) (mm)	Cross sectional breadth (b) (mm)	Cross sectional area (A) ($l \times b$) (mm^2)	Load (P) (N)	Compressive strength ($\sigma_c = P/A$) (MPa)	Average compressive strength (MPa)
	3	14	42	6,170	146.90	
	3.3	13.8	45.54	6,250	137.24	
1 × 1	3.5	13.6	47.6	6,530	137.18	136.05
	3.7	14.1	52.17	6,380	122.29	
	3.6	13.4	48.24	6,590	136.61	
	3.4	14.4	48.96	6,380	130.31	
	3.7	13.9	51.43	6,050	117.64	
3 × 3	3.6	13.7	49.32	6,010	121.86	122.54
	3.5	14.1	49.35	6,140	124.42	
	3.7	14.3	52.91	6,270	118.50	
	3.7	13.8	51.06	6,280	122.99	
	3.5	13.7	47.95	6,580	137.23	
5 × 5	3.7	13.9	51.43	6,110	118.80	123.94
	3.9	14.1	54.99	6,370	115.84	
	3.7	13.4	49.58	6,190	124.85	

that under the influence of the three-point bending force, all of the 1 × 1, 3 × 3, and 5 × 5 patterns bowed differently. This demonstrates that the properties exhibited by the composites were significantly influenced by the order in which the reinforcing fibers were woven into the composite materials. However, the figures did not represent the magnitude of the flexural load on the specimens. Instead, it was investigated using the test's quantitative data.

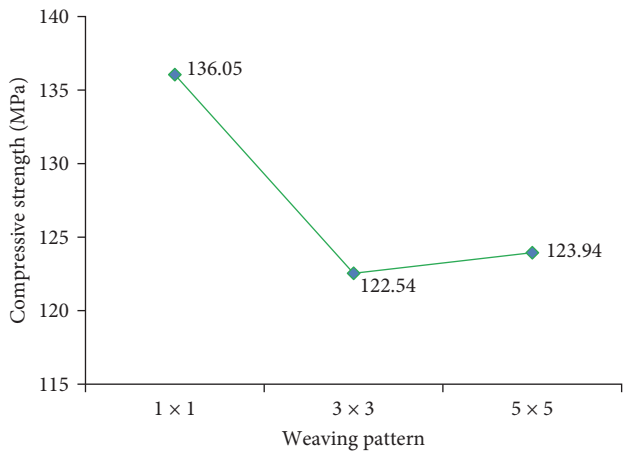

Figure 13: Compressive strength vs. specimens orientation.

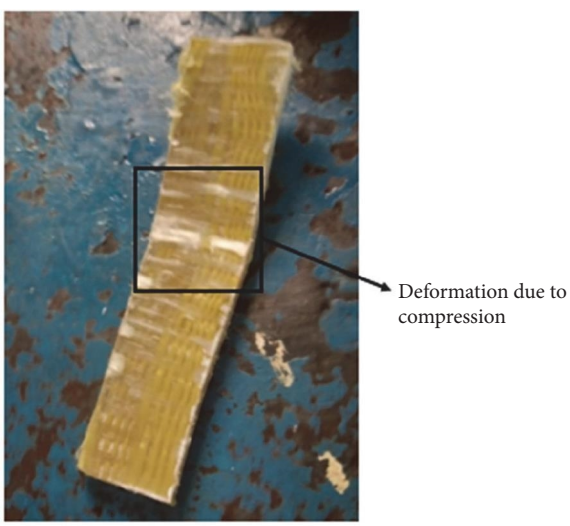

Figure 14: Test specimens after compression test.

The 1 × 1 pattern has the highest flexural strength of 905.68 MPa [9]. The flexural strength of the 3 × 3 pattern was 860.86 MPa, while the flexural strength of the 5 × 5 pattern was 859.79 MPa. The plain weaving pattern is less flexible and has more crossovers, so it has more bending resistance [30]. As a result, it can withstand a higher load before its deformation. The flexural strength of the 1 × 1 pattern is 4.9% higher than the 3 × 3 and 5.1% higher than the 5 × 5 pattern.

3.3. Compression Test. A compression test is used to determine the compressive force acting on a material. The specimen is pushed against it while it is being held in the fixture. The compressive strength needed to push the specimen to the point where it tends to crack is calculated. The results of compression testing are tabulated in Table 5. Figure 13 compares the compressive strengths of three hybrid composite laminates used in this study.

A sample undergoing a compression test is shown in Figure 14. Out of the three interwoven hybrid composite laminates, the 1 × 1 pattern has the highest compression strength of 136.05 MPa. The 3 × 3 pattern has the lowest compression strength of 122.54 MPa, and the 5 × 5 pattern has a compression strength of 123.94 MPa.

To withstand higher compressive loads, the material must be rigid enough. The twill and satin patterns are flexible and have fewer crossovers than the plain pattern. As a result, the plain pattern can withstand higher compressive loads [30]. The compressive strength of 1 × 1 pattern is 8.9% higher than the 5 × 5 pattern and 9.9% higher than the 3 × 3 pattern laminate.

3.4. Interlaminar Shear Test. The interlaminar shear strength test evaluates the composite's resistance to delaminating under shear forces parallel to the layers of the laminate and, consequently, to the interface between the adhesive and adherent [31]. The results of the interlaminar shear test are tabulated in Table 6. Figure 15 shows the variation of the interlaminar shear strengths of the three interwoven composite laminates used in this study.

The 5 × 5 hybrid composite laminate has the highest shear strength of the three interwoven hybrid composite laminates, measuring 132.66 MPa, and the 1 × 1 pattern has the lowest shear strength, measuring 129.37 MPa. 130.91 MPa is the shear strength of the 3 × 3 pattern. The interlacing is significantly less, the fabric is loose in satin weave compared to other parameters, and the density is high. As a result, fabric yarns move easily and bunch together [32]. The shear strength of the 5 × 5 pattern is 1.3% higher than the 3 × 3 pattern and 2.5% higher than the 1 × 1 pattern.

3.5. Izod Impact Test. The Izod impact strength test is a technique for evaluating a material's impact resistance [26]. The pivoting arm (pendulum) of weight 5 kg is released from a height of 150 mm at an angle of 90° to impact the specimen. The notch angle of the specimen is 45°. The sample is broken when the arm swings downward and strikes a notched sample. The material's resistance to impact is computed. The results of the impact test are tabulated in Table 7. Figure 16 compares the Izod impact strengths of the three hybrid laminates.

Figure 17 shows the specimen undergoing the Izod impact test. According to the study, the 3 × 3 pattern has an impact strength of 7.3 J, which is higher than the 4.5 and 4.8 J impact strengths of the 1 × 1 and 5 × 5 patterns, respectively.

When an arm hits the sample, the fibers take the impact to resist the breakage. The twill weave pattern absorbs more energy before failure as its crossovers are limited, and the weft is aligned diagonally [32]. The satin pattern is also flexible, but it does not have a more robust diagonal line in it; as a result, it has less impact strength than the 3 × 3 pattern. The impact strength of the 3 × 3 pattern is 34.2% higher than the 5 × 5 pattern and 38.3% higher than the 1 × 1 pattern.

3.6. Mode-1 Fracture Test. The decomposition of crack tip stresses into three loadings, or "modes," is referred to as modes of fracture. The modes are Mode-1 stress orthogonal to the crack surface's local plane. Mode-1 fracture test is performed to measure the material's fracture toughness. The specimen is held vertically in the fixture by two bolts, one on each side. The specimen is then permitted to be

Table 6: Interlaminar shear test results.

Orientation	Breadth (b) (mm)	Thickness (t) (mm)	Load (P) (N)	Shear strength ($\tau = 3P/4bt$) (MPa)	Average shear strength (MPa)
	9.4	3.1	4,970	127.92	
	9.6	3.2	4,960	121.09	
1 × 1	9.6	2.9	5,070	136.58	129.37
	9.5	3	5,210	137.11	
	9.4	3.2	4,980	124.17	
	9.2	3.2	5,105	130.05	
	9.4	3.1	5,015	129.08	
3 × 3	9.5	2.9	4,810	130.94	130.91
	9.3	3.1	5,040	131.11	
	9.6	2.8	4,780	133.37	
	9.1	3.1	4,680	124.42	
	9.3	2.8	5,120	147.47	
5 × 5	9.6	3	4,730	123.18	132.66
	9.5	3.1	5,070	129.12	
	9.3	2.8	4,830	139.11	

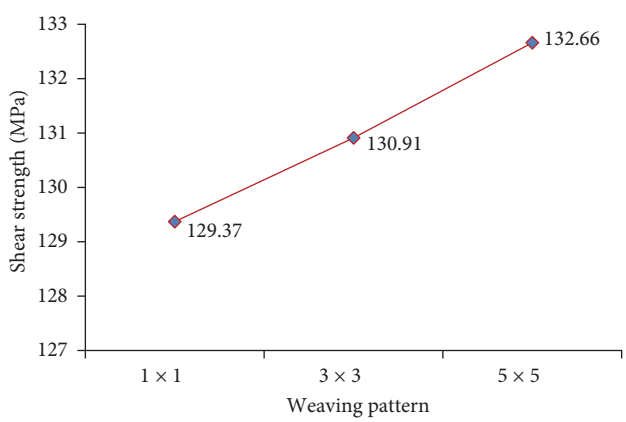

Figure 15: Shear strength vs. specimens orientation.

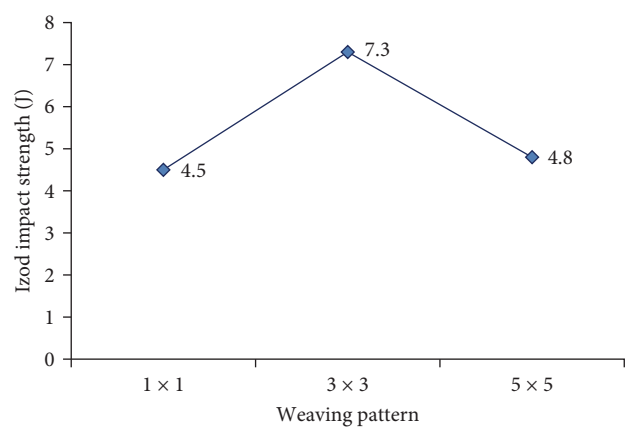

Figure 16: Impact strength vs. specimens orientation.

Table 7: Izod impact test results.

Orientation	Izod impact strength (J)
1 × 1	4.5
3 × 3	7.3
5 × 5	4.8

pulled in both the $+y$ and $-y$ axes by the fixture until it appears to fracture. The material's fracture toughness is calculated. An average value from four values per laminate type is calculated under testing. The results of Mode-1 fracture test are tabulated in Table 8. Figure 18 compares the facture toughness of three interwoven composites.

Figure 19 shows one of the specimens of Mode-1 fracture test. Out of all the specimens, the 5 × 5 pattern has a higher fracture toughness of 589.94 MPa, followed by the 1 × 1 pattern with 552.43 MPa. The 3 × 3 pattern has the lowest fracture toughness of 513.13 MPa.

The fibers in the 5 × 5 pattern are easily movable; it resists the propagation of cracks [30, 32]. The fracture toughness of the 5 × 5 pattern is 6.3% higher than the 1 × 1 pattern and 13.02% higher than the 3 × 3 pattern.

4. SEM Study

SEM images are taken to examine the interfacial properties, internal cracks, and internal structure of the fractured surfaces of the specimens [33]. SEM images of tensile, flexural, and impact tests were examined. The SEM images of the pattern having intermediate results (second highest results) from respective experiments were considered, as they might be used for further morphological studies. For tensile, flexural, and impact tests, 3 × 3, 3 × 3, and 5 × 5 patterns showed intermediate results; as a result, these SEM images were examined. Figure 20 depicts the SEM images obtained from the tensile test of the 3 × 3 pattern.

According to the SEM study, the matrix element bonded well with the reinforcing fibers. The fibers, however, were

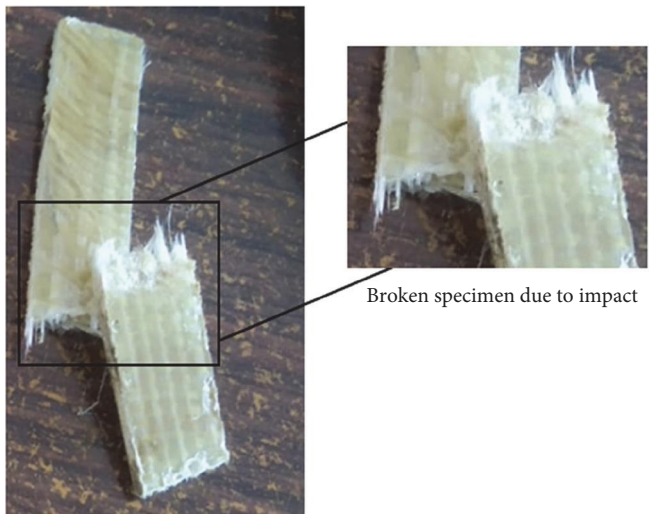

Figure 17: A test specimens completing izod impact test.

Table 8: Mode-1 fracture test results.

Orientation	Load P (N)	Length W (mm)	Thickness B (mm)	Crack length A (mm)	Fracture toughness K (MPa)	Average fracture toughness (MPa)
1 × 1	1,410	31.6	3.2	14	373.27	552.43
	1,455	32.5	2.8	13.2	668.17	
	1,470	31.3	3	11	555.04	
	1,355	32.9	3.1	14.7	613.24	
3 × 3	1,365	32.5	3.1	11	464.61	513.13
	1750	31.6	2.8	10	635.09	
	1,035	32.2	3	14.5	504.28	
	1,055	32.6	2.9	13	448.54	
5 × 5	1520	32.5	2.9	14	720.11	589.94
	1,180	31.2	2.8	11	478.04	
	1905	31.8	3	12	769.23	
	1,190	32.5	3.2	10.9	392.39	

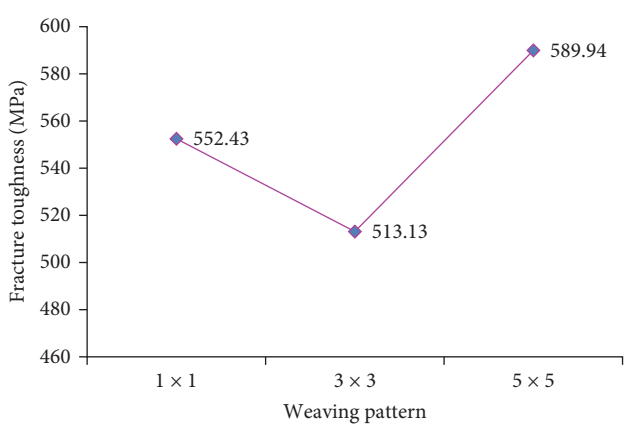

Figure 18: Fracture toughness vs. specimens orientation.

Figure 19: A test specimen undergone Mode-1 facture test.

ripped out due to the tensile load. Due to the applied tensile force, the reinforcing fibers were pushed out of the matrix and fractured by snapping in a brittle way. It is also deduced that during the tensile load, the fibers contribute primarily to the resistance to the imposed tensile load.

Figure 21 illustrates the SEM images obtained from the flexural test of the 3 × 3 pattern. According to the SEM examination, the reinforcement fibers deflected due to the shear

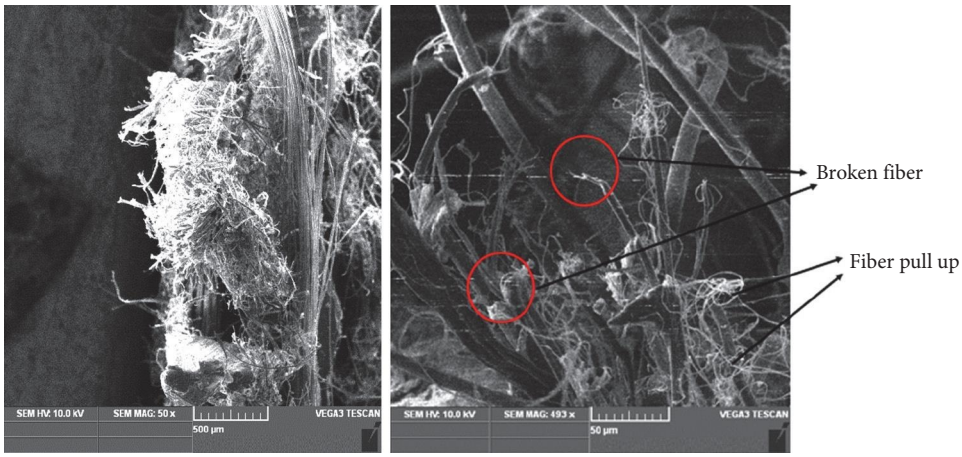

Figure 20: 3 × 3 Tensile test SEM images.

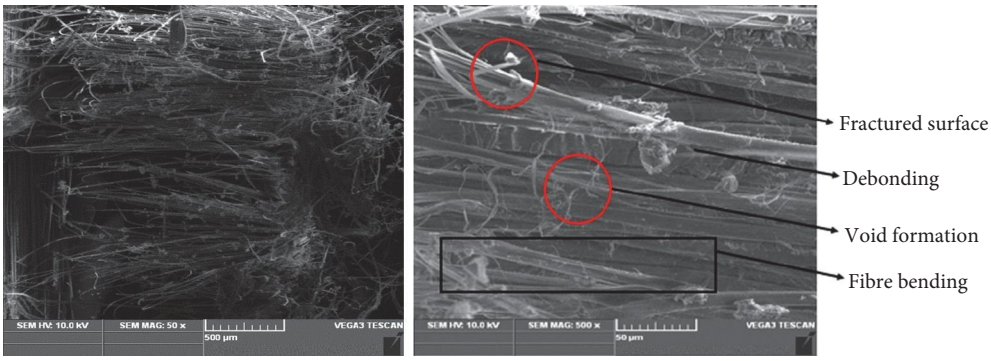

Figure 21: 3 × 3 Flexural test SEM images.

Figure 22: 5 × 5 Impact test SEM images.

force communicated through the three-point bending load. The matrix element crumbled due to the shear force, causing the reinforcing fibers to become misaligned. As a result, the fiber strands were intertwined. On the other hand, a layer of reinforcement fiber directly above the three-point bending load was unaffected. This demonstrates that the bending load affected the locations with higher shear strength.

Figure 22 shows the SEM images obtained from the impact test 5 × 5 pattern. The impact force caused the matrix element to break into a brittle mode due to the impact force, as observed via the fragments of the material in the SEM image. All the matrix elements along the impact path of the impact were crushed into smaller bits. Shear distortion caused the fibers in the middle layers to be pulled from their

weave. The fibers were also extensively damaged when the matrix element burst due to the impact force. The images are evident that delamination and fiber breakage occurred due to impact.

5. Conclusion

The tensile, compression, flexural, shear, impact, and Mode-1 fracture response of Kevlar/glass-reinforced interwoven epoxy laminates of different weaving patterns were investigated.

Overall 1×1 weaving pattern showed its dominance as the plain weave is less pliable and holds wrap and weft well.

The highest tensile, compressive, and flexural strength is found in the 1×1 pattern; plain fabric has a higher number of crossover points and is less porous.

As a result, the 1×1 pattern finds applications in the aerospace and transportation sectors. The shear strength and fracture toughness were found to be higher in the 5×5 pattern.

In the case of impact strength, the 3×3 pattern demonstrated its dominance as it has high impact strength; this laminate can be used in bulletproof applications and applications in the Aerospace industry, such as constituents of fighter aircraft.

Data Availability

The data used to support the findings of this study are included within the article.

Conflicts of Interest

The authors declare that they have no conflicts of interest.

References

[1] J. Babazadeh, K. Rahmani, S. J. Hashemi, and A. Sadooghi, "Effect of glass, carbon, and Kevlar fibers on mechanical properties for polymeric composite tubes produced by a unidirectional winding method," *Materials Research Express*, vol. 8, no. 4, Article ID 045301, 2021.

[2] S. H. Siyal, S. A. Jogi, S. Muhammadi et al., "Mechanical characteristics and adhesion of glass-Kevlar hybrid composites by applying different ratios of epoxy in lamination," *Coatings*, vol. 11, no. 1, Article ID 94, 2021.

[3] M. Nabeel, M. A. Nasir, M. Sattar et al., "Numerical and experimental evaluation of the mechanical behavior of Kevlar/glass fiber reinforced epoxy hybrid composites," *Journal of Mechanical Science and Technology*, vol. 34, pp. 4613–4619, 2020.

[4] Z. Yu, A. Ait-Kadi, and J. Brisson, "Nylon/Kevlar composites. I: mechanical properties," *Polymer Engineering & Science*, vol. 31, no. 16, pp. 1222–1227, 1991.

[5] M. Etcheverry and S. E. Barbosa, "Glass fiber reinforced polypropylene mechanical properties enhancement by adhesion improvement," *Materials*, vol. 5, no. 6, pp. 1084–1113, 2012.

[6] S. L. Valençaa, S. Griza, V. G. de Oliveira, E. M. Sussuchi, and F. G. C. de Cunha, "Evaluation of the mechanical behavior of epoxy composite reinforced with Kevlar plain fabric and glass/Kevlar hybrid fabric," *Composites Part B: Engineering*, vol. 70, pp. 1–8, 2015.

[7] V. Chinnasamy, S. P. Subramani, S. K. Palaniappan, B. Mylsamy, and K. Aruchamy, "Characterization on thermal properties of glass fiber and Kevlar fiber with modified epoxy hybrid composites," *Journal of Materials Research and Technology*, vol. 9, no. 3, pp. 3158–3167, 2020.

[8] V. Ramesh and P. Anand, "Evaluation on impact strength of basalt/Kevlar fiber reinforced hybrid composites," *International Journal of Engineering and Advanced Technology*, vol. 9, no. 1, pp. 4907–4909, 2019.

[9] M. Cheng, W. Chen, and T. Weerasooriya, "Mechanical properties of *Kevlar*® KM2 single fiber," *Journal of Engineering Materials and Technology*, vol. 127, no. 2, pp. 197–203, 2005.

[10] S. Kar, S. Pattnaik, and M. K. Sutar, "Ballistic performance of green woven fabrics—a short review," *Materials Today: Proceedings*, vol. 62, Part 10, pp. 5965–5970, 2022.

[11] R. Ganesamoorthy, R. Meenakshi Reddy, T. Raja et al., "Studies on mechanical properties of Kevlar/Napier grass fibers reinforced with polymer matrix hybrid composite," *Advances in Materials Science and Engineering*, vol. 2021, Article ID 6907631, 9 pages, 2021.

[12] S. Kumar, L. Prasad, and V. K. Patel, "Effect of hybridization of glass/Kevlar fiber on mechanical properties of bast reinforced polymer composites: a review," *American Journal of Polymer Science & Engineering*, vol. 5, no. 1, pp. 13–23, 2017.

[13] R. C. T. S. Felipe, R. N. B. Felipe, A. C. M. C. Batista, and E. M. F. Aquino, "Influence of environmental aging in two polymer-reinforced composites using different hybridization methods: glass/Kevlar fiber hybrid strands and in the weft and warp alternating Kevlar and glass fiber strands," *Composites Part B: Engineering*, vol. 174, Article ID 106994, 2019.

[14] Y. M. Kanitkar, A. P. Kulkarni, and K. S. Wangikar, "Characterization of Glass-Kevlar hybrid composite," http://www.ierjournal.org/pupload/mitpgcon/1626-1632.pdf.

[15] M. B. Gruber and T. Chou, "Elastic properties of intermingled hybrid composites," *Polymer Composites*, vol. 4, no. 4, pp. 265–269, 1983.

[16] A. Vasudevan, R. Pandiyarajan, B. Navin Kumar, and J. Vijayarangam, "Effect of Kevlar ply orientation on mechanical characterization of Kevlar-glass fiber laminated composites," *IOP Conference Series: Materials Science and Engineering*, vol. 988, Article ID 012088, 2020.

[17] S. Rajesh, B. Vijaya Ramnath, C. Elanchezhian, M. Abhijith, R. Dinesh Riju, and K. Kathir Kishan, "Investigation of tensile behavior of Kevlar composite," *Materials Today: Proceedings*, vol. 5, Part 1, no. 1, pp. 1156–1161, 2018.

[18] V. M. Fonseca, E. J. P. A. Oliveira, P. T. Lima, and L. H. Carvalho, "Development of Kevlar composites for ballistic application," in *4th Brazilian Conference on Composite Materials*, pp. 548–553, BCCM4, 2018.

[19] S. T. Tassew and A. S. Lubell, "Mechanical properties of glass fiber reinforced ceramic concrete," *Construction and Building Materials*, vol. 51, pp. 215–224, 2014.

[20] A. Wondimu, M. Kebede, and S. Palani, "Trash pineapple leaf fiber reinforced polymer composite materials for light applications," in *Bio-Fiber Reinforced Composite Materials*, K. Palanikumar, R. Thiagarajan, and B. Latha, Eds., Composites Science and Technology, pp. 13–30, Springer, Singapore, 2022.

[21] A. Divya Sadhana, J. Udaya Prakash, P. Sivaprakasam, and S. Ananth, "Wear behaviour of aluminium matrix composites (LM25/Fly ash)—a taguchi approach," *Materials Today: Proceedings*, vol. 33, Part 7, pp. 3093–3096, 2020.

[22] J. Udaya Prakash, P. Sivaprakasam, I. Garip et al., "Wire electrical discharge machining (WEDM) of hybrid composites (Al-Si12/B_4C/fly Ash)," *Journal of Nanomaterials*, vol. 2021, Article ID 2503673, 10 pages, 2021.

[23] A. Zegaoui, M. Derradji, A. Q. Dayo et al., "High-performance polymer composites with enhanced mechanical and thermal properties from cyanate ester/benzoxazine resin and short Kevlar/glass hybrid fibers," *High Performance Polymers*, vol. 31, no. 6, pp. 719–732, 2019.

[24] N. Shaari, A. Jumahat, and M. K. M. Razif, "Impact resistance properties of Kevlar/glass fiber hybrid composite laminates," *Jurnal Teknologi*, vol. 76, no. 3, pp. 93–99, 2015.

[25] R. Velmurugan and V. Manikandan, "Mechanical properties of palmyra/glass fiber hybrid composites," *Composites Part A: Applied Science and Manufacturing*, vol. 38, no. 10, pp. 2216–2226, 2007.

[26] A. Kumre, R. S. Rana, and R. Purohit, "A review on mechanical property of sisal glass fiber reinforced polymer composites," *Materials Today: Proceedings*, vol. 4, Part A, no. 2, pp. 3466–3476, 2017.

[27] C. Hui, C. Chen, X. Legrand, and P. Wang, "Investigation of the interlaminar shear performance of tufted preforms and composites under mode II loading condition," *Polymers*, vol. 14, no. 4, Article ID 690, 2022.

[28] X. Y. Xu and X. F. Xu, "Mechanical properties and deformation behaviors of acrylonitrile-butadiene-styrene under Izod impact test and uniaxial tension at various strain rates," *Polymer Engineering & Science*, vol. 51, no. 5, pp. 902–907, 2011.

[29] R. Bhanupratap and H. C. Chittappa, "Morphological study of the flexural behaviour of nanoclay filled jute/Kevlar reinforced epoxy hybrid composite," *IOP Conference Series: Materials Science and Engineering*, vol. 376, Article ID 012082, 2018.

[30] I. Jahan, "Effect of fabric structure on the mechanical properties of woven fabrics," *Advance Research in Textile Engineering*, vol. 2, no. 2, Article ID 1018, 2017.

[31] S. R. Tilak, S. A. Shuib Pasha, M. Nayeem Ahmed, and S. Daniel, "An experimental investigation of flexural and inter laminar shear stress on hybrid polymer based composites (E glass fibre–Kevlar fibre with Epoxy resin 5052) for different thickness," *Materials Today: Proceedings*, vol. 46, Part 18, pp. 8991–8994, 2021.

[32] W. Yang, "Weaving and mechanical properties test of polylactic acid/ramie composite fabric," *Journal of Physics: Conference Series*, vol. 2133, Article ID 012010, 2021.

[33] M. S. EL-Wazery, M. I. EL-Elamy, and S. H. Zoalfakar, "Mechanical properties of glass fiber reinforced polyester composites," *International Journal of Applied Science and Engineering*, vol. 14, no. 3, pp. 121–131, 2017.

Hindawi
Journal of Nanomaterials
Volume 2023, Article ID 7341542, 8 pages
https://doi.org/10.1155/2023/7341542

Research Article

Rice Bran Oil-Fueled IC Engine Performance and Emission Characteristics Improved by Nanoadditives

J. Renuraman,[1] **K. Yoganand**,[1] **P. V. Arunraj**,[1] **M. Subramanian**,[2] **and Elangomathavan Ramaraj**[3]

[1]*Department of Mechanical Engineering, Faculty of Engineering and Technology, SRM Institute of Science and Technology, Ramapuram, Tamilnadu, India*
[2]*Adithya Institute of Technology, Coimbatore, Tamilnadu, India*
[3]*Department of Biology, College of Natural and Computational Sciences, Debre Tabor University, Debre Tabor, Amhara Region, Ethiopia*

Correspondence should be addressed to Elangomathavan Ramaraj; elanmath@dtu.edu.et

Received 10 August 2022; Revised 24 September 2022; Accepted 30 September 2022; Published 12 May 2023

Academic Editor: N. Senthilkumar

In day-to-day life, fossil fuels play an important role in transportation and power generation. The consumption of fossil fuels increasing rapidly with increase in emission from engines. Due to habituation over fossil fuel, both the economy and environment are suffering. The researchers are in the position to find the best alternative for fossil fuels. The employment of biodiesel is taken to be the classy replacement for this snag. According to scores of research, using additions of nanoparticle is the greatest way to control emissions and improve engine performance. Here the assessment was employed though rice bran (RB) oil, rice bran oil blended with aluminum oxide (RB Al_2O_3), and rice bran oil blended with cerium oxide (RB CeO_2). Rice bran oil is extracted and converted into biodiesel by transesterification process. And the nanoadditives are prepared using the two-step method. The addition of nanoadditives showed an improved performance in the engine as well as emission parameters. The congruent assessment clearly demonstrates the improvement of brake thermal efficiency by around 28% for RB-Al_2O_3 and an improved brake-specific fuel of 16%. Both the blends exhibit good part loading traits.

1. Introduction

The rapid expansion of industrialization and motorization completely relies on petroleum products. But all petroleum-based products are available from limited sources. Only certain regions of the world have access to these finite resources. Countries without petroleum resources are experiencing economic problems. In addition to that emission is a major issue that suffers both human beings and environment. It is necessary to find the alternate to the existing petroleum-based products. Biodiesel obtained from animal fats, vegetable oil, and waste cooking oil are found to be a better replacement, and it is a clean burning alternative fuel that is a 100% renewable resource [1]. The experts encourage biodiesel as an alternative fuel in light of the present environmental changes and the devaluation of rising fossil fuel prices. Biodiesel can be obtained from vegetable oils like rice bran, sunflower oil, soya bean, palm oil, orange oil, etc.

This fuel is characterized by a high cetane number and sulfur content, as well as the absence of toxic chemicals and aromatics such as xylene and benzene [2, 3]. Because of this advantage, biodiesel is expected to have a lower environmental impact and a lower human impact.

2. Rice Bran Oil—Extraction and Synthesis

Husk or chaff, the outside brown coating of rice, is used to extract oil. It is available in every piece of rice. The extracted oil gives a gentle flavor and taste. Rice bran oil has been attracting a lot of attention among waste-oriented feedstock and nonedible oil feedstocks due to its potential to reduce biodiesel production costs [4]. Several countries, including Bangladesh, Vietnam, India, China, and Indonesia, primarily use rice bran as animal feed or the use of solid fuel as a low-cost source of energy [5, 6]. Rice bran can contain up to 32 wt% oil depending on the type of rice and method of milling.

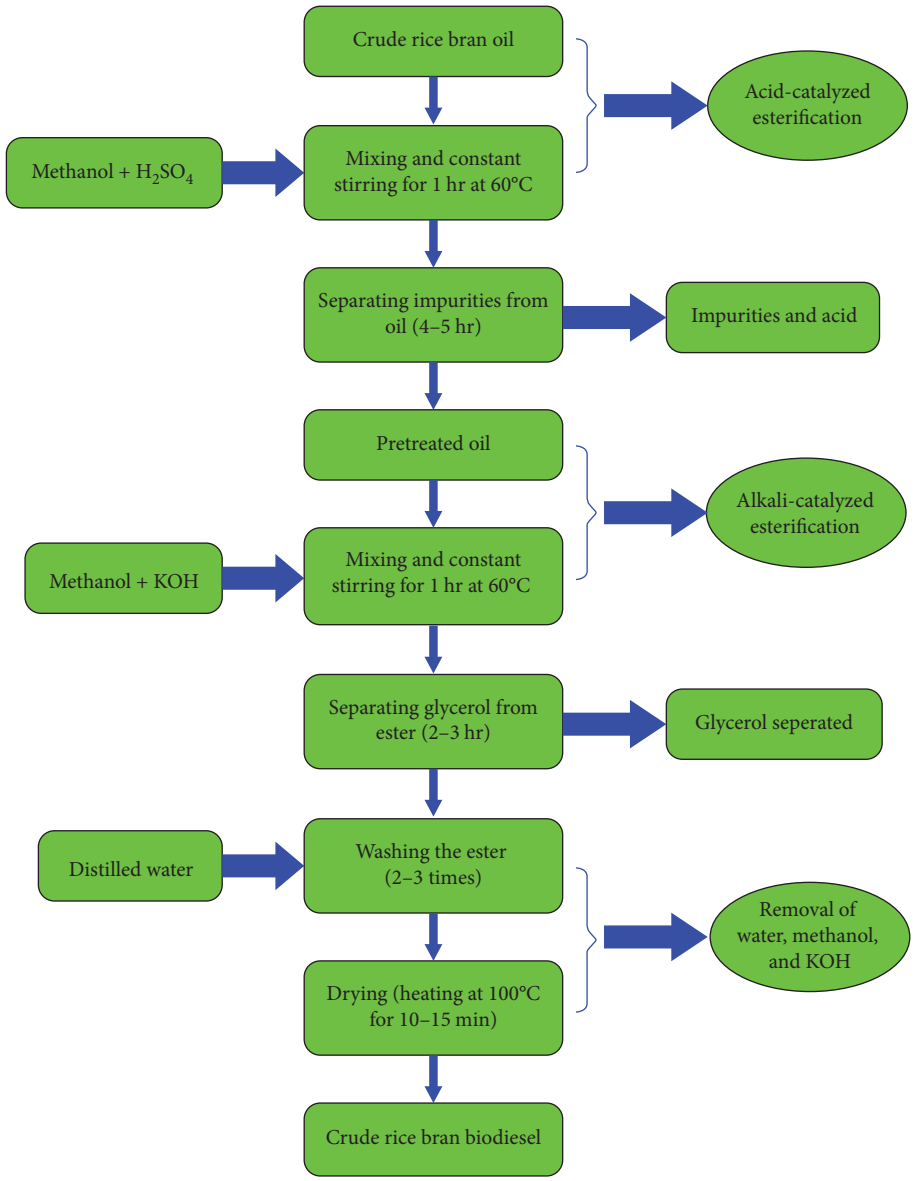

Figure 1: Methodology of extraction and synthesis of rice bran oil.

However, due to the presence of an active lipase, rice bran oil has substantially larger free fatty acid content than the bran oil of other cereals. As a result, up to 70% of the rice bran oil produced worldwide is unfit for human consumption [7, 8].

In areas where rice bran production is significant, nonedible rice bran oil can be made into biodiesel. Rice bran can differ in fatty acid composition depending on its type and quality. The amount of monounsaturated, polyunsaturated, and saturated fatty acids in rice bran oil are 39.3%, 35.0%, and 19.7%, respectively [9]. First, rice bran oil must be extracted from rice bran. A biodiesel's quality criteria are evaluated by its acid value (AV), which usually measures the quality of the extraction process. Additionally, rice bran includes a lot of protein [10]. A variety of techniques, including lipase- and acid-catalyzed transesterification, base-catalyzed transesterification, and noncatalytic techniques, have been purportedly utilized to produce biodiesel [11–14]. Due to its rapid reaction time and great efficiency, base-catalyzed alcoholysis is typically regarded as the most favorable of these techniques [15, 16].

Figure 1 displays the methodology of extraction and synthesis of rice bran oil. Transesterification of rice bran oil was carried out in two steps because of its high free-fatty-acid content [17]. For the first stage of transesterification, which is known as acid-catalyzed transesterification, small amounts of oil are placed in a conical flask and heated for 30 min at 60°C. A mixture of methanol and sulfuric acid was mixed with heated oil. An hour of shaking at a constant temperature inside the water bath shaker preceded the separation of the oil in the separating funnel.

The leftover oil that was collected from the separation funnel was measured and preheated to 60°C for the base-catalyzed

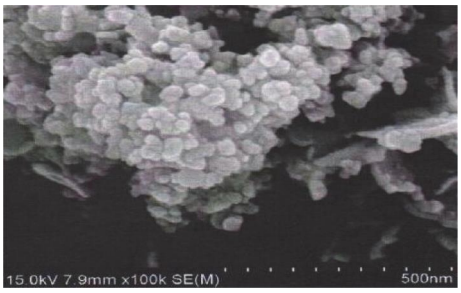

Figure 2: Analysis of CeO_2 using TEM.

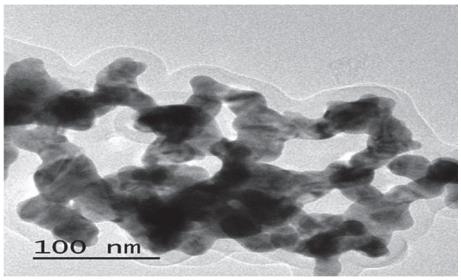

Figure 3: Analysis of Al_2O_3 using TEM.

procedure, which comes next. Then, some methanol and potassium hydroxide were added to the heated oil. The same approach used in the first section was used again. For an hour, the mixture was continuously mixed at a steady temperature. The remaining residue (methyl ester-biodiesel), which was acquired after the mixture was separated in a separating funnel to remove the glycerol, was obtained. The methyl ester was purified from this residue using washing and drying to get rid of any extra KOH, methanol, and water.

3. Nanoadditives—Materials Characterization and Synthesis

By using advanced nanotechnology, it is possible to create nanoparticles with enhanced properties. Increased brake thermal efficiency is achieved by adding nanoparticles to fuel [18, 19]. The addition of nanoparticles can increase cetane number, resulting in decreased viscosity and flash point [20]. SiO_2, CeO_2, $NiFeO_3$, Al_2O_3, MgO, ZnO, Fe_2O_3, NiO, and TiO_2 studies were performed with varying dispersion levels of 25, 50, and 100 ppm. As soon as nanoparticles are added to clean diesel fuel, the results are satisfactory [21–23]. Here we analyzed with CeO_2 and Al_2O_3 for our experiment.

Cerium oxide has a grid-like structure that can provide oxygen iotas to catalyze burning reactions [24–26]. By incorporating cerium oxide into biodiesel, unburned hydrocarbons and residue can be broken down, reducing the amount of these toxins released as fumes, NO_x emissions, and fuel consumption. Figure 2 displays the SEM analysis of cerium oxide nanoparticles.

Due to its high energy combustion, aluminum increases engine power, and it has been found that nanoscale aluminum particles perform better than microscale aluminum particles. As shown in Figure 3, aluminum oxide nanoparticles were analyzed by TEM.

Table 1: Measured fuel properties.

Fuel	Gross calorific value (kJ/kg)	Density (gm/ml)	Viscosity (cSt)
Rice bran oil	39,520	0.865	5.320
Rice bran oil + CeO_2	40,850	0.871	5.311
Rice bran oil + Al_2O_3	40,221	0.889	5.302

4. Examination of Fuel Properties

Table 1 lists the fuel qualities of rice bran oil and rice bran oil with nanoadditives as determined by IS: 1448 PART-6 & IS: 1448 PART-16 techniques. The gross calorific value of RB CeO_2 is higher than RB and RB Al_2O_3. But the viscosity of RB is higher than the other additive blends.

5. Investigational Setup

Figures 4 and 5 show the layout and the actual tested experimental setup, and Table 2 has a description of the single-cylinder diesel engine that was tested.

6. Results and Discussion

Biodiesel made from rice bran (RB), alcohol made from rice bran with 150 ppm aluminum oxide (RB Al_2O_3), and cerium oxide made from rice bran with 150 ppm (RB CeO_2) indicate the capabilities and emission characteristics of these fuel mixtures. During the experimental process, many factors were investigated, including thermal efficiency, fuel consumption, heat balance, volumetric efficiency, brake power, and other factors that influenced the results. Numerous engine loading conditions were used during the test. A set of blends was assessed for its brake-specific fuel consumption, change in cylinder pressure with crank angle, and change in heat release with crank angle as well as its brake thermal efficiency.

6.1. Performance Characteristics

6.1.1. Brake Power Variation with Brake Thermal Efficiency (BTE). The graph in Figure 6 shows the variation between brake power and brake thermal efficiency. Due to its calorific value, RB Al_2O_3 has been found to have a higher brake thermal efficiency than RB CeO_2. The primary cause may be that RB Al_2O_3 can mix with air to produce mixtures, which improve combustion efficiency and, in turn, brake thermal efficiency. Low ignition timing can be used to explain why RB CeO_2 has a lower brake thermal efficiency than RB Al_2O_3, and biodiesel mix has a significant ignition delay risk if injection occurs before TDC. In this case, more compression effort is performed, resulting in a lower brake thermal efficiency (BTE). The addition of nanoadditives reduced the delay period, and also the secondary atomization of nanoparticle took a longer period to promote its impact on improving brake thermal efficiency.

6.1.2. Brake Power Variation with Brake-Specific Fuel Consumption (BSFC). Since rice bran oil has a greater cetane number and oxygen concentration than RB Al_2O_3 and RB

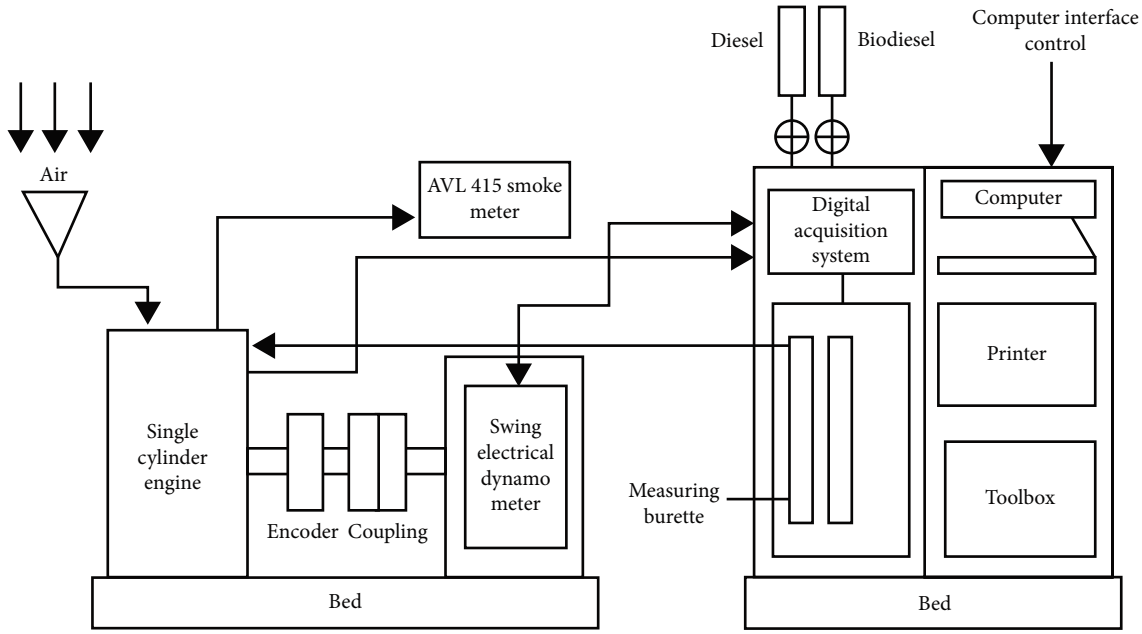

Figure 4: Layout of experimental setup.

Figure 5: Actual tested experimental setup.

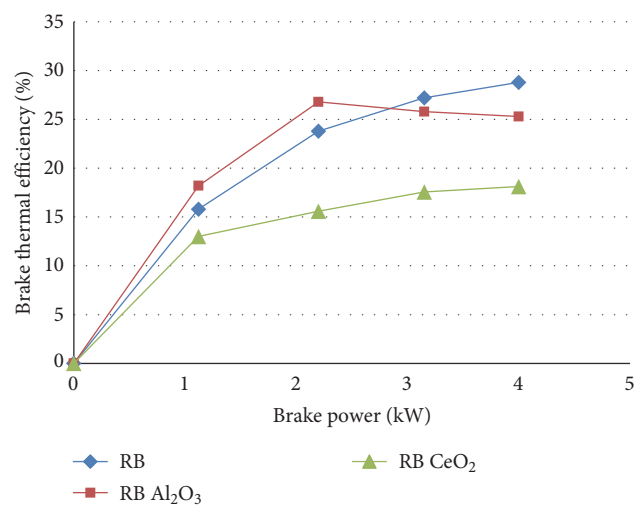

Figure 6: Brake power variation with BTE.

Table 2: Test engine specification.

Rated power	4.4 kW
Rated speed	1,500 rpm
Bore diameter (D)	87.5 mm
Stroke (L)	110 mm
Compression ratio	17.5 : 1
Orifice diameter	13.6 mm
Coefficient of discharge	0.6
Dynamometer	Swing field electrical
Smoke	AVL 415 smoke meter

CeO_2. it allows for better charge combustion and uses less energy as a result, lowering the brake-specific fuel consumption (BSFC) of rice bran oil. Here insufficient air–fuel mixing ratio may be the reason for the excessive specific-fuel consumption.

An illustration of the variation between brake power and brake-specific fuel consumption can be seen in Figure 7.

6.2. Combustion Characteristics

6.2.1. Crank Angle Variation with Heat Release. Figure 8 illustrates the variation in crank angle with a heat release for RB, RB Al_2O_3, and RB CeO_2. In both full-load and no-load conditions, the RB blend was able to release heat at a higher rate, which resulted in a shorter ignition delay. We saw that the RB oil has a somewhat longer ignition delay when compared with the RB Al_2O_3 and RB CeO_2 blends and expected that the premixed combustion process of the fuel would result in an increase in fuel combustion. As a result, peak pressure rises; however, since RB CeO_2 has less delay, less fuel is burned in the premixed condition at low

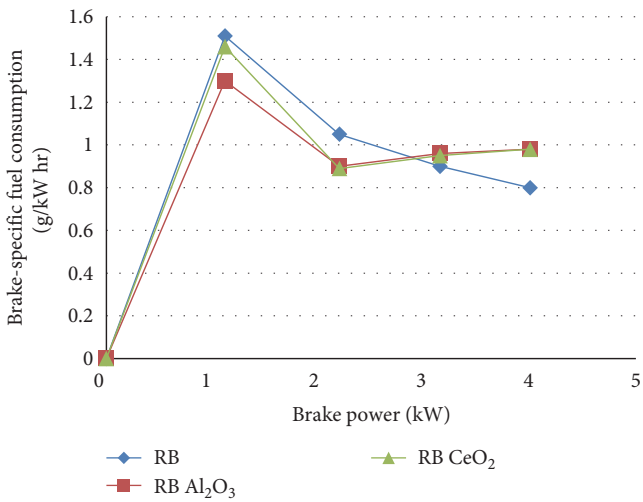

Figure 7: Brake power variation with BSFC.

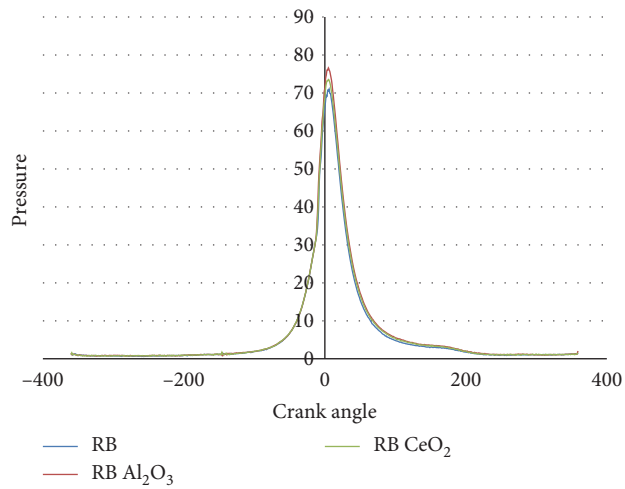

Figure 9: Crank angle variations with cylinder pressure.

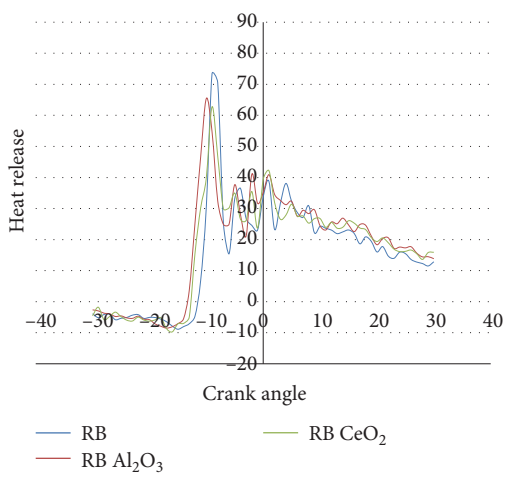

Figure 8: Crank angle variation with heat release.

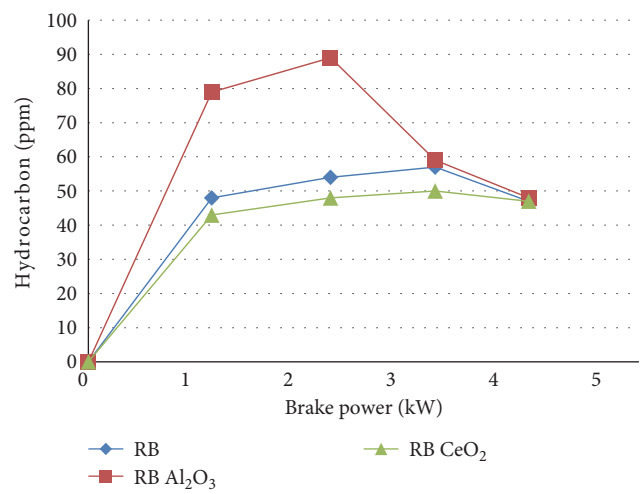

Figure 10: Brake power variations with HC.

and high loads. It is also possible that the premixed solution releases heat at a higher maximum rate because RB evaporates better than RB Al_2O_3 and RB CeO_2.

6.2.2. Crank Angle Variation with Cylinder Pressure. RB, RB Al_2O_3, and RB CeO_2 are shown in Figure 9 with their cylinder pressures fluctuating with crank angle. Maximum pressure is nearly the same for all of its mixes; although RB Al_2O_3 has higher pressure consequently aluminum oxide is present, which causes combustion to begin even before TDC.

6.3. Emission Characteristics. Here the emission characteristics are measured with the help of AVL 415S smoke meter. This type of smoke meter is used for measuring the soot content in the exhaust of diesel and GDI engines.

6.3.1. Brake Power Variation with Hydrocarbon (HC). It has been noted that RB Al_2O_3 produces higher hydrocarbon emissions than RB and RB CeO_2. One such explanation for their behavior could be incorrect ignition and fuel mixture ratios. A chart of the variation between brake power and hydrocarbon can be found in Figure 10.

6.3.2. Brake Power Variation with Carbon Dioxide (CO_2). Figure 11 illustrates the relationship between brake power and carbon dioxide. When compared with RB and RB Al_2O_3, the fluctuation in CO_2 emissions for RB CeO_2 is noticeably reduced. One explanation for this would be the high oxygen concentration, which helps better and properly burn fuels even at high temperatures in the engine's cylinder. Because there is less oxygen present under lighter loads than there is under heavier loads, carbon dioxide emissions rise as braking power rises.

6.3.3. Brake Power Variation with Carbon Monoxide (CO). Figure 12 depicts the fluctuation in carbon monoxide for RB, RB Al_2O_3, and RB CeO_2 from zero load to maximum load. Incomplete combustions and a lack of the proper proportionate oxygen fuel combination are the main causes of CO emissions. When the flame temperature is low or the air-to-fuel ratio is high, carbon monoxide emissions take place. Both

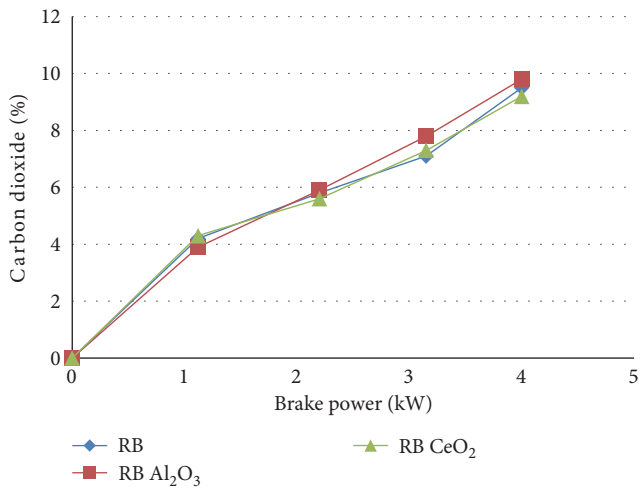

Figure 11: Brake power variations with CO_2.

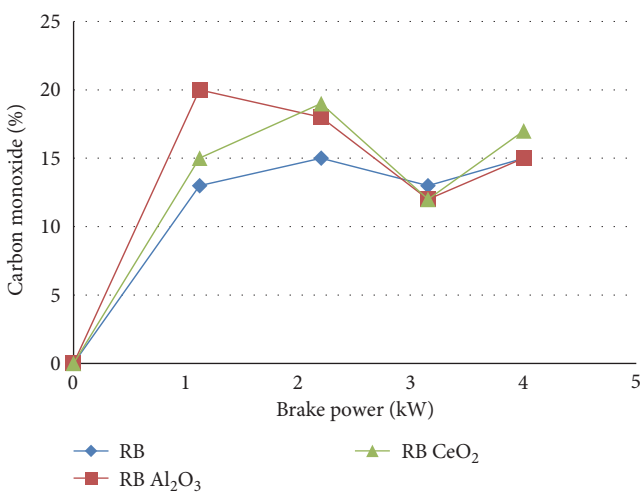

Figure 12: Brake power variations with CO.

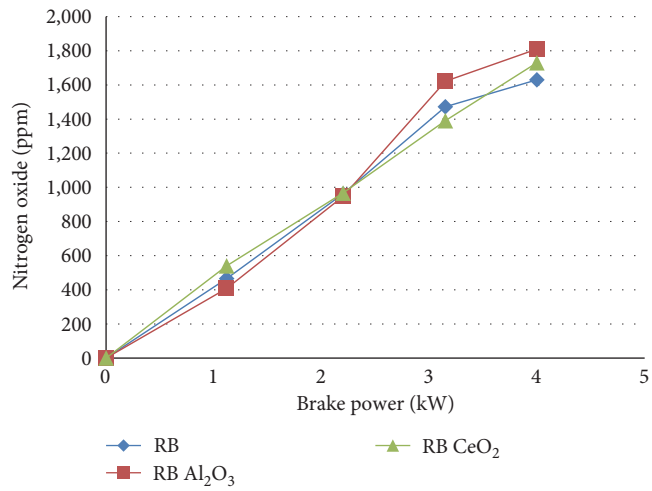

Figure 13: Brake power variations with NO_x.

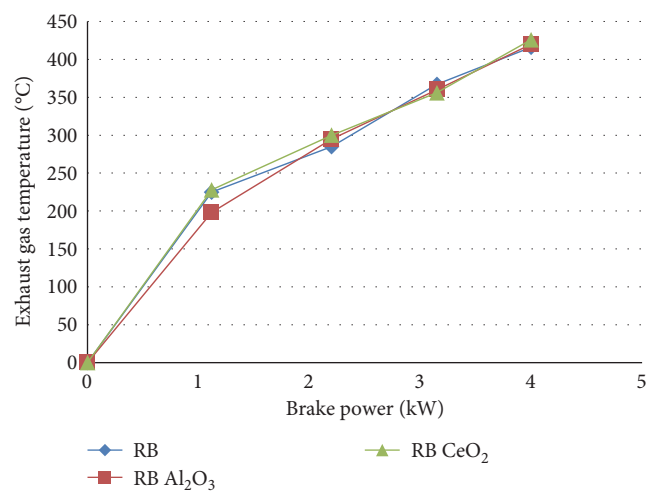

Figure 14: Brake power variations with EGT.

mixes have ups and downs depending on the blend type; rice bran emits less carbon dioxide than RB Al_2O_3 and RB CeO_2. As fuel consumption increases with load, and emissions increase as well.

6.3.4. Brake Power Variation with Nitrogen Oxide (NO_x). An illustration of the relationship between brake power and nitrogen oxide is shown in Figure 13. When compared with RB Al_2O_3 and RB CeO_2, it has been found that RB emits less nitrogen oxide. However, as braking power is increased, the NO_x emission rises. Both RB Al_2O_3 and RB CeO_2 emit nitrogen oxides at near ranges with lower loads. With increasing load, however, a distinct difference becomes apparent, which is attributed to high combustion temperatures. Comparing CeO_2 to Al_2O_3, an oxidation catalyst, reduces NO_x and ultimately increases combustion.

6.3.5. Brake Power Variation with Exhaust Gas Temperature (EGT). As the biodiesel blend increases, exhaust gas temperatures change as shown in Figure 14. It can be shown that, under all maximum loading situations, rice bran oil's exhaust gas temperature (EGT) is lower than that of RB Al_2O_3 and RB CeO_2. According to conventional wisdom, the EGT rises as engine loads rise. A rice bran blend's high oxygen content and low calorific value are other factors that contribute to its lower EGT.

7. Conclusion

In an experimental study, involving rice bran blended engines and compression ignition diesel engines, the following results were reported:

(i) At partial load condition, RB and RB CeO_2 pose similar UBHC emission, but RB Al_2O_3 showed an increased emission of about 46% than RB CeO_2. At peak condition, RB and RB CeO_2 pose similar UBHC emission, but RB Al_2O_3 showed an increased emission of about 3% than RB CeO_2.

(ii) At partial load condition, the BSFC of RB Al_2O_3 is 16% less than RB. At peak load condition, both RB Al_2O_3 and RB CeO_2 consume 18% more than RB.

(iii) CO_2 and CO emissions are well within the limits and pose no significant changes during the entire operation.

(iv) At peak load condition NO_x emission of RB Al_2O_3 is 10% higher than the RB.

(v) At partial load condition, RB Al_2O_3 poses 28% improved BTE than RB CeO_2 and 13% improved than pure blend.

This study recommends that the usage of nanoadditives shall bring a positive influence on engine performance and emission, but the diffusion of nanoparticles plays a vital role. It is also observed that the nanoadditives are well-proven for the part load as well as full load characteristics which make Al_2O_3 and CeO_2 potential additives for rice bran oil.

Data Availability

The datasets obtained and analyzed, related to the present study, are available with the corresponding author upon request.

Conflicts of Interest

The authors declare that they have no conflicts of interest.

References

[1] A. S. Ramadhas, S. Jayaraj, and C. Muraleedharan, "Use of vegetable oils as I.C. engine fuels—a review," *Renewable Energy*, vol. 29, no. 5, pp. 727–742, 2004.

[2] A. T. Hoang, "Prediction of the density and viscosity of biodiesel and the influence of biodiesel properties on a diesel engine fuel supply system," *Journal of Marine Engineering & Technology*, vol. 20, no. 5, pp. 299–311, 2021.

[3] H. Hosseinzadeh-Bandbafha, E. Khalife, M. Tabatabaei et al., "Effects of aqueous carbon nanoparticles as a novel nanoadditive in water-emulsified diesel/biodiesel blends on performance and emissions parameters of a diesel engine," *Energy Conversion and Management*, vol. 196, pp. 1153–1166, 2019.

[4] S. Zullaikah, C.-C. Lai, S. R. Vali, and Y.-H. Ju, "A two-step acid-catalyzed process for the production of biodiesel from rice bran oil," *Bioresource Technology*, vol. 96, no. 17, pp. 1889–1896, 2005.

[5] L. Lin, D. Ying, S. Chaitep, and S. Vittayapadung, "Biodiesel production from crude rice bran oil and properties as fuel," *Applied Energy*, vol. 86, no. 5, pp. 681–688, 2009.

[6] A. P. Hasan, M. A. Wakil, and M. A. Kafy, "Prospect of rice bran for biodiesel production in Bangladesh," *Procedia Engineering*, vol. 90, pp. 746–752, 2014.

[7] F. T. Orthoefer, "Rice Bran Oil," in *Bailey's Industrial Oil and Fat Products*, pp. 469–485, John Wiley & Sons, Ltd, 2005.

[8] S. A. El Khatib, S. A. Hanafi, Y. Barakat, and E. F. Al-Amrousi, "Hydrotreating rice bran oil for biofuel production," *Egyptian Journal of Petroleum*, vol. 27, no. 4, pp. 1325–1331, 2018.

[9] M. Sohail, A. Rakha, M. S. Butt, M. J. Iqbal, and S. Rashid, "Rice bran nutraceutics: a comprehensive review," *Critical Reviews in Food Science and Nutrition*, vol. 57, no. 17, pp. 3771–3780, 2017.

[10] H. Lei, X. Ding, J. Zhao et al., "In situ production of fatty acid ethyl ester from low quality rice bran," *Fuel*, vol. 90, no. 2, pp. 592–597, 2011.

[11] J. C. Juan, D. A. Kartika, T. Y. Wu, and T.-Y. Y. Hin, "Biodiesel production from jatropha oil by catalytic and non-catalytic approaches: an overview," *Bioresource Technology*, vol. 102, no. 2, pp. 452–460, 2011.

[12] A. Abbaszaadeh, B. Ghobadian, M. R. Omidkhah, and G. Najafi, "Current biodiesel production technologies: a comparative review," *Energy Conversion and Management*, vol. 63, pp. 138–148, 2012.

[13] J. M. Marchetti, "A summary of the available technologies for biodiesel production based on a comparison of different feedstock's properties," *Process Safety and Environmental Protection*, vol. 90, no. 3, pp. 157–163, 2012.

[14] G. Lourinho and P. Brito, "Advanced biodiesel production technologies: novel developments," *Reviews in Environmental Science and Bio/Technology*, vol. 14, pp. 287–316, 2015.

[15] M. Tabatabaei, M. Aghbashlo, M. Dehhaghi et al., "Reactor technologies for biodiesel production and processing: a review," *Progress in Energy and Combustion Science*, vol. 74, pp. 239–303, 2019.

[16] M. Aghbashlo, M. Tabatabaei, S. Hosseinpour, Z. Khounani, and S. S. Hosseini, "Exergy-based sustainability analysis of a low power, high frequency piezo-based ultrasound reactor for rapid biodiesel production," *Energy Conversion and Management*, vol. 148, pp. 759–769, 2017.

[17] D. N. A. Zaidel, I. I. Muhamad, N. S. M. Daud, N. A. A. Muttalib, N. Khairuddin, and N. A. M. Lazim, "Production of biodiesel from rice bran oil," in *Biomass, Biopolymer-Based Materials, and Bioenergy Construction, Biomedical, and other Industrial Applications*, Composites Science and Engineering, pp. 409–447, Woodhead, 2019.

[18] S. Manigandan, P. Gunasekar, J. Devipriya, and S. Nithya, "Emission and injection characteristics of corn biodiesel blends in diesel engine," *Fuel*, vol. 235, pp. 723–735, 2019.

[19] M. Annamalai, B. Dhinesh, K. Nanthagopal et al., "An assessment on performance, combustion and emission behavior of a diesel engine powered by ceria nanoparticle blended emulsified biofuel," *Energy Conversion and Management*, vol. 123, pp. 372–380, 2016.

[20] R. Vigneswaran, K. Annamalai, B. Dhinesh, and R. Krishnamoorthy, "Experimental investigation of unmodified diesel engine performance, combustion and emission with multipurpose additive along with water-in-diesel emulsion fuel," *Energy Conversion and Management*, vol. 172, pp. 370–380, 2018.

[21] T. Ozgur, G. Tuccar, E. Uludamar et al., "Effect of nanoparticle additives on NO_x emissions of diesel fuelled compression ignition engine," *International Journal of Global Warming*, vol. 7, no. 4, pp. 487–498, 2015.

[22] P. Vasanthkumar, A. R. Revathi, G. Ramya Devi, R. J. Kavitha, A. Muniappan, and C. Karthikeyan, "Improved wild horse optimizer with deep learning enabled battery management system for internet of things based hybrid electric vehicles," *Sustainable Energy Technologies and Assessments*, vol. 52, Part C, Article ID 102281, 2022.

[23] P. Vetrivezhan, C. Ayyanar, P. V. Arunraj, P. Vasanthkumar, and D. Ganesan, "Electroless deposition of aluminium alloy LM25 by SiC and Ni-P nano coating," *Materials Today: Proceedings*, vol. 45, Part 7, pp. 6449–6453, 2021.

[24] Y. Kumaravelu, V. Periyathambi, P. Udhayanan et al., "Influence of aluminum silicate and cerium (IV) oxide nanofluid on pool boiling characteristics," *International Journal of Photoenergy*, vol. 2022, Article ID 5357053, 11 pages, 2022.

[25] A. A. G. Dhas, B. Nagappan, K. Yoganand, T. Arvind, S. Varghese, and D. Christopherselvam, "Effect of nano-fluid on reducing the smoke emissions from diesel engine," *Petroleum Science and Technology*, vol. 37, no. 22, pp. 2283–2287, 2019.

[26] V. Arul Mozhi Selvan, R. B. Anand, and M. Udayakumar, "Effects of cerium oxide nanoparticle addition in diesel and diesel-biodiesel-ethanol blends on the performance and emission characteristics of a CI engine," *Journal of Engineering and Applied Sciences*, vol. 4, no. 7, pp. 1–6, 2009.

Hindawi
Journal of Nanomaterials
Volume 2023, Article ID 8175140, 8 pages
https://doi.org/10.1155/2023/8175140

Research Article

Analysis of MRR, Thrust Force, and Torque in Drilling Al/BN/Al_2O_3 Composites using Hybrid Grey–Taguchi Technique

S. Senthil Babu,[1] C. Dhanasekaran,[1] A. Parthiban,[1] N. Vasudevan,[2] and Addisalem Mekonnen [3]

[1]*Department of Mechanical Engineering, VELS Institute of Science, Technology & Advanced Studies, Chennai, India*
[2]*Department of Electronics and Communication Engineering, K. Ramakrishnan College of Technology, Samayapuram, Trichy, India*
[3]*Department of Mechanical Engineering, Faculty of Manufacturing, Institute of Technology, Hawassa University, Hawassa, Ethiopia*

Correspondence should be addressed to Addisalem Mekonnen; addisalemm@hu.edu.et

Received 29 June 2022; Revised 16 August 2022; Accepted 2 September 2022; Published 10 May 2023

Academic Editor: Ao Xia

The demand for hybrid composite materials has been expanding globally in all kinds of mechanical industries. Drilling is one of the basic operations required in manufacturing of various components and choosing optimum parameters of drilling is vital for getting good quality holes. The main objective of our work is to determine the ideal parameters of drilling and tool coatings required to minimize the thrust force and torque in drilling and to maximize the material removal rate (MRR) using Grey–Taguchi technique. Hybrid composite specimen made by reinforcing Al7075 alloy with 4% of aluminum oxide and 2% of boron nitride in stir casting process and drilling was carried out in a sequence at different drilling feed rates (40, 80, and 120 mm/min) and spindle speeds (1,200, 2,400, and 3,600 rpm) in a vertical machining center attached with drill tool dynamometer, using twist drills of diameter 5 mm and point angle 118° made of uncoated carbide, diamond-like carbon (DLC)-coated carbide and high carbon (HC)-coated carbide. The recorded thrust force and torque from the dynamometer and the computed MRRs during each drilling operation are tabulated as per Taguchi's L27 orthogonal array and the results are analyzed using hybrid Grey–Taguchi technique. In our analysis, the optimum thrust force of 62.12 N and torque of 0.766 Nm were obtained when using a DLC-coated tool at a maximum speed of 3,600 rpm and minimum feed rate of 40 mm/min. An optimum MRR of 178.79 mm^3/s was obtained while using DLC coated at a maximum speed of 3,600 rpm and a maximum feed rate of 120 mm/min.

1. Introduction

The aluminum hybrid composites have been focused by many investigators in recent years, mainly due to their excellent mechanical properties, extreme resistance to corrosion, and wide scope of applications [1]. While fabricating mechanical components using composite materials, effective drilling operation is unavoidable at the stage of assembly by mechanical joining processes like riveting, bolting, etc., and this task is highly formidable one because of the reinforcement by hard ceramic particles [2]. These kinds of challenges provide more scope for research in this domain. Various responses, like high material removal rate (MRR), better surface finish, minimum drilling force and torque, minimum cylindricity, and least circularity error, are considered for effective drilling process and among these responses, MRR, thrust force, and torque are viewed in our investigations.

Taguchi technique is one of the statistical methods developed by Genichi Taguchi, a Japanese statistician, to improve the quality of a manufacturing process or product by keeping the variance very low at the output. In our investigations, Taguchi technique is integrated with Grey relational analysis (GRA) [3, 4] to find out the ideal drilling parameters that minimize the thrust force and maximize the MRR. Multi-performance features integrating many parameters at a time can be effectively analyzed by GRA by converting the multiple performance characteristics into one numerical score known as Grey relational grade (GRG) [5]. Based on GRG, the optimum level of parameters can be obtained.

1.1. Related Works. Udaya Prakash et al. [6] investigated the effect of various drilling parameters on burr height and the force induced on drilling LM6/B4C/Fly ash composites using GRA and found that the feed rate is the most influencing

Table 1: Al7075 composition.

Element	Zinc	Magnesium	Copper	Iron	Chromium	Manganese	Silicon	Titanium	Aluminum
%	5.5	2.5	1.5	0.5	0.25	0.3	0.4	0.2	Balance

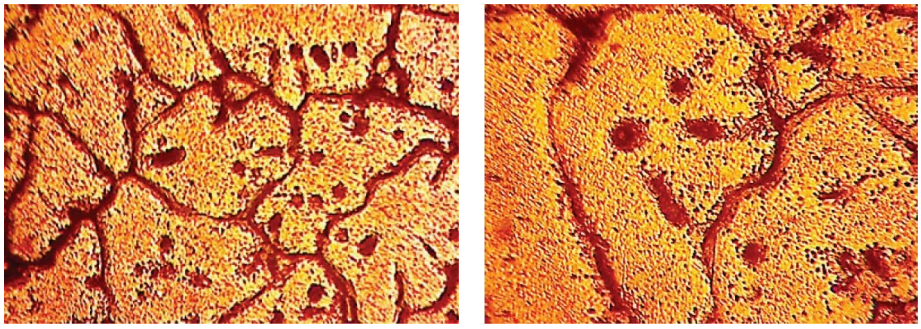

(a) (b)

Figure 1: (a) First picture; (b) second picture.

factor subsequently the reinforcement percentage and drilling speed. Bammidi et al. [7] investigated the drilling behavior of Ti–6Al–4V alloy and found out the optimum parameters to maximize MRR and minimize the circularity error using Taguchi and analysis of variance (ANOVA) techniques. Palanikumar and Muniaraj [8] carried out drilling experiments on Al6061 reinforced with SiC and graphite using carbide drills of varying diameters coated with TiN and the effect of various drilling parameters influencing thrust force is determined by response surface methodology. Sarala and Udaya Prakash [9] investigated the influence of various drilling criteria, tool materials, and reinforcement percentages on surface finish, drilling force, etc., while drilling LM6-based hybrid composite materials to find out ideal parameters using GRA technique. In this study, we have chosen aluminum–zinc alloy (AA7075) as the base material because. It exhibits very good mechanical properties with great fatigue and corrosion resistance. Boron nitride and alumina have chosen as reinforcement materials to improve the tribological properties of the base material further and find its applications in automobiles, aerospace, and high-stressed structural components [10]. The size of reinforcement particles used are 70 μm of BN and 50 μm of alumina. Because of the extremely abrasive nature of the reinforcement materials used, drilling of this hybrid composite material is tedious and so there is more scope for research in this area.

According to the literature review, few studies have been conducted on the machining of hybrid aluminum metal matrix composites reinforced with primary (aluminum oxide) and secondary (boron nitride) ceramic particles because of wettability limitations. Therefore, conducting drilling experiments on the developed hybrid metal matrix composites while using diamond-like carbon (DLC)- and high carbon (HC)-coated carbide drills with different point angles, feed rates, and drilling speeds is considered to be novel in this work. To design and analyze experiments, Taguchi methodology is employed.

Our objective is to examine and explore the effect of tool coatings, drilling speed, and the drilling feed rate on the MRR, drilling force developed, and drilling torque during the drilling process. The drilling process was carried out by VF30 computer numerical control (CNC) machining center.

2. Materials and Methods

For our investigation, we have chosen aluminum7075 as the base material, boron nitride, and alumina as reinforcements. The major composition of Al7075 is given in Table 1.

The hybrid composite specimen was prepared by stir casting method, in which small pieces of Al7075 cut from a long rod are heated in a crucible above the liquidous temperature and the molten metal is mixed with preheated BN of APS 70 μm with a density of 3.7 g/cm^3 and Al_2O_3 of APS 50 μm with a density of 3.75 g/cm^3 by mechanical stirring at the speed of 300–400 rpm for half an hour and the semisolid mixture is poured into the cavity and permitted to become hardened in the air. The cast specimen is milled to the size of 100 mm × 100 mm × 10 mm for our experimentation.

Figure 1 shows the microstructures of the specimen under magnification of 100x and 200x, here, the boron nitride particles in the composite are shown by distinct and thick grain fringes and few of the particles are scattered in the matrix. It also shows the homogeneous mixing of aluminum oxide in the aluminum matrix.

The homogeneity of the reinforcements boron nitride and alumina in the base metal Al7075 is assured by the scanning electron microscopy image of the prepared specimen with 500x and 1,500x magnification as shown in Figure 2. The surface becomes fine and the aluminum flakes are extruded on the surface. Figure 2 also shows the aluminum oxide particles on the surface as gray dots.

The hardness of aluminum hybrid composites was analyzed as per American Society for Testing and Materials standards

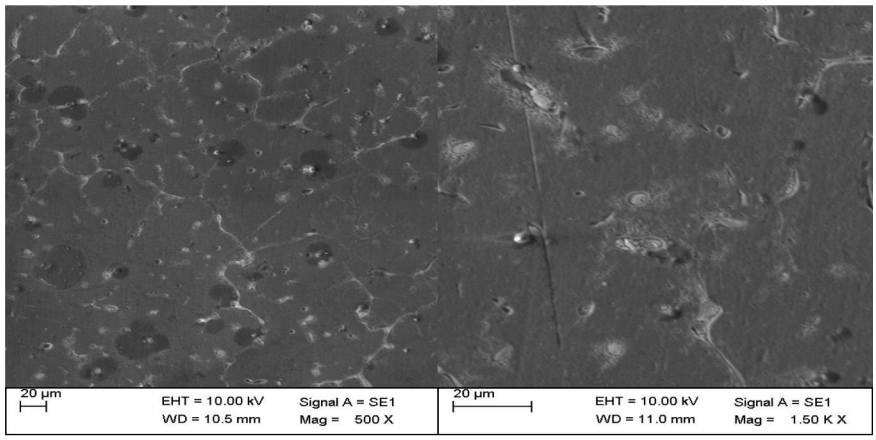

Figure 2: Scanning electron microscopy images.

Table 2: Drilling parameters and levels.

Level	Tool material	Spindle speed (rpm)	Feed rate (mm/min)
1	Uncoated carbide (A)	1,200	40
2	DLC coated (B)	2,400	80
3	HC coated (C)	3,600	120

DLC: diamond like carbon, HC: high carbon. Diameter of all the twist drills is 5 mm and their point angle is 118°.

and it was observed that the presence of hard ceramic reinforcement increases the hardness of synthesized composites. This is due to the fact that these hard ceramic reinforcement hinders the motion of dislocation and it reduces the grain size. It was observed that the hardness of synthesized composites (169 MPa) increased to 49% in comparison with cast alloy. Considering this as a prime factor it was decided to perform drilling operation using CNC for manufacturing applications.

The induced force and torque during drilling were measured with the help of Kistler dynamometer coupled with the machine and recorded by dynaware software. By measuring the weight of the specimen before and after drilling every hole and the time taken, the MRR can be calculated. The three levels of drilling speed, feed, and tool coating materials used are mentioned in Table 2.

We planned our experimental design according to Taguchi's L27 orthogonal array for the three parameters under three levels, to determine the most effective tool coating material for the optimum speed and feed of the drilling process to attain minimum drilling force, torque and maximum MRR using GRA coupled with Taguchi technique.

Taguchi technique is an effectively coordinated way to find the most influencing combination of input factors. In this technique, a tailor made L27 orthogonal array was utilized to detect the most influencing factors.

Grey analysis involves a transparent group of statements concerning system solutions. Mostly, there is no solution at one end and at the other end, this system with excellent data features a distinctive solution. Within the middle, Grey systems can provide a kind of obtainable solution. GRA does not commit to notice the simplest result, however, will offer techniques to determine a decent and an applicable result for real-world issues [11].

The results of our experiments are investigated for optimization using Grey–Taguchi technique, which is a hybrid technique used for optimization. Taguchi technique is one of the significant techniques used to determine the optimal level of the input parameters for a single objective function. But this approach is not suitable for multiobjective problems and so we go for a hybrid technique like Grey–Taguchi method [12, 13].

For Taguchi technique, we have performed drilling experiments using 27 different combinations of the three parameters, and their responses viz, thrust force, drilling torque, and MRR are determined and tabulated. Induced force and torque during drilling operations were taken directly from the output of drill tool dynamometer using dynaware software and the MRR value was calculated by the weight loss during each experiment.

The three output responses of 27 drilling experiments were evaluated by their corresponding SNR values (S/N ratio) using smaller the better formula for thrust force and torque and larger the better formula for MRR and are named SNR1, SNR2, and SNR3, respectively.

For larger the better,

$$\mathrm{SNR} = -10\log_{10}\left(\frac{\Sigma\left(\frac{1}{Y^2}\right)}{n}\right). \quad (1)$$

For smaller the better,

$$\mathrm{SNR} = -10\log_{10}\left(\frac{\Sigma(Y^2)}{n}\right). \quad (2)$$

Table 3: Experimental results.

Trial no.	Tool material	Speed (rpm)	Feed rate (mm/min)	Thrust force (N)	Torque (Nm)	MRR (mm^3/s)	SNRA1	SNRA2	SNRA3
1	A	1,200	40	135.6	1.349	34.06	−42.645	−2.599	30.646
2	A	1,200	80	198.5	1.808	67.85	−45.955	−5.144	36.631
3	A	1,200	120	269.82	2.501	106.78	−48.621	−7.963	40.570
4	A	2,400	40	120.7	1.191	42.19	−41.634	−1.521	32.504
5	A	2,400	80	166.84	1.749	86.85	−44.446	−4.855	38.775
6	A	2,400	120	190.82	2.015	122.18	−45.612	−6.086	41.740
7	A	3,600	40	102.04	0.995	53.52	−40.175	0.046	34.570
8	A	3,600	80	120.9	1.160	101.32	−41.649	−1.291	40.114
9	A	3,600	120	161.2	1.595	146.78	−44.147	−4.053	43.333
10	B	1,200	40	112.71	1.154	31.93	−41.039	−1.246	30.084
11	B	1,200	80	182.8	1.902	87.59	−45.240	−5.582	38.849
12	B	1,200	120	235.21	2.297	125.99	−47.429	−7.225	42.006
13	B	2,400	40	78.84	0.809	51.63	−37.935	1.839	34.258
14	B	2,400	80	122.84	1.310	107.86	−41.787	−2.348	40.657
15	B	2,400	120	162.54	1.813	157.39	−44.219	−5.166	43.939
16	B	3,600	40	62.12	0.766	58.39	−35.865	2.318	35.327
17	B	3,600	80	94.72	0.970	126.52	−39.529	0.266	42.043
18	B	3,600	120	112.7	1.201	179.78	−41.038	−1.588	45.095
19	C	1,200	40	128.71	1.311	36.50	−42.192	−2.349	31.245
20	C	1,200	80	190.21	2.047	77.73	−45.585	−6.222	37.811
21	C	1,200	120	280.2	2.683	111.39	−48.949	−8.573	40.937
22	C	2,400	40	104.27	1.091	52.20	−40.363	−0.757	34.353
23	C	2,400	80	157.8	1.619	100.99	−43.962	−4.184	40.086
24	C	2,400	120	188.38	1.922	156.79	−45.501	−5.674	43.906
25	C	3,600	40	83.03	0.892	58.53	−38.385	0.997	35.347
26	C	3,600	80	111.08	1.099	113.92	−40.913	−0.816	41.132
27	C	3,600	120	153.92	1.561	175.18	−43.746	−3.867	44.870

The formulae to calculate the SNR values are given in Equations (1) and (2), where Y is the response value and n is the number of trials. As we need to compare the SNR values of all the three responses and all the responses are in different ranges, we have to normalize SNR1, SNR2, and SNR3 values into the range of 0–1. Equations (3) and (4) show the formulae for normalization [15].

For the strategy of larger the better, normalized value

$$\psi_i = \frac{\lambda_i - \min \lambda_i}{\max \lambda_i - \min \lambda_i}. \quad (3)$$

For the strategy of smaller the better, normalized value

$$\psi_i = \frac{\max \lambda_i - \lambda_i}{\max \lambda_i - \min \lambda_i}, \quad (4)$$

where ψ_i represents the normalized SNR value and λ_i represents SNR value for any particular response for an experiment [14].

In hybrid Grey–Taguchi analysis, the Grey relational coefficient (GRC) can be calculated from the normalized SNR values, using the formula given in Equation (5), following which the GRG can be determined, which is helpful to find the relation between the best experimental result and the actual one.

Grey relational coefficient

$$\zeta_i(k) = \frac{\Delta_{\min} + \epsilon\Delta_{\max}}{\Delta_{oi}(k) + \epsilon\Delta_{\max}}, \quad (5)$$

where $\zeta_i(k)$ is the GRC of any trial k, $\Delta_{oi}(k)$ is the deviation sequence of the trial k, and distinguishing coefficient ϵ is assumed to be 0.5.

Since the values are normalized, $\Delta_{\min}$ and $\Delta_{\max}$ are always equal to 0 and 1, respectively. The GRG is estimated by taking the mean value of GRC for each and every trial [16].

3. Results and Discussion

The tool material, drilling speed in rpm, and the tool feed rate in mm/min are the three input factors considered in our experimental study and the output parameters thrust force, drilling torque, and the MRR values are determined and tabulated as per Taguchi's L27 array as shown in Table 4. SNR values for thrust force, drilling torque, and the MRR are estimated individually for 27 trials and are named SNR1, SNR2, and SNR3, respectively in Table 3.

Table 4: Grey relational grade.

Trial no.	Normalizing sequence			Deviation sequence			Grey relational coefficient			GRG
	Thrust force (N)	Torque (Nm)	MRR (mm^3/s)	Thrust force (N)	Torque (Nm)	MRR (mm^3/s)	Thrust force (N)	Torque (Nm)	MRR (mm^3/s)	
1	0.518	0.451	0.037	0.482	0.549	0.963	0.509	0.477	0.342	0.443
2	0.771	0.685	0.436	0.229	0.315	0.564	0.686	0.614	0.470	0.590
3	0.975	0.944	0.699	0.025	0.056	0.301	0.952	0.899	0.624	0.825
4	0.441	0.352	0.161	0.559	0.648	0.839	0.472	0.436	0.373	0.427
5	0.656	0.659	0.579	0.344	0.341	0.421	0.592	0.594	0.543	0.576
6	0.745	0.772	0.776	0.255	0.228	0.224	0.662	0.686	0.691	0.680
7	0.329	0.209	0.299	0.671	0.791	0.701	0.427	0.387	0.416	0.410
8	0.442	0.331	0.668	0.558	0.669	0.332	0.473	0.428	0.601	0.501
9	0.633	0.585	0.883	0.367	0.415	0.117	0.577	0.546	0.810	0.644
10	0.395	0.327	0.000	0.605	0.673	1.000	0.453	0.426	0.333	0.404
11	0.716	0.725	0.584	0.284	0.275	0.416	0.638	0.645	0.546	0.610
12	0.884	0.876	0.794	0.116	0.124	0.206	0.811	0.802	0.708	0.774
13	0.158	0.044	0.278	0.842	0.956	0.722	0.373	0.343	0.409	0.375
14	0.453	0.428	0.704	0.547	0.572	0.296	0.477	0.467	0.628	0.524
15	0.638	0.687	0.923	0.362	0.313	0.077	0.580	0.615	0.867	0.687
16	0.000	0.000	0.349	1.000	1.000	0.651	0.333	0.333	0.435	0.367
17	0.280	0.188	0.797	0.720	0.812	0.203	0.410	0.381	0.711	0.501
18	0.395	0.359	1.000	0.605	0.641	0.000	0.453	0.438	1.000	0.630
19	0.484	0.429	0.077	0.516	0.571	0.923	0.492	0.467	0.351	0.437
20	0.743	0.784	0.515	0.257	0.216	0.485	0.660	0.698	0.507	0.622
21	1.000	1.000	0.723	0.000	0.000	0.277	1.000	1.000	0.643	0.881
22	0.344	0.282	0.284	0.656	0.718	0.716	0.432	0.411	0.411	0.418
23	0.619	0.597	0.666	0.381	0.403	0.334	0.567	0.554	0.600	0.574
24	0.736	0.734	0.921	0.264	0.266	0.079	0.655	0.653	0.863	0.724
25	0.193	0.121	0.351	0.807	0.879	0.649	0.382	0.363	0.435	0.393
26	0.386	0.288	0.736	0.614	0.712	0.264	0.449	0.412	0.654	0.505
27	0.602	0.568	0.985	0.398	0.432	0.015	0.557	0.536	0.971	0.688

Table 5: Response table.

Factors	Level 1	Level 2	Level 3	Delta	Rank
A	0.5662	0.5414	0.5824	0.0162	3
B	0.6206	0.5539	0.5155	0.1051	2
C	0.4083	0.5558	0.7260	0.3177	1
Mean Grey relational grade = 0.5633.					

The SNRs of all the responses are normalized using Equation (4) for thrust force and drilling torque and Equation (5) for MRR and the normalizing sequences for the 27 trials are entered in Table 3. The deviation sequences and calculated by subtracting normal sequence values from 1 and also entered in Table 3.

Assuming the distinguishing coefficient of 0.5, the GRCs for all the trails were evaluated by Equation (5), and the mean GRCs of all the three responses for each trial are estimated as GRG and tabulated in Table 4.

For all the three responses, the average GRGs are estimated at all the three levels and are tabulated as response table which is shown in Table 5. Finally, the mean of all these nine GRGs is marked as mean GRG in the same table.

The ideal level of input factors for the drilling operations are found to be the maximum GRG for each factor from the response table and so the optimum parameters are level 3 for the factor A (high carbon-coated tool), level 1 for the factor B (spindle speed of 1,200 rpm), and level 3 for the factor C (feed rate of 120 mm/min). The highly influencing factors of drilling to optimize the drilling force, drilling torque, and MRR are found to be the tool feed rate followed by spindle speed and tool material as shown by the rank in the response table.

Minitab has been used to obtain the main effect plot for thrust force which is shown in Figure 3. The main effect plots represent the influence of various parameters on thrust force graphically. The effect of drilling speed and feed are high on thrust force as the range of their means are higher than that of the tool material. It is inferred from the main effect plots that the thrust force is minimum when using DLC tool with high speed and low feed.

Similarly, the main effect plot for the drilling torque is obtained and is shown in Figure 4. From the plots, we can conclude that the influence of various factors of drilling on the torque is more or less similar to that of the thrust force

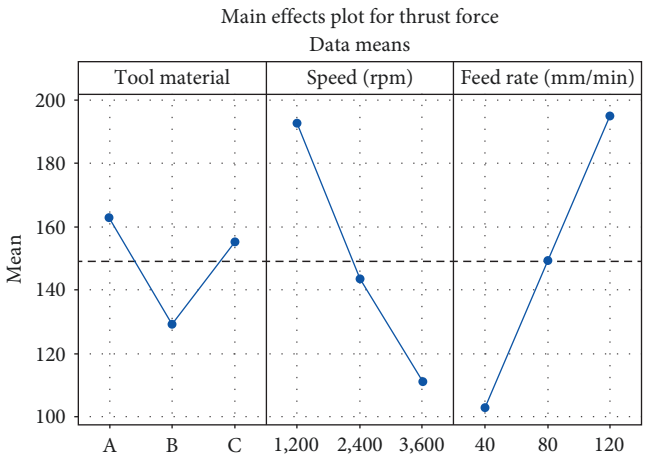

Figure 3: Main effect plot for thrust force.

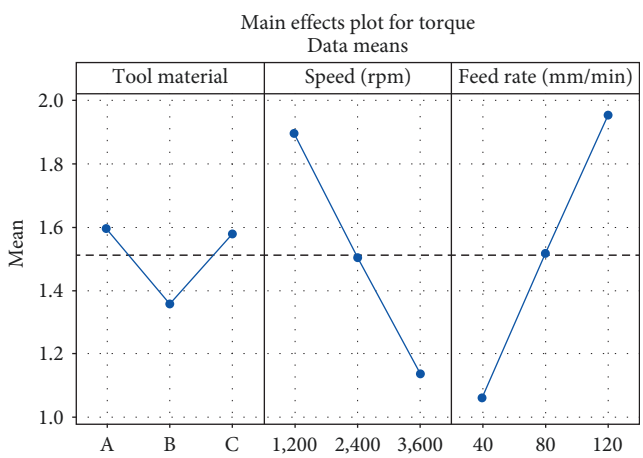

Figure 4: Main effect plot for drilling torque.

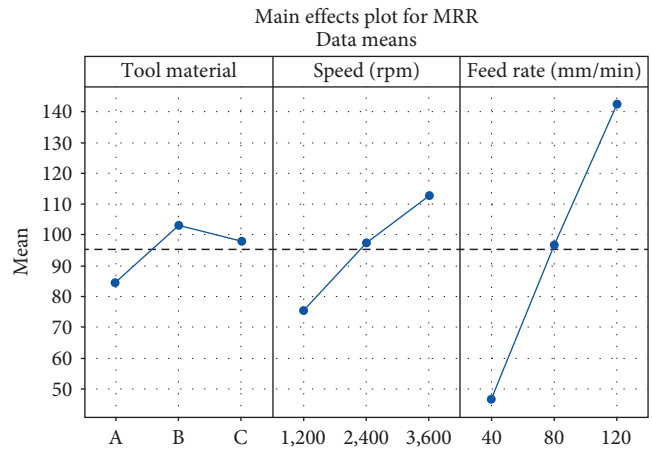

Figure 5: Main effect plot for MRR.

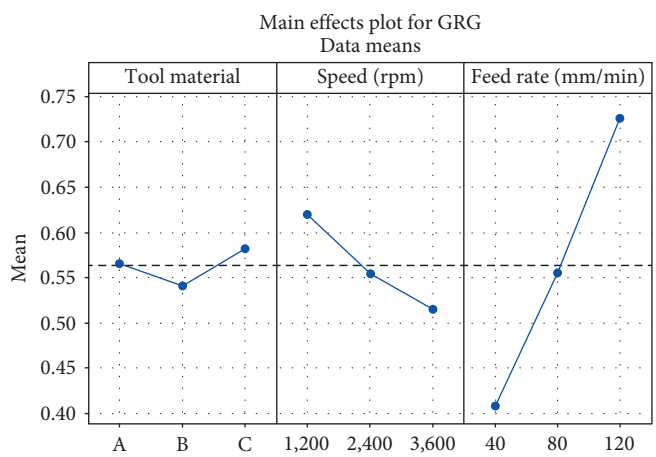

Figure 6: Main effect plot for Grey relational grade.

and so the torque will be when using DLC tool with high speed and low feed.

Figure 5 shows the main effect plot for MRR, and the parameters to maximize the MRR are found to be DLC tool with high speed and high feed. The plot also indicates that the range of the mean data are maximum for feed rate and we can conclude that the feed rate is the most influencing factor for MRR.

Figures 3–5 show the main effect plots for single objective function viz, to minimize thrust force, torque, and to maximize MRR, respectively, and the combined multiobjective function can be optimized by optimizing the GRGs estimated by the hybrid Taguchi–Grey analysis.

The main effect plot for the GRG is shown in Figure 6, and the drilling parameters to optimize the GRG are found to be a HC-coated tool with a lower speed and higher feed rate. The graphs also indicate that the range of the mean data are higher for feed rate than that of speed and tool material and we can conclude that the feed rate is the most influencing factor affecting the combined objective function.

The ANOVA is found and shown in Table 6. The confidence level is 95% and so the probability of various input factors less than or equal to 0.05 show their noticeable influence of them on the GRGs. The percentage contributions of the three factors on GRG also shown in the table and it can be concluded that the tool feed rate is the most influencing factor (% contribution of 84.82) for GRG followed by speed and the tool coating.

Similar kind of results were recorded for thrust force and MRR by Palanikumar and Muniaraj [8] and Kamath et al. [17], respectively.

4. Confirmation Test

To conduct the confirmation test, the predicted GRG value is to be estimated first using the formula given in Equation (6).

Predicted GRG

$$\zeta_P = \zeta_m + \sum_{r=1}^{n} \zeta_r' - \zeta_m. \quad (6)$$

Here ζ_m denotes the mean or average GRG value and ζ_r' denotes the GRG value at the optimum level. r represents the response and n represents the number of parameters.

Table 6: ANOVA table for GRG.

Source	*df*	Adj. SS	Adj. MS	*F*-value	*P*-value	% Contribution
Tool material	2	0.007706	0.003853	3.37	0.050	1.44
Speed (rpm)	2	0.050877	0.025439	22.25	0	9.49
Feed rate (mm/min)	2	0.45493	0.227465	198.98	0	84.82
Error	20	0.022863	0.001143			4.26
Total	26	0.536376				100.00

Table 7: Confirmation test results.

Response	Thrust force (N)	Torque (Nm)	MRR (mm^3/s)
Value	103.01	3.6	2.94

Using Equation (6), it was found that the value of predicted GRG for the drilling experiments is 0.8023.

Finally, a confirmation drilling experiment is carried out to validate the result of Taguchi–Grey analysis. For confirmation experiment, the optimum input factors have been selected, that is high carbon-coated drilling tool is used at the speed of 1,200 rpm and the feed rate of 120 mm/min, and all the response values are taken and tabulated in Table 7.

The GRG for the values obtained from the confirmation test is evaluated as 0.8386, which is in excellent concurrence with the predicted value of GRG, that is, 0.8023.

5. Conclusions

Aluminum-based hybrid composite (Al7075/BN/Al_2O_3) specimens in the shape of square slabs were cast by stir casting and machined, in which the drilling was carried out as per Taguchi's L27 orthogonal array using three different drill tools under three different drilling speeds, and three different feed rates. The inferences concluded from the experimental investigations are mentioned here.

From the consequences of various examinations:

(i) It is noticed that a minimum drilling force of 62.12 N and torque of 0.766 Nm were induced on the material while using DLC-coated drilling tool under higher drilling speed (3,600 rpm in our case) and at a lower feed rate (40 mm/min).

(ii) The findings of the analysis have revealed that the MRR could be maximized (178.79 mm^3/s) when the drilling speed and feed rate are higher (3,600 rpm and 120 mm/min, respectively) with DLC-coated carbide drills.

(iii) The multiobjective function of thrust force, drilling torque, and MRR is optimized by hybrid Taguchi–Grey analysis method, and it was concluded that the high carbon-coated drilling tool with lower cutting speed and higher feed are producing optimum results.

(iv) Also, ANOVA was carried out and the percentage contribution of all the three input parameters to get optimum results were found. By ANOVA technique, it was concluded that feed rate is influencing more on the responses than speed and tool coatings.

(v) Finally, confirmation drilling test was carried out using optimum parameters, and the responses are analyzed by hybrid TaguchiGrey method to find out the GRG. It is inferred that there is a great agreement between the predicted and actual GRG values.

Data Availability

The data used to support the findings of this study are included in the article. Should further data or information be required, these are available from the corresponding author upon request.

Conflicts of Interest

The authors declare that they have no conflicts of interest.

Funding

Authors declared that no funding was received for this research and publication. It was performed as a part of the Employment Hawassa University, Ethiopia.

Acknowledgments

The authors would like to thank the VELS Institute of Science, Technology & Advanced Studies, Chennai, India for their excellent support for the submission of their papers.

References

[1] V. V. Kalyan Chakaravarthy, T. Rajmohan, D. Vijayan, K. Palanikumar, and B. Latha, "Sustainable drilling performance optimization for nano SiC reinforced Al matrix composites," *Materials and Manufacturing Processes*, vol. 35, no. 12, pp. 1304–1312, 2020.

[2] B. S. Senthil, B. K. Vinayagam, and J. Arunraj, "Experimental evaluation of various parameters influencing thrust force, torque and circularity in drilling of Al based composites using response surface methodology," *Indian Journal of Science and Technology*, vol. 9, no. 36, pp. 1–10, 2016.

[3] M. Kumar, G. Kumar, O. P. Singh, and A. Tomer, "Multi-performance optimization of parameters in deep drilling of SS-321 by Taguchi-based GRA," in *Recent Advances in Mechanical Engineering. Lecture Notes in Mechanical Engineering*, M. Muzammil, A. Chandra, P. K. Kankar and H. Kumar, Eds., pp. 675–681, Springer, Singapore, 2021.

[4] Khushboo Sharma, Gaurav Kumar, and Mukesh Kumar, "Application of Taguchi method coupled with GRA for optimization of drilling process parameters," in *IOP Conference*

Series: Materials Science and Engineering, vol. 1149, IOP Publishing, 2021.

[5] N. Tosun, "Determination of optimum parameters for multi-performance characteristics in drilling by using Grey relational analysis," *The International Journal of Advanced Manufacturing Technology*, vol. 28, pp. 450–455, 2006.

[6] J. Udaya Prakash, C. S. Rubi, C. Rajkumar, and S. Jebarose Juliyana, "Multi-objective drilling parameter optimization of hybrid metal matrix composites using Grey relational analysis," *Materials Today: Proceedings*, vol. 39, pp. 1345–1350, 2021.

[7] R. Bammidi, K. Sai Krishna, B. V. S. S. Kiran, B. Gayatri, K. Srikar, and P. J. Sai Kumar, "Experimental investigation of drilling process parameters of Ti–6Al–4V using Taguchi technique," *Journal of Xi'an University of Architecture & Technology*, vol. 12, no. 4, pp. 4565–4575, 2020.

[8] K. Palanikumar and A. Muniaraj, "Experimental investigation and analysis of thrust force in drilling cast hybrid metal matrix (Al-15% SiC-4% graphite) composites," *Measurement*, vol. 53, pp. 240–250, 2014.

[9] C. S. Rubi and J. U. Prakash, "Drilling of hybrid aluminum matrix composites using Grey–Taguchi method," *INCAS Bulletin*, vol. 12, no. 1, 2020.

[10] C. Kannan, R. Ramanujam, and A. S. S. Balan, "Machinability studies on Al7075/BN/Al_2O_3 squeeze cast hybrid nanocomposite under different machining environments," *Materials and Manufacturing Processes*, vol. 33, no. 5, pp. 587–595, 2018.

[11] R. Sreenivasulu and C. S. Rao, "Application of gray relational analysis for surface roughness and roundness error in drilling of Al6061 alloy," *International Journal of Lean Thinking*, vol. 3, no. 2, 2012.

[12] H. Pekşen and A. Kalyon, "Optimization and measurement of flank wear and surface roughness via Taguchi based Grey relational analysis," *Materials and Manufacturing Processes*, vol. 36, no. 16, pp. 1865–1874, 2021.

[13] Y. Pu, Y. Zhao, J. Meng, G. Zhao, H. Zhang, and Q. Liu, "Process parameters optimization using Taguchi-based Grey relational analysis in laser-assisted machining of Si_3N_4," *Materials (Basel)*, vol. 14, no. 3, Article ID 529, 2021.

[14] K. Saravanan, J. Francis Xavier, M. P. Sudeshkumar, T. Maridurai, V. Suyamburajan, and V. Jayaseelan, "Optimization of SiC abrasive parameters on machining of Ti–6Al–4V alloy in AJM using Taguchi–Grey relational method," *Silicon*, vol. 14, pp. 997–1004, 2021.

[15] P. S. C. Bose and C. S. P. Rao, "Grey Relational Analysis and Response Surface Methodology for Modeling, Analyzing and Optimization of machining parameters for turning Niobium C-103," in *Proceedings of the International Conference on Advances in Civil, Structural and Mechanical Engineering*, vol. 107, 2015.

[16] V. C. Reddy, K. Thota, T. Niskala, and G. M. P. Yadav, "Analysis and optimization of laser drilling process during machining of $AISI_{303}$ material using Grey relational analysis approach," *SN Applied Sciences*, vol. 3, Article ID 335, 2021.

[17] G. B. Kamath, K. Subramaniam, S. Devesh et al., "Multi-response optimization of milling process parameters for aluminium–titanium diboride metal matrix composite machining using Taguchi-data envelopment analysis ranking approach," *Engineered Science*, vol. 18, pp. 271–277, 2022.

Hindawi
Journal of Nanomaterials
Volume 2023, Article ID 7858827, 6 pages
https://doi.org/10.1155/2023/7858827

Research Article

Microstructure and Mechanical Characteristics of Stir-Casted AA6351 Alloy and Reinforced with Nanosilicon Carbide Particles

S. Thirugnanam,[1] G. Ananth,[1] T. Muthu Krishnan,[1] and Tewedaj Tariku Olkeba[2]

[1]*Department of Mechanical Engineering, SRM Valliammai Engineering College, Chennai, Tamil Nadu, India*
[2]*Department of Mechanical Engineering, Ambo University, Ambo, Ethiopia*

Correspondence should be addressed to Tewedaj Tariku Olkeba; tewedaj.tariku@ambou.edu.et

Received 17 July 2022; Revised 12 September 2022; Accepted 5 October 2022; Published 20 April 2023

Academic Editor: N. Senthilkumar

The main aim of this research is to analyze the mechanical performances of the influence of silicon carbide (SiC) particles with AA6351 aluminum alloy. The aluminum metal matrix composites were prepared with liquefying stir casting to produce the metal matrix composites (MMCs). The following weight fractions are AA6351-0% SiC, AA6351-2.5% SiC, AA6351-5% SiC, and AA6351-7.5% SiC utilized to compose the MMCs. The mechanical performances like hardness, flexural, impact, compressive, and tensile studies were investigated on the processed MMCs. The scanning electron microscope (SEM) was employed to examine the strengthened particle of SiC. During the SEM examinations, uniformly dispersed SiC-strengthened particles were analyzed. The entire MMCs specimens achieve greater mechanical characteristics; the specimen fabricated with a maximum volume fraction of 7.5 wt% of SiC accumulates higher strength than the other volume fractions samples. The SiC plays a very tedious role in improving mechanical attributes. The fabricated MMCs were highly utilized in the applications of automotive and aerospace usages. This application is fully employed with lesser weight and maximum strength conditions to fulfill the mechanical performances. The stir-casting process was a highly efficient technique to compose better MMCs to achieve greater strength.

1. Introduction

Commonly matrix-based composites like metal matrix composites (MMCs), ceramic-categorized matrix composites, polymer, and hybrid composites are classified as per the reinforcement phases (strengthened particles) and matrix [1]. The matrix composites are fabricated through the varied condition of mixed materials and are highly capable of gaining mechanical performances compared to the base material. Generally, one or more assorted metals are developed to produce the MMCs along the properly strengthened reinforcements and the parent material [2]. In recent decades, automotive and its related manufacturing sectors have been highly utilized to withstand the heavy load weight on the body, keeping less weight, and maximum strength combinations are majorly required. So this condition is possibly satisfied with aluminum matrix composites (AMCs) [3]. Specifically, superior characteristics are mainly accomplished with extraordinary combinations, namely lesser weight and greater strength to execute outstanding performances like less in density, resistance to wear, and exceptional strength in the AMCs [4]. Last recent periods, production development people mainly contemplated producing efficient mechanical-related components with the capability of resistance to corrosion and wear materials. The prominent ductility state and more excellent mechanical properties are highly attained in aluminum matrix composites and accommodate the mechanical deformation conditions [5]. In the same way, automotive spare materials, namely pistons, drum sections, brake lining parts, and cylinder blocks, are accomplished with maximum life span and incomparable alternates for automotive productions [6]. The aluminum alloys are reputed when this alloy is mingled with proper arrangements of strengthened materials. Because the formability structure, resistance to wear, resistance to corrosion, and improved clear-cut strength are mainly adapted in automotive and

aerospace applications [7]. In this research, AA6351 is considered the parent material. Normally this alloy contains greater age-hardening characters with the generation of transistors Mg–Si intermetallic multiparts and a small quantity of silicon and magnesium. Another specific reason to select AA6351 due to less expensive materials compared to 7xxx and 2xxxx series of alloy [8]. Other significant relations are about the microstructure examination with their impacts on mechanical behaviors, which is a better understanding to obtain superior properties. Therefore, AA6351 is the best-suited material for this study, and this base alloy is an essential choice for blending the reinforcements to get desired applications on AMCs [9]. The mechanical attributes of processed AMCs are mainly based on base metal and suitable reinforcements. It is revealed that the intrinsic properties among the base and strengthened particles and its volume ratio to improve their AMCs performances [10]. This study used nanosilicon carbide (nSiC) as strengthened particles for AA6351 alloy. The intricate surface layers are diminished with advanced incorporation nSiC blended on the AA6351. Similarly, the robust interfacial bonding is accumulated with nSiC-strengthened reinforcements and AA6351 alloys. In special cases, inhomogeneous scattering is occurred on the processed MMCs by the contemptible wetting during the other processes like powder metallurgy, squeeze casting, and solid-state process. To overcome these issues, stir-casting liquefied process is as suitable technique [11].

Sekar et al. [12] fabricated the stir-casted MMCs on AA6082 with strengthened zirconium oxide particles and silicon carbide. The hardness strength was improved at 1 wt% of SiC and ZrO_2 compared to the base material. SiC as major reason to enhance the mechanical strength with uniform dispersion of reinforcements. Rajmohan et al. [13] optimized the machining parameters of processed MMCs by drilling. The MMCs were prepared with Al356 and SiC combinations by stir-casting process. During the machining, surface roughness and wear of the tool was enhanced surface finishes with proper mixing of base metal Al356 and SiC due to carbide particles. Daniel et al. [14] investigated the MMCs and developed the optimized milling parameters on processed MMCs of Al5059 and SiC combinations. The influence of SiC plays a significant aspect in improving the machining characteristics by increasing the SiC content. Christy et al. [15] focused the stir-casted process on the alumina and aluminum oxide. Most of the samples occurred with porosities on the MMCs. Mainly, models with 5.95 wt% of Al_2O_3 attained lesser porosity when compared to another set of pieces. Kannan et al. [16] studied the optimized turning process parameters on the processed MMCs. These MMCs were prepared by the combinations of Al7075 and SiC with 10 wt% by stir-casting technique. The optimal parameters are attained at the MMCs, which were processed at 3% SiC, while the surface finish appeared to be the best. Kumar et al. [17] investigated the MMCs prepared from their combinations of aluminum and SiC-strengthened particles. The machining characteristics like surface roughness and material removal rate are attained in 9 wt% SiC with the presence of aluminum.

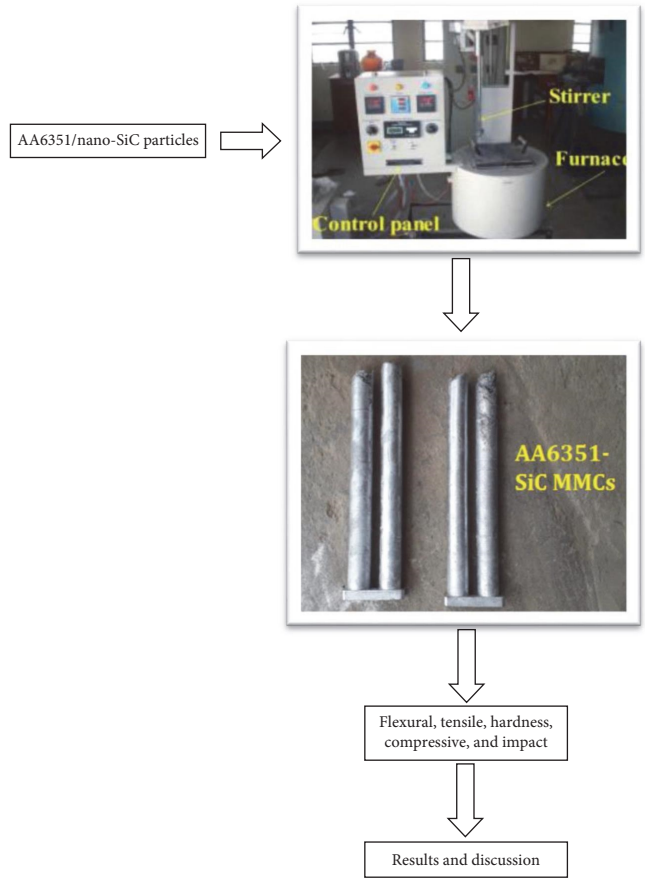

Figure 1: Experimental layout with graphical representation.

From the detailed survey of the literature, there is some lacking investigations have been accomplished on AA6351 and SiC arrangements. This paper considered AA6351 and nSiC composites with different fractions of weight, namely, 0%–7.5%, by increasing of 2.5 wt%. The following mechanical performances hardness, flexural, impact, compressive, and tensile studies were made on the processed MMCs.

2. Material Details and Processing Procedure and Testing Standards of Processed MMCs

AA6351 and nSiC are the materials to consider the stir-casting process in this investigation. The following chemical elements of AA6351 are 1 wt% of Si, 0.6 wt% of Fe, 0.75 wt% of Mg, 0.5 wt% of Mn, 0.2 wt% of Ti, 0.1 wt% of C, 0.1 wt% of Zn, Bal of Al, and nSiC particle size is 10 nm, and it was purchased from the CBE metal mart, Kovai, respectively. The matrix and strengthened particle volumes are evenly measured per the indicated fractions by weight balancing. Initially, the AA6351 is poured into the crucible heating system with a maintained temperature at 750°C. Then nSiC was preheated at 430°C. The indicated weight fractions of strengthened particles were added to the molten stage of AA6351 to compose the four sets of MMCs specimens. The processed MMCs specimens are AA6351-0% nSiC, AA6351-2.5% nSiC, AA6351-5% nSiC, and AA6351-7.5% nSiC. During the process, samples

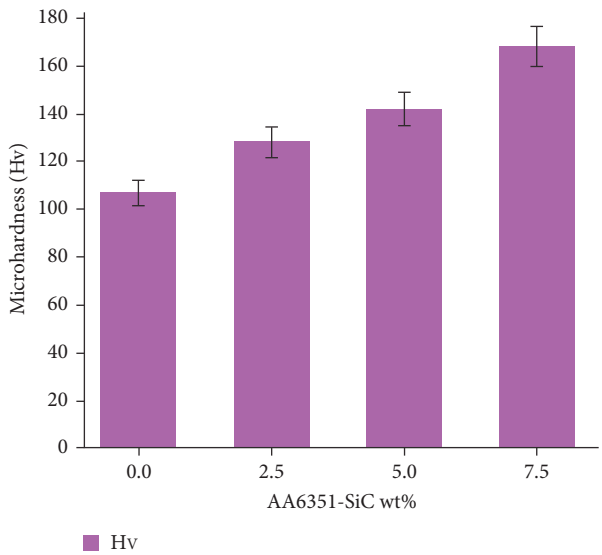

Figure 2: Hardness analysis on processed MMCs (AA6351-SiC wt%).

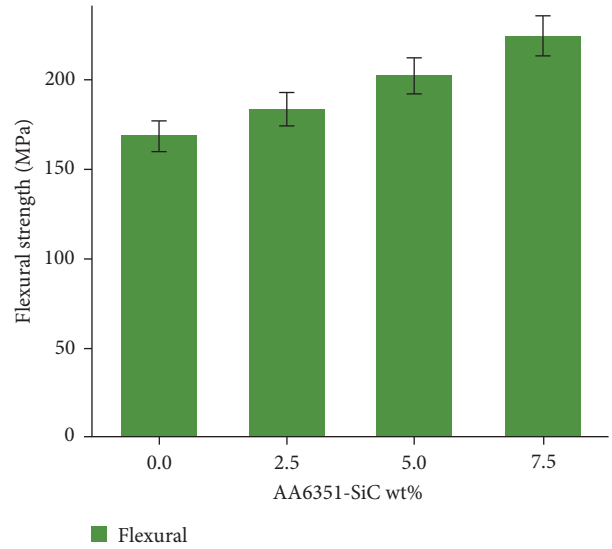

Figure 3: Flexural properties on processed MMCs (AA6351-SiC wt%).

were prepared at a maintained stirring speed and time of 650 rpm and 7 min, respectively. Figure 1 shows the experimental layout with a graphical representation.

The scanning electron microscope (SEM) examination was used to analyze the dispersion of strengthened particles on the processed MMCs. The round-shaped die was utilized to compose the desired shapes of MMCs specimens, mainly derived from the molten state of composites. The following mechanical tests with their ASTM standards are hardness (E384-08), flexural (C1161), impact (E23), compressive (E9), and tensile studies (E8-08), respectively [18].

3. Results and Discussions

3.1. Hardnessstudies on Processed MMCs Specimens. Figure 2 displays the hardness results of AA6351 and nSiC MMCs. The grain refinement was successfully accompanied by the proper dispersion of mixed pores in the maximum volume fraction of AA6351-7.5 wt% of nSiC. It is revealed that the maximum SiC incorporated well in the aluminum alloy improves the hardness due to the presence of carbide elements [19]. Also, the SiC creates the strengthened materials for hardening purposes when accomplished with AA6351. The MMCs specimens were increased gradually by developing the volume fraction of SiC. Therefore, Figure 2 indicates that the more significant fraction of AA6351-7.5 wt% of nSiC increases the hardness strength (168 Hv). It is implicit that the insertion of nSiC-strengthened nanoparticles with AA6351 generates enhanced hardness strength based on the Orowan mechanism [20]. The lesser hardness strength (107 Hv) was attained at AA6351-0 wt% of nSiC.

3.2. Flexuralstudies on Processed MMCs Specimens. Figure 3 exhibits the bar charts of flexural properties on fabricated MMCs on AA6351-SiC wt%. The greater flexural properties (224 MPa) are attained by the more excellent weight ratio of AA6351 and 7.5 wt% of SiC, compared to other various sets

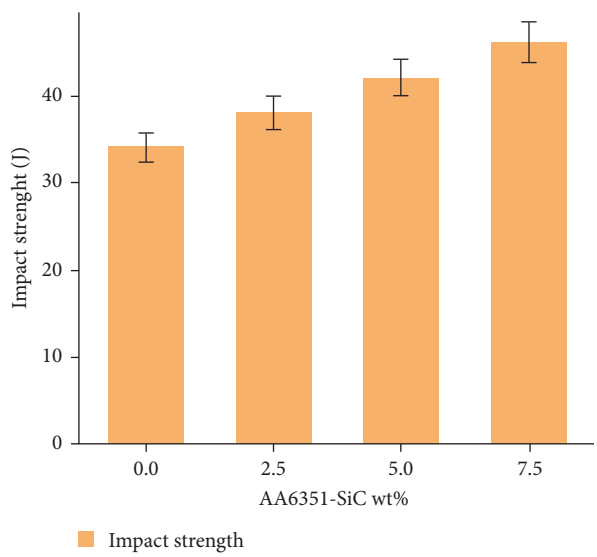

Figure 4: Impact properties on processed MMCs (AA6351-SiC wt%).

of weighted samples. It is implicit that the expanding weight ratio of SiC establishes the flexural potency in the composed MMCs. It is revealed that the secondary phase strengthened particle SiC was migrated the load from the AA6351 alloy [21]. At the same time, interfacial bonding was well created in the improved flexural specimens [22].

3.3. Impact Properties on Fabricated MMCs Specimens. The impact properties of fabricated MMCs of AA6351 and wt% of SiC are presented in Figure 4. The impact properties were successfully performed on the processed MMCs with potential and robustness performances. Due to the bear-up with a lack of caution was accumulated below the vibration of MMCs, which was close to the rupture below the rapid stress [23]. The proper interfacial bonding improved the impact

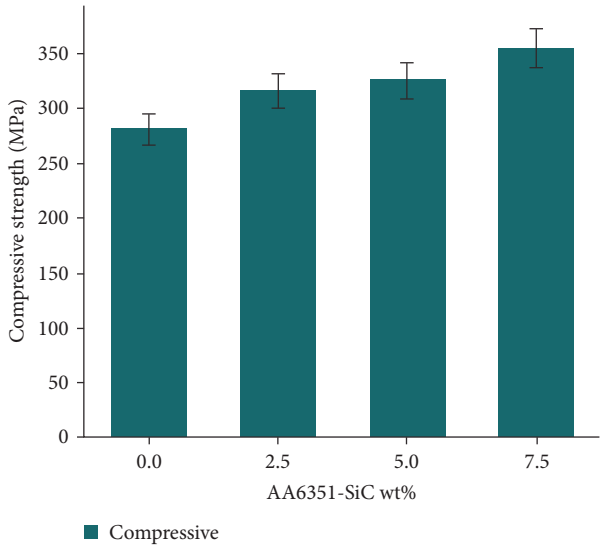

Figure 5: Compressive properties on processed MMCs (AA6351-SiC wt%).

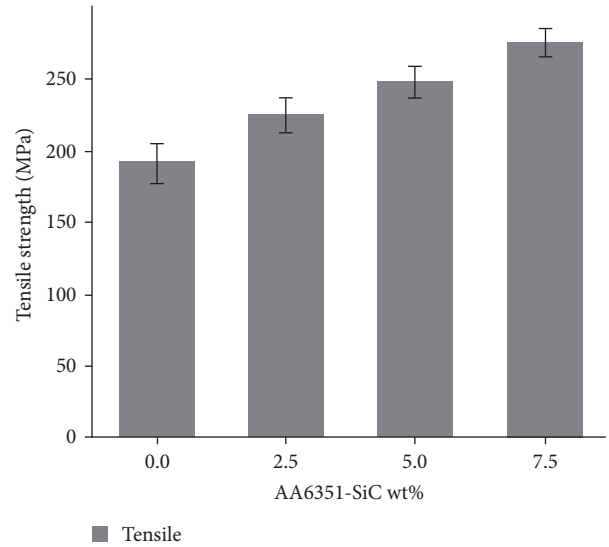

Figure 6: Tensile strength on processed MMCs (AA6351-SiC wt%).

properties created in the MMCs. The increment of SiC-strengthened nanoparticles enhances their impact strength (46 J) and is exhibited in Figure 4.

3.4. Compressive Strength on Processed MMCs Samples. Figure 5 displays the compressive strength contributions on processed MMCs of AA6351 and various fractions of SiC. It is concluded that the compressive properties were superior, with a maximum weight fraction of 7.5 wt% of nSiC, and its maximum compressive value is 355 MPa. This processed specimen was entirely protected with even scattering of SiC on the base material during the process [24]. During the performance test, the load was relocated from parent metal to the uniform dispersed strengthened regions to produce the refinement structure in the grain boundary areas. These results were mainly supported by Orowan strengthening mechanism [25]. The lesser value was composed in the without strengthened composite specimens. The specimens having 2.5 and 5 wt% in SiC was better results when compared to naked AA6351. The distributed SiC-strengthened particles are very minimized during the stir casting while strength was slightly maximum and far minimum than the highest volume fraction of SiC. The presence of carbide particles in the MMCs created more compressive strength during the test, and it was a major reason to enhance the compressive in entire reinforced composites.

3.5. Tensile Properties Studied on Various SiC Weight Fractions on MMCs. The tensile properties of stir cast AA6351 and SiC wt% fractions are presented in Figure 6. From Figure 6, AA6351 and its nano-based SiC-strengthened particles attained greater tensile strength with a uniform dispersion of reinforcements. AA6351 and nSiC gathered intermetallic bonding potency through solid phases protected by their strengthened materials [26]. Meanwhile, migrated load was satisfactory in developing the MMCs attributes. Normally, the SiC is a significant factor in enhancing the intermetallic potency of strengthened MMCs than the other strengthened ceramic particles. The MMCs processed at 7.5 wt% in SiC with AA6351 accommodates the greater tensile strength (276 MPa) than other MMCs specimens AA6351-0 wt% of SiC (192 MPa), AA6351-2.5 wt% of SiC (225 MPa) and AA6351-5 wt% of SiC (248 MPa), respectively [27]. The increment of SiC on the AA6351 at particular weight fraction results in superior tensile properties. The Ororwan strengthening mechanism significantly improves their strength in the processed MMCs. This same specimen also gets better-reinforced dispersion in the maximum weight fraction samples. The grain refinement achieves better tensile strength in the MMCs.

4. Microstructure on the Processed Specimen with a Maximum Fraction of AA6351/SiC

Figure 7 exhibits the micrographs on processed MMCs with 7.5 wt% of SiC/AA6351 combinations. During the process, some minor porosity and small cracks were accumulated in the MMCs. But in this case, SiC significantly removes these minor issues during the stir casting. Figure 7 shows that the sample was accomplished with evenly dispersed SiC-strengthened particles, and mechanical characteristics also improved simultaneously [28]. Identifying the SiC particles in the micrographs is necessary for revealing the evidence. Thermal stability was maintained in the interface of MMCs when analyzing the mechanical properties. The interfacial betterment occurred in this specimen due to SiC by in situ reactions, and well bonded was created in the examined micrograph [29]. Figure 7(a)–7(d) indicates that SiC particles with different weight fractions of nSiC and which were spread more in the processed MMCs by the various-volume fraction. The micrograph analysis clearly shows the intermetallic particles in the processed specimen. The SEM image was analyzed with 100 μm to identify the particles.

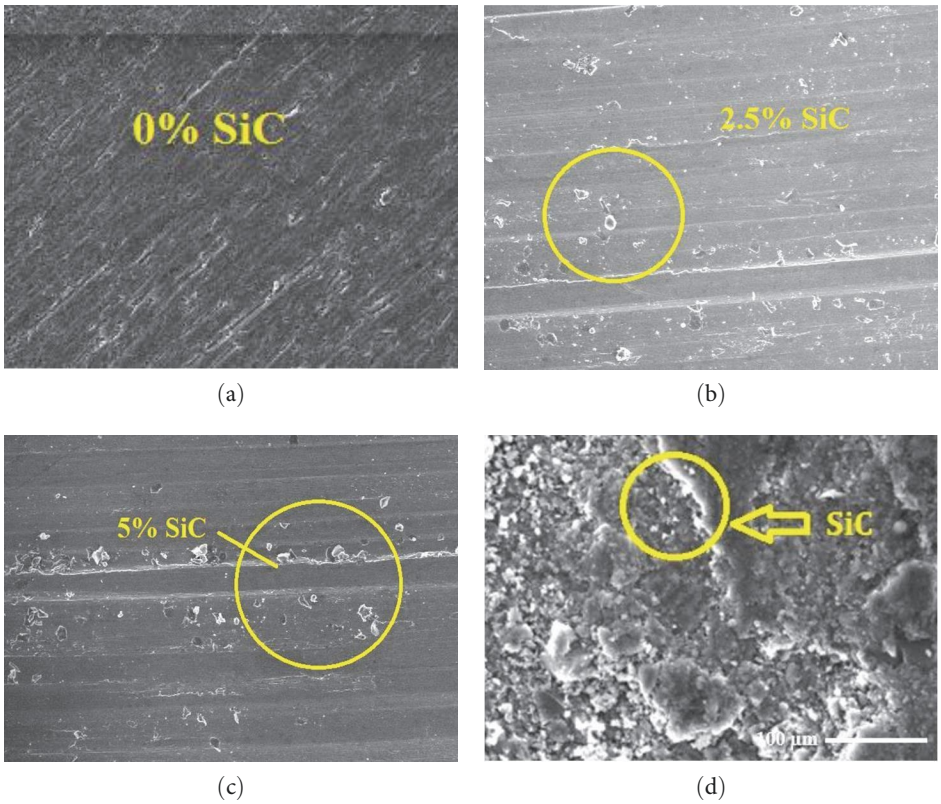

(a) (b) (c) (d)

Figure 7: (a) SEM analysis on AA6351-SiC 0 wt%; (b) SEM analysis on AA6351-SiC 2.5 wt%; (c) SEM analysis on AA6351-SiC 5 wt%; (d) SEM analysis on AA6351-SiC 7.5 wt%.

5. Conclusion

(i) The stir-casting liquefying technique was effectively employed with AA6351 and SiC arrangements.

(ii) The mechanical performance, like hardness, flexural, impact, compressive, and tensile studies, was successfully conducted on the processed MMCs.

(iii) These properties were enhanced by increasing the weight fraction SiC on the base alloy AA6351.

(iv) The specimen was fabricated with a high volume fraction of SiC 7.5 wt%, and AA6351 combinations procured maximum strength when compared to other processed MMCs.

(v) The SEM analysis was studied effectively on the same high-fraction specimen. The presence of SiC particles was dispersed uniformly during SEM analysis, and identified strengthened particles were seen in the processed MMCs.

(vi) The future implications of processed MMCs investigations are gray, and TOPSIS approaches will be implemented to identify the optimal parameters.

Data Availability

The data used to support the findings of this study are included in the article. Should further data or information be required, these are available from the corresponding author upon request.

Conflicts of Interest

The authors declare that they have no conflicts of interest.

References

[1] K. V. Mahindra and K. Radhakrishna, "Characterization of stir cast Al-Cu–(fly ash + SiC) hybrid metal matrix composites," *Journal of Composite Materials*, vol. 44, no. 8, pp. 989–1005, 2010.

[2] L. Natrayan, A. Merneedi, G. Bharathiraja, S. Kaliappan, D. Veeman, and P. Murugan, "Processing and characterization of carbon nanofibre composites for automotive applications," *Journal of Nanomaterials*, vol. 2021, Article ID 7323885, 7 pages, 2021.

[3] A. Lehtinen, L. Laurson, F. Granberg, K. Nordlund, and M. J. Alava, "Effects of precipitates and dislocation loops on the yield stress of irradiated iron," *Scientific Reports*, vol. 8, Article ID 6914, 2018.

[4] B. Nayak, R. K. Sahu, and P. Karthikeyan, "Study of tensile and compressive behaviour of the in-house synthesized Al-alloy nano composite," *IOP Conference Series: Materials Science and Engineering*, vol. 402, Article ID 012070, 2018.

[5] B. Vinod, S. Ramanathan, V. Ananthi, and N. Selvakumar, "Fabrication and characterization of organic and in-organic reinforced A356 aluminium matrix hybrid composite by

improved double-stircasting," *Silicon*, vol. 11, pp. 817–829, 2019.

[6] N. Balaji, L. Natrayan, S. Kaliappan, P. P. Patil, and N. S. Sivakumar, "Annealed peanut shell biochar as potential reinforcement for aloe vera fiber-epoxy biocomposite: mechanical, thermal conductivity, and dielectric properties," *Biomass Conversion and Biorefinery*, 2022.

[7] M. Samaee, S. Najafi, A. R. Eivani, H. R. Jafarian, and J. Zhou, "Simultaneous improvements of the strength and ductility of fine-grained AA6063 alloy with increasing number of ECAP passes," *Materials Science & Engineering: A*, vol. 669, pp. 350–357, 2016.

[8] C. Chanakyan and S. Sivasankar, "Parametric studies in friction stir welding on Al–Mg alloy with (HCHCr) tool by Taguchi based desirability function analysis (DFA)," *Journal of Ceramic Processing Research*, vol. 21, no. 6, pp. 647–655, 2020.

[9] M. Shayan, B. Eghbali, and B. Niroumand, "Fabrication of AA2024−TiO_2 nanocomposites through stir casting process," *Transactions of Nonferrous Metals Society of China*, vol. 30, no. 11, pp. 2891–2903, 2020.

[10] R. Ramaswamy, S. V. Gurupranes, S. Kaliappan, L. Natrayan, and P. P. Patil, "Characterization of prickly pear short fiber and red onion peel biocarbon nanosheets toughened epoxy composites," *Polymer Composites*, vol. 43, no. 8, pp. 4899–4908, 2022.

[11] T. Anandaraj, P. P. Sethusundaram, M. Meignanamoorthy, and M. Ravichandran, "Investigations on properties and tribological behavior of AlMg4.5Mn0.7(AA5083)-MoO_3 composites prepared by stir casting method," *Surface Topography: Metrology and Properties*, vol. 9, no. 2, Article ID 025011, 2021.

[12] K. Sekar, G. Jayachandra, and S. Aravindan, "Mechanical and welding properties of A6082-SiC-ZrO_2 hybrid composite fabricated by stir and squeeze casting," *Materials Today: Proceedings*, vol. 5, no. 9, Part 3, pp. 20268–20277, 2018.

[13] T. Rajmohan, K. Palanikumar, and M. Kathirvel, "Optimization of machining parameters in drilling hybrid aluminium metal matrix composites," *Transactions of Nonferrous Metals Society of China*, vol. 22, no. 6, pp. 1286–1297, 2012.

[14] S. A. A. Daniel, R. Pugazhenthi, R. Kumar, and S. Vijayananth, "Multi objective prediction and optimization of control parameters in the milling of aluminium hybrid metal matrix composites using ANN and Taguchi–Grey relational analysis," *Defence Technology*, vol. 15, no. 4, pp. 545–556, 2019.

[15] J. V. Christy, R. Arunachalam, A.-H. I. Mourad, P. K. Krishnan, S. Piya, and M. Al-Maharbi, "Processing, properties, and microstructure of recycled aluminum alloy composites produced through an optimized stir and squeeze casting processes," *Journal of Manufacturing Processes*, vol. 59, pp. 287–301, 2020.

[16] A. Kannan, R. Mohan, R. Viswanathan, and N. Sivashankar, "Experimental investigation on surface roughness, tool wear and cutting force in turning of hybrid (Al7075+SiC+Gr) metal matrix composites," *Journal of Materials Research and Technology*, vol. 9, no. 6, pp. 16529–16540, 2020.

[17] M. R. Kumar, H. N. Reddappa, R. Suresh, and M. Gangadharappa, "Effect of heat treatment on tensile strength of Al7075/Al_2O_3/SiCp hybrid composite by stir casting technique," *Materials Today: Proceedings*, vol. 5, no. 10, Part 3, pp. 22460–22465, 2018.

[18] K. R. Ramkumar, H. Bekele, and S. Sivasankaran, "Experimental investigation on mechanical and turning behavior of Al 7075/x% wt. TiB_2-1% Gr in situ hybrid composite," *Advances in Materials Science and Engineering*, vol. 2015, Article ID 727141, 14 pages, 2015.

[19] Y. Sesharao, T. Sathish, K. Palani et al., "Optimization on operation parameters in reinforced metal matrix of AA6066 composite with HSS and Cu," *Advances in Materials Science and Engineering*, vol. 2021, Article ID 1609769, 12 pages, 2021.

[20] T. Anandaraj, P. P. Sethusundaram, C. Chanakyan, S. Sakthivelu, and M. Meignanamoorthy, "Influence of different reinforcements on properties of metal matrix composites: a review," *Materials Today: Proceedings*, vol. 37, Part 2, pp. 3480–3484, 2021.

[21] V. A. Vincent, C. Kailasanathan, G. Ramesh, T. Maridurai, and V. R. Arun Prakash, "Fabrication and characterization of hybrid natural fibre-reinforced sandwich composite radar wave absorbing structure for stealth radomes," *Transactions on Electrical and Electronic Materials*, vol. 22, pp. 794–802, 2021.

[22] A. Merneedi, L. Natrayan, S. Kaliappan et al., "Experimental investigation on mechanical properties of carbon nanotube-reinforced epoxy composites for automobile application," *Journal of Nanomaterials*, vol. 2021, Article ID 4937059, 7 pages, 2021.

[23] M. Meignanamoorthy, M. Ravichandran, S. V. Alagarsamy, C. Chanakyan, S. D. Kumar, and S. Sakthivelu, "Effect of various reinforcements on properties of metal matrix composites: a review," *Materials Today: Proceedings*, vol. 27, Part 2, pp. 1118–1121, 2020.

[24] L. Natrayan, S. Balaji, G. Bharathiraja, S. Kaliappan, D. Veeman, and W. D. Mammo, "Experimental investigation on mechanical properties of TiAlN thin films deposited by RF magnetron sputtering," *Journal of Nanomaterials*, vol. 2021, Article ID 5943486, 7 pages, 2021.

[25] P. Sharma, S. Sharma, and D. Khanduja, "A study on microstructure of aluminium matrix composites," *Journal of Asian Ceramic Societies*, vol. 3, no. 3, pp. 240–244, 2015.

[26] N. M. Nachippan, A. Backiyaraj, V. R. Navaneeth et al., "Structural analysis of hybridized glass fiber hemp fiber reinforced composite wheel rim," *Materials Today: Proceedings*, vol. 46, Part 9, pp. 3960–3965, 2021.

[27] A. Velhinho, J. D. Botas, E. Ariza, J. R. Gomes, and L. A. Rocha, "Tribocorrosionstudies in centrifugally cast Al-matrix SiCp-reinforced functionally graded composites," *Materials Science Forum*, vol. 455–456, pp. 871–875, 2004.

[28] S. Suthagar, T. Kumaran, G. Gowtham, T. Maridurai, T. Sathish, and S. Deivanayagi, "Computational analysis of INVELOX wind turbine to analyze the venturi velocity by change the parameter of diffuser," *Materials Today: Proceedings*, vol. 46, Part 9, pp. 4245–4249, 2021.

[29] S. H. Anand, N. Venkateshwaran, J. V. S. P. Kumar, D. Kumar, C. R. Kumar, and T. Maridurai, "Optimization of aging, coating temperature and reinforcement ratio on biosilica toughened in-situ Al-TiB_2 metal matrix composite: a Taguchi grey relational approach," *Silicon*, vol. 14, pp. 4337–4347, 2022.

Hindawi
Journal of Nanomaterials
Volume 2023, Article ID 5668025, 7 pages
https://doi.org/10.1155/2023/5668025

Research Article

Synthesis and Antimicrobial Activity Assay of Nanometal Oxide-Doped Liquid Crystal

S. Deepthi,[1] **S. Srikiran**,[2] **M. Satyanarayana Gupta**,[3] **and Adamu Mulatu Kumara**[4]

[1]*Department of Science and Humanities, Lendi Institute of Engineering and Technology, Vizianagaram, India*
[2]*Centre for Nanotechnology, Andhra University College of Engineering, Visakhapatnam, India*
[3]*Department of Aeronautical Engineering, MLR Institute of Technology, Hyderabad, Telangana, India*
[4]*College of Engineering and Technology, Wollega University, Nekemte, Ethiopia*

Correspondence should be addressed to Adamu Mulatu Kumara; adamum@wollegauniversity.edu.et

Received 30 August 2022; Revised 21 October 2022; Accepted 27 January 2023; Published 7 April 2023

Academic Editor: B. Deepanraj

The spread of infectious diseases across the globe as a result of numerous bacterial and fungal variations has become a serious threat to human life. A critical global situation is the need to search for antibiotic resistance and develop new treatments. The most crucial role is for academics to advise the pharmaceutical industry about substances with antimicrobial assessments. One of the challenges in implementing novel medicine delivery is the discovery of compounds having antibacterial and antifungal characteristics against Gram-positive and Gram-negative bacteria and fungi. The superiority of the metal oxide-doped liquid crystal technology for antibiotic resistance is revealed. In this work, a bacterially triggered drug delivery system using a nanometal oxide-doped lipid-based liquid crystal system was explored. Copper oxide (CU) and cholesteryl stearate (CS) are processed using ultrasonication to produce the complex chemical in powder form (CSCU). Functional groups are predicted by Fourier transform infrared (FTIR) analyses, while surface appearance and dimensions that support the compound CSCU's biological characteristics are revealed by scanning electron microscope (SEM) and transmission electron microscope (TEM) analyses. Using the agar-well diffusion method, this substance was tested for antibacterial and antifungal activities against the Gram-positive bacteria *Streptococcus pyogenes* at various concentrations ranging from 0.6 to 1.25 μg/ml. Additionally, this substance exhibits a range of moderate to good antifungal efficacy against *Aspergillus niger*.

1. Introduction

Infections with bacteria and fungi can have a mild to serious impact on human health. These microorganisms exist on the mucosal epithelial surfaces of human bodies, causing infections [1]. Many diseases, from minor infections to infectious, life-threatening infections, are caused by microbes. These microorganisms produce toxic shock syndrome and invasive infections that have significant morbidity and mortality rates. *Streptococcus pyogenes*, an exclusive human pathogen, is a genus of Gram-positive bacteria that causes a variety of illnesses that are extremely contagious. Hand-to-hand contact, nasal discharge, and even airborne droplets can all be ways that infections spread. The virulence factors produced by *S. pyogenes* as it spreads within the human body have an impact on the host immune system [2, 3]. The cause of several infections is also by the fungus *Aspergillus fumigatus*. It can be found everywhere in the environment, including in the dust, soil, and plant debris. This fungus produces conidia-like spores that are airborne. It is also one of the frequent causes of otomycosis, a condition that results in temporary hearing loss and ear pain [4, 5]. These bacteria and fungi spread into the human host system by creating colonies that have an impact on human health.

Rapid sequential scientific procedures are being used to conduct an in-depth investigation of the bacterial and fungal communities in a systematic manner. Due to the fact that bacteria and fungi can cause mild to severe diseases, the development of antimicrobials is necessary [6, 7]. The development of new medications to combat germs and fungus is time- and money-consuming. Drugs that are currently in the market could be expedited and made more affordable

through reformulation [8]. Both bacteria and fungi undergo repeated iterations of evolution over time. Therefore, it is vital to introduce new medications or reformulate existing ones with the appropriate admitters. Drugs that are efficient and cutting edge are being created in this procedure to combat bacterial and fungal infections and slow down or stop their growth [9]. Recently, nontoxic bioactive molecules attached to specific targeting ligands have been used to carry out the majority of work in the biological area.

The dual functions of lipid-based liquid crystals as carriers and drug delivery methods make them potentially useful in the pharmaceutical industry [10, 11]. Due to their hydrophobic and hydrophilic characteristics and their role as carriers for antimicrobial peptides, lipid-based liquid crystals play a significant role in biological phenomena [12]. These have a wide range of medical uses, such as drug delivery, carrier capsules, biocompatibility, and biodegradability [13, 14]. Because of its hydrophobic properties, which result in an antibacterial phenomenon, lipid-based liquid crystals have cellular storage and have become important in biological investigations. Cholesteryl stearate (CS) is an ester of cholesterol and stearic acid, which is a class of lipid-based liquid crystal [15, 16]. These bioactive compounds' excellent capabilities are released through nanocontainment [17]. Due to their outstanding achievements against bacteria and fungi, metal oxide nanomaterials were first appeared in the biological field. The effectiveness of metallic nanocrystals as antibacterial agents has been demonstrated in numerous researches [18, 19]. Copper oxide nanoparticles stand out among the metal oxide nanoparticles for their effectiveness in repelling microorganisms [20, 21]. This research focuses on the antibacterial properties of nanometal oxide-doped lipid-based liquid crystals and their active engagement as antimicrobial peptide carriers. Doping of nanoparticles into lipid-based liquid crystal compound results in the enhancement of physical, chemical, and biological properties.

In this study, ultrasonication method is used to mix the lipid-based liquid crystalline compound CS with the metal oxide nanocompound copper oxide in a specific mass to volume ratio. The combined molecular structure of CSCU is shown in Figure 1.

The compound's capacity for antibacterial testing is encapsulated by its supramolecular structure and hydrophobic character [22–24].

The complex CSCU has distinct spectral peaks that can be seen using Fourier transform infrared (FTIR) spectroscopy [25, 26]. High surface areas and crystal morphologies that have been verified by scanning electron microscope (SEM) and transmission electron microscope (TEM) studies are used in the preparation of CSCU [27–29]. The agar-well diffusion method was used to assess the potential antibacterial uses of the CSCU compound [30]. *S. pyogenes*, a Gram-positive bacteria, and *A. fumigatus*, a fungus, are both susceptible to the antibacterial and antifungal properties of this nanoliquid crystalline substance [31, 32]. Lipid-based liquid crystals have gained importance in the field of biology due to their compatibility. They are good in dissolution and are very feasible in biodrugs. Nano-doped lipid-based liquid crystals enhance the biological properties which could be observed through TEM and SEM studies. The compound used by us "CS" is a lipid-based liquid crystal which has withstanding biological properties and the nanocompound copper oxide also competes with the chosen liquid crystal in biological properties. Hence, the chosen compound (CSCU) promotes good antibacterial and antifungal properties, which is a proof for a new compound to be used.

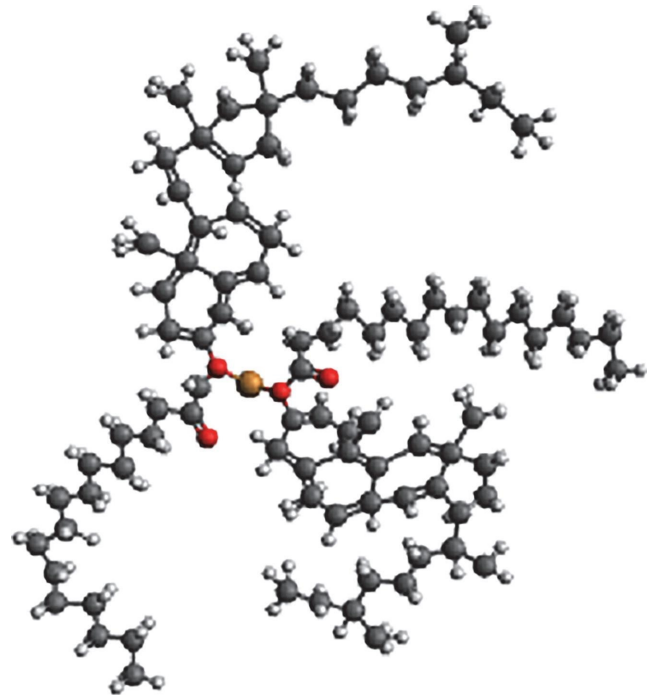

Figure 1: Molecular structure of CSCU.

The compound CSCU with its antimicrobial activities shows prominence in drug delivery mechanism. Crystalline nature and equal surface morphological distribution of molecules in complex compound may have controlled release of drug.

2. Materials and Methods

The various materials used for the purpose of experimentation and the methods for preparing the cultures are discussed in the continuing section.

2.1. Synthesis. Without additional purification, CS and copper oxide nanoparticles were employed after being obtained from Sigma-Aldrich. CS (500 mg) was dissolved in 15 ml of ethanol and sonicated for 10 min. In a separate beaker, copper oxide (0.012 mg) was dissolved in 5 ml of ethanol. The copper oxide solution was added dropwise to the ethanolic solution of CS and further sonicated for 30 min. Both substances were dissolved in an ethanol solution and ultrasonically processed using PCI Analytics. The reaction mixture was kept overnight and vacuum filtered and dried to obtain a solid precipitate [33].

2.2. Preparation of Bacterial Cultures. To test the antimicrobial activities of obtained powder (CSCU), agar-well diffusion method is used. In this method, 24 hr young cultures were

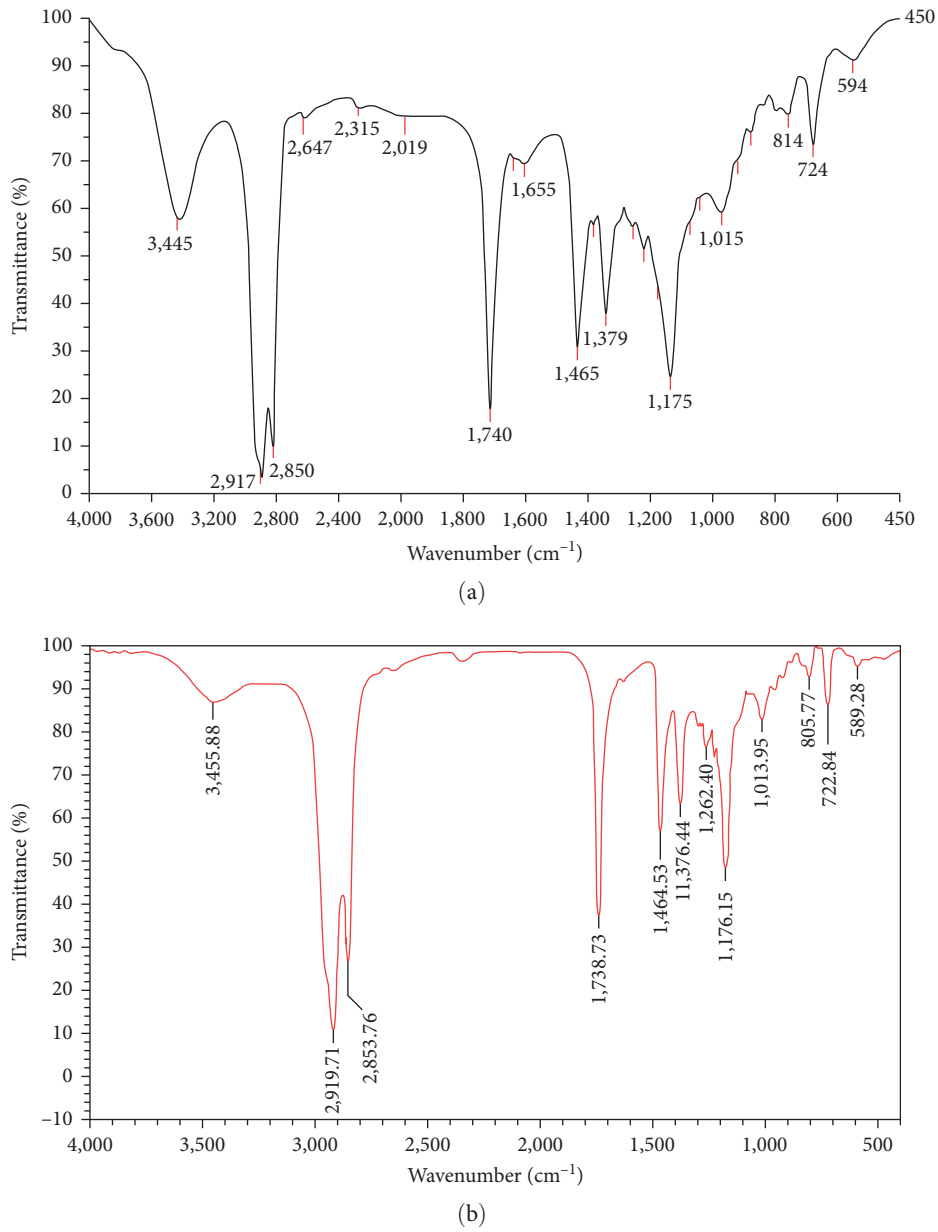

Figure 2: FTIR spectrum of (a) CS and (b) CSCU.

used to test the complex compound's antimicrobial activity. Microbes were cultivated after the media had been autoclaved for about 30 min at 1,200°C (15 psi). Nutrient agar medium, seeded with the appropriate strains of bacteria, was placed aseptically into each sterile petri dish, amounting to about 20 ml per plate. For solidification, the plates were kept at room temperature. A number 3 cup borer (6 mm in diameter) was used to create five uniform cups or wells in each petri dish once the material had solidified. Each cap's base had a drop of molten nutritional agar that had applied to seal it.

Young cultures with CSCU compound were used for 24 hr to test the antifungal activity using the agar-well diffusion method. An autoclave was used to sterilize the potato dextrose agar (PDA) medium for around 30 min. PDA medium in the amount of 20 ml (per petri dish), seeded with the appropriate fungal strains, was transferred aseptically into the petri dish. The plates were remained so that they could solidify.

3. Results and Discussion

The discussion below deals with the results associated with the work.

3.1. Spectral Analysis. The complex compound's FTIR spectra's spectrum analysis demonstrates that the crystalline lipid material and nanoparticles have been properly amalgamated. FTIR was used to conduct spectrum analyses on the complex chemical CSCU (Thermo Nicolet 6700). The bonding nature of CS and copper oxide has been confirmed through FTIR analyses

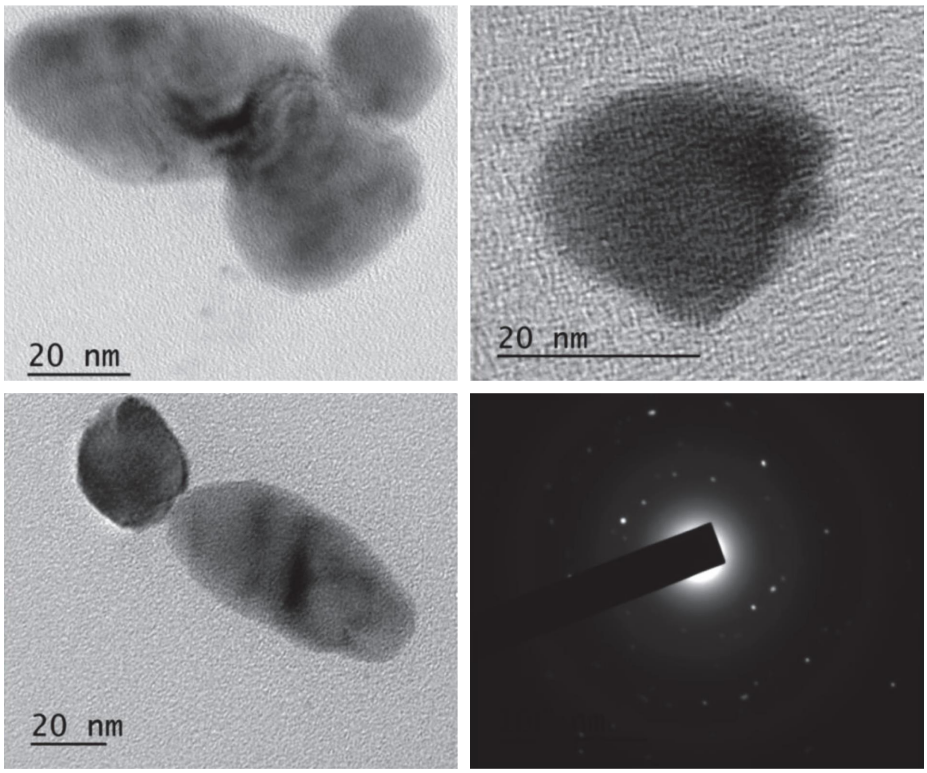

Figure 3: TEM analysis of CSCU.

of the complex compound (CSCU) from the shifts in both fingerprint and functional regions. The spectral wavenumbers between 400 and 4,000 nm were taken into consideration. The peaks that correspond to CS are 2,917, 1,415, and 840 cm^{-1}. By observing downward movements in C–H stretching and bending, copper oxide bonding was found to enhance the peaks. Also, C–O stretch was noticeable with a downward tilt. As shown in Figure 2, there is no discernible change in bonding when C=C and CH_3 are bent. Pyridine group, ketone group, and benzene ring structures make up the majority of original CS. Individual carbon atoms had an impact on the hydrophobicity of the CS during complex formation with metal oxide nanoparticles, which demonstrate an improved chemical potential in the alkyl group. From the peaks of FTIR, the amalgamation of CSCU compound is estimated and the same was interpreted through the structural evaluation.

3.2. TEM Analysis. Figure 3 shows TEM pictures of complicated compounds. TEM examination revealed the complicated compound's crystalline form. The concentration of both the compounds, CS and CU, is visible in TEM pictures, which also demonstrate an equal distribution of particles. The TEM image clearly shows that the complex molecule's morphology is practically spherical in shape. Figure 3 also shows that selected area electron diffraction (SAED) pattern reveals the complicated material's crystalline structure. Particles of synthetic CSCU are about 20 nm in size. The spreading of the substance into the petri dish with the nutrient agar media seeded is relatively simple, thanks to the special characteristics of nanocrystalline CSCU. Crystalline nature of the compound was revealed by TEM analysis. The significance of the biogenic material in terms of antimicrobial activities of complex compound strongly depends on its crystalline nature.

3.3. SEM Analysis. The SEM analysis of CSCU was performed on JSM-6390 for 5, 10, and 50 μm. Morphological studies were performed on complex compound to visualize the distribution of copper oxide nanocrystals on CS compound. The composition of elements can be known with topographical properties. The resolution of SEM images extends from 5 to 50 μm with magnification of 500–3,000x. As the magnification of the image increases, it reveals that CS and CU are well dispersed to form complex clusters, as shown in Figure 4.

SEM images demonstrate the appropriate cluster formation of the CSCU complex and its effectiveness as an antibacterial agent. Because the complex CSCU particles were equally dispersed, the substance had an antimicrobial effect on the *S. pyogenes* organism. The complex substance successfully eliminates the germs at higher concentrations and works down to lower ones. The complex substance demonstrates its perfection when antifungal activity against the *Aspergillus niger* bacterium is tested at different concentrations. Equally dispersed copper oxide nanoparticles on CS compound reveal the complex cluster of CSCU. As there is equal distribution of particles, the complex compound CSCU is effective on bacteria and fungi. The intricate cluster permits antifungal activity that is on par with industry norms.

3.4. Antibacterial and Antifungal Activities of CSCU. The complex compound CSCU was reconstituted with suitable solvent like dimethyl sulfoxide (DMSO) and tested at various concentrations (1, 2, 3, 4, 5, 6, 7, and 8 μg/ml). The test was

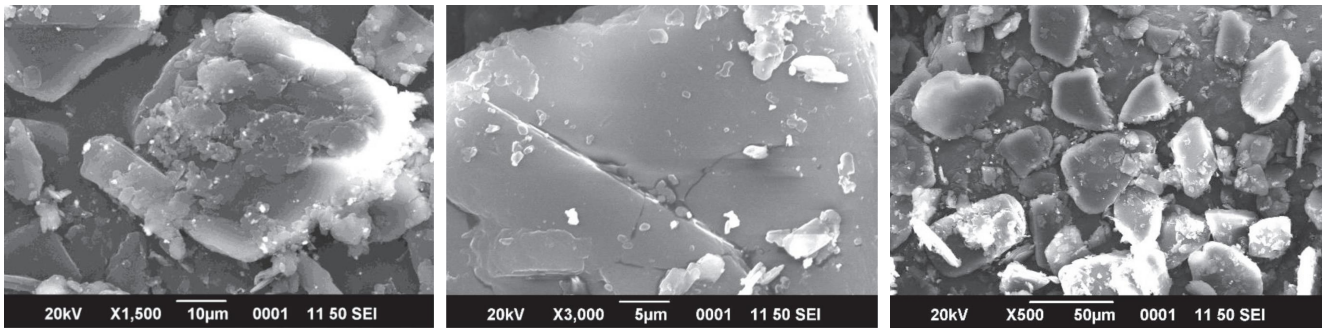

Figure 4: SEM analysis of CSCU.

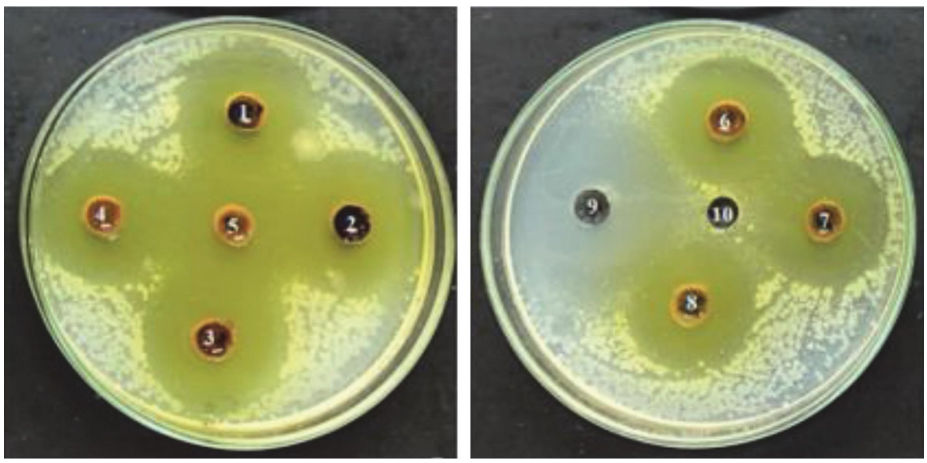

Figure 5: Antibacterial activity of CSCU.

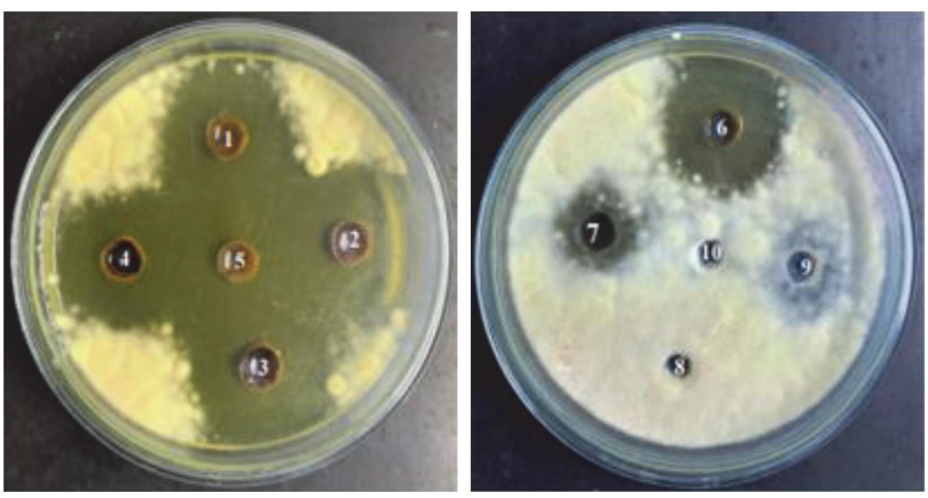

Figure 6: Antifungal activity of CSCU.

performed under control DMSO and standard antibiotic ciprofloxacin was carefully placed in the well. Petri plates were incubated at $37 \pm 2°C$ for about 12 hr. The $5\,\mu g/ml$ concentration was used as positive control. Figures 5 and 6 show the antibacterial and antifungal activities of the complex compound CSCU. The absence of bacterial growth is indicated by clear wells, as shown in Figure 5.

The chemical was reconstituted with DMSO, a suitable solvent, and added to petri dishes containing various bacterial and fungal strains at various concentrations.

3.5. Statistical Analysis. The zone of inhibition of *S. pyogenes* bacterial decay in petri dish of reconstituted compound (CSCU) at various concentrations along with the standard

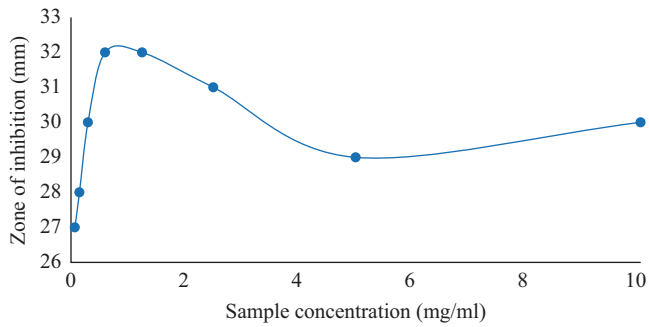

Figure 7: Concentration of sample against zone of inhibition.

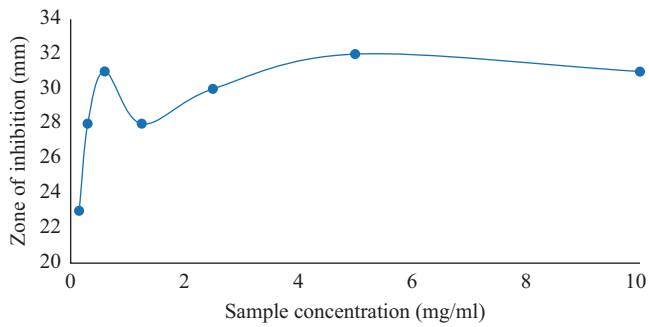

Figure 8: Concentration of CSCU against zone of inhibition.

ciprofloxacin and control DMSO in the incubated petri plates was incubated at $37 \pm 2°C$, as shown in Figure 7. The zone diameter in petri dish shows the active involvement of complex compound CSCU with concentration ranging from 0.6 to 1.25 μg/ml against bacterial strains.

The compound CSCU also exhibits antifungal properties. Strains of fungi at different concentrations are compared with standard values. The zone of inhibition of decay in petri dish of reconstituted compound (CSCU) at various concentrations along with the standard fluconazole and control DMSO in the incubated petri plates was incubated at $28 \pm 2°C$ about 24 hr. A standard with 5 μg/ml concentration was used as a positive control. The zone diameter in petri dish shows the active involvement of complex compound CSCU with concentration ranging from 2.5 to 5 μg/ml against fungal strains, as shown in Figure 8.

4. Conclusion

Due to the daily emergence of novel bacterial and fungal illnesses, drug delivery systems are concentrating on the development of various new substances. Utilizing an ultrasonication method, a liquid crystalline substance doped with nanometal oxide was created. Bonding between CS and CU is confirmed by significant wavenumber shifts with abrupt peaks in selected areas. By using the agar-well diffusion method, the hydrophobicity and supramolecular structure of CSCU well establish antibacterial and antifungal properties.

Lipid-based liquid crystals have gained importance in biology due to their compatibility. They have excellence in dissolution and are most feasible in bioavailability of drugs. Nano-doped lipid-based liquid crystals enhance their biological properties and could be observed through TEM and SEM studies. Our compound CS is a lipid-based liquid crystal which has withstanding biological properties and our nano-compound copper oxide also competes with the chosen liquid crystal in biological properties. So, our chosen compounds are properly sonicated to obtain the new compound (CSCU) which promotes good antibacterial and antifungal properties. Due to the individual performances of both on bacteria and fungi, we thought to have more pronouncement of the complex compound on these two that had obtained good results. The compound CSCU can further be tested for antioxidant and anticancer properties.

The development of a novel medication from the complex chemical CSCU is the main focus of this research.

Data Availability

The datasets generated during and/or analyzed during this study are available from the corresponding author on reasonable request.

Conflicts of Interest

The authors declare that they have no conflicts of interest.

Acknowledgments

The authors thank the support extended by Centre for Nanotechnology, Andhra University College of Engineering, Visakhapatnam for allowing us to use their facilities and for recording infrared spectra, STIC, SEM, and TEM images. The authors also thank to Adhya Biotech Laboratories, Visakhapatnam for duly performing with hands on experience with agar-well diffusion method.

References

[1] D. W. K. Acheson and S. Luccioli, "Mucosal immune responses," *Best Practice & Research Clinical Gastroenterology*, vol. 18, no. 2, pp. 387–404, 2004.

[2] S. Kanwal and P. Vaitla, *Streptococcus Pyogenes*, Vol. 1, StatPearls Publishing, Treasure Island, FL, 2022.

[3] L. R. K. Brooks and G. I. Mias, "*Streptococcus pneumoniae's* virulence and host immunity: aging, diagnostics, and prevention," *Frontiers in Immunology*, vol. 9, Article ID 1366, 2018.

[4] M. Pal, "Morbidity and mortality due to fungal infections," *Journal of Applied Microbiology and Biochemistry*, vol. 1, no. 1-2, pp. 1–3, 2017.

[5] D. Malcolm, K. B. Richardson, and W. Hope, "*Aspergillus*," in *Clinical Mycology (Second Edition)*, pp. 271–296, Elsevier, 2009.

[6] R. J. Fair and Y. Tor, "Antibiotics and bacterial resistance in the 21st century," *Perspectives in Medicinal Chemistry*, vol. 6, pp. 25–64, 2014.

[7] T. Roemer and D. J. Krysan, "Antifungal drug development: challenges, unmet clinical needs, and new approaches," *Cold Spring Harbor Perspectives in Medicine*, vol. 4, no. 5, Article ID a019703, 2014.

[8] A. Miró-Canturri, R. Ayerbe-Algaba, and Y. Smani, "Drug repurposing for the treatment of bacterial and fungal infections," *Frontiers in Microbiology*, vol. 10, Article ID 41, 2019.

[9] D. Taylor, "The pharmaceutical industry and the future of drug development," in *Pharmaceuticals in the Environment*, pp. 1–33, The Royal Society of Chemistry, 2015.

[10] J. Barauskas, C. Cervin, M. Jankunec et al., "Interactions of lipid-based liquid crystalline nanoparticles with model and cell membranes," *International Journal of Pharmaceutics*, vol. 391, no. 1-2, pp. 284–291, 2010.

[11] Y. Chen, P. Ma, and S. Gui, "Cubic and hexagonal liquid crystals as drug delivery systems," *BioMed Research International*, vol. 2014, Article ID 815981, 12 pages, 2014.

[12] L. Boge, H. Bysell, L. Ringstad et al., "Lipid-based liquid crystals as carriers for antimicrobial peptides: phase behavior and antimicrobial effect," *Langmuir*, vol. 32, no. 17, pp. 4217–4228, 2016.

[13] S. Singh, T. R. Dodiya, R. Dodiya, Y. V. Ushir, and S. Widodo, "Lipid nanoparticulate drug delivery systems: approaches toward improvement in therapeutic efficacy of bioactive molecules," in *Drug Carriers*, L. J. Villarreal-Gómez, Ed., IntechOpen, London, UK, 2022.

[14] A. A. Attama, M. A. Momoh, and P. F. Builders, "Lipid nanoparticulate drug delivery systems: a revolution in dosage form design and development," in *Recent Advances in Novel Drug Carrier Systems*, A. D. Sezer, Ed., IntechOpen, London, UK, 2012.

[15] C. Reyes Mateo, A. Ulises Acufia, and J.-C. Brochon, "Liquid-crystalline phases of cholesterol/lipid bilayers as revealed by the fluorescence of *trans*-parinaric acid," *Biophysical Journal*, vol. 68, pp. 978–987, 1995.

[16] J. R. Harris, S. Bhakdi, U. Meissner et al., "Interaction of the *Vibrio cholerae* cytolysin (VCC) with cholesterol, some cholesterol esters, and cholesterol derivatives: a TEM study," *Journal of Structural Biology*, vol. 139, no. 2, pp. 122–135, 2002.

[17] M. Makowski, Í. C. Silva, C. P. do Amaral, S. Gonçalves, and N. C. Santos, "Advances in lipid and metal nanoparticles for antimicrobial peptide delivery," *Pharmaceutics*, vol. 11, no. 11, Article ID 588, 2019.

[18] A. Singh, P. K. Gautam, A. Verma et al., "Green synthesis of metallic nanoparticles as effective alternatives to treat antibiotics resistant bacterial infections: a review," *Biotechnology Reports*, vol. 25, Article ID e00427, 2020.

[19] A. Vassallo, M. F. Silletti, I. Faraone, and L. Milella, "Nanoparticulate antibiotic systems as antibacterial agents and antibiotic delivery platforms to fight infections," *Journal of Nanomaterials*, vol. 2020, Article ID 6905631, 31 pages, 2020.

[20] S. Mahmoodi, A. Elmi, and S. Hallaj-Nezhadi, "Copper nanoparticles as antibacterial agents," *Journal of Molecular Pharmaceutics & Organic Process Research*, vol. 6, no. 1, Article ID 140, 2018.

[21] S. Meghana, P. Kabra, S. Chakraborty, and N. Padmavathy, "Understanding the pathway of antibacterial activity of copper oxide nanoparticles," *RSC Advances*, vol. 5, no. 16, pp. 12293–12299, 2015.

[22] B. Hu, C. Owh, P. L. Chee et al., "Supramolecular hydrogels for antimicrobial therapy," *Chemical Society Reviews*, vol. 47, no. 18, pp. 6917–6929, 2018.

[23] X. Wang, Y. Zhang, S. Gui et al., "Characterization of lipid-based lyotropic liquid crystal and effects of guest molecules on its microstructure: a systematic review," *AAPS PharmSciTech*, vol. 19, pp. 2023–2040, 2018.

[24] K. Kuroda, G. A. Caputo, and W. F. DeGrado, "The role of hydrophobicity in the antimicrobial and hemolytic activities of polymethacrylate derivatives," *Chemistry - A European Journal*, vol. 15, no. 5, pp. 1123–1133, 2009.

[25] H. Arshad, M. A. Sami, S. Sadaf, and U. Hassan, "*Salvadora persica* mediated synthesis of silver nanoparticles and their antimicrobial efficacy," *Scientific Reports*, vol. 11, Article ID 5996, 2021.

[26] K. Raja, P. S. Ramesh, and D. Geetha, "Structural, FTIR and photoluminescence studies of Fe doped ZnO nanopowder by co-precipitation method," *Spectrochimica Acta Part A: Molecular and Biomolecular Spectroscopy*, vol. 131, pp. 183–188, 2014.

[27] V. Dengle-Pulate, P. Chandorkar, S. Bhagwat, and A. A. Prabhune, "Antimicrobial and SEM studies of sophorolipids synthesized using lauryl alcohol," *Journal of Surfactants and Detergents*, vol. 17, pp. 543–552, 2014.

[28] A. H. Phakatkar, E. Firlar, L. Alzate et al., "TEM studies on antibacterial mechanisms of black phosphorous nanosheets," *International Journal of Nanomedicine*, vol. 15, pp. 3071–3085, 2020.

[29] S. Shanmugan, N. Saravanan, V. Chithambaram, B. Deepanraj, and G. Palani, "Investigation on single crystal by tartaric acid–barium chloride: growth and characterization of novel NLO materials," *Bulletin of Materials Science*, vol. 43, Article ID 202, 2020.

[30] B. Bonev, J. Hooper, and J. Parisot, "Principles of assessing bacterial susceptibility to antibiotics using the agar diffusion method," *Journal of Antimicrobial Chemotherapy*, vol. 61, no. 6, pp. 1295–1301, 2008.

[31] A. H. Cheung Lam, N. Sandoval, R. Wadhwa et al., "Assessment of free fatty acids and cholesteryl esters delivered in liposomes as novel class of antibiotic," *BMC Research Notes*, vol. 9, Article ID 337, 2016.

[32] R. Teixeira-Santos, M. Gomes, L. C. Gomes, and F. J. Mergulhão, "Antimicrobial and anti-adhesive properties of carbon nanotube-based surfaces for medical applications: a systematic review," *iScience*, vol. 24, no. 1, Article ID 102001, 2021.

[33] V. Chithambaram, T. S. Franklin Rajesh, G. Palani, E. Ilango, B. Deepanraj, and S. Santhanakrishnan, "Growth and investigation of novel nonlinear optical single crystal of urea potassium dichromate by solution growth technique for photonic application," *Journal of Optics*, vol. 49, pp. 181–186, 2020.

Hindawi
Journal of Nanomaterials
Volume 2023, Article ID 7470200, 11 pages
https://doi.org/10.1155/2023/7470200

Research Article

Preparation of Nanosize Bone Powder from Waste and Development of Al Composite through Squeeze Casting Process

R. Muthu Kamatchi,[1] **R. Muraliraja**,[1] **C. Sabari Bharathi**,[1] **T. Sathish**,[1] **S. Sathyaraj**,[1] **and Leevesh Kumar**[2]

[1]*Department of Mechanical Engineering, Vels Institute of Science Technology and Advanced Studies, Chennai, India*
[2]*Department of Construction Technology and Management, Ambo University, Ambo, Oromia, Ethiopia*

Correspondence should be addressed to Leevesh Kumar; leevesh.kumar@ambou.edu.et

Received 24 August 2022; Revised 25 September 2022; Accepted 30 September 2022; Published 23 February 2023

Academic Editor: N. Senthilkumar

Al6061 alloy is most commonly used in automotive, marine, and aerospace applications to lighten the composite and increase its strength. Al6061 alloy is a precipitation-hardened aluminum alloy used as a matrix material. Beef bone is a biowaste that has polluted the environment and the people who live in the vicinity of its manufacturing and disposal sites. Biowaste has been used in a variety of ways by researchers in recent years, including activated carbon, water purification, reinforcement in composites, fillers, additives, etc. Beef bones that had been abandoned as waste were collected, cleaned, and grounded into a fine powder with a particle size of 50–100 nm and used as reinforcement. Squeeze casting process is used to create the newly created aluminum composite (Al6061 + 0%, 5%, 10% of bone powder). The aluminum composite was fabricated and three samples were successfully obtained for further testing and analysis. The prepared Al composites with nanopowder reinforcement are analyzed for surface morphology, elemental identification, hardness, porosity, tensile strength, and compression strength. The percentage of porosity in the composite is improved by 36.7% when compared to the Al6061 alloy. Similarly, the tensile strength of the produced composite is increased to 5.59%. A significant improvement is observed in the wear resistance and hardness of the composite as 54.55% and 48.65%, respectively.

1. Introduction

Aluminum matrix composites (AMCs) are high-tech materials with remarkable characteristics. AMCs are made up of numerous materials, one of which is aluminum, which may be improved by combining them [1]. Aluminum alloys are being phased out of many uses in the automotive, aerospace, marine, and nuclear sectors [2]. Heavy-duty industrial applications need lightweight materials with high specific stiffness, strength, and heat resistance, and metal matrix composites (MMCs) like the Al600 series (Al6061/6063) fit the bill. The casting method for MMCs can be used to produce near-net form composites at a low cost [3]. Particle-reinforced Al MMCs are well-suited for use in the aerospace, automotive, military, and leisure sectors because of their unique mixture of features [4]. Their characterization has been hampered by unknown properties such as wettability, adsorption properties, chemical compatibility, and the development of complex stress states as a result of changes in temperature and moisture expansion [5]. AMCs have partially achieved this goal because of their excellent qualities such as stiffness, low density and high damping, enhanced wear resistance, and simplicity of production [6]. It is possible to enhance the performance of Al–Si alloys by altering the particle size, shape, and content of Si particles. Al–Si cast alloys may also be strengthened with hard ceramic reinforcements such as Al_2O_3, SiO_2, ZrB_2, SiC, TiC, and B_4C to boost their performance even more. Adding hard-ceramic particles to composites improves their performance but their greater cost raises the whole cost. Red mud, bagasse ash, fly ash, rice husk ash (RHA), eggshells (ESs), and other industrial wastes are used as efficient aluminum alloy-reinforcing materials. Many researchers have reported better physical, mechanical, and thermal characteristics with the effective use of these materials as reinforcement [7]. Air and soil pollution are major concerns all around the globe. Typically, industrial waste is the

Table 1: Mechanical properties of composite material prepared using various organic reinforcements.

Sl. no.	Matrix	Reinforcement	Hardness	Compression or tensile	References
1	Al6061	Rice husk	48.4 BHN	171.3 MPa (T)	[10]
2	AMC	Aloe vera	33.8 BHN	119.83 MPa (T)	[11]
3	Al6082	Red mud	95 HV	169.87 MPa (T)	[12]
4	Al7075	Coconut shell fly ash	169.5 BHN	189 MPa (T)	[13]
5	Al6063	Fly ash	86 BHN	169 MPa (T)	[14]
6	Al2024	Eggshell	109 BHN	208.9 MPa (T)	[15]
7	Al6061	Eggshell	103 HRC	138.62 MPa (T) 351.22 MPa (C)	[16]
8	Al7075	Rice husk	121 HV	260 MPa (T) 563 MPa (C)	[17]
9	Al356	Fly ash	88.45 BHN	320.65 MPa (T)	[18]
10	Al2025	Red mud	79.99 HV	186.42 MPa (T)	[19]

source of this form of pollution. Agricultural and industrial wastes such as cement, red mud, fly ash, ESs, rice husks, coconut shells, and bagasse may be used to reduce the processing costs of composites [8]. The presence of $CaCO_3$ in ESs demonstrates its ability to enhance the mechanical characteristics of any material when used as reinforcement. ES may serve as a useful reinforcing material when working with aluminum to improve the properties [9]. The mechanical properties of composite materials are collected from the previous research work, as shown in Table 1. The organic waste materials were prepared, and composites were prepared for various applications. Many researchers reported that the addition of prepared particles elevates the properties of the composite when compared to the Al alloy.

Dwivedi and Srivastava [7] postulated that collagen powder and Al_2O_3 ceramic particles serve as major reinforcement with aluminum as a basic material. The results of the microstructural investigation indicate homogeneous distribution of collagen powder and Al_2O_3 particles in the matrix material. Tensile strength was increased by 14.32% by incorporating 5% Al_2O_3 and 1.25 wt% collagen powders into the aluminum matrix material. The addition of 6.25 wt% Al_2O_3 to aluminum resulted in a 35.29% increase in hardness. It was also discovered that adding 2.5 wt% Al_2O_3 and 3.75 wt% collagen powder to aluminum at the same time increased its durability by 27.77%. For further confirmation of the existence of Al_2O_3 and Cr, an X-ray diffraction investigation was also carried out. Aluminum alloy 6,063 was strengthened with different weight percentages from 2.5% to 12.5% of palm kernel shell particles. In a permanent mild steel mold, a stir casting process was used to create the composite. The morphological study revealed that the secondary phase of palm kernel shell reinforcements was disseminated uniformly in the main phase of the aluminum matrix. The incorporation of palm kernel shell particles into the composites resulted in a higher density and greater porosity than the basic alloy. The development of composites revealed the formation of intermetallic compounds [20]. Imran and Anwar Khan [21] investigation have been carried out on alloys and reinforcements that are used to fabricate aluminum metal matrix composite (AMMC) materials. According to the findings, a mechanical property has improved significantly. Low coefficient of thermal expansion was compared to standard base alloys; superior wear and corrosion resistance. In their research, Omoniyi et al. [22] looked at physical and mechanical factors such as density, impact strength, tensile strength, hardness, and microstructure. The density reduces as the proportion of reinforcement increases. 97.69 MPa is the highest ultimate tensile strength (UTS) of the aluminum–wood composite, whereas 40.189 MPa is the maximum UTS of the unreinforced aluminum alloy. There are wide variations in impact energy, with a maximum of 89.00 J at 10% weight of wood particle addition but the hardness is more or less constant, ranging from 52.33 to 62.0 BHN at 10% weight. The aluminum–wood composite had better mechanical qualities than pure aluminum in all of the mechanical tests. According to the microstructure study, the wood particles were evenly dispersed in the MMC. Saravanan and Senthil Kumar's [23] work showed the possibility of strengthening aluminum alloy (AlSi10Mg) using locally accessible and affordable RHA for the development of a novel material. Liquid metallurgy was employed to generate MMCs with a RHA particle content of 3%, 6%, 9%, and 12% by weight. According to the findings, increasing the proportion of RHA reinforcement increases the composite's ultimate tensile, compressive, and hardness strength. Islam et al. [24] explained the synthesis of industrial and agricultural wastes loaded onto AMMC, as well as their mechanical, corrosion, and physical properties. Innovative filler particles that are inexpensive, accessible, and have better properties than standard particles are discussed in this study. An electron microscopic image of the hybrid composite, as well as measurements of density and hardness, was used to verify its validity. The surface hardness of the composite with 6% ES powder produces a hardness value of 197 HV. Calcium oxide, which is tougher than carbide particles reinforced in the hybrid composite material, is the type of biological ES found in it. The hybrid composite with 3% SiC and 6% ES has high wear resistance, so it is a suitable choice for construction. A hybrid composite containing 6% of Al_2O_3 and 6% of SiC has good adhesive morphology and shows less wear. So, it has been found that a decrease in hard particles or an increase in ES could affect sliding wear [25]. According to Ikubanni et al. [26], hybrid-reinforced AMCs were explored

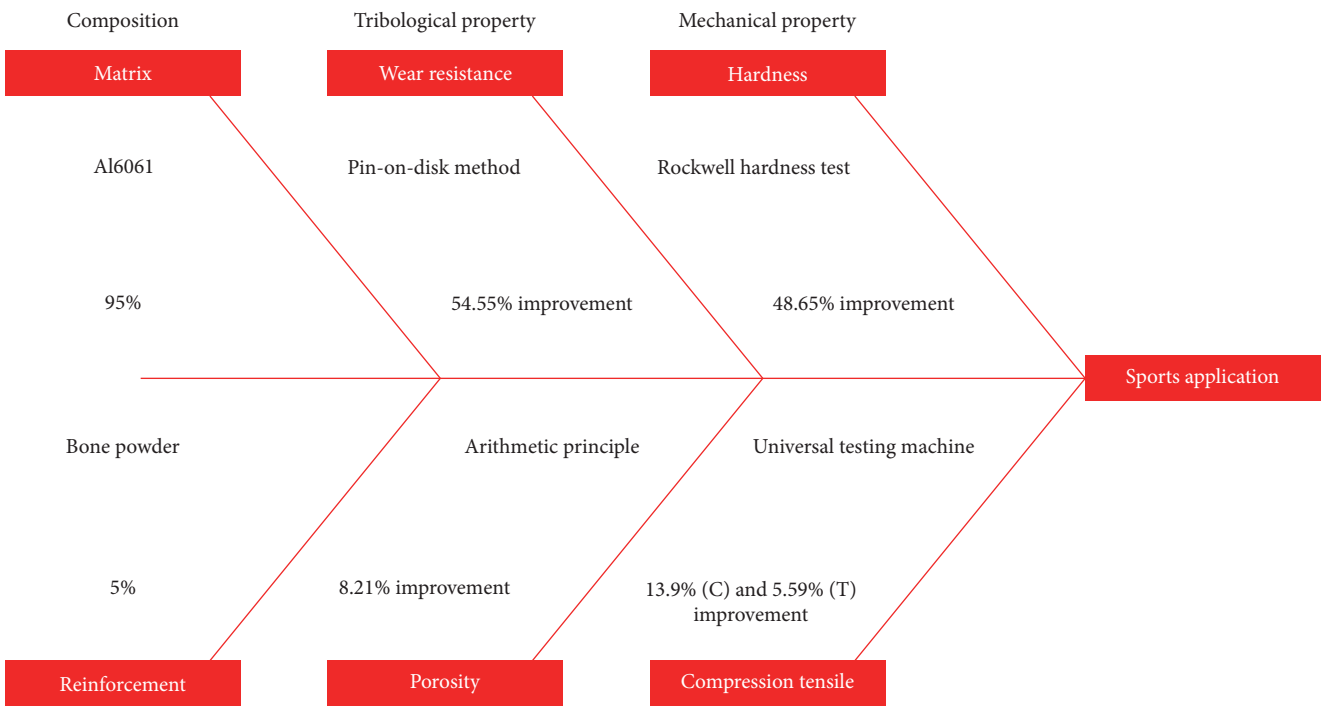

Figure 1: Fishbone diagram for research work carried out.

by using Al6063 alloy, SiC, and palm kernel shell ash (PKSA) reinforcements. With the use of the double stir casting process, different amounts of SiC and PKSA were incorporated into the matrix metal at various ratios. During the experiments, the samples' densities and porosities were assessed. The findings showed that the density of the composite decreased with an increase in PKSA, whereas the density improved in other samples with an increase in SiC. Double stir casting process yielded appropriate porosity percentages for cast MMCs, as shown by the findings, which revealed that the percentages of fell were within the allowable range. Verma and Kumar [27] have found that using rice husk and fly ash to generate an AMMC results in increased quality, including physical and superior wear resistance abilities. The primary objective is to evaluate the feasibility of using the stir casting method to make aluminum alloys with the specified reinforcements. The machinability of the material has been examined via the use of electrical discharge machining (EDM) tests, and analysis of the agrowaste and fly ash distribution in aluminum composites has been done by scanning electron microscopy (SEM). Composites have also been studied for their mechanical and corrosion characteristics. According to Yadav et al. [28], adding RHA to an aluminum alloy matrix improves the mechanical and physical characteristics and increases the wear rate resistance of the composite. Composites' scanning electron micrographs reveal a uniform distribution of grain ash in the aluminum matrix. When exposed to high temperatures, aluminum alloys lose their microcutting properties and begin to oxidation. The composite material's strain fields and wear resistance are enhanced because of the difference in coefficients of thermal expansion between the matrix and reinforcing materials. Yadav et al. [29] created AMMCs using ES and RHA reinforcements. In the AMMC study, ES and RHA reinforcements at 4.75 and 1 wt% Cr increased tensile strength and hardness by 22.41% and 45.5%, respectively. There are no data available regarding the bone powder used as reinforcement. However, it is also found that most of the waste materials used as reinforcement, so far, improve the strength of the material.

Thus, in this research work, new material composition is formulated and developed using the squeeze casting process. Al6061 alloy is used as as matrix material, which is the most commonly used material in sports applications. For the first time, the bone powder is prepared and used as reinforcement to produce the new Al composite. The morphological study is done using a scanning electron microscope and the presence of added elements is identified through energy dispersive X-ray (EDAX) analysis. The percentage of porosity is measured using the arithmetic principle for the composite. A hardness tester, a universal testing machine, and a pin-on-disk tribometer are used to check the finished composite. The overview of the work is given with the help of a fishbone diagram for better understanding, as shown in Figure 1. The composition of the matrix in this work is Al6061 at 95%, and the reinforcement material is beef bone powder at 5%, produced using the squeeze casting process. The physical properties of the composites, such as porosity and hardness, are improved by 36.7% and 48.6%, respectively. The mechanical properties such as tensile and compression strengths of the composites are improved by 5.59% and 13.97%, respectively. The tribological properties of the composites were improved by 54%, and measured using the pin-on-disk method.

2. Experimental Details and Procedures

2.1. Matrix and Reinforcement Materials. The matrix material, aluminum Al6061, was procured from the metal market.

Table 2: Chemical composition of Al6061.

Element	Mn	Fe	Mg	Si	Cu	Zn	Ti	Cr	Other	Al
%	0.15	0.70	1.20	0.80	0.40	0.25	0.15	0.35	0.05	Balance

Table 3: Chemical composition of beef bone.

Element	CaO	P_2O_5	MgO	SiO_2	Others
%	48.21	37.77	1.29	0.12	12.61

Table 4: Squeeze casting process parameters used for the fabrication of composites.

Sl. no.	Process parameters	Recommended conditions	References
1	Squeeze pressure	100 MPa	[30]
2	Squeeze pressure holding time	45 s	[31]
3	Melting temperature	700°C	[32]
4	Die temperature	250°C	[33]
5	Stirring time	5 min	[34]
6	Stirring speed	600 rpm	[33]
7	Reinforcement percentage	5% (in μ)	[35]
8	Reinforcement preheating temperature	300°C	[35]

Composites were developed using waste cow bone, which was gathered from a butcher market and used as reinforcing material. The bones were initially cleaned with sufficient amount of water to remove the skin and then cleaned with acetone. The collected bones were bigger in size, to make it into smaller size, portable hand wheel cutter made it as powder using grinder machine. Finally, it was reduced to nanosize using ball milling machine. A portable X-ray fluorescence (XRF) analyzer was used to determine the Al6061's elemental makeup, as shown in Table 2. Table 3 shows the composition of reinforced waste beef bones.

2.2. Production of MMCs using the Squeeze Casting Method. Using the squeeze casting procedure, the composites were made, and the parameters employed in this study are shown in Table 4. To eliminate filth and oil, an aluminum rod was procured from the market and cleaned with acetone. To make it fit through the crucible's entry, the rod was sliced into small pieces. In the beginning, 300°C was applied to the permanent hardened steel dies measuring 50 mm in diameter and 250 mm in length. To keep the melt temperature at 700°C, the pressure-casting furnace with temperature control was turned on and set to 750°C. A nonstick boron carbide coating was then applied to the stirrer rod and stirrer, which was then cured at 250–300°C to protect the stirrer edges from deterioration at high temperatures. At 300°C, the preheating chamber warmed the reinforcement particles so that they would be free of moisture and clump together less easily. When the crucible temperature reached 350°C, the matrix materials were loaded into the furnace and subsequently heated to 700°C, at which point the alloy fully melted. It was then time to turn on the stirring rod and place it 30 mm above the bottom of the reaction vessel with its stirring speed set to 600 revolutions per minute. Magnesium (1 wt%) was added to the molten matrix to increase the wettability between the matrix and the reinforcement. A 5-min stirring period followed the addition of the warmed reinforcement particles. A bottom tapping mechanism was used to transport the molten mixture into the preheated route pipe that was linked to the die of the squeeze casting system. The molten liquid was squeezed at 100 MPa for 45 s after it was put onto the prepared die at 250°C. The following three samples were made using the same method. Squeeze casting process parameters for the AMCs are shown in Table 4.

2.3. Microstructural and Elemental Composition Characterization. Using an automated mounting press, samples were trimmed to the desired size and then mounted (Buehler SimpliMet 1000). A Buehler AutoMet 250 was used to grind and polish the samples. Using 400, 600, and 1,200 grit abrasive papers, three phases of diamond suspension were used to physically polish the surface for 5 min. The samples were etched using Keller's reagent using the ASTM E3-01 standard. The KEYENCE optical microscope 1,000x VHZ100R was used for surface morphological examination. A field-emission scanning electron microscope (FESEM) (JEOL JSM-7600F) with an associated energy-dispersive spectroscopy was used to investigate the samples' microstructures, elemental composition, and fracture and wear analyses. The Panalytical Axios Max machine was used to perform XRF investigations of the matrix and reinforcement to determine their composition.

2.4. Porosity Measurement. Porosity of AMC was quantified by measuring the density of the matrix and reinforcement. Measurements were made using the Archimedes method using a sample size of 30 mm in length by 10 mm in breadth and 3 mm in thickness. A rule of the mixture was used to compute the theoretical density of composites [18]. According to Equation (1), the samples' porosity is calculated.

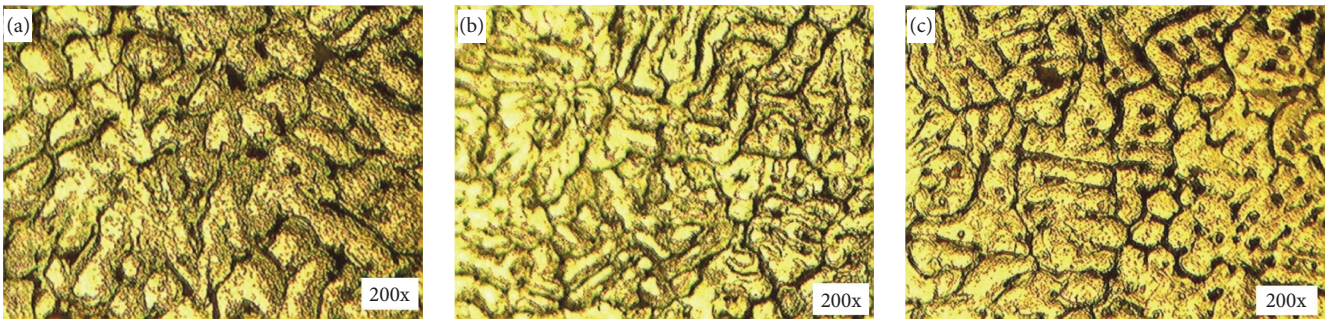

Figure 2: Optical micrograph captured at 200x magnification of AA6061 prepared with various percentages of reinforcement: (a) 0% bone powder; (b) 5% bone powder; (c) 10% bone powder.

$$P = 1 - \frac{\rho_{\text{experimental}}}{\rho_{\text{theoretical}}} \times 100. \quad (1)$$

2.5. Mechanical and Wear Characterization. The samples were subjected to tests to determine their hardness, compressive strength, tensile strength, and wear resistance. Using a Universal Hardness Tester (UH250), the indentation method was used to determine the hardness of the material under test. The standard deviation value was calculated based on five repeated observations taken at different sites. At room temperature, according to the ASTM B647 standard, the hardness is measured using Vicker's hardness testing apparatus. The 0.5 kgf weight is applied using the indenter for 15 s. The average of three readings from five indentations is chosen as the hardness value. The tensile load was applied to the specimen while it was held in place by the specimen's two ends. Using the machine's stress–strain curve, mechanical characteristics like yield and ultimate stress were determined for the samples. The tensile test's strain rate was 8.33 10-4/s. A 100 kN universal testing machine was used to perform compression tests in accordance with ASTM E9. Cylindrical samples with a diameter and height of 20 mm and a crosshead speed of 1 mm/min (a strain rate of about 8.33 10-4/s) were used for the uniaxial compression testing. Each sample was allowed to compress to 10 mm or half its height before the load-stroke data were transformed into the stress–strain curves and the results were compared. A pin-on-disk tribometer is used to assess the manufactured composites' particular wear rate while applying a 10 N load. The sample's 10 mm diameter and 30 mm height were prepared for this analysis. Stainless steel with a high carbon and high chromium content is employed as the analysis' counterpart. The sample's initial and final weights are taken into account to calculate the sample's weight loss. The formula is used to compute a certain wear rate (w).

$$w = \Delta V/(L \times d), \quad (2)$$

where ΔV is the volume loss (in mm^3), L is load (in Newton), and d is the sliding distance (in m).

3. Results and Discussion

3.1. Characterization of Microstructure and Elemental Composition in Composites. Images of three distinct composites at 200x magnification are shown in Figure 2(a)–2(c). In the images, dark parts are reinforcements, white portions are Al matrix, and black regions are porosity flaws. At grain boundaries, all-optical microstructures have a morphology that is practically nondendrites due to the squeezing pressure, resulting in finer dendrite and smaller dendrite arm spacing [36]. From the microstructure, as shown in Figure 2(b), it can be seen that the composites have reinforcement with approximately uniform dispersion and a dense structure without microlevel voids, thanks to the inclusion of pure bone. Figure 2(c) shows that although certain bone particles were clustered together, the overall distribution of the particles was homogeneous, as shown in Figure 2(b). It demonstrates that increasing the amount of bone in the aluminum matrix results in increased porosity on the samples. This is due to the longer particle feeding time, which increases the amount of time the particles are in contact with the air [37].

Figure 3 shows the 1,000x magnifications of the FESEM images of the three samples. The distribution of reinforcement in the matrix of the composite material is visible on the microscope. The matrix and reinforcement are represented by the bright and dark particles, respectively. Figure 3(b) shows that the 5% reinforcement particles were effectively disseminated in the matrix but some tiny clusters were remained in the microstructure, and also shows a uniform particle distribution in a 5% reinforcement composite. Reinforcement particles with a 5% content were distributed along the grain boundaries of the aluminum matrix. An intergranular distribution on grain boundaries improves mechanical characteristics and avoids grain boundary failure. Figure 3(c) shows the 10% reinforcement composites with distributing the reinforcements equally across the sample. However, it is produced with a higher percentage of porosities. The elements in the composite are identified using EDAX analysis, as shown in Figure 4. From the analysis, the percentage of added elements as reinforcement is found in the sample, as shown in Figures 4(b) and 4(c), with the variation in the percentages. As shown in Figure 4(a), the Ca percentage is 0% as the sample 1 is not added with reinforcement.

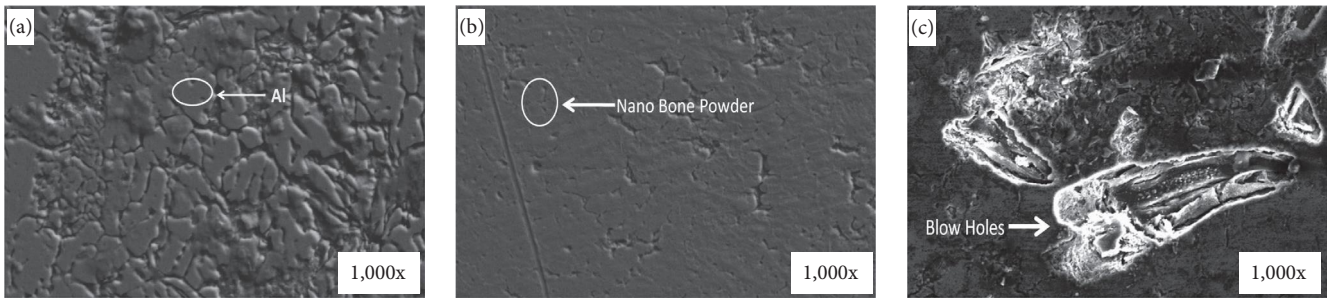

Figure 3: Field-emission scanning electron microscope images of the three composites: (a) without reinforcement; (b) 5% reinforcement; (c) 10% reinforcement.

3.2. Physical Properties of the Composite. The distribution of reinforcements, pore size, and other factors all have a role in how porous a material is. When the porosity is low, there are fewer empty areas in the composite material, which increases its strength. The computed porosity findings are in agreement with the optical microscopy results. As shown in Figure 5, the 5% composite sample shows very little porosity, while samples that have 10% reinforcement exhibit high porosity. In squeeze casting process, increased solidification pressures help in excellent die filling, decreasing casting flaws, notably porosity. Figure 5 shows that with the experimental density, the squeeze casting technique is quite effective in producing experimental densities that are very near to theoretical densities [38]. As shown in Figure 5, it is also evident that the strength of the 5% reinforcement could be highest, followed by 10% due to the increase in the porosity in the sample which has 10% reinforcement.

Table 5 shows the hardness values of all the produced composites. From the obtained results, it can be concluded that the composite (Al6061 + 5% bone powder) is the hardest one, followed by the Al6061 + 10% bone powder composite, as shown in Figure 6. The Al6061 + 0% bone powder is found to be the least hard material, followed by the Al6061 + 10% bone powder composite. The maximum hardness of 105.1 HV is achieved for the Al6061 + 5% bone powder composite because of the lower porosity and uniform distribution of reinforcements in the matrix, especially at the grain boundaries. The porosity test also confirmed less porosity in the Al6061 + 5% bone powder sample. The grain size in the composite is also relatively smaller, as it is evident in the optical microscope images. With the decrease in the grain size, the hardness of the material increases [39].

3.3. Characterization of Mechanical and Tribological Properties. As shown in Figure 7, three distinct kinds of composite materials exhibit varied strain/tension relationships. These stress–strain curves reveal the tensile qualities such as elongation to fracture (ε_f), yield strength (σ_y) and UTS (σ_{uts}). The σ_y of Al6061 without bone has been found to be 106.26 MPa. The σ_{uts} of Al6061 without bone is 127.53 MPa with ε_f of 3.88%. The tensile characteristics of Al6061 without bone were found to be superior to those of other combinations. In the case of Al6061 + 5% bone, the values for σ_y, σ_{uts}, and f are 112.4, 134.6 MPa, and 2.48%, respectively. Al6061 + 5% bone recorded the predominant tensile characteristics in comparison to other sample combinations. The data observed using the stress–strain curve are plotted and given in Figure 8. The sample which has Al6061 + 5% reinforcement shows high tensile strength and less porosity, as clearly seen in the micrograph and the computed percentage of porosity. The most ductile specimen was Al6061 + 5% bone, which was followed closely by Al6061 + 10% bone. As a result, bone reinforcement is more evenly distributed in the matrix, which may have contributed to the reduced porosity.

A compression test was conducted to establish the samples' compressive and fracture characteristics. A barrel-like deformation or bulging was detected in all samples, and this persisted until the samples formed a pancake shape. Figure 9 shows the load versus displacement curves derived from compression experiments. It is observed that Al6061 + 5% bone exhibited the highest ultimate stress of 212.2 MPa at a deformation of up to 6.9 mm from the original length. The break load of 28.3 KN has been measured and shown in Figure 10. It is notable that after the fracture initiation, the curve tends to proceed upward. The ultimate stress for Al6061 + 10% bone is roughly 165 MPa at a deformation of 6.7 mm and a break load of 21.94 KN. Al6061 + 10% bone has a poorer load-bearing capability than Al6061. In the compressive response of a 10% composite, a greater hardening rate in the Al6061 alloy matrix is observed. According to the results, 186 MPa was measured to be the ultimate stress in Al6061 without reinforcement composite at a deformation of 7.1 mm from the original length. This corresponds to the porosity seen in micrographs and the percentage of porosity.

As a function of sliding distance, the weight loss in the samples is calculated, and the weight loss is then used to compute the specific wear rate of the manufactured composites, which is shown in Figure 11. The composites containing Al6061 + 5% bone powder exhibit a low rate of wear. The waste bone particles in the composite protect the composite's surface by creating a scratching action on the material's counter surface. The resistance is proportional to the amount of hard waste bone on the surface of the composite sample. Figure 12 illustrates the wear trends of the produced composites.

The frictional force of composite material is shown in Figure 13. Tribofilm generation at the pin/disk contact gives the samples a higher coefficient of friction (COF) value. Increase in applied load lead to an increase in the contact area, which in turn leads to a rise in the force needed to break them and, hence, an increase in COF. Other studies have

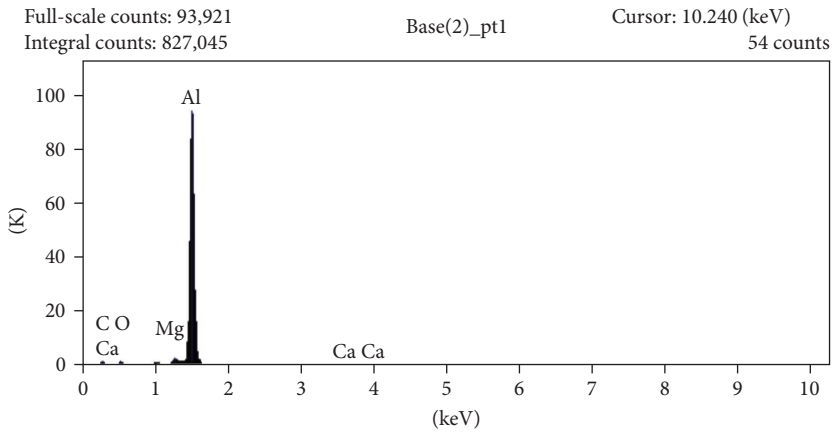

	C	O	Mg	Al	Ca
Base(2)_pt1	4.25	2.59	0.86	92.29	0.00

(a)

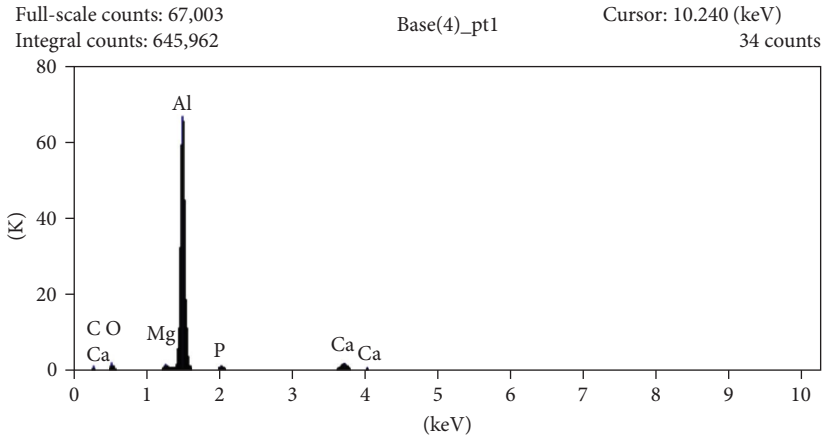

	C	O	Mg	Al	P	Ca
Base(4)_pt1	7.33	10.96	0.75	73.40	2.62	4.93

(b)

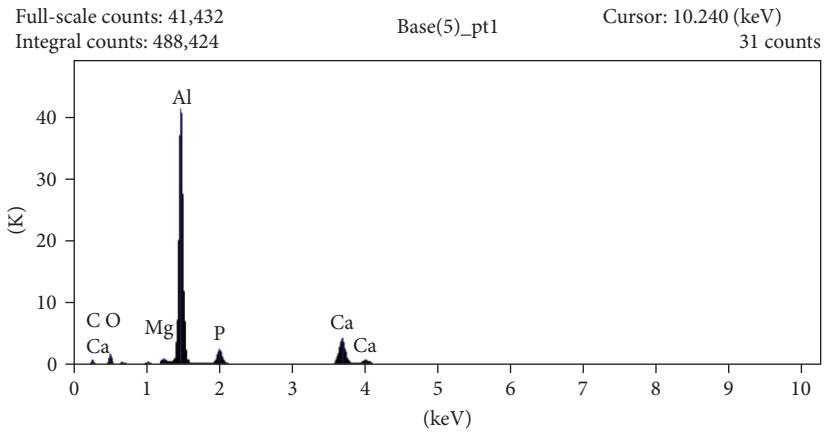

	C	O	Mg	Al	P	Ca
Base(5)_pt1	9.27	13.57	0.65	59.30	6.38	10.83

(c)

Figure 4: EDAX images of the three composites: (a) without reinforcement; (b) 5% reinforcement; (c) 10% reinforcement.

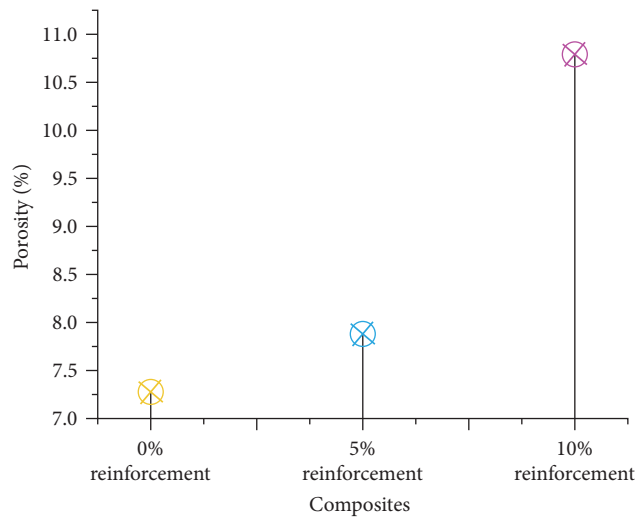

Figure 5: Percentage of porosity in the composites.

Table 5: Hardness values of produced composites.

Sample Id (%)	Hardness values in HV @ 0.5 kgf		
0	67.5	68.9	70.7
5	103.2	104.8	105.1
10	97.6	85.5	84.7

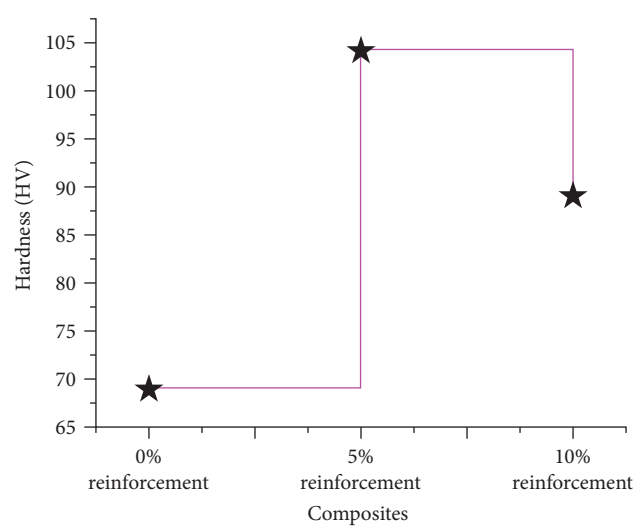

Figure 6: Hardness values of produced composites.

made similar findings [40]. Archard's equation captures the relationship between wear rate and hardness, according to which a material's hardness has an inverse correlation with its wear rate. Since the wear surface contains greater resistance and bone particles that are hard, the material has a higher rate of wear [41].

According to the findings, bone particles are far more efficient than alumina in resisting penetration and cutting into the surface. It has been shown that an abrasion wear

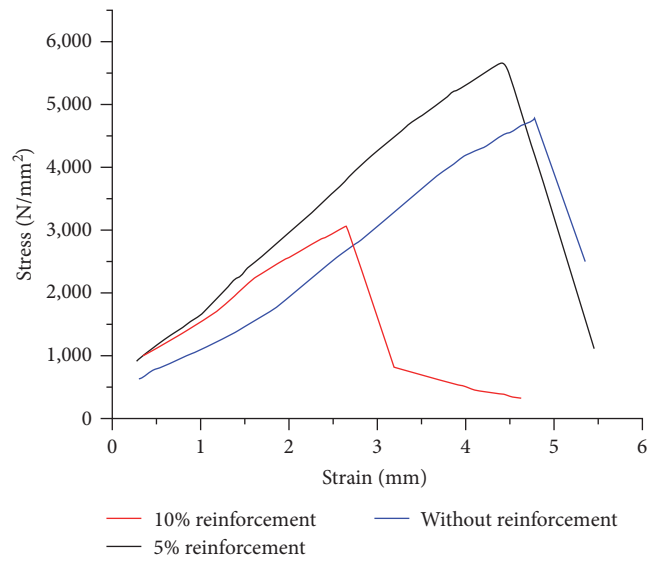

Figure 7: Tensile stress–strain curves of the composites.

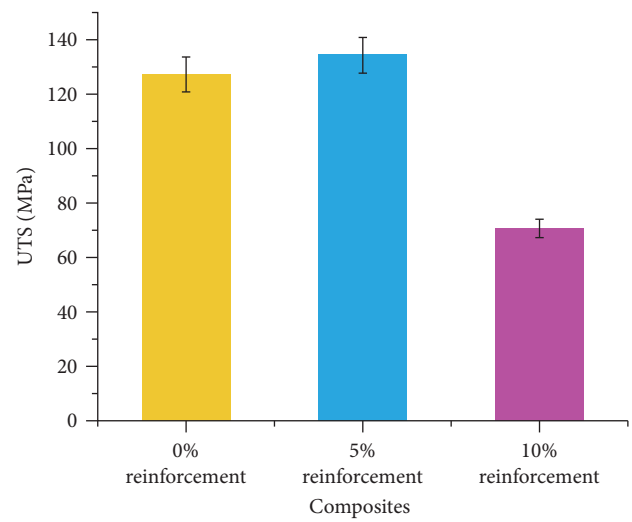

Figure 8: Ultimate stress of the various samples prepared.

mechanism exists in the composite surfaces [12, 13]. It is observed that the reinforcement of 5% bone improves the abrasion and wear resistance of the aluminum composite. The reinforcing particle slows the rate of wear by shrinking the abrasion between the contact surfaces [42]. As a result, asperities are generated from the harder and softer surfaces of the materials. This mechanism of three-body abrasion wear mechanisms increases the surface roughness and frictional force values. The SEM topography of the wear track is shown in Figure 14. The topography of the region was seen to have narrow grooves, material flow, a greater degree of wear, and localized adhesion, as well as other characteristics that were observed. There are some ploughing and cutting effects in the wear pattern of all composites [43]. Plastic deformation is the predominant mode of wear in all composites. The ploughing effect is predominant in the topography of the composites, which have 10% reinforcement.

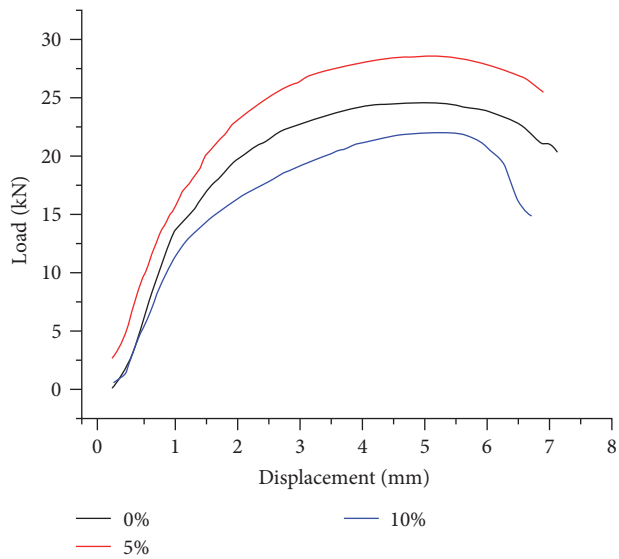

Figure 9: Load and displacement curve of the composites.

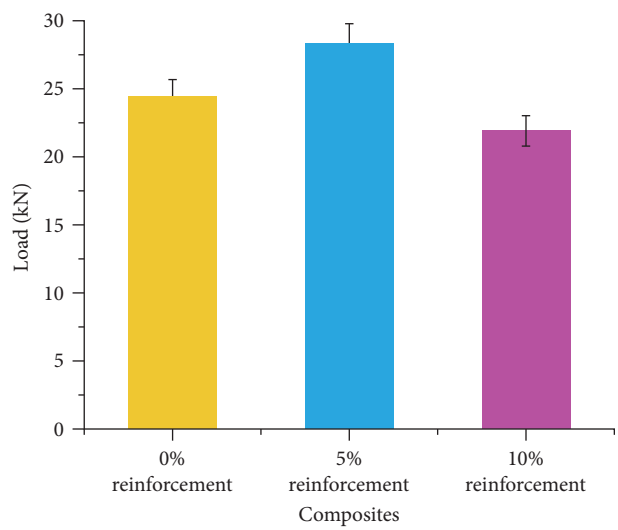

Figure 10: Maximum load obtained on the composites.

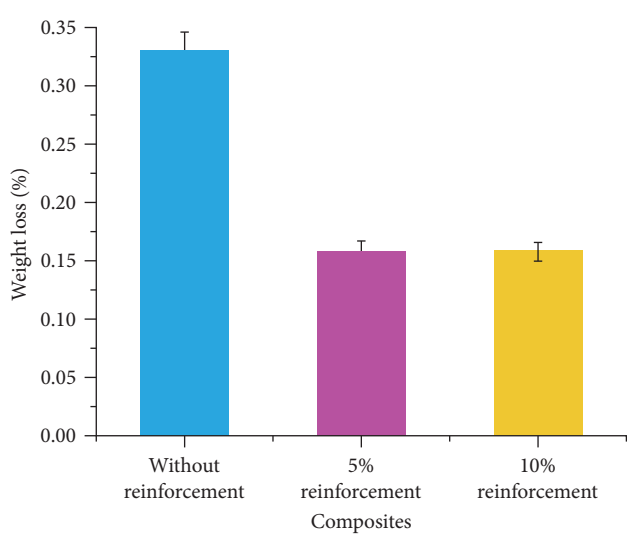

Figure 11: Weight loss in composites.

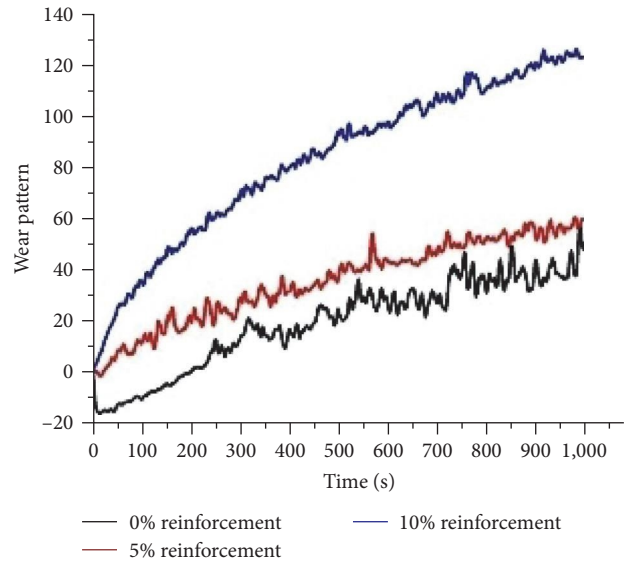

Figure 12: Wear pattern of the composites.

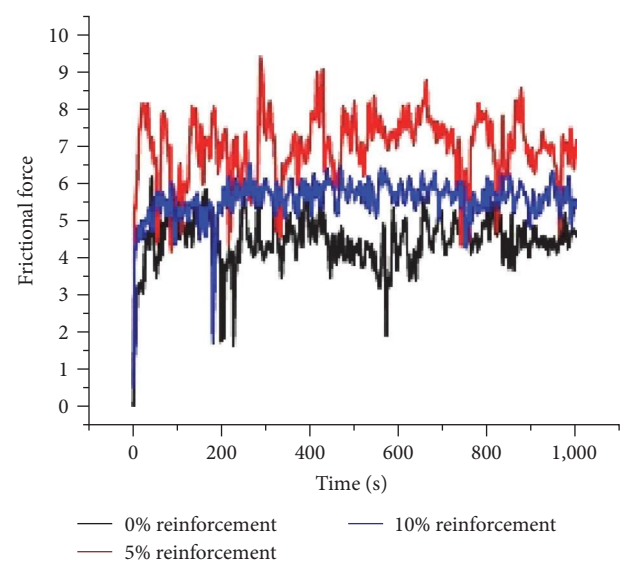

Figure 13: Frictional force versus time.

4. Conclusion

The outcomes of the data collection have led to the following conclusions:

(1) The SEM examination has shown the production of a novel star structure for the first time using bone powder, and the existence of elements added has been confirmed by elemental analysis.

(2) The composite's porosity has grown from 7.9% to 10.8%, which is a good improvement. The porosity in the composites was disclosed by optical microscopy.

(3) In comparison to the 6061 aluminum alloy, the hardness value of the composite increased by a substantial amount from 70.7 to 105.1.

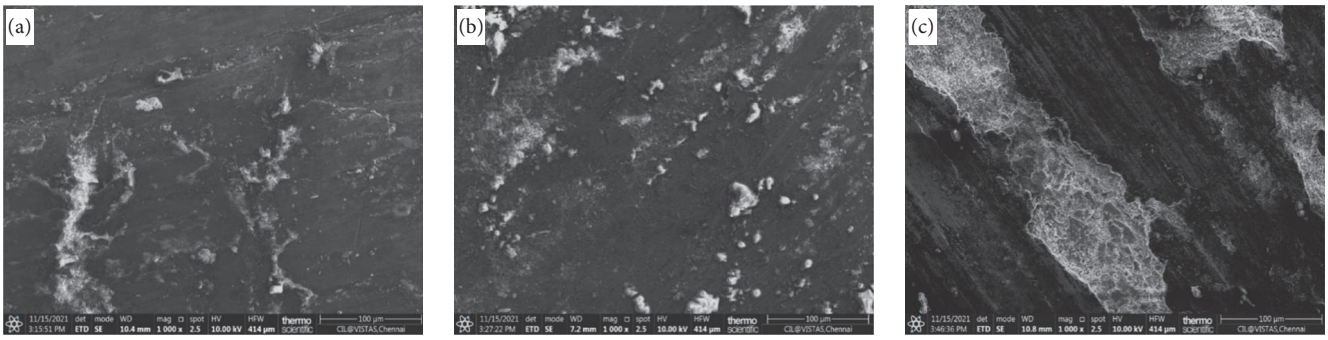

Figure 14: Wear track of the composites: (a) without reinforcement; (b) 5% reinforcement; (c) 10% reinforcement.

(4) When compared to aluminum alloy, the composite's tensile strength is greatly enhanced, reaching 127.53–134.67 MPa, and the compression strength of the composite is marginally improved, reaching 186–212 MPa.

(5) The increased hardness value of the beef bone powder reinforcement composite may be reason for improvement in wear resistance up to 54.55%.

According to the findings of this study, the development of composites has substantially improved the physical, mechanical, and tribological characteristics of aluminum composites.

Data Availability

The data used to support the findings of this study are available from the corresponding author upon request.

Conflicts of Interest

The authors declare that they have no conflicts of interest.

References

[1] H. I. Akbar, E. Surojo, and D. Ariawan, "Investigation of industrial and agro wastes for aluminum matrix composite reinforcement," *Procedia Structural Integrity*, vol. 27, pp. 30–37, 2020.

[2] I. Dinaharan, R. Nelson, S. J. Vijay, and E. T. Akinlabi, "Microstructure and wear characterization of aluminum matrix composites reinforced with industrial waste fly ash particulates synthesized by friction stir processing," *Materials Characterization*, vol. 118, pp. 149–158, 2016.

[3] P. P. Kulkarni, B. Siddeswarappa, and K. S. H. Kumar, "A survey on effect of agro waste ash as reinforcement on aluminium base metal matrix composites," *Open Journal of Composite Materials*, vol. 9, no. 3, pp. 312–326, 2019.

[4] S. Rama Rao and G. Padmanabhan, "Fabrication and mechanical properties of aluminium–boron carbide composites," *International Journal of Materials and Biomaterials Applications*, vol. 2, no. 3, pp. 15–18, 2012.

[5] Z. Haktan Karadeniz and D. Kumlutas, "A numerical study on the coefficients of thermal expansion of fiber reinforced composite materials," *Composite Structures*, vol. 78, no. 1, pp. 1–10, 2007.

[6] G. Arora and S. Sharma, "A comparative study of AA6351 mono-composites reinforced with synthetic and agro waste reinforcement," *International Journal of Precision Engineering and Manufacturing*, vol. 19, pp. 631–638, 2018.

[7] S. P. Dwivedi and A. K. Srivastava, "Utilization of chrome containing leather waste in development of aluminium based green composite material," *International Journal of Precision Engineering and Manufacturing-Green Technology*, vol. 7, pp. 781–790, 2020.

[8] H. Kumar, R. Prasad, P. Kumar, S. P. Tewari, and J. K. Singh, "Mechanical and tribological characterization of industrial wastes reinforced aluminum alloy composites fabricated via friction stir processing," *Journal of Alloys and Compounds*, vol. 831, Article ID 154832, 2020.

[9] S. P. Dwivedia, A. Saxena, S. Sharma, A. K. Srivastava, and N. K. Maurya, "Influence of SAC and eggshell addition in the physical, mechanical and thermal behaviour of Cr reinforced aluminium based composite," *International Journal of Cast Metals Research*, vol. 34, no. 1, pp. 43–55, 2021.

[10] S. Sarkar, A. Bhirangi, J. Mathew, R. Oyyaravelu, P. Kuppan, and A. S. S. Balan, "Fabrication characteristics and mechanical behavior of rice husk ash-silicon carbide reinforced Al-6061 alloy matrix hybrid composite," *Materials Today: Proceedings*, vol. 5, Part 2, no. 5, pp. 12706–12718, 2018.

[11] C. Hima Gireesh, K. G. Durga Prasad, K. Ramji, and P. V. Vinay, "Mechanical characterization of aluminium metal matrix composite reinforced with aloe vera powder," *Materials Today: Proceedings*, vol. 5, Part 1, no. 2, pp. 3289–3297, 2018.

[12] P. Samal, R. K. Mandava, and P. R. Vundavilli, "Dry sliding wear behavior of Al 6082 metal matrix composites reinforced with red mud particles," *SN Applied Sciences*, vol. 2, Article ID 313, 2020.

[13] B. Subramaniam, B. Natarajan, B. Kaliyaperumal, and S. J. S. Chelladurai, "Investigation on mechanical properties of aluminium 7075 - boron carbide - coconut shell fly ash reinforced hybrid metal matrix composites," *China Foundry*, vol. 15, pp. 449–456, 2018.

[14] A. Patil, N. R. Banapurmath, A. M. Hunashyal, and S. Hallad, "Enhancement of mechanical properties by the reinforcement of fly ash in aluminium metal matrix composites," *Materials Today: Proceedings*, vol. 24, Part 2, pp. 1654–1659, 2020.

[15] S. Jannet, R. Raja, S. Rajesh Ruban et al., "Effect of egg shell powder on the mechanical and microstructure properties of AA 2024 metal matrix composite," *Materials Today: Proceedings*, vol. 44, Part 1, pp. 135–140, 2021.

[16] R. Girimurugan, R. Pugazhenthi, T. Suresh, P. Maheskumar, and M. Vairavel, "Prediction of mechanical properties of hybrid aluminium composites," *Materials Today: Proceedings*, vol. 39, Part 1, pp. 712–716, 2021.

[17] N. Verma and S. C. Vettivel, "Characterization and experimental analysis of boron carbide and rice husk ash reinforced AA7075 aluminium alloy hybrid composite," *Journal of Alloys and Compounds*, vol. 741, pp. 981–998, 2018.

[18] S. P. Dwivedi, S. Sharma, and R. K. Mishra, "Microstructure and mechanical behavior of A356/SiC/fly-ash hybrid composites produced by electromagnetic stir casting," *Journal of the Brazilian Society of Mechanical Sciences and Engineering*, vol. 37, pp. 57–67, 2015.

[19] M. Challan, S. Jeet, D. K. Bagal, L. Mishra, A. K. Pattanaik, and A. Barua, "Fabrication and mechanical characterization of red mud based Al2025-T6 MMC using Lichtenberg optimization algorithm and Whale optimization algorithm," *Materials Today: Proceedings*, vol. 50, Part 5, pp. 1346–1353, 2022.

[20] F. O. Edoziuno, A. A. Adediran, B. U. Odoni, O. G. Utu, and A. Olayanju, "Physico-chemical and morphological evaluation of palm kernel shell particulate reinforced aluminium matrix composites," *Materials Today: Proceedings*, vol. 38, Part 2, pp. 652–657, 2021.

[21] M. Imran and A. R. Anwar Khan, "Characterization of Al-7075 metal matrix composites: a review," *Journal of Materials Research and Technology*, vol. 8, no. 3, pp. 3347–3356, 2019.

[22] P. Omoniyi, A. Adekunle, S. Ibitoye, O. Olorunpomi, and O. Abolusoro, "Mechanical and microstructural evaluation of aluminium matrix composite reinforced with wood particles," *Journal of King Saud University - Engineering Sciences*, vol. 34, no. 6, pp. 445–450, 2022.

[23] S. D. Saravanan and M. Senthil Kumar, "Effect of mechanical properties on rice husk ash reinforced aluminum alloy (AlSi10Mg) matrix composites," *Procedia Engineering*, vol. 64, pp. 1505–1513, 2013.

[24] A. Islam, S. P. Dwivedi, R. Yadav, and V. K. Dwivedi, "Development of aluminium based composite by utilizing industrial waste and agro-waste material as reinforcement particles," *Journal of the Institution of Engineers (India): Series D*, vol. 102, pp. 317–330, 2021.

[25] S. Arunkumar and A. Senthil Kumar, "Studies on egg shell and SiC reinforced hybrid metal matrix composite for tribological applications," *Silicon*, vol. 14, pp. 1959–1967, 2022.

[26] P. P. Ikubanni, M. Oki, A. A. Adeleke et al., "Tribological and physical properties of hybrid reinforced aluminium matrix composites," *Materials Today: Proceedings*, vol. 46, Part 12, pp. 5909–5913, 2021.

[27] J. Verma and H. Kumar, "Rice husk ash as reinforcement with aluminium metal matrix composite: a review of technique, parameter and outcome," in *Advances in Manufacturing and Industrial Engineering*, R. M. Singari, K. Mathiyazhagan, and H. Kumar, Eds., pp. 953–962, Springer, Singapore, 2021.

[28] A. K. Yadav, K. M. Pandey, and A. Dey, "Aluminium metal matrix composite with rice husk as reinforcement: a review," *Materials Today: Proceedings*, vol. 5, Part 3, no. 9, pp. 20130–20137, 2018.

[29] R. Yadav, V. K. Dwivedi, A. Islam, and S. P. Dwivedi, "Analysis of mechanical properties of Al-based metal matrix composite reinforced with ES and RHA," *World Journal of Engineering*, vol. 18, no. 6, pp. 930–937, 2021.

[30] M. Dhanashekar and V. S. Senthil Kumar, "Squeeze casting of aluminium metal matrix composites—an overview," *Procedia Engineering*, vol. 97, pp. 412–420, 2014.

[31] R. Arunachalam, S. Piya, P. K. Krishnan et al., "Optimization of stir–squeeze casting parameters for production of metal matrix composites using a hybrid analytical hierarchy process—Taguchi-Grey approach," *Engineering Optimization*, vol. 52, no. 7, pp. 1166–1183, 2020.

[32] S. Niyomwas, "Preparation of aluminum reinforced with TiB_2-Al_2O_3-Fe_xAl_y composites derived from natural ilmenite," *International Journal of Self-Propagating High-Temperature Synthesis*, vol. 19, pp. 150–156, 2010.

[33] J. V. Christy, R. Arunachalam, A.-H. I. Mourad, P. K. Krishnan, S. Piya, and M. Al-Maharbi, "Processing, properties, and microstructure of recycled aluminum alloy composites produced through an optimized stir and squeeze casting processes," *Journal of Manufacturing Processes*, vol. 59, pp. 287–301, 2020.

[34] T. Arunkumar, T. Selvakumaran, R. Subbiah, K. Ramachandran, and S. Manickam, "Development of high-performance aluminium 6061/SiC nanocomposites by ultrasonic aided rheo-squeeze casting method," *Ultrasonics Sonochemistry*, vol. 76, Article ID 105631, 2021.

[35] P. Chandrasekar and D. Nagaraju, "Improvement of bonding strength at the interfaces in scrap Al alloy composites using electroless Ni-P coated SiC," *Silicon*, vol. 14, pp. 2941–2952, 2022.

[36] M. Singh, R. S. Rana, R. Purohit, and K. Sahu, "Development and analysis of Al-matrix nano composites fabricated by ultrasonic assisted squeeze casting process," *Materials Today: Proceedings*, vol. 2, no. 4-5, pp. 3697–3703, 2015.

[37] M. Kok, "Production and mechanical properties of Al_2O_3 particle-reinforced 2024 aluminium alloy composites," *Journal of Materials Processing Technology*, vol. 161, no. 3, pp. 381–387, 2005.

[38] C. Kannan and R. Ramanujam, "Comparative study on the mechanical and microstructural characterisation of AA 7075 nano and hybrid nanocomposites produced by stir and squeeze casting," *Journal of Advanced Research*, vol. 8, no. 4, pp. 309–319, 2017.

[39] G. Liu, N. Zhao, C. Shi et al., "*In-situ* synthesis of graphene decorated with nickel nanoparticles for fabricating reinforced 6061Al matrix composites," *Materials Science and Engineering: A*, vol. 699, pp. 185–193, 2017.

[40] S. Kundu, S. K. Das, and P. Sahoo, "Tribological behaviour of electroless Ni-P deposits under elevated temperature," *Silicon*, vol. 10, pp. 329–342, 2018.

[41] P. Chandrasekar and D. Nagaraju, "Improvement of bonding strength at the interfaces in scrap Al alloy composites using electroless Ni-P coated SiC," *Silicon*, vol. 14, pp. 2941–2952, 2022.

[42] C. Fenghong, C. Chang, W. Zhenyu, T. Muthuramalingam, and G. Anbuchezhiyan, "Effects of silicon carbide and tungsten carbide in aluminium metal matrix composites," *Silicon*, vol. 11, pp. 2625–2632, 2019.

[43] R. Muraliraja and R. Elansezhian, "Effect of zwitterionic surfactant on tribological behaviour of electroless plating," *Surface Engineering*, vol. 30, no. 10, pp. 752–757, 2014.

Hindawi
Journal of Nanomaterials
Volume 2023, Article ID 6752950, 7 pages
https://doi.org/10.1155/2023/6752950

Research Article

A Study of Lithium Ferrite and Vanadium-Doped Lithium Ferrite Nanoparticles Based on the Structural, Optical, and Magnetic Properties

S. Malathi,[1] **B. Sridhar**,[2] **and Shiferaw Garoma Wayessa**[3]

[1]*Department of Physics, Muthurangam Government Arts College (Autonomous), Vellore, India*
[2]*Department of Electronics and Communication Engineering, MLR Institute of Technology, Hyderabad, India*
[3]*College of Engineering and Technology, Wollega University, Nekemte, Ethiopia*

Correspondence should be addressed to Shiferaw Garoma Wayessa; shiferawg@wollegauniversity.edu.et

Received 20 September 2022; Revised 20 October 2022; Accepted 24 November 2022; Published 14 February 2023

Academic Editor: B. Deepanraj

Lithium ferrite and vanadium-doped lithium ferrite have been extensively studied in recent research because of their potential applications in thermochromic materials, optoelectronic devices, and as a cathode material for rechargeable lithium batteries. In the present investigation, lithium ferrite and lithium vanadium ferrite are synthesized by sol–gel process. According to the Scherrer formula, the average particle size of lithium ferrite is 22 nm and that of vanadium-doped lithium ferrite is 29 nm. The lattice parameters and dislocation density are calculated from the X-ray diffraction results. According to the Fourier transform infrared spectroscopy analysis, ferrites were formed that exhibit strong absorption bands. According to the energy-dispersive X-ray analysis spectrum, the predicted elements are present in the sample. With the use of a vibrating sample magnetometer (VSM), the materials' magnetic behavior is investigated.

1. Introduction

Recently, considerable attention on synthesis of metal oxide nanoparticles, because of their unique material properties and potential applications, is extending in many fields such as catalysts, electronics devices, solid oxide fuel cells, magnetic storage, and optical materials [1]. Nanotechnology indicates the design, production, and applicability of source materials at various scales of atomic and molecular to establish various nanosized materials. The classification of nanomaterials is based on one, two, and three dimensions [2, 3]. Thin film or manufactured surfaces are under the one-dimension system, and it has been used in electronics industries and engineering. Manufacturing of thin films (sizes 1–100 nm) is now commonplace in the field of solar cells.

Carbon nanotubes (CNTs), which have a diameter of 1 nm and a length of 100 nm, are two-dimensional nanoparticles composed of a layer of graphite coiled up into a cylinder. Three-dimensional nanoparticles are called fullerenes. This is a hollow ball that resembles a soccer ball made of connected carbon pentagons and hexagons. The class of materials known as fullerenes has distinctive physical characteristics. Extreme pressure can be applied to them, and when the pressure is relieved, they can return to their original shape. Fullerenes are empty structures that can be filled with various substances and have potential uses in medicine since they have dimensions that are close to those of several biologically active compounds [4].

The dendrimer is a brand-new class of controlled-structure polymers with nanometric dimensions. Given that they typically range in size from 10 to 100 nm and have a variety of functional groups on their surface, dendrimers are effective drug-delivery vehicles [5]. The small objects called quantum dots have a very small amount of free electrons in them. QDs are colloidal semiconductor nanocrystals with diameters between 2 and 10 nm. Colloidal synthesis or electrochemistry can be used to create QDs from a variety of semiconductor materials. Cadmium selenide (CdSe), cadmium telluride (CdTe), indium phosphide (InP), and indium arsenide are the most widely used QDs (InAs). Nanomedicines, materials, electronics, scientific tools,

environment and energy, and chemical and cosmetics are just a few of the fields where nanotechnology is being used [6]. Numerous technical applications have made extensive use of ferrite material, including the magnetically controlled delivery of anticancer medications, color imaging, gas-sensitive materials, and catalytic materials [7–13]. An extensive survey on various synthesis and characterization techniques of ferrite nanoparticles has been carried out in this paper.

The structural, magnetic, and electrical characteristics of the $Li_{0.5}Fe_{2.5}O_4$ small particles are produced in sol–gel [14]. The sol–gel method was used to view and measure grains that were around 12 nm in size. When the magnetic characteristics of lithium ferrite nanoparticles with grain sizes ranging from 12 to 32 nm were explored, magnetic measurements revealed that the magnetic behavior of the $Li_{0.5}Fe_{2.5}O_4$ small particles deviates from what is expected. The sample displayed a maximum saturation magnetization of 75 emu/g; the change in coercivity is related to the change in nature from multidomain to single-domain.

The structure and its magnetic properties of nanocrystalline $LiFeO_2$ is synthesized by sol–gel method. To confirm the several phases involved in $LiFeO_2$ production, Rietveld analysis was done. According to quantitative Rietveld refinement, the sample comprises 39.9 wt% of cubic $LiFeO_2$, 58.5 wt% of monoclinic $LiFeO_2$, and 1.7 wt% of tetragonal $LiFeO_2$. The particle size distribution is uneven, with an average particle size of 100 nm, as shown by the morphology [15]. At normal temperatures, $LiFeO_2$ powder exhibited spontaneous magnetism. It exhibits ferromagnetic behavior and has a coercivity of 189 Oe and a maximum magnetization value of 0.2 emu/g. SEM examinations revealed nanocrystallinity with 100 nm sized particle size.

Al_2O_3 is used in the evaluation of the nanoparticle production process. Thin films and aluminum oxide nanoparticles are produced using the sol–gel technique. Hitachi S-3400N SEM is used to investigate surface morphologies. Following centrifugation, a particle size between 60 and 90 nm is observed [16]. It has been discovered that the grain size is significantly influenced by the precursors used, the synthesis circumstances, and the aging temperature. The energy bandgap was measured at 4.13 eV. The refractive index was measured between 1.55 and 1.79. The observed value of the extinction coefficient was 0.103. The real and imaginary parts of the dielectric constant were determined to be 2.83 and 0.5, respectively.

By using the sol–gel spin coating process, the pure and aluminum-doped ZnO ($Zn_{1-x}Al_xO$) $x = 0$ to 5 wt% thin films. The aluminum concentrations in ZnO thin films is affected its structural, surface, optical, and photo-conducting characteristics. It is found that doping with aluminum reduces the average grain size. According to AFM images [17], 1.5% of doped films displayed better smoothness than other materials. According to the photoconductivity measurements, the photocurrent for the Al-doped ZnO is greater than the dark current. After attaining its maximum value for ZnO : Al-1.5%, the photocurrent decreases when the concentration of Al is raised.

A new approach to create V_2O_5 nanostructures using the polyvinyl alcohol-based sol–gel process was proposed [18]. In order to create a homogeneous polymeric gel, the precursors NH_4VO_3 and polyvinyl alcohol are dissolved in a binary (ethanol/water) solvent to create a sol solution. SEM, TEM, XRD, and TGA-DTA are used to evaluate the prepared samples. This technique makes it possible to create consistent V_2O_5 nanoflakes with an average thickness of 37 nm. By using cyclic voltammetry, the electrochemical behaviors of V_2O_5 samples are also studied in a 0.1 M $LiClO_4$ electrolyte solution made in a 1 : 1 (V/V) solvent mixture of ethylene carbonate and dimethyl carbonate.

Reactive grinding was used to create nanoparticles of vanadium-doped rutile TiO_2 [19]. As a result of the vanadium doping, size of the particle of vanadium-modified rutile TiO_2 obtained around 22 nm, but under the same conditions, better solar light absorption was found in the 5% vanadium-doped rutile, with an estimated bandgap energy value of 2.7 eV. Lithium nanoferrites with the general formula $Li_{0.5}Al_xFe_{2.5-x}O_4$ were proposed to be synthesized by Aravind and Ravinder [20] using the citrate gel technique at low temperature (1,800°C). The powders produced were sintered for 4 hr at 500°C. The sintered powders' crystal structure was examined using X-ray diffraction (XRD). The average particle size of the synthesized powders ranged from 13 to 27 nm. However, due to vanadium's several oxidation states, materials doped with it showed complex properties [21–24]. Vanadium ions in V-doped $CoFe_2O_4$ nanoferrite are found at the octahedral site for samples doped with less than or equal to 10% V, but some vanadium ions shifted to the tetrahedral position in samples doped with >10% V [25].

According to published research, the type of surfactant and reductant, pH level of the suspension, stirring rate, concentration of precursors, reaction rate, and temperature all affect the structural, electrical, and optical properties of synthesized materials. In this paper, surfactant-free growth and large area uniform of prepared products are discussed.

2. Experimental Method

This work deals with the synthesis of lithium ferrite and vanadium-doped lithium ferrite. Brief descriptions of the various tools in characterizing these samples are also presented.

2.1. Synthesis of Lithium Ferrite through Sol–Gel Route. A well-known colloidal chemistry method called sol–gel gives the ability to create a variety of materials with brand-new, predetermined features through a straightforward process at a reasonably low cost. The chemicals used to synthesize $LiFe_2O_3$ were $Fe(NO_3)_3{\cdot}9H_2O$, $Li(NO_3)$, and citric acid. The acitic acid solution is prepared by sprinkling acitic acid powder in deionized water under continuous stirring to avoid clumping of the material in water. Lithium nitrate and ferric nitrate were dissolved in deionized water in a 1 : 2 ratio to create the sols. After 3 hr of nonstop stirring, citric acid solution was applied to the sols. The resultant mixture was then heated while being constantly stirred to produce the gel. The water molecules were then removed from the gel by keeping it in the muffle furnace for 2 days. The color of the precursor was altered before it was calcinized.

2.2. Synthesis of Lithium Vanadium Ferrite through Sol–Gel Route. The chemicals used to synthesize $LiV_2Fe_2O_3$ were $Fe(NO_3)_3{\cdot}9H_2O$, $Li(NO_3)$, V_2O_5, and citric acid. All of the compounds were of the analytical grade and were utilized directly. In order to prevent the material from clumping in the water, PVA solution was made by slowly sprinkling PVA powder in deionized water while stirring continuously. Lithium nitrate and ferric nitrate were dissolved in deionized water in a 1 : 2 ratio to create the sols. Then, the solution was added to V_2O_5. Three hours of nonstop stirring was followed by the addition of citric acid solution to the sols. The resultant mixture was then heated while being constantly stirred to produce the gel. The water molecules were then removed from the gel by keeping it in the muffle furnace for 2 days. The color of the forerunner was altered. After that, it was ground into a fine powder using a mortar and pestle for an hour. The same technique was used to prepare the sample for vanadium-doped lithium ferrite.

3. Characterization Techniques

Numerous characterization techniques are required to estimate the various properties of the prepared sample. The findings reveal details of the various structural and optical characteristics of the sample. The basis for the occurrence of the diffraction pattern is the unit cell and lattice; it is dispersed in a normal 3D pattern in space. These lattice structures create a collection of several parallel planes, each with distance spacing and varying orientations. Bragg's law is derived from incident monochromatic X-ray reflection from successive crystal lattice planes when the wavelength gap between the planes is n.

$$n\lambda = 2d \sin\theta, \tag{1}$$

where d is the interatomic distance in angstroms, n is an integer (1, 2, 3, etc.), λ is the wavelength in angstroms (1.54 for copper), and θ is the diffraction angle in degrees. The sample-specific pattern is produced by plotting the angular positions and radiation peak intensities that result from the radiation being diffracted. The two areas where XRD has been utilized most frequently are the fingerprint characterization of crystalline materials and the assessment of their structure.

The scanning electron microscope (SEM) uses high-energy electrons to create a variety of signals at the surface of solid specimens. In addition to the sample's exterior morphology (texture), chemical composition, and orientation and crystalline structure of the components that make up the sample, these signals generated by the electrons also provide information about the sample. The sample's surface is often selected for data collection, and a two-dimensional image is made to illustrate the spatial differences in these features. Regions with widths ranging from ~1 cm to 5 μm can be scanned in a scanning mode using conventional SEM techniques.

The UV–vis NIR spectroscopy was used to examine the optical characteristics of the produced nanorods. The apparatus is built to allow for a comparison of the two beams' intensities as it moves over the necessary wavelength range. The substance absorbs light of a specific wavelength, and the sample beams (IS) intensity will be lower than the reference beams. By calculating the radiation's absorption by a sample at various wavelengths and registering the results, the wavelength vs. the absorption (A) of light at each wavelength is shown.

4. Results and Discussion

The synthesized nanoparticles of lithium ferrite and vanadium-doped lithium ferrite are subjected to following characterizations and the properties also incorporated. The impact of V_2 doping on the prepared samples' microstructure was investigated. Due to the formation of cation vacancies and the substitution of Fe with V, the lattice parameter (a) often decreased nonlinearly with the vanadium concentration (x).

4.1. X-Ray Diffraction Analysis. X-ray diffraction analysis to determine the nature of the crystal, its structure, size, strain, and dislocation density is evaluated for the lithium ferrite and vanadium-doped lithium ferrite are done with the help of "D8 Advanced, BRUKER X-Ray Diffractometer" of wavelength $\lambda = 1.5406$ Å. The average particle size of the crystal is evaluated from XRD by using the Debye–Scherrer formula [26, 27] that is given in Equation (2).

$$D = \frac{K\lambda}{\beta \cos\theta}, \tag{2}$$

where D indicates the average size of the crystalline, K represents the Scherrer constant (0.89), λ is the beam wavelength used, β is the full-width half maximum (FWHM) of diffraction, and θ is the Bragg's angle. With the help of the XRD data, we can calculate the strain and dislocation values. Williamson–Hall plot helps to calculate the strain value. The calculated values are tabulated in the Table 1.

The SEM micrographs evident that the $LiFe_2O_4$ and V_2-doped $LiFe_2O_4$ were in the form of nanoparticles which were speculated that the agglomeration of particles. Figures 1 and 2 represent the SEM images of $LiFe_2O_4$ and V_2-doped $LiFe_2O_4$.

4.2. UV–Visible Spectral Study. The UV–vis spectrometer of "JASCO, V-670" was used to evaluate the absorption level of the optical parameters in the nanoparticles. The regions from 200 to 2,500 nm were studied at room temperature. Figure 3 shows the wavelength absorbance graph of $LiFe_2O_4$ and $LiV_2Fe_2O_4$.

The values noted with respect to the cutoff wavelengths for lithium ferrite and vanadium-doped lithium ferrite are 413 and 415 nm, respectively. This demonstrates the viewable region's cutoff. These samples can be utilized to manufacture the semiconductors, optical devices, solar energy conversion devices, etc. The indirect bandgap values for lithium ferrite and vanadium-doped lithium ferrite are 1.01 and 1.01 eV, respectively.

Table 1: Structural properties.

Sr. No.	Properties	$LiFe_2O_4$	$LiV_2Fe_2O_4$
1.	Crystal structure	Monoclinic	Monoclinic
2.	Lattice parameters	$a = 7.748054$ Å $b = 4.797752$ Å $c = 7.516238$ Å $\alpha = \gamma \neq \beta$	$a = 10.22835$ Å $b = 4.92298$ Å $c = 8.717566$ Å $\alpha = \gamma \neq \beta$
3.	Size of the crystal	22 nm	29 nm
4.	Strain	0.6822	0.25934
5.	Dislocation density	$2.066 \times 10^{-15}\ m^{-2}$	$1.1891 \times 10^{-15}\ m^{-2}$

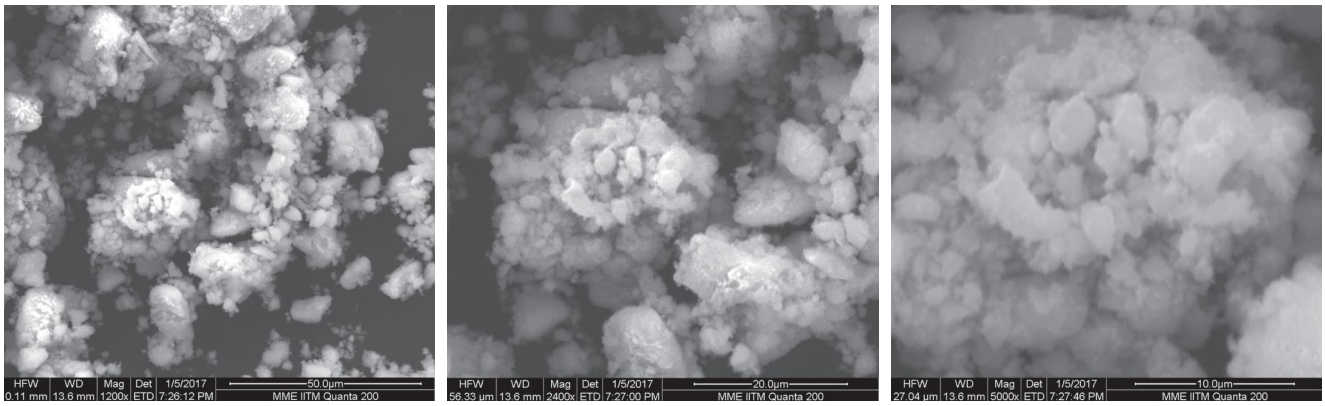

Figure 1: SEM images of $LiFe_2O_4$ nanopowder.

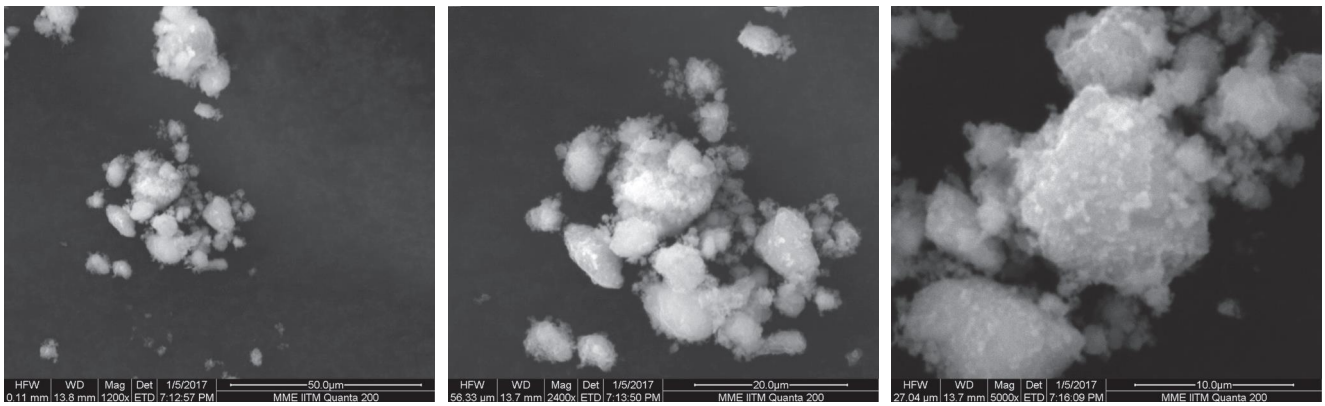

Figure 2: SEM images of V_2-doped $LiFe_2O_4$ nanopowder.

4.3. FTIR Analysis. Fourier transform infrared spectroscopy (FTIR) spectrum analysis is performed for lithium ferrite and vanadium-doped lithium ferrite nanoparticles in the range of 400–4,000 cm^{-1}. The FTIR analysis shows that the change in temperature changes the nature of the bond of the samples. The peak range of both the samples ranges from 3,200 to 3,600 shows the O—H bond. Figures 4 and 5 describe the FTIR spectrum for $LiFe_2O_4$ and $LiV_2Fe_2O_4$.

The range of 1,620–1,680 corresponds to the bond present as C═C. The value range of 1,350–1,480 shows —C—H bond. 866.04 cm^{-1} for lithium ferrite corresponds ═C—H bond. The values of vanadium-doped lithium ferrite for the ranges 675–1,000 correspond to ═C—H bond.

4.4. Vibrating Sample Microscope. The vibrating sample micrograph at room temperature for both the samples is

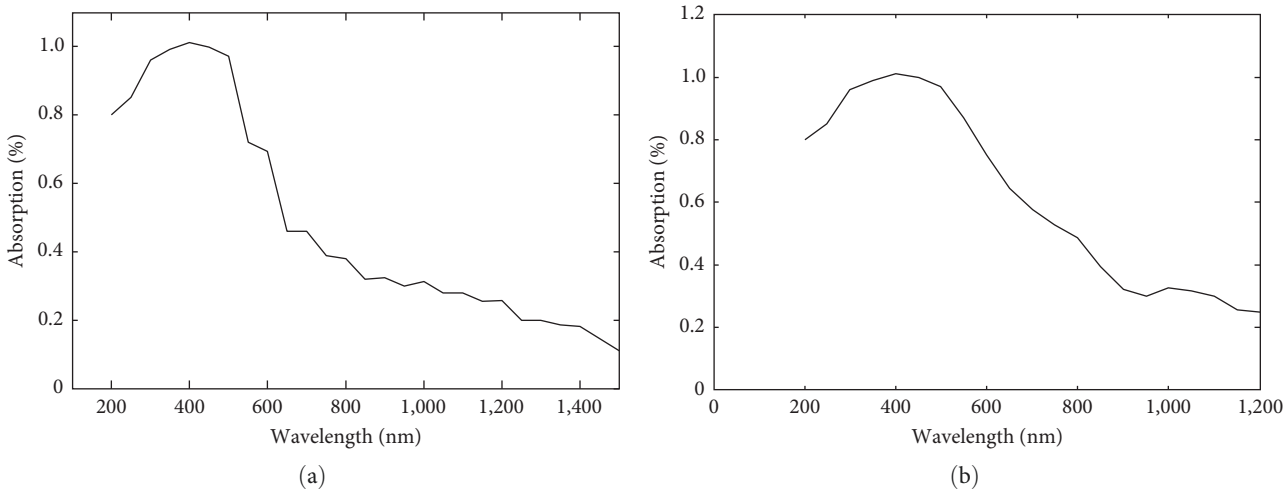

Figure 3: (a) Wavelength–absorbance graph of $LiFe_2O_4$; (b) wavelength–absorbance graph of $LiV_2Fe_2O_4$.

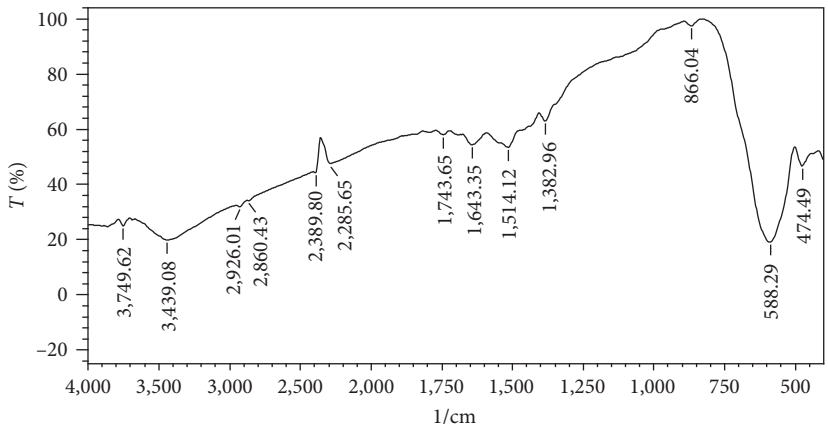

Figure 4: FTIR spectrum of $LiFe_2O_4$.

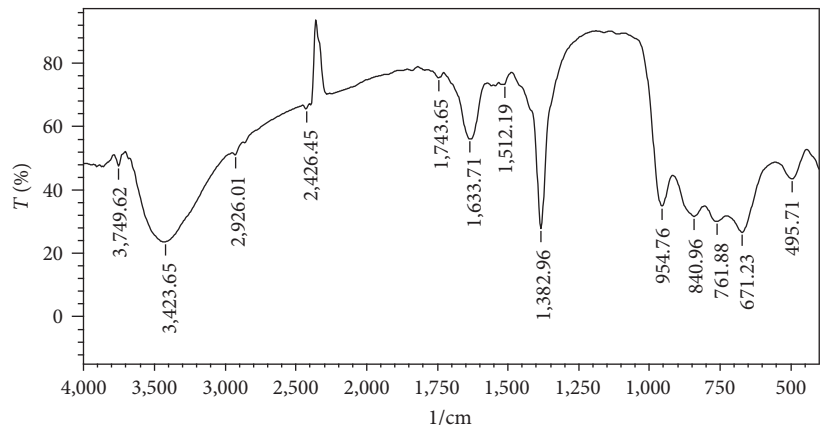

Figure 5: FTIR spectrum of $LiV_2Fe_2O_4$.

shown. The corresponding magnetic properties are listed in Table 2.

Both samples' natures demonstrate excellent soft magnetic properties and extraordinary paramagnetic behavior [28–30]. Figures 6 and 7 represent the VSM graph for $LiFe_2O_4$ and $LiV_2Fe_2O_4$. Due to their low coercive values, these ferrites can be employed to create magnetic storage devices and other objects without causing any flux loss or

Table 2: Magnetic properties.

Sr. No.	Properties	$LiFe_2O_4$	$LiV_2Fe_2O_4$
1.	Coercivity	16.099 G	2.4305 G
2.	Magnetization	0.58657 emu	18.795^{-3} emu
3.	Retentivity	5.3467 emu	4.8057^{-6} emu

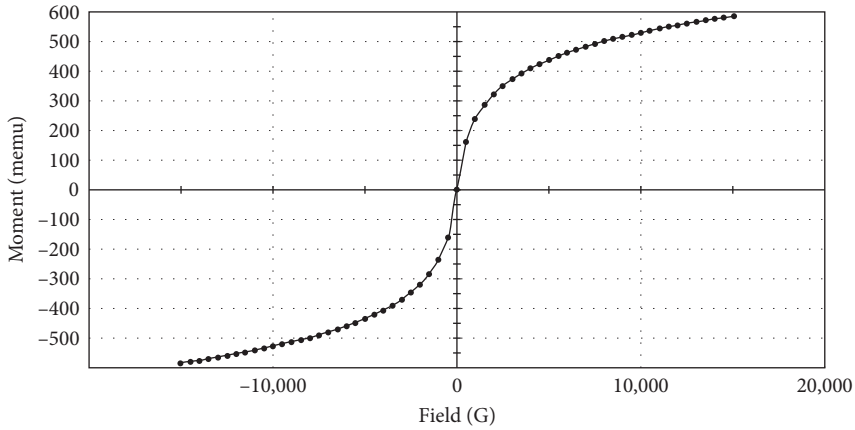

Figure 6: VSM graph of $LiFe_2O_4$.

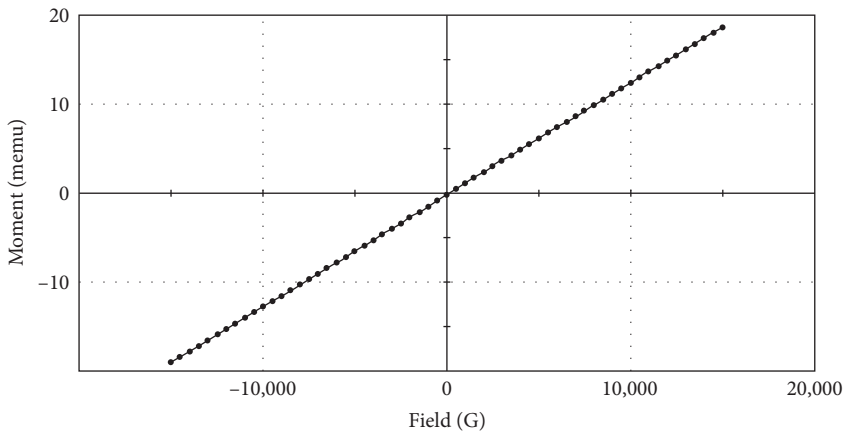

Figure 7: VSM graph of $LiV_2Fe_2O_4$.

difficulty magnetizing the particles. Ferrites, notably magnetoplumbite and spinel ferrite, can be used as pigments, microwave devices, recording media, and other things.

Due to its high-saturation magnetization and high coercivity, strontium ferrite has drawn more scientific study recently compared to magnetoplumbite ferrites and spinel ferrite.

5. Conclusion

The nanoparticles of lithium ferrite and vanadium-doped lithium ferrite are prepared with the help of sol–gel synthesis. The XRD data show the samples are monoclinic in structure. The strain values and dislocation density are also calculated. The particle size is in the range of 22–29 nm. The UV–vis values show the cutoff value present in the visible region. So, we can use these materials in making optoelectronic devices like photovoltaic cells, photoconduction cells, photodiodes, lasers, CD players, etc. The VSM results reveal that the samples have a superparamagnetic nature, so it is possible that these materials may be used to make pigments, humidity sensors, microwave devices, recording media, and other things. Due to their high-saturation magnetization, high coercivity, and high uniaxial magnetic anisotropy, strontium ferrites have recently drawn more scientific attention than magnetoplumbite ferrite and spinel ferrite.

Data Availability

The datasets generated and/or analyzed during the current study are available from the corresponding author on reasonable request.

Conflicts of Interest

The authors declare that they have no conflicts of interest.

References

[1] W. I. Hagens, A. G. Oomen, W. H. de Jong, F. R. Cassee, and A. J. A. M. Sips, "What do we (need to) know about the kinetic properties of nanoparticles in the body?" *Regulatory Toxicology and Pharmacology*, vol. 49, no. 3, pp. 217–229, 2007.

[2] A. Hett, *Nanotechnology: Small Matters, Many Unknown*, Swiss Reinsurance Company, 2004.

[3] M. Köhler and W. Fritzsche, *Nanotechnology: An Introduction to Nanostructuring Techniques*, Wiley, Weinheim, 2004.

[4] D. A. Tomalia, "Dendrimer as quantized building blocks for nanoscale synthetic organic chemistry," *Aldrichmica Acta*, vol. 37, no. 2, pp. 39–57, 2004.

[5] E. Wiener, M. W. Brechbiel, H. Brothers et al., "Dendrimer-based metal chelates: a new class of magnetic resonance imaging contrast agents," *Magnetic Resonance in Medicine*, vol. 31, no. 1, pp. 1–8, 1994.

[6] Y. Li, Y. Cheng, and T. Xu, "Design, synthesis and potent pharmaceutical applications of glycodendrimers: a mini review," *Current Drug Discovery Technologies*, vol. 4, no. 4, pp. 246–254, 2007.

[7] N. M. Deraz and S. Shaban, "Optimization of catalytic, surface and magnetic properties of nanocrystalline manganese ferrite," *Journal of Analytical and Applied Pyrolysis*, vol. 86, no. 1, pp. 173–179, 2009.

[8] N. M. Deraz, M. K. El-Aiash, and S. A. Ali, "Novel preparation and physicochemical characterization of a nanocrystalline cobalt ferrite system," *Adsorption Science & Technology*, vol. 27, no. 8, pp. 797–810, 2009.

[9] N. M. Deraz, A. Alarifi, and S. A. Shaban, "Removal of sulfur from commercial kerosene using nanocrystalline $NiFe_2O_4$ based sorbents," *Journal of Saudi Chemical Society*, vol. 14, no. 4, pp. 357–362, 2010.

[10] Y. Köseoğlu, A. Baykal, F. Gözüak, and H. Kavas, "Structural and magnetic properties of $Co_xZn_{1-x}Fe_2O_4$ nanocrystals synthesized by microwave method," *Polyhedron*, vol. 28, no. 14, pp. 2887–2892, 2009.

[11] S.-W. Cao, Y.-J. Zhu, G.-F. Cheng, and Y.-H. Huang, "$ZnFe_2O_4$ nanoparticles: microwave-hydrothermal ionic liquid synthesis and photocatalytic property over phenol," *Journal of Hazardous Materials*, vol. 171, no. 1–3, pp. 431–435, 2009.

[12] Z. H. Zhou, J. M. Xue, J. Wang, H. S. O. Chan, T. Yu, and Z. X. Shen, "$NiFe_2O_4$ nanoparticles formed *in situ* in silica matrix by mechanical activation," *Journal of Applied Physics*, vol. 91, no. 9, Article ID 6015, 2002.

[13] Y. Köseoğlu, F. Yıldız, G. Slazar-Alvarez, M. Toprak, M. Muhammed, and B. Aktaş, "Synthesis, characterization and ESR measurements of CoNiO nanoparticles," *Physica Status Solidi (b)*, vol. 42, no. 8, pp. 1712–1718, 2005.

[14] M. George, S. S. Nair, A. M. John, P. A. Joy, and M. R. Anantharaman, "Structural, magnetic and electrical properties of the sol–gel prepared $Li_{0.5}Fe_{2.5}O_4$ fine particles," *Journal of Physics D: Applied Physics*, vol. 39, no. 5, Article ID 900, 2006.

[15] K. Vijaya Kumar, A. Sangeetha, A. T. Raghavender, Z. Skoko, and G. Nanda Kumar, "Rietveld refinement of nanocrystalline $LiFeO_2$ synthesized by sol–gel method and its structural and magnetic properties," *Journal of Crystallization Process and Technology*, vol. 2, no. 4, pp. 152–155, 2012.

[16] F. Majid, S. Riaz, M. I. Akram, S. Atiq, and S. Naseem, "Preparation and characterization of electrodeposited aluminum oxide thin films," in *International Conference on Advanced Computer Science and Electronics Information (ICACSEI 2013)*, pp. 523–526, Atlantis Press, August 2013.

[17] T. Ganesh, S. Rajesh, and F. P. Xavier, "Sol–gel preparation, deposition and characterization of nanostructured aluminium doped zinc oxide," *Journal of Nano Research*, vol. 24, pp. 96–106, 2013.

[18] H. Karami and A. Mohammadi, "Poly vinyl alcohol-based sol–gel synthesis of V_2O_5 nanoflakes as positive electrodes of Li-ion batteries," *International Journal of Electrochemical Science*, vol. 10, pp. 7392–7408, 2015.

[19] T. M. Nguyet Tran, T. H. Yen Quach, Q. C. Tran et al., "Synthesis of vanadium-modified rutile TiO_2 nanoparticle by reactive grinding method and its photocatalytic activity under solar light at room temperature," *Advances in Natural Sciences: Nanoscience and Nanotechnology*, vol. 4, no. 3, Article ID 035010, 2013.

[20] G. Aravind and D. Ravinder, "Preparation and structural properties of aluminium substituted lithium nano ferrites by citrate-gel auto combustion method," *International Journal of Engineering Research and Applications*, vol. 3, no. 6, pp. 1414–1421, 2013.

[21] Z. K. Heiba, M. B. Mohamed, A. M. Wahba, and M. I. Almalowi, "Effect of vanadium doping on structural and magnetic properties of defective nano-nickel ferrite," *Applied Physics A*, vol. 124, Article ID 290, 2018.

[22] M. A. Almessiere, Y. Slimani, H. Güngüneş, H. S. El Sayed, and A. Baykal, "AC susceptibility and hyperfine interactions of vanadium substituted barium nanohexaferrites," *Ceramics International*, vol. 44, no. 15, pp. 17749–17758, 2018.

[23] A. D. Korkmaz, S. Güner, Y. Slimani et al., "Microstructural, optical, and magnetic properties of vanadium-substituted nickel spinel nanoferrites," *Journal of Superconductivity and Novel Magnetism*, vol. 32, pp. 1057–1065, 2019.

[24] M. A. Almessiere, Y. Slimani, and A. Baykal, "Structural, morphological and magnetic properties of hard/soft $SrFe_{12-x}V_xO_{19}/(Ni_{0.5}Mn_{0.5}Fe_2O_4)y$ nanocomposites: effect of vanadium substitution," *Journal of Alloys and Compounds*, vol. 767, pp. 966–975, 2018.

[25] Z. K. Heiba, M. B. Mohamed, and S. I. Ahmed, "Cation distribution correlated with magnetic properties of cobalt ferrite nanoparticles defective by vanadium doping," *Journal of Magnetism and Magnetic Materials*, vol. 441, pp. 409–416, 2017.

[26] V. Chithambaram, T. S. Franklin Rajesh, G. Palani, E. Ilango, B. Deepanraj, and S. Santhanakrishnan, "Growth and investigation of novel nonlinear optical single crystal of urea potassium dichromate by solution growth technique for photonic application," *Journal of Optics*, vol. 49, pp. 181–186, 2020.

[27] B. D. Cullity, *Elements of X-ray Diffraction*, Addison-Wesley Publishing Co. Inc., 1976.

[28] I. Zālīte, G. Heidemane, M. Kodols, J. Grabis, and M. Maiorov, "The synthesis, characterization and sintering of nickel and cobalt ferrite nanopowders," *Materials Science*, vol. 18, no. 1, 2012.

[29] S. Shanmugan, N. Saravanan, V. Chithambaram, B. Deepanraj, and G. Palani, "Investigation on single crystal by tartaric acid–barium chloride: growth and characterization of novel NLO materials," *Bulletin of Materials Science*, vol. 43, Article ID 202, 2020.

[30] S. Rehman, A. Mumtaz, and S. K. Hasanain, "Size effects on the magnetic and optical properties of CuO nanoparticles," *Journal of Nanoparticle Research*, vol. 13, pp. 2497–2507, 2011.

Hindawi
Journal of Nanomaterials
Volume 2023, Article ID 1194158, 8 pages
https://doi.org/10.1155/2023/1194158

Research Article

Nanoclay-Incorporated Polycaprolactone Matrix via Electrospinning Techniques-Enriched Spectroscopic Responses

D. Devina Merin,[1] **R. Anith Jose**,[2] **T. S. Arulananth**,[3] **Antony Allwyn Sundarraj**,[4] **T. M. Inbamalar**,[5] **and Meseret Getnet Meharie**[6]

[1]*Department of Biotechnology, Udaya School of Engineering, Vellamodi, Tamil Nadu, India*
[2]*Department of Electronics and Communication Engineering, Ponjesly College of Engineering, Nagercoil, Tamil Nadu, India*
[3]*Department of Electronics and Communication Engineering, MLR Institute of Technology, Hyderabad 500043, Telangana, India*
[4]*Department of Food Technology, Sri Shakthi Institute of Engineering and Technology, Coimbatore, Tamil Nadu, India*
[5]*Department of Electronics and Communication Engineering, RMK College of Engineering and Technology, Puduvoyal, Tamil Nadu, India*
[6]*School of Civil Engineering and Architecture, Adama Science and Technology University, Adama, Ethiopia*

Correspondence should be addressed to D. Devina Merin; devinamerin@gmail.com and Meseret Getnet Meharie; meseret.getnet@astu.edu.et

Received 22 August 2022; Revised 30 September 2022; Accepted 10 October 2022; Published 13 February 2023

Academic Editor: B. Deepanraj

Nanotechnology is one of the most common areas for current research and development in almost all technological fields. A significant factor is the synergistic benefit of nanoscale dimensions over larger scale alteration. Polymer nanoscience is the analysis and application of nanotechnology to polymer nanoparticle matrices, with nanoparticles described as those with at least one dimension of less than 100 nm. The use of polymer nanotechnology and nanocomposites in practical applications is a rapidly developing area. For making polymeric nanofibers from polymer melts and solutions, a spinning technique is used known as electrospinning. Electrospinning is an easy way to produce ultrafine fibers, which is nanosize. For its wide range of variety of spinning polymeric fibers, it is recommended, as well as producing fibers in nanosize accurately. The aim of this project is to use electrospinning to make nanoclay integrated polycaprolactone membranes. The effects of the nanoclay on morphology, thermal, and sorption behaviors of the electrospun membrane were further studied. The scope of this project work is that the electrospun nanocomposites are best studied for biomedical applications. Because of their influence over porosity, pore size, and fiber diameter, they make excellent scaffold materials.

1. Introduction

Every living being is made up of matter. Matter is made up of an infinite number of atoms once more. A simple molecular structure is formed when atoms cluster together to form molecules, which then interact with many other molecules [1]. Acting with matter on a scale of one-billionth of a meter, or 1 nm, is called nanotechnology. Nanotechnology modifies the matter at molecular and atomic levels. For modern research and wide range of scientific disciplines, nanotechnology is most used [2].

In various fields, like biochemistry, physical chemistry, surface microscopy, etc., all have been transformed by nanotechnology. Nanotubes, nanofibers, nanorods, nanowires, nanospheres, nanocrystals, and nanocomposites are only a few examples of nanoscale materials or structures that have piqued interest for a variety of high-tech applications [3–6]. A significant factor is the synergistic benefit of nanoscale dimensions over larger scale alteration [2]. Two or more materials with different chemical and physical properties and separate at a macroscopic scale are made to form composite materials. These materials are combined to form composite materials which have several properties. It has a fantastic and diverse variety of uses. Composites possess plenty of engineering advantages over that of the synthetic polymers and copolymers.

Polymer nanoscience is the research and application of nanoscience to polymer nanoparticle matrices, with nanoparticles having at least one dimension of less than 100 nm. In polymer nanotechnology, polymer nanocomposites play an important role. To increase the polymer's performance properties, nanoscopic inorganic materials, usually 10–100 Å in at least one dimension, are distributed in an organic polymer matrix. Nanocomposites are normally transparent due to the nanometer length scale, which minimizes light scattering. Polymer nanocomposites are a modern form of polymer that can be used instead of conventionally filled polymers. Filler dispersion nanocomposites have stronger properties than pure polymers because of their nanometer sizes [7].

For fabricating polymeric ultrafine fiber matrices, several methods are available, these include electrospinning temperature-induced separation, etc. Electrospinning, on the other hand, has proven to be one of the most effective method for making polymeric nanofibers from polymer melts and solutions. The diameter range of 3–10 nm is applicable to manufacture polymeric fibers with an increasing solution concentration using the same electrospinning experimental setup [8].

A simple electrospinning system typically includes three major components: a power supply with high voltage, a spinneret, and a disc for grounded collecting, which can be a metal plate or screen. In an external electric field, a suspended conical droplet is created where the electric field and surface tension are maintained at an equilibrium state. The droplet is created by spinneret when the charged polymer solution is fed into it [9].

Many variables influence fiber thickness and morphology. These include solution properties such as temperature and humidity as well as solution properties (density, elasticity, and surface tension) and the spinneret and collecting plate distance [4].

To produce control-sized fiber diameter distribution with error-free nanofibers, certain parameters should be followed [10]. These parameters are mostly based on the properties of the polymer solution, which include molecular weight and flow rate and atmospheric properties of the polymer solution can influence the electrospinning [11]. Through electrospinning processing technology in the biomedical field, the applications which include the morphology and diameter of the nanofibers can be regulated and modified through electrospun. Not only these but also 3D patterns and porosity can be modified. In a number of biomedical applications like scaffold preparation, coating materials, and several applications in the field of tissue engineering, electrospun fibers are used. Mostly multifunctional membranes are used in composite reinforcement and filtering the submicron particles media in the separation industry [12].

The ability to produce several varieties of drugs through electrospun fibers whether the drug may be solid or amorphous solution. Through these fibers, the resulting drug will be more efficient in drug release, high permeability (it has interconnecting porous structure), and can be the delivery vehicles that are some of the appropriate features of electrospun fibers in drug delivery. After surgery adhesion for preventing membranes, it can be used [13]. Therapeutic agents are delivered by electrospun fibers. Therapeutic agents using carriers made of polymeric nanofibers matrices have been delivered locally at particular application sites. Through this, the solubility of the drug and drug diffusion increases because the surface area is wide and porous structure is high in nanofiber-based systems [11]. Clay, a natural material with low loadings, may be used as a replacement for polymer reinforcers [7].

As a prosthetic or implant unit, electrospun nanofiber plays a crucial role. Polymeric nanofiber matrices have been successfully used as implants, either alone or in conjunction with other materials and structures [11]. Polyurethane, polyesters, polystyrene, and polypropylene are just a few of the latest polymer clay nanocomposites that have been created. Various approaches and clay loadings have been used to synthesize biocompatible polymers (polycaprolactone) [7].

Tissue engineering requires scaffolds that will not inhibit but rather enable stem cell to grow. The polymer chosen for this work is polycaprolactone (PCL) as it supports stem cell growth with its nontoxic and biodegradable nature [14]. It is a synthetic polymer that is used in food processing, tissue engineering, wound dressings, and drug delivery [15]. PCL is made by opening the ring of caprolactone in the presence of metal alkoxides. It is a good electrical conductor that is essential for electrospinning. The nanometer scale diameter products are produced by electrospinning [16–19]. The scaffolds can be made for any tissue required [20–26]. Flexibility, medium melting point (65°C), and low T_g (−61°C) are several of PCL's unique characteristics [27–32]. PCL is a biodegradable material and can be used in treatment process too [33–37]. The nanoclay was incorporated into PCL and was electrospunned. The changes in the morphology, thermal, and sorption behaviors of the membrane were further studied and briefly described in this paper.

2. Methodology

2.1. Feed Solution. Nanoclay (Cloisite 10A, Cloisite 10B) was taken at four different concentrations (1, 3, 5, and 9 wt%) in dichloromethane. The benefits of nanoclays include their widespread availability, ease of processing, high performance, and low cost. The different polymer solutions used in electrospinning are hexafluoroisopropanol, trifluoroethanol, dichloromethane, and chloroform. It was then kept overnight stirring for exfoliation to result. The term exfoliation refers, here, to remove the unwanted material of nanoclay and preparing the material with polymer solution for the process of electrospinning. To the well- stirred solution, PCL 10 wt% (PCL with a molecular weight of 80,000) was dissolved and again kept for overnight stirring. The resulting solution is taken as the feed solution for electrospinning. Electrospinning has been used to create nanofibers from various materials. Organic polymers in solution or in melt form are the most commonly used materials. Small

molecules can also be electrospun directly into nanofibers if they self-assemble and generate enough chain entanglement. The viscosities of polymer solution have an impact on the electrospinning process. The electrospinning parameters include the applied electric field, needle-to-collector distance, flow rate, and needle diameter. The solvent, polymer concentration, viscosity, and solution conductivity are all solution parameters. The environmental parameters include relative humidity, temperature, and relative humidity.

2.2. Synthesis of Electrospun PCL Clay Nanocomposite Membrane. Electrospun PCL clay nanocomposite membranes were fabricated by the electrospinning process. The conditions used for electrospining of PCL clay nanocomposite membranes were maintained at 12 cm in the tip of the collector and voltage of 15 kDa (kilo Dalton) was applied at solution feed rate of 1 ml/hr. The main distinction between electrospinning and electrospun is the viscosity and viscoelasticity of the liquid involved, which affects the rate of reaction. The main advantages of the electrospinning technique are the ability to produce very thin fibers with large surface areas, the ease of functionalization for various purposes, superior mechanical properties, and ease of process.

2.3. Morphological Analysis of Nanocomposite Membrane. By scanning electron microscope, here, we analyze both the average fiber diameter of electrospun fibers and fiber morphology. To observe the surface morphology, JEOL JSM-6390 SEM instrument was used. To probe the crystal lattice structure of the nanocomposite, it is subjected to X-ray powder diffraction, which is a rapid analytical technique. For the sample, an X-ray is used, followed by X-ray diffractometry analyses of the clay dispersion. By Bruker AXS automated XRD model and D8 equipment X-ray, diffractograms were recorded with CuKα1 radiation ($\lambda = 1.54$ nm), 2θ range from 1° to 15°.

2.4. Thermal Analysis of Nanocomposite Membrane. During temperature changes at different rates, the weight loss of the sample may occur. To determine the balance, thermogravimetric analysis is used. On the balance, the pan is placed, and the sample is loaded on the pan. Now the sample is closed by a furnace and at a given rate and given environment, the temperature is changed.

Due to the varying in different rates of temperature, the constituents in the sample may burn off, so the weight percent of the constituents is recorded. Shimadzu TGA instrument was used to measure the TGA measurements. The heating rate of the sample ranges from 25 to 700°C at 10°C/min under nitrogen. At 410°C, the residue of the clay is removed before that the measurement of clay content is recorded. The concentration of the nanofiber synthesis is efficient and there is reduction of fiber diameter and bead formation.

2.5. Sorption Behavioral Study of Nanocomposite Membrane by Determination of Water Uptake and Water Retention. The electrospun membranes were kept in water for 24 hr to measure the water uptake. After 24 hr, the immersed samples were taken out from the water and weighed [38]. The water uptake of the membranes was calculated as before and after weight difference of the water uptake, by the following formula [39]:

$$\text{Water uptake} = \left[\frac{W_s - W_d}{W_d}\right] \times 100, \quad (1)$$

where W_s is the weight after water uptake and W_d is the weight of the dry membrane.

Water retention was calculated as defined in Equation (2):

$$\text{Water retention} = \left[\frac{(W_s - W_d)}{(W_e - W_d)}\right] \times 100, \quad (2)$$

where W_e is the equilibrium water content.

3. Results and Discussion

3.1. Morphological Analysis. Morphological analysis is the simple process of investigative possible resolutions to unquantifiable, complex problems connecting many factors.

3.1.1. Effect of Polymer Concentration. SEM is used to obtain information about the morphology of the nanofibers. The polymer concentration effect in the electrospun PCL nanofibers synthesis using dichloromethane as solvent is shown in Figure 1. As shown in Figure 1, with increase in polymer concentration, the nanofiber synthesis is efficient and there is reduction of fiber diameter and bead formation.

3.1.2. Effect of Nanoclay Content. Nanoclay was used as the nanofiller to enhance the properties of PCL. Nanoclays are layered with mineral silicate nanoparticles. Nanoclays are classified into several groups based on their chemical composition and nanoparticle morphology, including montmorillonite, bentonite, kaolinite, hectorite, and halloysite. Nanoclay, also known as layered silicates, is a widely used and researched nanoagent employed in the preparation of nanocomposites for packaging materials. Nanoclays are natural nanomaterials found in the clay content of soil, the most significant of which are montmorillonite and allophane. Montmorillonite is a hydrous crystalline phyllosilicate. In Figure 2, the influence of nanoclay on the morphology of the electrospun PCL membranes is shown. The fiber diameter is large and there is bead formation in the absence of nanoclay. As the concentration of nanoclay increases, the fiber diameter and the bead formation are greatly reduced.

3.1.3. Effect of Applied Voltage. The morphology of PCL nanofibers on the effect of applied voltage on is shown in Figure 3. At reduced voltage, 8 kV, there is reduced amount of fiber formation and an increased amount of bead formation. The nanofiber synthesis increases, and the bead formation decreases at high applied voltage, 15 kV. PCL solution of 10 wt%, nanoclay of 5 wt% with solvent dichloromethane, and solution feed rate of 0.5 ml/hr are the electrospinning parameters carried out.

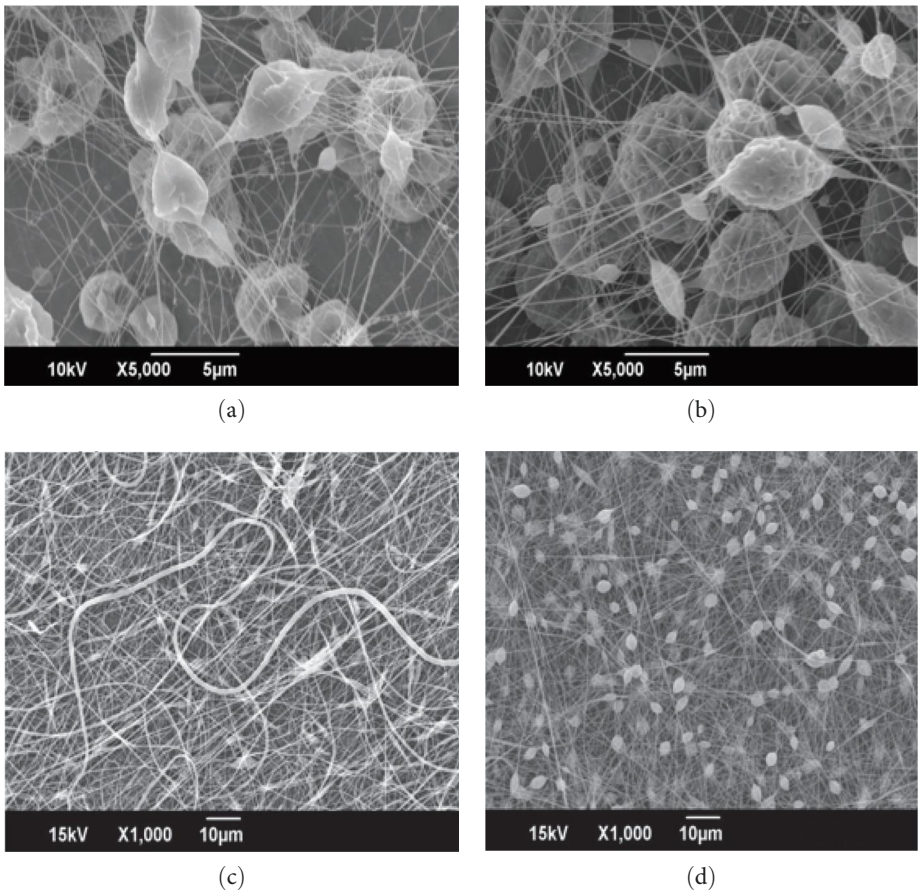

Figure 1: SEM micrographs of electrospun PCL nanofibers using DCM as solvent. (a) At 5,000x magnification of the first area of nanofiber; (b) at 5,000x magnification of the second area of nanofiber; (c) at 1,000x magnification of the first area of nanofiber; (d) at 1,000x magnification of the second area of nanofiber.

3.2. X-Ray Diffraction by Morphological Review. The fundamental principle of X-ray diffraction (XRD) is the constructive interference of monochromatic X-rays with a crystalline sample. A cathode ray tube generates these X-rays, which are then filtered to produce monochromatic radiation, collimated to concentrate, and directed toward the sample. XRD is a nondestructive technique for determining a material's crystallographic structure, chemical composition, and physical properties. It works by using the constructive interference of monochromatic X-rays with a crystalline sample. X-ray powder diffraction (XRD) is a rapid analytical technique that can provide information on unit cell dimensions and is primarily used for phase identification of crystalline materials. The analyzed material is finely ground and homogenized before determining the average bulk composition. As compared to pure clay, XRD offers quantitative details about the exfoliation and d-spacing of the clay layers in the polymer matrix. Cloisite 10A and Cloisite 15A XRD patterns are shown in Figure 4. It is evident from the figure that when nanoclay is incorporated into PCL, the d-spacing increases as result of intercalcation, as there is a shift in the 2θ value to lower angles.

3.3. Thermal Analysis by Thermal Gravimetric Analyzer. Thermal gravimetric analyzer weighs a sample as it is heated or cooled in a furnace. A TGA is made up of a sample pan supported by a precision balance. During the experiment that pan is heated or cooled in a furnace. Throughout the experiment, the mass of the sample is measured. Nanocomposite and polymer thermal stability is evaluated by using TGA. A TGA analysis is carried out by gradually raising the temperature of a sample in a furnace while its weight is measured on an analytical balance that remains outside of the furnace. If a thermal event results in the loss of a volatile component, mass loss is observed in TGA. The PCL clay nanocomposite membranes are more stable than pure polymers, their improvement in thermal stability because polymer matrices are incorporated of clay fillers. Figure 5 represents the TGA curves for pure PCL and electrospun PCL clay nanocomposite membrane. By heating them at 10°C/min, the pure polymer and the composite polymer of the TGA are obtained. The PCL clay thermal stability and virgin PCL are relatively similar. As compared to pure PCL, both intercalated and exfoliated nanocomposites have greater thermal stability. The onset temperature of degradation is the maximum for the nanocomposite with 1% clay. A plot of weight percentage vs. temperature obtained by measuring the mass of a sample while it is being heated gives the thermal gravimetric analysis graph. Instrumental factors include the furnace

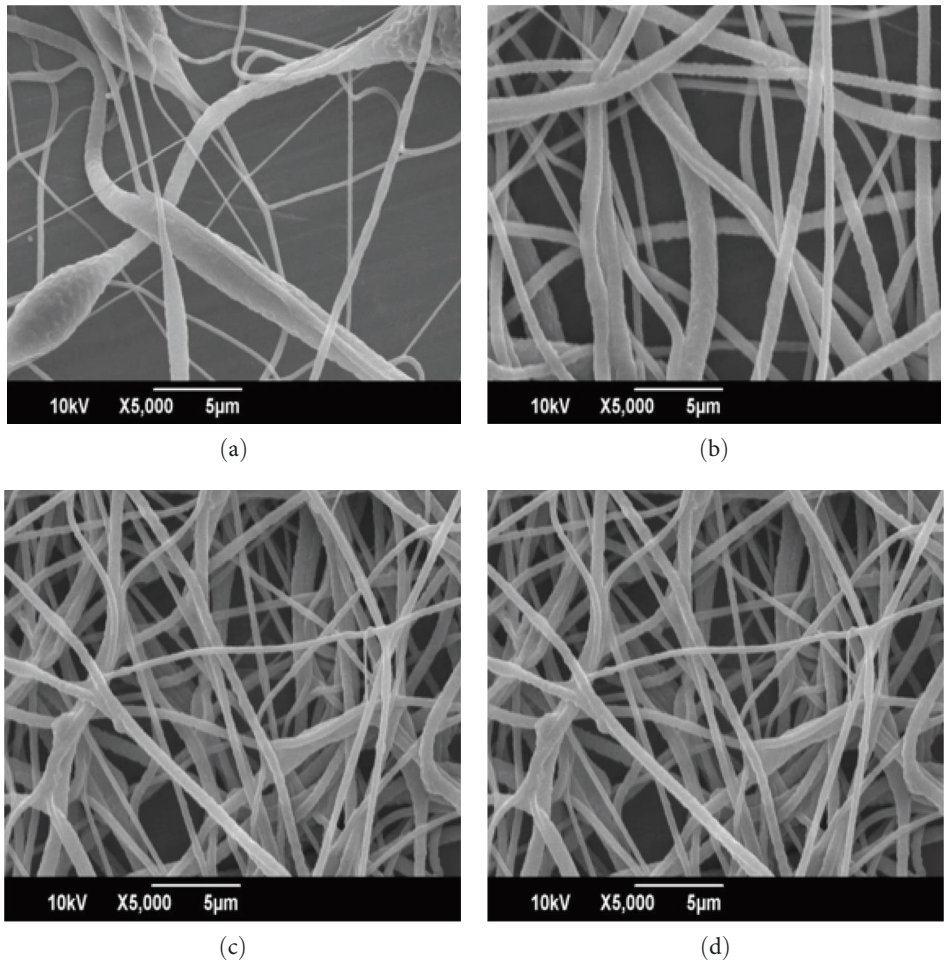

(a) (b) (c) (d)

Figure 2: SEM images showing electrospun fibers of PCL containing (a) 0 wt% clay, (b) 1 wt% clay, (c) 3 wt% clay, and (d) 9 wt% clay.

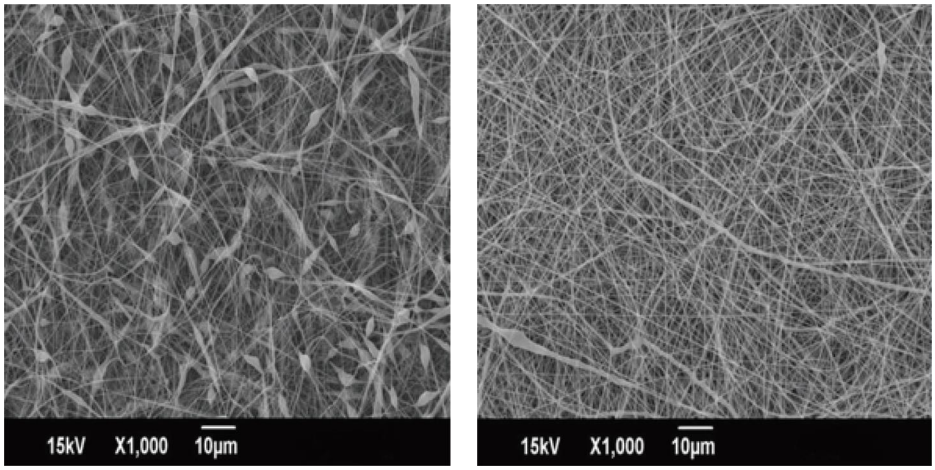

(a) (b)

Figure 3: Electrospun PCL clay nanocomposite membrane at varying voltage (SEM image): (a) 8 kV; (b) 15 kV.

environment, gas flow rate; heating rate, geometry, and pan material affect the thermal gravimetric analysis. Typically, a heating rate of 3.5°C per minute is considered adequate for TGA reliability and reproducibility. TGA instruments can measure a variety of parameters, such as moisture loss, decarboxylation, pyrolysis, solvent loss, plasticizer loss, oxidation, and decomposition for biomass or other substances.

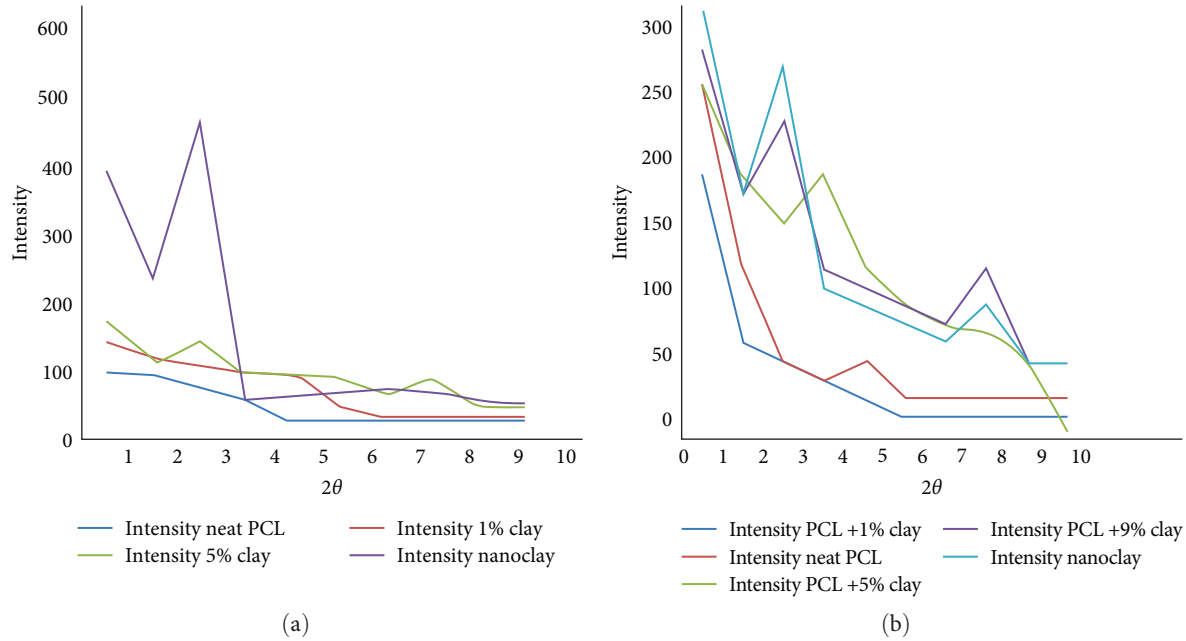

Figure 4: Images of XRD patterns: (a) Cloisite 10A; (b) Cloisite 5A.

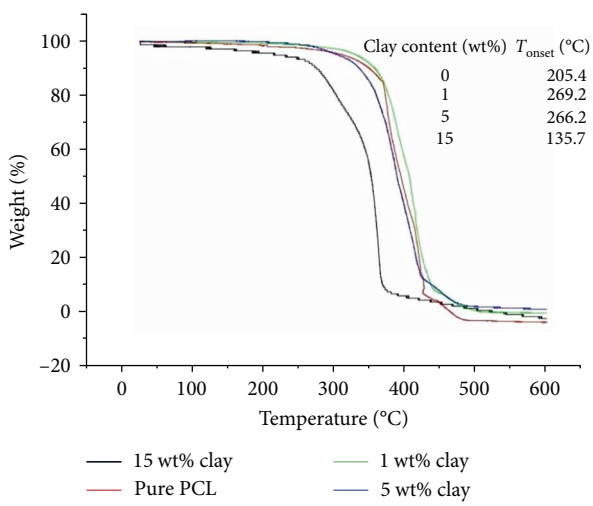

Figure 5: TGA curves for pure PCL and electrospun PCL clay nanocomposite membrane.

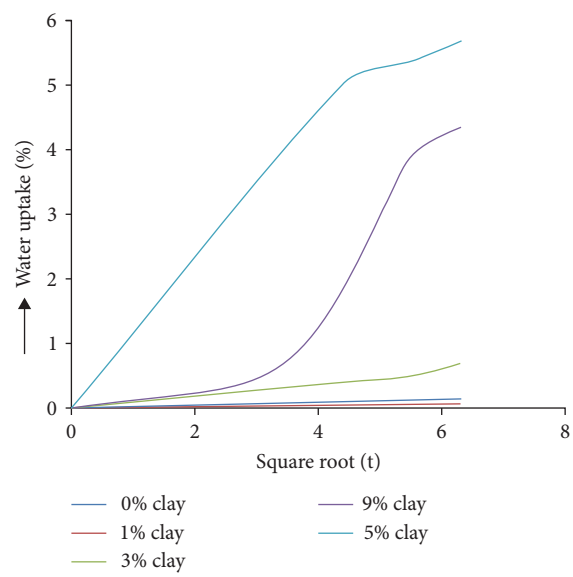

Figure 6: Water uptake of PCL Cloisite 15A nanocomposite.

3.4. Water Sorption Behavioral Study. The water uptake of the nanocomposites was found to be lower compared to the pristine polymer. Figures 6 and 7 indicate that the water absorption of the nanocomposite films is prepared by Cloisite 10A and Cloisite 15A. It may be seen that in both cases, there was a decrease in water absorption with the increment of clay content. For the penetrating molecule to move through the nanocomposites, the impermeable clay layers dictate a tortuous route. Two factors affect the nanocomposites water absorption: they are filler geometry and matrix molecular level interaction and filler. These nanosfilled samples produce decrease water uptake values with high tortuosity path, this is because silicates have platelet-like morphology.

When the water retention of the nanocomposites was studied, it was found that the water retention was higher for the 0% clay than that for the 9% of clay. There is fine distribution of the clay at lower loading and the clay begins to agglomerate at higher loading leading to poor water retention, as shown in Figure 8.

4. Conclusion

Instead of conventional filled polymers, polymer nanocomposites are used. It may be in the form of fibers, tubes, and crystals that are arranged together into several nanostructures for a

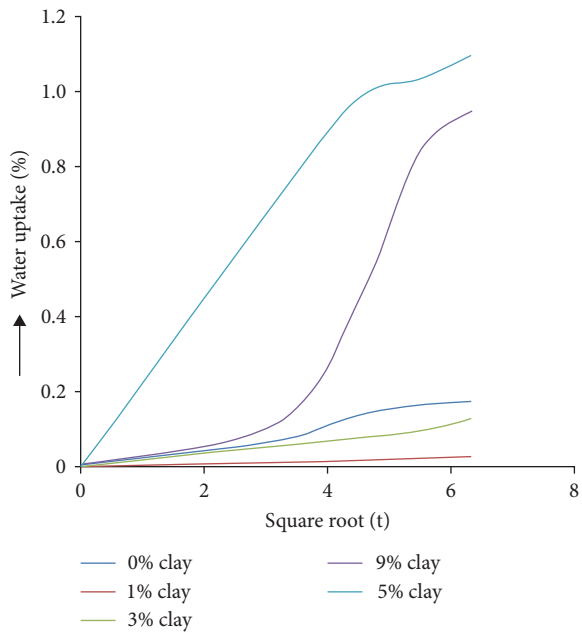

Figure 7: Water uptake of PCL Cloisite 10A nanocomposite.

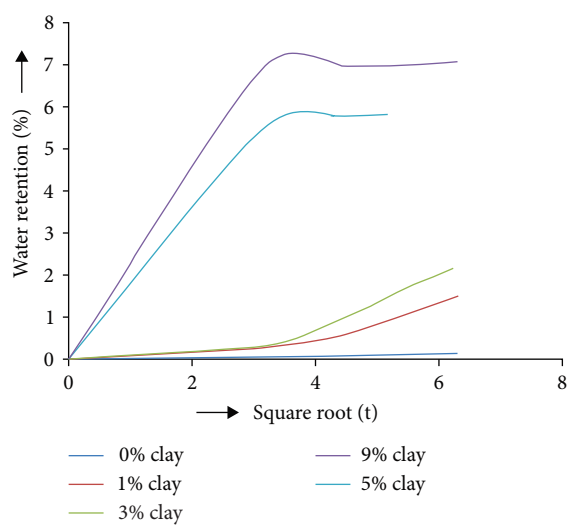

Figure 8: Water retention of PCL Cloisite 10A nanocomposite.

wide range of high-tech applications. Electrospinning has emerged as a popular nanotechnology in manufacturing nanofibers from a variety of materials. Nanofibers have a wide range of potential technological and commercial applications. Tissue engineering, drug delivery, seed-coating material, cancer diagnosis, lithium–air battery, optical sensors, air filtration, redox-flow batteries, and composite materials fields all make use of nanofibers. In this paper, the PCL clay nanocomposites were electrospuned at a voltage of 15 V, feed rate of 1 ml/min and 12 cm of tip-to-collector distance. This process is selected due to its simplicity, elegance, versatility, consistency, and by its own advantages. Compared to pure polymers, filler dispersion nanocomposites have increased applications because of their ultrafine meter sizes. The nanoclay filter, here, is used to improve the applications of pure polymers because it has manometer sizes. By introducing the nanoclay into the polymers, it increases the thermal stability, sorption, and morphology of the membrane. The nanocomposites obtained are best suited for scaffold production in the field of tissue engineering by improving the growth of the cell and organizing the tissues. These nanocomposites can able to manufacture nanosize fibers with special characteristics like high surface area and aspect ratio and have the ability to control the pore geometry. These special characteristics are helpful in cell growth (because of cell adhesion), expression of cell, and oxygen and nutrients transportation to the cells. If polymers of low molecular weight can be electrospun with low fiber diameter and the negligible bead formation, then it will be a remarkable achievement at the industrial level. These polymer clay nanocomposites possess diverse biomedical applications and are excellent materials for tissue engineering purposes.

Data Availability

The datasets generated and/or analyzed during the current study are available from the corresponding author on reasonable request.

Conflicts of Interest

The authors declare that they have no conflicts of interest.

References

[1] S. G. Kumbar, R. James, S. P. Nukavarapu, and C. T. Laurencin, "Electrospun nanofiber scaffolds: engineering soft tissues," *Biomedical Materials*, vol. 3, no. 3, Article ID 034002, 2008.

[2] D. R. Paul and L. M. Robeson, "Polymer nanotechnology: nanocomposites," *Polymer*, vol. 49, no. 15, pp. 3187–3204, 2008.

[3] Y. Fang, Y. Xu, and P. He, "DNA biosensors based on metal nanoparticles," *Journal of Biomedical Nanotechnology*, vol. 1, no. 3, pp. 276–285, 2005.

[4] Z.-M. Huang, Y.-Z. Zhang, M. Kotaki, and S. Ramakrishna, "A review on polymer nanofibers by electrospinning and their applications in nanocomposites, composites science and technology," *Composites Science and Technology*, vol. 63, no. 15, pp. 2223–2253, 2003.

[5] S. P. Nukavarapu, S. G. Kumbar, L. S. Nair, and C. T. Laurencin, "Nanostructures for tissue engineering/regenerative medicine," in *Biomedical Nanostructures*, K. E. Gonsalves, C. R. Halberstadt, C. T. Laurencin, and L. S. Nair, Eds., pp. 377–401, John Wiley & Sons, Inc., New York, 2008.

[6] N. A. Peppas and D. N. Robinson, "Nanospheres of intelligent networks for biomedical and drug delivery applications," in *Nanotechnology in Therapeutics: Current Technology and Applications*, pp. 361–379, Horizon Bioscience, Wymondham, 2007.

[7] A. Lagashetty and A. Venkataraman, "Polymer nanocomposites," *Resonance*, vol. 10, pp. 49–57, 2005.

[8] Z.-M. Huang, Y.-Z. Zhang, M. Kotaki, and S. Ramakrishna, "A review on polymer nanofibers by electrospinning and their applications in nanocomposites," *Composites Science and Technology*, vol. 63, no. 15, pp. 2223–2253, 2003.

[9] D. Liang, B. S. Hsiao, and B. Chu, "Functional electrospun nanofibrous scaffolds for biomedical applications," *Advanced Drug Delivery Reviews*, vol. 59, no. 14, pp. 1392–1412, 2007.

[10] S. G. Kumbar, S. Bhattacharyya, S. Sethuraman, and C. T. Laurencin, "A preliminary report on a novel electrospray technique for nanoparticle based biomedical implants coating: precision electrospraying," *Journal of Biomedical Materials Research*, vol. 81, no. 1, pp. 91–103, 2007.

[11] S. G. Kumbar, S. P. Nukavarapu, R. James, M. V. Hogan, and C. T. Laurencin, "Recent patents on electrospun biomedical nanostructures: an overview," *Recent Patents on Biomedical Engineering*, vol. 1, no. 1, pp. 68–78, 2008.

[12] W. Cui, Y. Zhou, and J. Chang, "Electrospun nanofibrous materials for tissue engineering and drug delivery," *Science and Technology of Advanced Materials*, vol. 11, no. 1, Article ID 014108, 2010.

[13] Z. Ma, M. Kotaki, T. Yong, W. He, and S. Ramakrishna, "Surface engineering of electrospun polyethylene terephthalate (PET) nanofibers towards development of a new material for blood vessel engineering," *Biomaterials*, vol. 26, no. 15, pp. 2527–2536, 2005.

[14] B. P. Sautter, *Continuous Polymer Nanofibres Using Electrospinning, NSF-REU Summer Program*, University of Illinois at Chicago, 2005.

[15] J. Y. Liu, L. Reni, Q. Wei et al., "Fabrication and characterization of polycaprolactone/calcium sulfate whisker composites," *Express Polymer Letters*, vol. 5, no. 8, pp. 742–752, 2011.

[16] S. Abdolmohammadi, S. Siyamak, N. A. Ibrahim et al., "Enhancement of mechanical and thermal properties of polycaprolactone/chitosan blend by calcium carbonate nanoparticles," *International Journal of Molecular Sciences*, vol. 13, no. 4, pp. 4508–4522, 2012.

[17] M. Mirjalili and S. Zohoori, "Review for application of electrospinning and electrospun nanofibers technology in textile industry," *Journal of Nanostructure in Chemistry*, vol. 6, pp. 207–213, 2016.

[18] T. A. Telemeco, C. Ayres, G. L. Bowlin et al., "Regulation of cellular infiltration into tissue engineering scaffolds composed of submicron diameter fibrils produced by electrospinning," *Acta Biomaterialia*, vol. 1, no. 4, pp. 377–385, 2005.

[19] K. J. Shields, M. J. Beckman, G. L. Bowlin, and J. S. Wayne, "Mechanical properties and cellular proliferation of electrospuncollagen type II," *Tissue Engineering*, vol. 10, no. 9-10, pp. 1510–1517, 2004.

[20] A. Atala, "Tissue engineering and regenerative medicine: concepts for clinical application," *Rejuvenation Research*, vol. 7, no. 1, pp. 15–31, 2004.

[21] A. Ivkovic, I. Marijanovic, D. Hudetz, R. M. Porter, M. Pecina, and C. H. Evans, "Regenerative medicine and tissue engineering in orthopaedic surgery," *Frontiers in Bioscience*, vol. 3, no. 3, pp. 923–944, 2011.

[22] R. A. Surmenev, S. Shkarina, D. S. Syromotina et al., "Characterization of biomimetic silicate- and strontium-containing hydroxyapatite microparticles embedded in biodegradable electrospun polycaprolactone scaffolds for bone regeneration," *European Polymer Journal*, vol. 113, pp. 67–77, 2019.

[23] Y. K. Noh, A. Dos Santos Da Costa, Y. S. Park, P. Du, I.-H. Kim, and K. Park, "Fabrication of bacterial cellulose-collagen composite scaffolds and their osteogenic effect on human mesenchymal stem cells," *Carbohydrate Polymers*, vol. 219, pp. 210–218, 2019.

[24] M. Zaborowska, A. Bodin, H. Bäckdahl, J. Popp, A. Goldstein, and P. Gatenholm, "Microporous bacterial cellulose as a potential scaffold for bone regeneration," *Acta Biomaterialia*, vol. 6, no. 7, pp. 2540–2547, 2010.

[25] D. Ramani and T. P. Sastry, "Bacterial cellulose-reinforced hydroxyapatite functionalized graphene oxide: a potential osteoinductive composite," *Cellulose*, vol. 21, pp. 3585–3595, 2014.

[26] A. M. Cakmak, S. Unal, A. Sahin et al., "3D printed polycaprolactone/gelatin/bacterial cellulose/hydroxyapatite composite scaffold for bone tissue engineering," *Polymers*, vol. 12, Article ID 1962, 2020.

[27] Plastics Europe, "Plastics—the facts," *Plastics Facts*, vol. 38, pp. 1–60, 2018.

[28] S. Mohan Bhasney, K. Mondal, A. Kumar, and V. Katiyar, "Effect of microcrystalline cellulose [MCC] fibres on the morphological and crystalline behaviour of high density polyethylene [HDPE]/polylactic acid [PLA] blends," *Composites Science and Technology*, vol. 187, Article ID 107941, 2020.

[29] D. Civancik-Uslu, R. Puig, M. Hauschild, and P. Fullana-i-Palmer, "Life cycle assessment of carrier bags and development of a littering indicator," *Science of the Total Environment*, vol. 685, pp. 621–630, 2019.

[30] D. Civancik-Uslu, L. Ferrer, R. Puig, and P. Fullana-i-Palmer, "Are functional fillers improving environmental behavior of plastics? a review on LCA studies," *Science of the Total Environment*, vol. 626, pp. 927–940, 2018.

[31] R. Abejón, J. Laso, M. Margallo et al., "Environmental impact assessment of the implementation of a Deposit-Refund System for packaging waste in Spain: a solution or an additional problem?" *Science of the Total Environment*, vol. 721, Article ID 137744, 2020.

[32] Marc Delgado-Aguilar, Rita Puig, Ilija Sazdovski, and Pere Fullana-i-Palmer, "Polylactic acid/polycaprolactone blends: on the path to circular economy, substituting single-use commodity plastic products," *Materials (Basel)*, vol. 13, no. 11, Article ID 2655, 2020.

[33] J.-M. Chen, D. Lee, J.-W. Yang, S.-H. Lin, Y.-T. Lin, and S.-J. Liu, "Extrusion additive manufacturing of biodegradable polycaprolactone," *Applied Sciences*, vol. 10, no. 9, Article ID 3189, 2020.

[34] T. D. Ngo, A. Kashani, G. Imbalzano, K. T. Q. Nguyen, and D. Hui, "Additive manufacturing (3D printing): a review of materials, methods, applications and challenges," *Composites Part B: Engineering*, vol. 143, pp. 172–196, 2018.

[35] D. G. Bekas, Y. Hou, Y. Liu, and A. Panesar, "3D printing to enable multifunctionality in polymer-based composites: a review," *Composites Part B: Engineering*, vol. 179, Article ID 107540, 2019.

[36] N. Beheshtizadeh, N. Lotfibakhshaiesh, Z. Pazhouhnia, M. Hoseinpour, and M. Nafari, "A review of 3D bio-printing for bone and skin tissue engineering: a commercial approach," *Journal of Materials Science*, vol. 55, pp. 3729–3749, 2020.

[37] P. F. Egan, "Integrated design approaches for 3D printed tissue scaffolds: review and outlook," *Materials (Basel)*, vol. 12, no. 15, Article ID 2355, 2019.

[38] B. Zhang, R. Lalani, F. Cheng, Q. Liu, and L. Liu, "Dual functional electrospun poly (2-hydroxyethyl methacrylate)," *Journal of Biomedical Materials Research A*, vol. 99, no. 3, pp. 455–466, 2011.

[39] L.-S. Wan, Z.-K. Xu, and H.-L. Jiang, "Fibrous membranes electrospinning from acrylonitrile-based polymers: specific absorption behaviors and states of water," *Macromolecular Bioscience*, vol. 6, no. 5, pp. 364–372, 2006.

Hindawi
Journal of Nanomaterials
Volume 2022, Article ID 8200856, 15 pages
https://doi.org/10.1155/2022/8200856

Research Article

Comparative Performance Study of Difference Differential Amplifier Using 7 nm and 14 nm FinFET Technologies and Carbon Nanotube FET

Anand Kumar,[1] M. Janakirani,[1] M. Anand,[1] Sudeep Sharma,[2] Chettiyar Vani Vivekanand,[3] and Ankit Chakravarti[4]

[1]*Department of Electronics and Communication Engineering, Dr. M.G.R. Educational and Research Institute University, Maduravoyal, Chennai, Tamil Nadu, India*
[2]*Department of Electronics and Communication Engineering, MLR Institute of Technology, Hyderabad, 500043 Telangana, India*
[3]*Department of Electronics and Communication Engineering, RMK College of Engineering and Technology, Puduvoyal, Tamil Nadu, India*
[4]*School of Civil and Environmental Engineering, Ambo University, Ethiopia*

Correspondence should be addressed to Ankit Chakravarti; ankit.chakravarti@ambou.edu.et

Received 22 August 2022; Revised 16 September 2022; Accepted 26 September 2022; Published 17 October 2022

Academic Editor: Senthilkumar N

Difference differential amplifiers (DDA), which were built on FinFET and carbon nanotube FET (CNTFET), are frequently used for signal processing owing to their advantages of low-power dissipation and reduced device dimension. In this work, high-performance DDA was established using CNTFET model parameters as well as FinFET 7 nm and 14 nm technology. The DDA circuit used in this scenario was identically the same to the one used previously. With the use of Verilog AMS code-based Stanford model parameters applied CNTFET and 7 nm and 14 nm FinFETs, schematic capture and simulations of the DDA were carried out in the Symica environment. The mostly used measurements for assessing the performance of operational amplifiers were also adopted for DDA. The CNTFET-based difference differential amplifiers have slew rates of 10.8 V/femtosecond and 11.2 mV/femtosecond, respectively, with settling times of 0.65 femtosecond and 0.43 femtosecond, respectively. The power supply rejection ratio (PSRR) is 2.53 dB with a dynamic range of 198 mV and 6 mV for CNTFET DDA operating at 0.6 V DC. The incentives of CNTFET appropriateness for DDA designed in this study for any analogue front end were further demonstrated by using CNTFET for DDA with the achievement of open loop differential gain of 116.03 dB with BW of 4 GHz and phase margin of 270 and common mode gain of -28.65 dB with BW of 55.14 MHz and phase margin of 270.

1. Introduction

The size of transistors must be decreased as integrated circuits (ICs) develop in order to meet the rising requirements for devices with greater speed and reduced power consumption. Currently, silicon planar technologies dominate the market; however, certain of its factors, indeed the regular thickness of the gate oxide layer (Tox), are very close to the physical limit [1]. Thus, in order to build new devices and maintain Moore's law in the growth of integrated circuits, it is necessary to investigate novel materials and production techniques. The carbon nanotube field effect transistors (CNTFETs) and fin field effect transistors (FinFETs), which have electrical properties identical to those of silicon metal-oxide semiconductor field effect transistors (MOSFETs), become two potential candidates.

For any feasible enhancements, numerous technological and device structural variations, namely, single gate FETs, SOI FETs, multiple gate FETs, and CNFETs, are available.

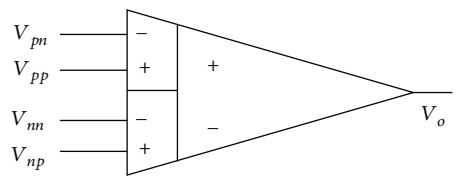

Figure 1: Schematic symbol of the DDA.

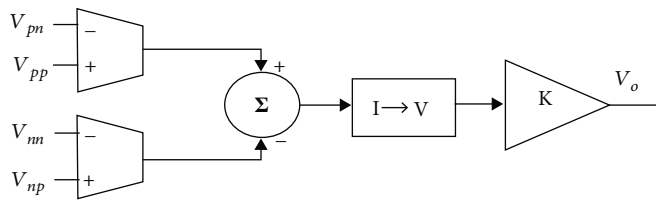

Figure 2: DDA block diagram.

Additionally, FinFETs and CNFETs have recently emerged as crucial advancements for low-power, low-voltage applications. Due to its greater electrostatics, adaptability, and stability, double gate-based transistors can eventually replace CMOS, thus becoming essential component for any types of analogue circuits like differential amplifier and operational amplifier [2]. Current carbon nanotubes are the only known scenario in which the size of exploratory devices will be reduced to incredibly small sizes. It is possible that the results will complement the expectations, enabling, theoretically, for the experimental validation of analytical models and device architecture [3].

It is essential to design phenomenal analogue integrated circuits operate at low supply voltages. Gain, slew rate and power, and other performance metrics were usually traded off at higher supply voltages. In this paper, the proposed design and analysis of low-voltage, low-power difference differential amplifiers (DDAs) using CNTFET and FinFET technologies were focused. The simulation comparative analysis was performed between CNTFET-based DDA and traditional CMOS-based DDA also with FinFET-based DDA. All of the device types, including CNTFET and FinFET, were subjected to simulations of DDA and were then compared for the best outcome from each kind.

1.1. Design of DDA. The main challenges in the design of DDA is making out circuit with supply voltages (vdd) of the order of several saturation voltages of an MOS transistor (Vdsat). Poor signal swing at extreme supply conditions, relatively poor CMRR and PSRR with tail current source, and drawback of CMOS topology are significant limitation on DC responses and the occurrence of asymmetry, if low-voltage processes are used. Figure 1 depicts the schematic representation of the DDA [4, 5] which is an expanded version of an operational amplifier. As opposed to two single-ended inputs like op-amps, it contains two differential input pins. The DDA's output is thus defined.

$$V_o = A_o\left[\left(V_{pp} - V_{pn}\right) - \left(V_{np} - V_{nn}\right)\right]. \quad (1)$$

A_o is an open loop gain. The model equation can be derived provided negative feedback is given to V_{pn} and/or V_{np}, which provides a negative relation in (1):

$$\left(V_{pp} - V_{pn}\right) = \left(V_{np} - V_{nn}\right) \text{ on } A_o \longrightarrow \infty. \quad (2)$$

With increasing open-loop gain, A_o, the difference between the two differential voltages reduces. Figure 1 depicts the DDA. The DDA is actually be implemented as depicted in Figure 2 [3], with two V-I converters acting as the input pins of DDA to transform the two differential voltages into currents that are ultimately subtracted, converted to voltage, and boosted. The use of FinFET/CNTFET devices enabled the development of a DDA with a broad input range. A linear FinFET/CNTFET V-I converter that can be tuned was used to build a DDA with a large input range for wide signal operation.

The main approach for constructing the DDA is to use two differential pairs to develop the V-I converters [6]. The following formula can be used to calculate the differential current I_d of a differential pair biased by a given current source I_s:

$$I_d = \begin{cases} \dfrac{V_d}{|V_d|} I_s, & \text{for } |V_d| \geq \sqrt{\dfrac{2I_s}{\beta}}, \\ \dfrac{V_d}{|V_d|} V_d \sqrt{\beta I_s \left(1 - \dfrac{\beta V_d{}^2}{4I_s}\right)}, & \text{for } |V_d| < \sqrt{\dfrac{2I_s}{\beta}}. \end{cases} \quad (3)$$

In this equation, V_d is the input differential voltage, $\beta = \mu C_{ox}(W/L)$, W/L is the width to length ratio of the device, μ is their mobility, and C_{ox} is their gate oxide capacitance for anunit area. The component under square root states as the percent deviation from the significance level of $g_m V_d$, wherein g_m is the transconductance when $V_d = 0$, produces nonlinearity in I_d rather than the linear relationship between I_d and V_d. It implies

$$g_m = \left|\frac{dI_d}{dV_d}\right| = \sqrt{\beta I_s}. \quad (4)$$

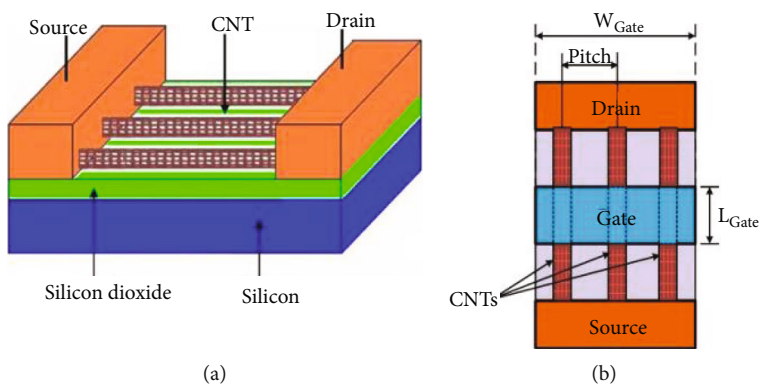

Figure 3: Carbon nanotube field effect transistor (CNFET). (a) Schematic. (b) Top view [26].

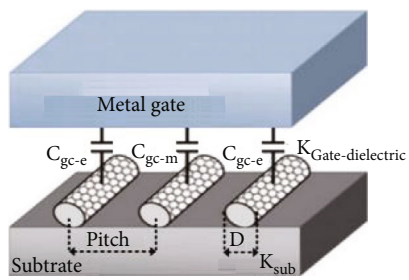

Figure 4: CNFET gate to channel capacitance [26].

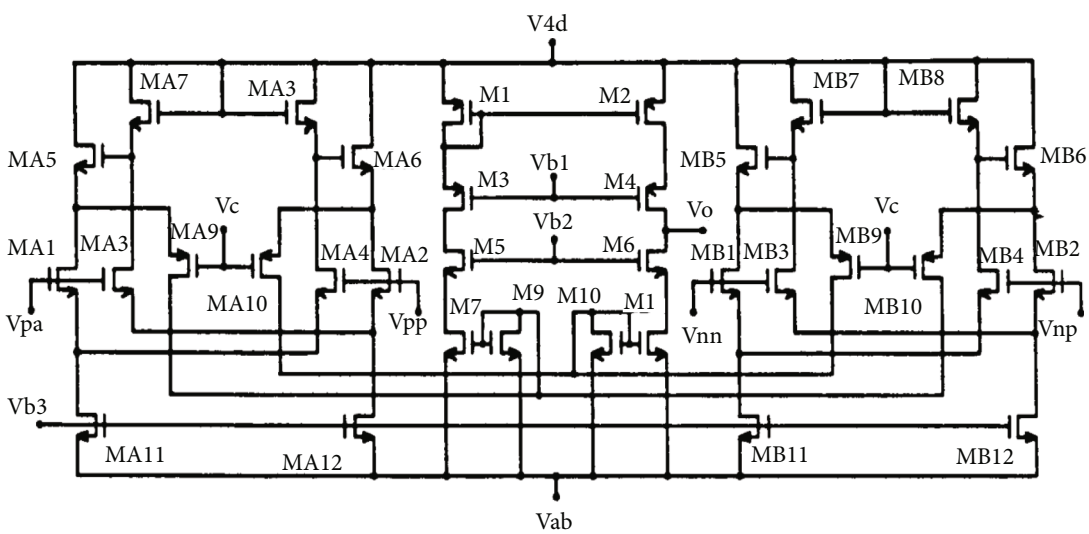

Figure 5: DDA circuit.

The differential pair is always operating at $V_d \approx 0$ due to the virtual short property of op-amps, and thus, the differential pair's transconductance is approximately the g_m.

2. Literature Survey

The extensive survey was done to study the role of CNTFET that started to apply in analogue circuits to enhance their performance. This paper makes an effort to evaluate the performance of DDA using the FinFET and CNTFET.

Crippa et al. [7] analyzed high-gain 90 nm length and 1 μm width CNTFET-based broadband inductor-less low noise amplifier (LNA) and confirmed the overall validity of the proposed high-gain LNA design while comparing both conventional 32 nm CMOS technologies and CNTFET with the limitation of restricted to 90 nm technology. Akhoon et al. [8] designed and simulated a current source load

Table 1: The Stanford CNFET model parameters.

Parameter	Description	Value
V	Power supply	0.7 V
L_g	Physical channel length	16 nm
S_T	CNT pitch	10 nm
(n_1, n_2)	CNT chirality	(19, 0)
L_{ceff}	Mean free path in intrinsic CNT	200 nm
V_{fbn}	N-type CNFET flat band voltage	0
High – K_{ox}	Dielectric material of top gate	HfO_2 (16)
L_s	Source-side length of doped CNT	16 nm
L_d	Drain-side length of doped CNT	16 nm
T_{ox}	Oxide thickness	4 nm
K_{sub}	Dielectric constant	SiO_2 (4)
L_{eff}	Mean free path in doped CNT	15 nm
E_{fo}	Fermi level of n+-doped drain/source CNT region	0.6 eV
N_T	Total number of CNT used per CNFET	~

Table 2: Setting of DC voltage sources for the circuit of Figure 3.

Parameters	7 nm/14 nm	CNTFET
Supply voltage (V)	+0.8/-0.8	+0.6/-0.6
Vb1	0.1	0.1
Vb2	0.1	0.1
Vb3	0.1	0.1
Vc	0	0

differential amplifier (CSL-DA) using n-type carbon nanotube field effect transistors (CNTFET) investigated using HSPICE simulation restricted to 45 nm CNTFET. Yasir and Alam [9] designed CNTFET single-stage-based 5 T single-stage operational transconductance amplifier (OTA) and two-stage operational amplifier using g_m/I_D technique for low-voltage and low-power applications investigated using HSPICE simulation showing the importance of g_m/I_D technique to implement CNTFET-based OTA design. Their results provided accuracy within acceptable limits with input specifications restricted to OTA specifications of GBW and CMRR. Bendre et al. [10] used SPICE compatible Stanford University 32 nm CNFET model and determined that CNTFET-based circuits are considerably competent than that of conventional 32 nm CMOS-based circuits in nanoscale regime. Bhargav et al. [11] designed sinusoidal oscillator CNTFET-based OTA simulated for the transient response, noise analysis, and noise sensitivity restricted to 32 nm CNTFET. Chithambaram et al. [12] proposed voltage differencing transconductance amplifier using CNTFET which operates as a voltage and transconductance operation to achieve high performance and find low power and low voltage and better DC transfer characteristics. Nizamuddin et al. [13] designed and calibrated simulation of multistage operational amplifiers (OP-AMPs) using CNTFET investigated using HSPICE simulation showing increase in DC gain and slew rate of 19.14% and 274.6% and reduced output resistance and power consumption by 133-fold and 200% restricted to 45 nm CNTFET. Puri et al. [14] implemented high-performance, low-power CNTFET-based two-stage op-amp for biomedical A/D converters using SPICE compatible Stanford University 32 nm CNFET model with various numbers of tubes across different transistors and compared DC gain, GBW, and slew rate parameters of CNTFET-based op-amp circuit with 32 nm MOSFET-based op-amp. Loan et al. [15] designed and simulated OTA using n-type carbon nanotube field effect transistors (CNTFETs) investigated using HSPICE simulation increasing gain by 218%, slew rate by 55.2%, and power consumption decrease by 193-fold but compared various channel lengths of CNTFET.

3. Carbon Nanotube Field Effect Transistor

One of the primary benefits of MOSFET technology is its fast-processing speed, but the significant power consumption is a problem and a major roadblock to the development of devices [16]. The basis for developing terascale microchips is complementary MOS (CMOS), which is recognised for its low-power consumption and high noise margin. It is quite difficult to

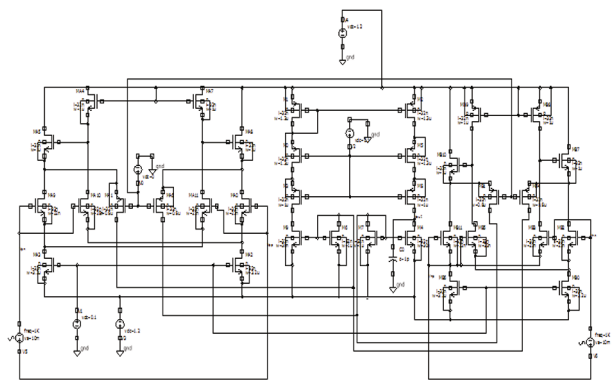

Figure 6: Schematic circuit of FinFET-based DDA used for differential mode gain analysis.

Table 3: 7 nm and 14 nm FinFET device sizes.

Parameters	7 nm process	14 nm process
Gate length (Lg)	10 nm	20 nm
Fin width	4 nm	6.5 nm
Fin height	35 nm	26 nm
Gate height	50 nm	50 nm
EOT	0.65 nm	1.05 nm

scale MOS dimension. The substantial short channel effects, gate leakage, complexity in fabrication, sensitivity to process variables at the nanoscale, and other issues are huge challenges to continually increasing device dimensions [16, 17]. Consequently, a variety of device topologies have been developed, including silicon on insulator [18], FinFETs [19], and carbon nanotube field effect transistors (CNTFETs) [20]. An electrical and mechanical property of it is greatly enhanced when carbon nanotubes (CNTs) are used. A CNTFET is distinguished by its superior electrostatic stability, high carrier transport, large thermal conductivity, and ballistic movement of charge carriers that results in high mobility [19, 21, 22].

A CNTFET, essentially uses an array of single-wall CNTs that are separated and integrated as the conduction channel, is a significant application of CNTs. Iijima of Japan is credited with discovering the first multiwalled CNT in 1991 [23], and Donald Bethune independently developed single-wall (SW) CNTs in 1993. A semiconducting CNT is coupled to two metal electrodes to create the first carbon nanotube field effect transistor, according to Tans et al. [24]. A CNTFET's schematic is shown in Figure 3, and its gate to channel capacitance is shown in Figure 4. The channel has undoped CNTs, while the source and drain areas are identical to those of a typical MOSFET [19, 22, 25, 31].

Owing to its superior electrical, mechanical, chemical, and thermal capabilities, carbon nanotubes (CNTs), which are graphite cylindrical sheets (GCSs), are viewed as the best material for new submicron devices and applications. Single-wall and multiwall CNTs are the two types of CNTs. Whereas multiwall CNT comprises of many GCS, single-wall CNT is focused on a completely GCS. The chirality vector (C_h) affects the single-wall CNT's characteristics [23]. The positive integer vector indices n_1 and n_2 specify the C_h. C_h determines the angle at which the carbon atoms are arranged along the CNT. Based on the vector indexes n_1 and n_2, the single-wall CNT may exhibit crystalline characteristics.

The single-wall CNT operates as a metallic material if $|n_1 - n_2|$ is an integral multiple of 3 or if $n_1 = n_2$, else it operates as a semiconductor. The equations describe the relationships between a CNT's C_h, diameter (DT), and threshold voltage (V_{th}).

$$C_h = a\sqrt{n_1{}^2 + n_2{}^2 + n_1 n_2}, \tag{5}$$

$$D_T = \frac{C_h}{\pi}, \tag{6}$$

$$V_{\text{th}} = \frac{a^{V_\pi}}{\sqrt{3}eD_T}, \tag{7}$$

wherein a is the graphene-lattice factor with a magnitude of 2.49 A^{o} and e is the standard electron charge. With a magnitude of 3.033 eV, V_π is the π to π bond energy in the tight-bonding model [24]. Carbon nanotube FET (CNTFET) based on different analogue signal processing applications such as inverting amplifier, noninverting amplifier, summer, subtractor, differentiator, integrator, half-wave and full-wave rectifiers, clipper, clamper, inverting and noninverting comparators, peak detector, and zero crossing detector is

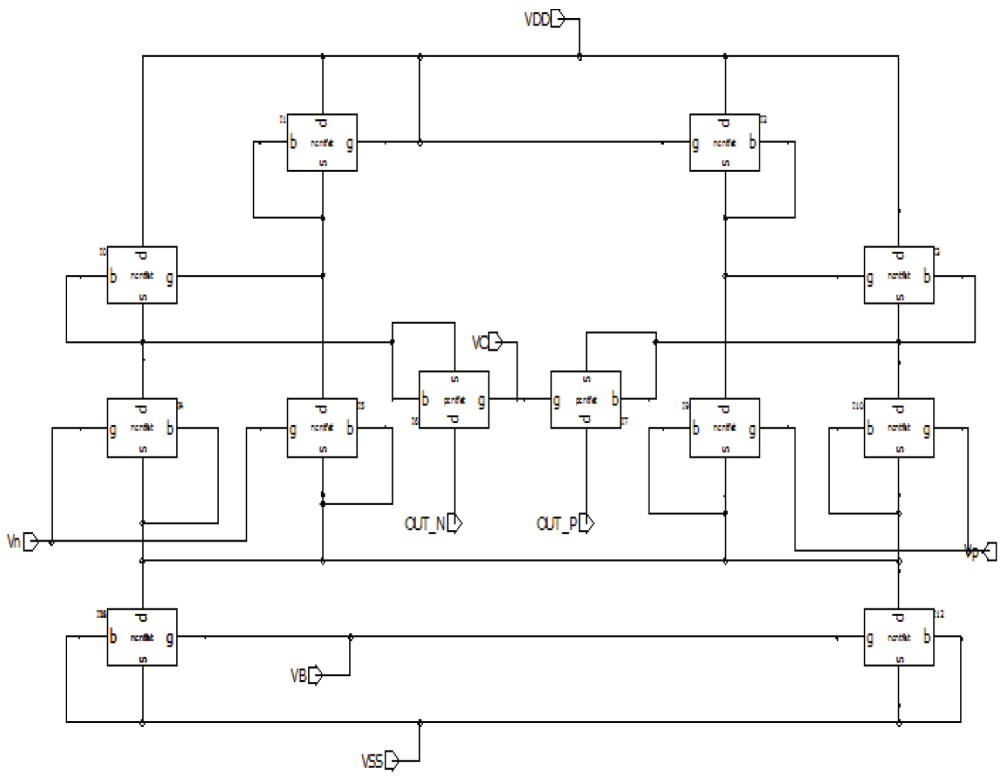

(a)

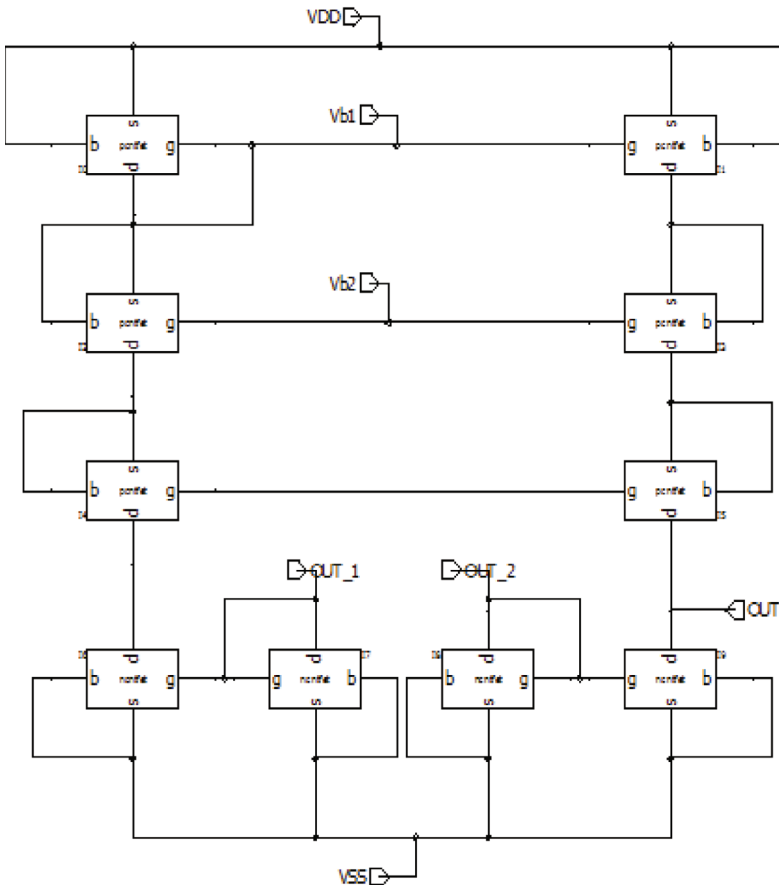

(b)

Figure 7: (a) Schematic circuit of VI converter. (b) Schematic circuit of OTC.

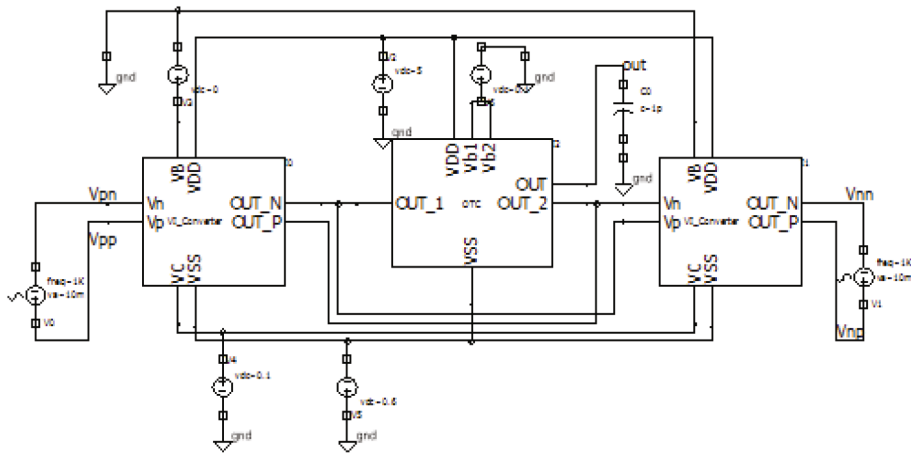

Figure 8: Schematic circuit of CNTFET-based DDA used for differential mode gain analysis.

implemented using low-power folded cascode operational amplifier (op-amp) implemented using CNTFET.

3.1. Circuit Setting for Simulation. To design FINFET technology, use a robust and precise mode to simulate in predictive technology model (PTM). The W/L ratios and PTM models were changed with device technologies. Symica EDA was used to construct the DDA circuits shown in Figure 5. FinFET transistors and CNTFETs were designed in DDA employing Verilog AMS, and Stanford CNFET model parameters are presented in Table 1. Using Symica EDA tool can construct the DDA circuits, FinFET transistors, and carbon nanotube FETs and can employ Verilog AMS and Stanford carbon nanotube FET model parameters.

Performance analyses of DDA CNTFETs with 15 carbon nanotubes in 16 nm technology and FinFETs with 7 nm and 14 nm technologies were done in Symica EDA. Comparative data for DC voltage sources given to a DDA circuits with different devices is shown in Table 2

3.1.1. Differential Mode Gain. To design FINFET technology, use a robust and precise mode to simulate in predictive technology model (PTM). Differential mode gain is obtained by setting the configuration of both input transconductance amplifiers as shown in Figure 6. Verilog A code which includes the device parameters as stated in Table 3 was used to simulate the 7 nm and 14 nm FinFET transistors. Their Symica schematic DDA circuit used for different gain AC analysis is depicted in Figure 7(a) showing the realization of voltage to current (VI) converters and output transconductance (OTC) for the CNTFET-based realization of DDA shown in Figure 7(b).

Figures 6 and 8 show the Symica schematic DDA circuits that were used for various gain AC analyses. The comparison results of the AC analysis, including the gain, phase margin, output voltage, and differential input voltage of the DDA, are shown in Figures 9(a)–9(c). The differential inputs of DDA are connected to a sinusoidal source of 10 mV and 1 kHz, and the output is coupled to a 1 pf capacitor. Then, AC analysis is carried out by sweeping the frequency with steps of 10 kHz from 1 kHz to 4 GHz. The parameters of AC sources are shown in Table 4. Table 5 compares the values of the differential mode gain AC analysis of DDA.

3.1.2. Common Mode Gain. The configuration of DDA is established as indicated in Figure 10 to achieve common mode gain. Verilog A is used in the instance of 7 nm/14 nm FinFETs and CNTFET with Stanford parameters. To simulate the transistors, the codes use the device parameters listed in Table 2 for CNTFET and Table 3 for FinFETs. Figure 11 shows the DDA circuits that were utilised for the common mode gain AC analysis. The comparison of AC analysis parameters such as gain, phase margin, output voltage, and common input voltage of DDA is shown in Figure 12.

The differential inputs of DDAs are connected to a sinusoidal source of 10 mV and 1 kHz, and the output is coupled to a 1 pf capacitor. Then, AC analysis is carried out by sweeping the frequency with steps of 10 kHz from 1 kHz to 4 GHz. The parameters of the input sources are shown in Table 6. Table 7 compares the characteristics of the DDA's common mode gain AC analysis.

3.1.3. Common Mode Rejection Ratio (CMRR). The comparison of CMRR, including gain and phase margin, output voltage, and common input voltage of DDA, is shown in Figure 13 because CMRR is the ratio of differential mode gain to common mode gain. These results were produced using Python using SPICE-exported CSV files. The CMRR of DDAs, which were calculated from Figure 13, are compared in Table 8.

3.1.4. Slew Rate. Slew rate measures the ratio of voltage change over time for both the rise and fall of the output voltage in relation to the input voltage. Table 9 compares the slew rate parameters of DDAs using various transistor technologies and varieties. The role of slew rate analysis in carbon nanotube FET DDA gives the maximum rate of change of an amplifier

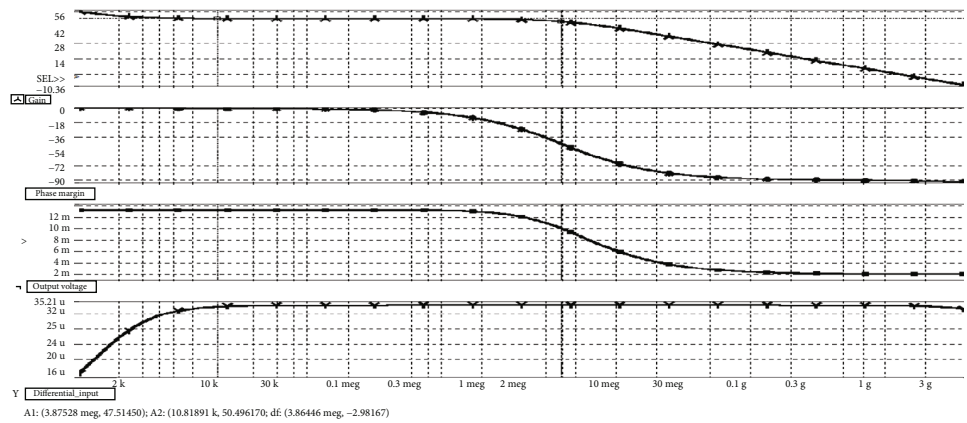

(a)

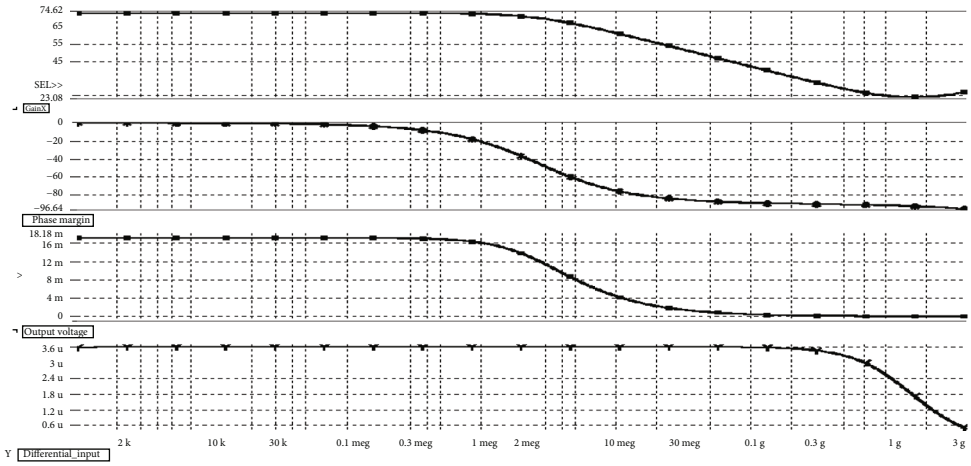

(b)

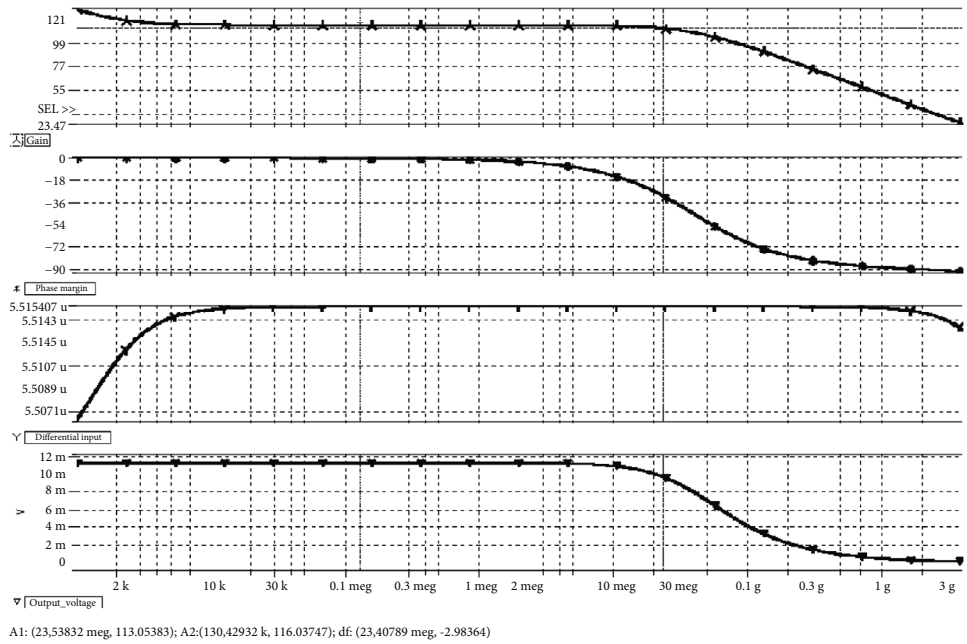

(c)

Figure 9: (a) Differential mode AC analysis of DDA which contains transistors of 7 nm FinFET. (b) Differential mode AC analysis of DDA which contains transistors of 14 nm FinFET. (c) Differential mode AC analysis of DDA which contains transistors of CNTFET.

Table 4: Setting of input source for differential mode gain AC analysis.

Parameters	V_{pp} and V_{pn}	V_{np} and V_{nn}
Source type	AC	AC
Amplitude	10 m	10 m
Frequency	1 kHz	1 kHz
Phase shift	0	180

Table 5: Comparison of differential mode gain AC analysis of DDA.

Parameters/devices	7 nm FinFET	14 nm FinFET	16 nm CNTFET
Gain	50.6	74.62	116.03
Gain 3 dB	47.6	71.62	113.03
3 dB frequency	3.76 MHz	2.1 MHz	23.54 MHz
Phase margin at -3 dB	-44.22	-50	-26.43
Cutoff frequency at 0 dB	1.4 GHz	1.2 GHz	4 GHz
Phase margin at 0 dB	-90	-90	-107
Differential input voltage	34.2 μV	3.6 mV	5.15 μV
Output voltage	11.32 mV	18.18 mV	11.8 mV
Differential input voltage at 3 dB	34.2 μV	3.6 μV	5.15 μV
Output voltage at 3 dB	mV	12 mV	9.9 mV

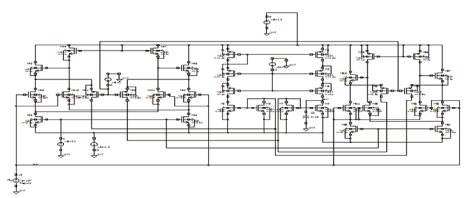

Figure 10: Schematic circuit of FinFET DDA used for common mode gain analysis.

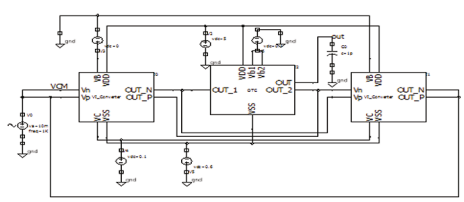

Figure 11: Schematic circuit of CNTFET DDA used for common mode gain analysis.

output voltage, and its makes higher bandwidth. Slew rate changes with the change of voltage gain.

3.1.5. Power Supply Rejection Ratio (PSRR). Power supply rejection ratio or PSRR is described as a capacity of the circuit to absorb power supply changes at its output signal. It is also known as supply-voltage rejection ratio. A measure of a capability of an amplifier to maintain a consistent output voltage as the DC power supply voltage varies. So it needs to analyze because a lower output current decreases the dropout voltage and helps improve power supply rejection ratio (PSRR).

The equation in calculating the PSRR is PSRR = 20 log (Power Supply Variation)/(Input Offset Voltage Variation)[dB].

In theory, PSRR is frequency dependent and decreases with increasing frequency. Figures 14 and 15 show the DDA circuits that were used for PSRR. Figure 16 compares PSRR metrics like gain and phase margin of DDA. The comparison of PSRR of DDA parameters that were calculated from Figure 16 is shown in Table 10.

PSRR decrease in carbon nanotube FET is beneficial for circuits because a lower output current decreases the dropout voltage and helps improve power supply rejection ratio (PSRR) which is the ratio of O/P noise and I/P noise.

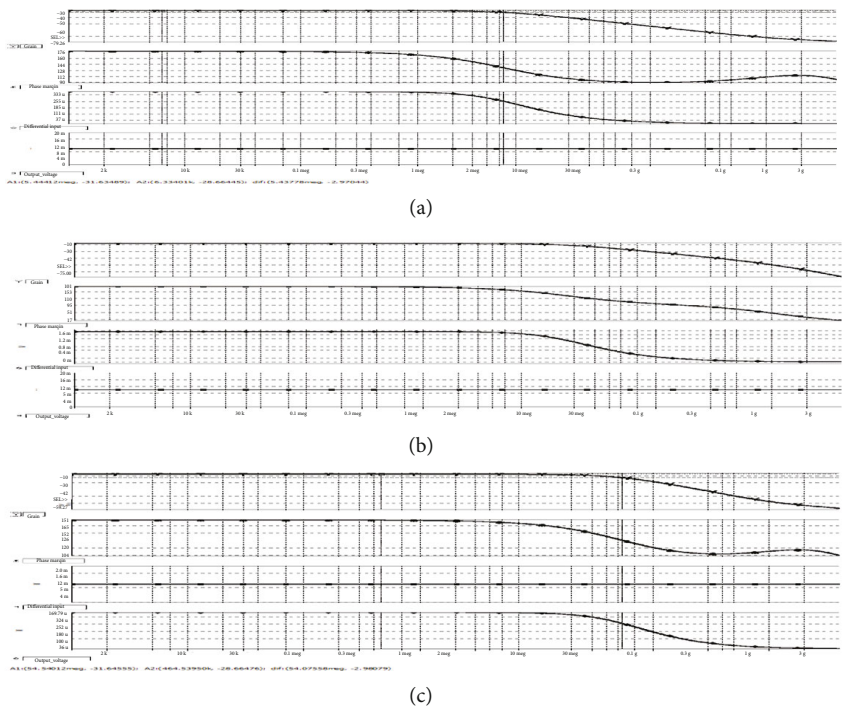

(a)

(b)

(c)

Figure 12: (a) Common mode AC analysis of DDA of 7 nm FinFET based. (b) Common mode AC analysis of DDA of 14 nm FinFET based. (c) Common mode AC analysis of DDA of CNTFET based.

Table 6: Setting of input source for common mode gain AC analysis.

Parameters	V_{pp}, V_{pn}, V_{np}, and V_{nn}
Source type	AC
Amplitude	10 mV
Frequency	1 kHz
Phase shift	0

Table 7: Comparison of common mode gain AC analysis of DDA.

Parameters/devices	7 nm FinFET	14 nm FinFET	16 nm CNTFET
Gain	-28.66	-37.8	-28.65
Gain 3 dB	-31.66	-40.8	-31.65
3 dB frequency	5.44 MHz	21 MHz	55.14 MHz
Phase margin at -3 dB	-56.22	-119	-136
Common input voltage	10 mV	10 mV	10 mV
Output voltage	368.78 μV	1.6 mV	369.79 μV
Common input voltage at 3 dB	10 mV	10 mV	10 mV
Output voltage at 3 dB	259.43 μV	0.8 mV	255 μV

3.1.6. Input Common Mode Range (ICMR). The device comparison of the ICMR change in V_0 vs. V_{ss} is shown in Figure 17. The supply voltage is V_{ss}. Offset voltage is used as the differential input for the ICMR analysis, and a DC sweep is then run on V_{ss} to measure changes in the output voltage V_0. Table 11 compares the ICMR DDA parameters that were generated from Figure 17 in terms of each other.

4. Results and Discussions

Table 12 compares the DC analysis of DDA for various devices, including CNTFET, 7 nm FinFET, and 14 nm FinFET. According to Table 12, the CNTFET operates with DC voltage of 0.6 V, which is lower than that of other devices using 7 nm and 14 nm FinFETs but still essential for determining chip size. The 2.1 nA drawn by the CNTFET is less than that of other devices using 7 nm and 14 nm FinFETs, making it a crucial requirement in deciding the chip power. Additionally, the input impedance of the CNTFET is 255 MΩ, which is higher than that of analogous devices made of 7 nm and 14 nm FinFETs and is also more important for evaluating the sensitivity of devices to input signals.

According to Table 13, the differential mode gain of CNTFET, which is higher than those of other transistors using 7 nm and 14 nm FinFETs, is 116.03 dB with a BW of 23.4 MHz. The differential mode gain must be high, and those frequencies must be in the low frequency range for any instrumentation amplifier.

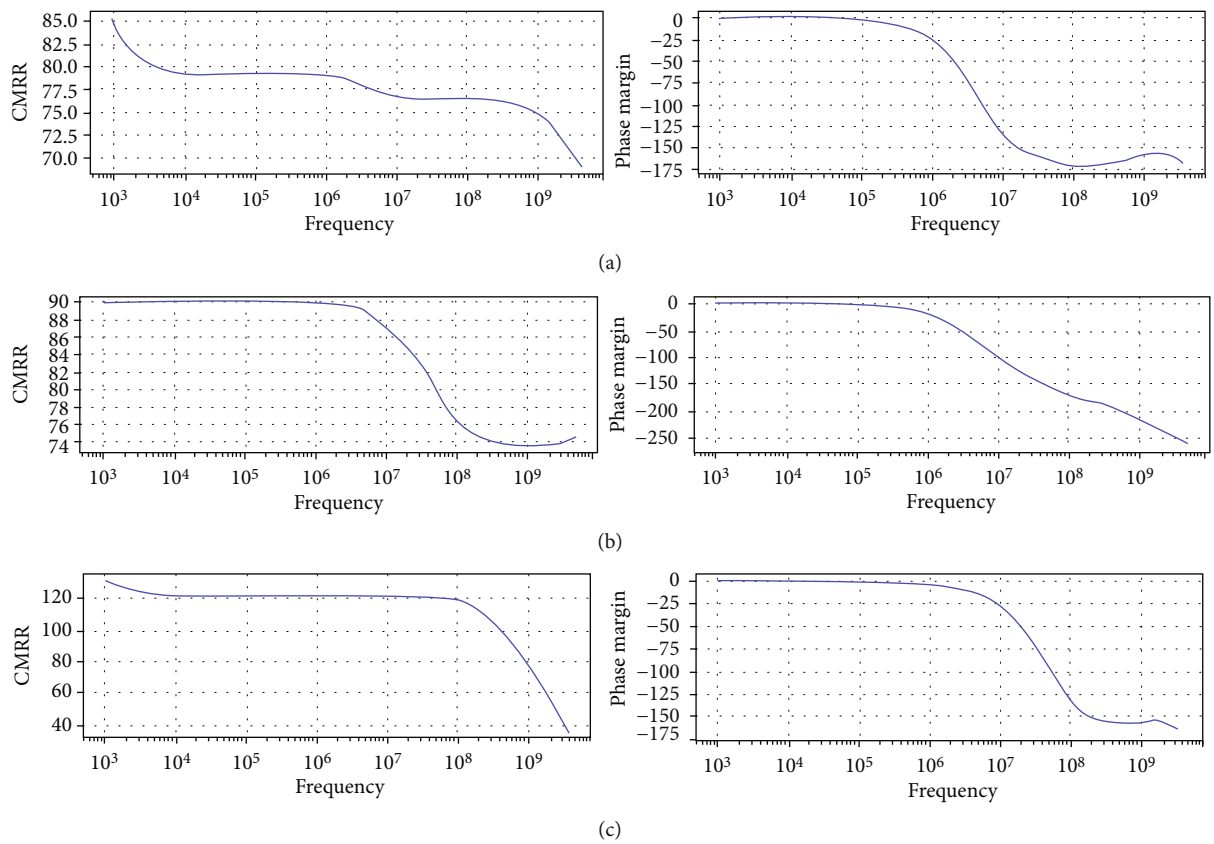

Figure 13: (a) CMRR of DDA of 7 nm FinFET based. (b) CMRR of DDA of 14 nm FinFET based. (c) CMRR of DDA of CNTFET based.

Table 8: Comparison of CMMR of DDA.

Parameters/devices	7 nm FinFET	14 nm FinFET	16 nm CNTFET
Gain	79.18	89.8	131.78
Gain 3 dB	76.18	86.8	128.78
3 dB frequency	238.5 MHz	20 MHz	134.2 M
Phase margin at -3 dB	-166.22	-150	-152.22

Table 9: Comparison of slew rate of DDA.

Parameters/devices	7 nm FinFET	14 nm FinFET	16 nm CNTFET
Rise slew rate	110 V/fs	127 V/fs	10.8 V/fs
Fall slew rate	107 V/fs	126 V/fs	11.2 V/fs
High amplitude	1.5 mV	1.84 mv	1.58 mV
Low amplitude	1.39 mV	1.83 mV	1.53 mV

Compared to other devices, such as 7 nm and 14 nm FinFETs, the CNTFET's common mode gain of -28.65 dB with a BW of 55.14 MHz is more tolerable. The common mode gain must be exceptionally low for any instrumentation amplifier, and those frequencies must be in the low range.

According to Table 13, the CNTFET has a CMRR of 131.78 dB and a BW of 134.2 MHz, which is better than previous devices with 7 nm and 14 nm FinFETs. The CMMR needs to be high and they need to have a greater bandwidth for any instrumentation amplifier.

According to Table 13, the CNTFET possesses output slew rates of 10.8 V/femtosecond for input rise and 11.2 V/femtosecond for input fall that are more acceptable when compared to other devices, such as 7 nm and 14 nm

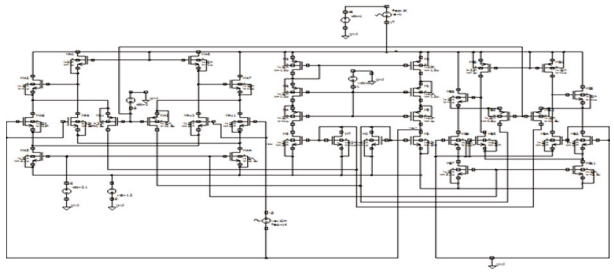

Figure 14: Schematic circuit of DDA used for PSRR analysis by FinFET devices.

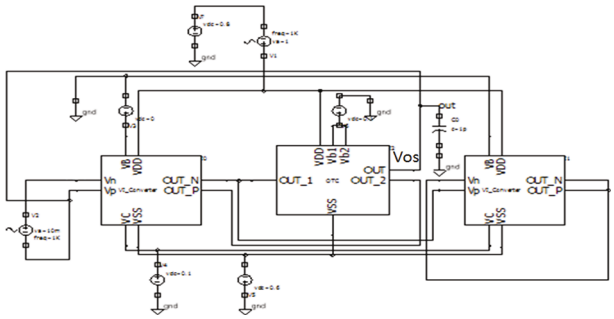

Figure 15: Schematic circuit of DDA used for PSRR analysis by CNTFET device.

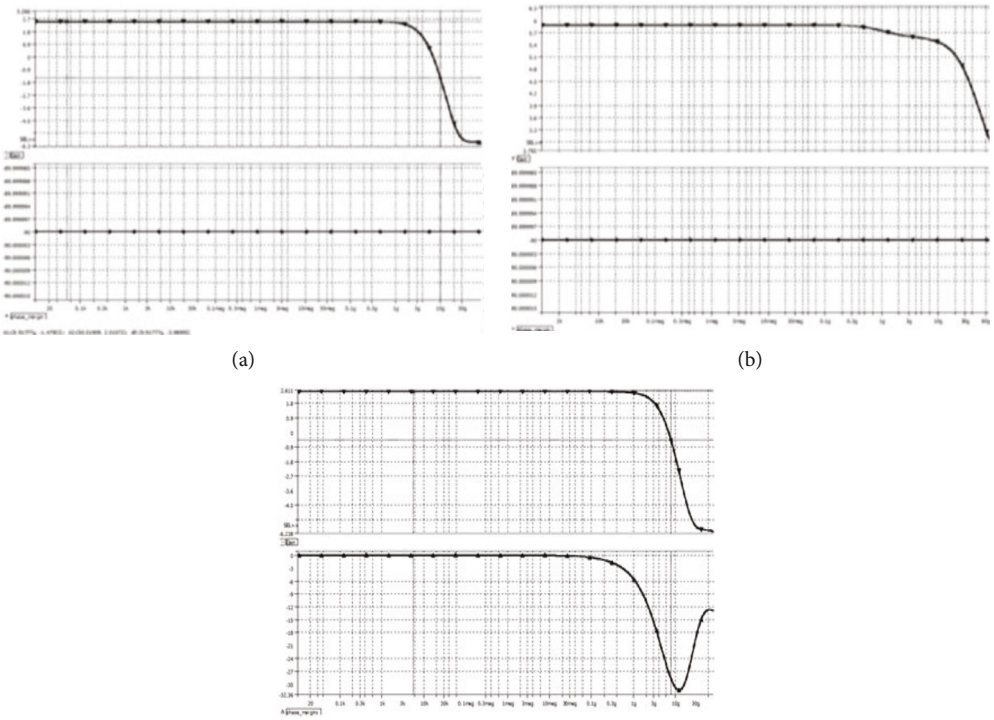

Figure 16: PSRR of DDA using (a) 7 nm FinFET, (b) 14 nm FinFET, and (c) CNTFET.

Table 10: Comparison of PSRR of DDA.

Parameters/devices	7 nm FinFET	14 nm FinFET	16 nm CNTFET
Gain	6.51	7.02	2.53
Gain 3 dB	3.51	4.02	-0.47
3 dB frequency	9.73 GHz	70 GHz	998 kHz
Phase margin at -3 dB	-90	-90	-28

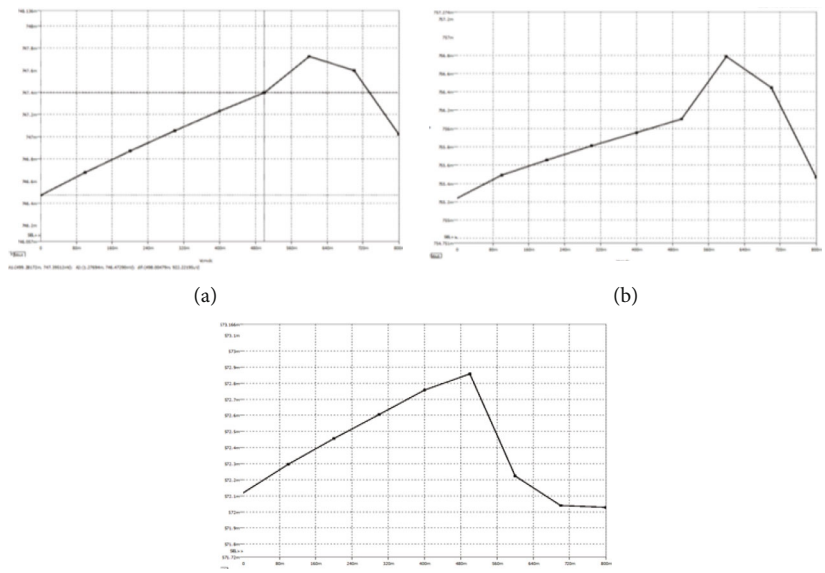

(a) (b) (c)

Figure 17: ICMR of DDA using (a) 7 nm FinFET, (b) 14 nm FinFET, and (c) CNTFET.

Table 11: Comparison of ICMR of DDA.

Voltage levels	7 nm FinFET	14 nm FinFET	16 nm CNTFET
Low	0	752 mV	572.15 mV
High	mV	758 mV	572.8 mV

Table 12: Comparison of DC analysis of DDA.

Technology	Vdc	Rin	Io^+/Io^-
32 nm CMOS	1.2	9.1 MΩ	1.43 μA
22 nm CMOS	1.2	41.3 MΩ	0.27 μA
7 nm FinFET	0.8	123 MΩ	6.5 nA
14 nm FinFET	0.8	186 MΩ	4.3 nA
CNTFET	0.6	255 MΩ	2.1 nA

FinFETs. Any instrumentation amplifier needs a high enough slew rate to function properly.

According to Table 13, the CNTFET has a PSRR of 2.53 dB and a BW of 998 kHz, which is better than comparable devices like 7 nm and 14 nm FinFETs. The PSRR needs to be high and the bandwidth needs to be wider for any instrumentation amplifier.

According to Table 11, the ICMR values for the CNTFET are between 572.15 mV and 572.8 mV, which is more acceptable when compared to other devices like 7 nm

Table 13: Comparison of the performance between current and previous researches.

Parameters	Matthus et al. [27]	Khateb et al. [28]	Khateb and Kulej [29]	Anand Kumar et al. [30]	This research
Technology	0.18 μm bipolar, CMOS	0.18 μm CMOS TSMC	0.18 μm CMOS TSMC	14 nm FinFET PTM model	16 nm CNTFET
DC supply	1.8 V	0.5 V	0.3 V	0.8 V	0.6 V
Gain	46 dB	61.4 dB	60 dB	74.62 dB	116.03 dB
Bandwidth	2 MHz	6.98 kHz	1.85 kHz	20 MHz	23.4 MHz
Power consumption	—	246.6 nW	22 nW	3.44 nW	1.42 nW
CMRR	—	100 dB	—	89.8 dB	131.78 dB
PSRR	—	127.8 dB	57 dB	7.02 dB	2.53 dB
Slew rate	—	500 V/μs	1.55 V/μs	127 V/fs	10.8 V/fs

and 14 nm FinFETs. The ICMR must be low for any instrumentation amplifier to detect low signal voltages; however, 14 nm FinFET performance is subpar and has limited linear operation. Table 13 shows that the 16 nm CNTFET outperforms earlier research in terms of performance.

5. Conclusions

This paper provided a useful comparison of various FinFETs and CNTFET device technologies applied to a differential difference amplifier (DDA) and ultimately recommended CNTFET as a remarkable optional device for DDA-based instrumentation amplifier in order to improve the performance of DDA on fairly close rail-to-rail input changes and with output changes, a rather increased DC input resistance, and with incredible CMRR. Anywhere where a comparison between two weak differential voltages is required, this CNTFET-based DDA can be used. This device can also be used as a versatile building block to create a variety of useful analogue circuits, some of which will be investigated in the future. By substituting alternative polymer devices for CNTFET, future study will aim to further enhance DDA performance, such as improved open loop gain and PSRR.

CNT FinFETs with optimized threshold voltages can provide an EDP advantage of approximately 50 times over Si FinFETs under a low supply voltage (V dd = 0.4 V), suggesting great potential for CNT FinFET. Compared with a Si FinFET, the CNT FinFET presents obvious advantages in speed and EDP arising from its almost much larger current density but also results in a higher total power dissipation, especially at a low threshold voltage (V th = 1/3 V dd). Carbon nanotube FET DDA will be better than silicon because carbon nanotubes are almost thin ferry electricity. In principle, carbon nanotube could run three times faster while consuming about one-third of the energy of silicon. Carbon nanotube FET DDA replace silicon with their excellent electrical conductivity, and carbon nanotubes have long been seen as a potential replacement for silicon. Three main challenges are involved: material defects, manufacturing defects, and functional issues.

If carbon nanotube FinFET is compared with a Si FinFET, CNT FinFETs with optimized threshold voltages can provide an EDP advantage of approximately 50 times over Si FinFETs under a low supply voltage (V dd = 0.4 V), suggesting great potential for CNT FinFET. Compared with a Si FinFET, the CNT FinFET presents obvious advantages in speed and EDP arising from its almost much larger current density but also results in a higher total power dissipation, especially at a low threshold voltage (V th = 1/3 V dd). Carbon nanotube FET DDA was used as a versatile building block to create a variety of useful analogue circuits, some of which will be investigated in the future. Substituting alternative polymer devices for CNTFET can enhance DDA performance, such as improved open loop gain and PSRR.

Data Availability

The datasets generated during and/or analyzed during the current study are available from the corresponding author on reasonable request.

Conflicts of Interest

The authors declare that they have no conflicts of interest.

References

[1] M. J. Smith, *Application-specific integrated circuits*, Addison-Wesley, Boston, Massachusetts, 1997.

[2] P. A. G. Sankar and K. Udhayakumar, "Design and analysis of two stage operational amplifier based on emerging sub-32nm technology," in *International Conference on Advanced Nanomaterials and Emerging Engineering Technologies*, pp. 24–26, Chennai, India, 2013.

[3] F. Rahman, A. M. Zaidi, N. Anam, and A. Akter, "Performance evaluation of a 32-nm CNT-OPAMP: design, characteristic optimization and comparison with CMOS technology," in *14th International Conference on Computer and Information Technology*, pp. 22–24, Dhaka, Bangladesh, 2011.

[4] A. D. L. Plaza and P. Morlon, "Power-supply rejection in differential switched-capacitor filters," *IEEE Solid-State Circuits.*, vol. 19, no. 6, pp. 912–918, 1984.

[5] S. R. Zarabadi, F. Larsen, and M. Ismail, "A configurable op-amp/DDA CMOS amplifier architecture," *IEEE Transactions on Circuits and Systems I: Fundamental Theory and Applications*, vol. 39, no. 6, pp. 484–487, 1992.

[6] F. Balestra, S. Cristoloveanu, M. Benachir, J. Brini, and T. Elewa, "Double-gate silicon-on-insulator transistor with volume inversion: a new device with greatly enhanced performance," *IEEE Electron Device Letters*, vol. 8, no. 9, pp. 410–412, 1987.

[7] P. Crippa, G. Biagetti, C. Turchetti et al., "A high-gain CNTFET-based LNA developed using a compact design-oriented device model," *Electronics*, vol. 10, no. 22, p. 2835, 2021.

[8] M. S. Akhoon, A. G. Alharbi, M. A. Bhat, S. A. Suandi, J. Ashraf, and S. A. Loan, "Design and simulation of carbon nanotube based current source load differential amplifier," in *2021 International Conference on Microelectronics (ICM)*, pp. 140–143, New Cairo City, Egypt, 2021.

[9] M. Yasir and N. Alam, "Systematic design of CNTFET based OTA and Op amp using gm/ID technique," *Analog Integrated Circuits and Signal Processing.*, vol. 102, pp. 293–307, 2019.

[10] V. S. Bendre, A. K. Kureshi, and S. Waykole, "Design of analog signal processing applications using carbon nanotube field effect transistor-based low-power folded cascode operational amplifier," *Journal of Nanotechnology*, vol. 2018, Article ID 2301421, 15 pages, 2018.

[11] A. Bhargav, A. Srinivasulu, and D. Pal, "An operational transconductance amplifiersbased sinusoidal oscillator using CNTFETs," in *2018 International conference on Applied Electronics*, Pilsen, Czech Republic, 2018.

[12] V. Chithambaram, T. S. F. Rajesh, G. Palani, E. Ilango, B. Deepanraj, and S. Santhanakrishnan, "Growth and investigation of novel nonlinear optical single crystal of urea potassium dichromate by solution growth technique for photonic application," *Journal of Optics (India)*, vol. 49, no. 2, pp. 181–186, 2020.

[13] M. Nizamuddin, S. A. Loan, A. M. Alamoud, and A. G. Alharbi, "Design, simulation and the comparative analysis of carbon nanotube field effect transistors based multistage operational amplifiers," *Journal of Nanoelectronics and Optoelectronics*, vol. 12, no. 10, pp. 1045–1055, 2017.

[14] A. Puri and A. Rana, "Performance analysis of CNTFET based low power operational amplifier in analog circuits for biomedical applications," in *IEEE International Conference on Electronics, Computing and Communication Technologies*, pp. 1–15, Bangalore, India, 2015.

[15] S. A. Loan, M. Nizamuddin, A. R. Alamoud, and S. A. Abbasi, "Design and comparative analysis of high performance carbon nanotube-based operational transconductance amplifiers," *Nano*, vol. 10, no. 3, 2015.

[16] A. E. Islam, "Current status of reliability in extended and beyond CMOS devices," *IEEE Transactions on Device and Materials Reliability*, vol. 16, no. 4, pp. 647–666, 2016.

[17] Y. Song, H. Zhou, Q. Xu et al., "Mobility enhancement technology for scaling of CMOS devices: overview and status," *Journal of Electronic Materials*, vol. 40, no. 7, pp. 1584–1612, 2011.

[18] J. Colinge, E. Demoulin, D. Bensahel, G. Auvert, and H. Morel, "Transistors made in single-crystal SOI films," *IEEE Electron Device Letters*, vol. 4, no. 4, pp. 75–77, 1983.

[19] M. Nizamuddin, S. A. Loan, S. A. Abbasi, and A. R. M. Alamoud, "Design and simulation of high performance carbon nanotube based three stage operational amplifiers," *Materials Today: Proceedings*, vol. 3, no. 2, pp. 449–453, 2016.

[20] H. Dai, A. Javey, E. Pop, D. Mann, W. Kim, and Y. Lu, "Electrical transport properties and field effect transistors of carbon nanotubes," *Nano*, vol. 1, no. 1, pp. 1–13, 2006.

[21] R. Ho, C. Lau, G. Hills, and M. M. Shulaker, "Carbon nanotube CMOS analog circuitry," *IEEE Transactions on Nanotechnology*, vol. 18, pp. 845–848, 2019.

[22] A. Gupta, R. Mathur, and M. Nizamuddin, "Design, simulation and comparative analysis of a novel FinFET based astable multivibrator," *AEU-International Journal of Electronics and Communications*, vol. 100, pp. 163–171, 2019.

[23] S. Iijima, "Helical microtubules of graphitic carbon," *Nature*, vol. 354, no. 6348, pp. 56–58, 1991.

[24] S. J. Tans, A. R. M. Verschueren, and C. Dekker, "Room-temperature transistor based on a single carbon nanotube," *Nature*, vol. 393, no. 6680, pp. 49–52, 1998.

[25] M. Nizamuddin, S. A. Loan, A. R. Alamoud, and S. A. Abbassi, "Design, simulation and comparative analysis of CNT based cascode operational transconductance amplifiers," *IOP Nanotechnology*, vol. 26, no. 39, article 395201, 2015.

[26] M. Masud, A. A'ain, I. Khan, and N. Husin, "Design of voltage mode electronically tunable first order all pass filter in ±0.7 V 16 nm CNFET technology," *Electronics*, vol. 8, no. 1, p. 95, 2019.

[27] C. D. Matthus, S. Buhr, M. Kreißig, and F. Ellinger, "High gain and high bandwidth fully differential difference amplifier as current sense amplifier," *IEEE Transactions on Instrumentation and Measurement*, vol. 70, pp. 1–11, 2021.

[28] F. Khateb, T. Kulej, M. Kumngern, and C. Psychalinos, "A compact power-efficient 0.5 V fully differential difference amplifier," *International Journal of Electronics and Communications*, vol. 105, pp. 71–77, 2019.

[29] F. Khateb and T. Kulej, "Design and implementation of a 0.3-V differential difference amplifier," *IEEE Transactions on Circuits and Systems I: Regular Papers*, vol. 66, no. 2, pp. 513–523, 2018.

[30] M. Anand Kumar and M. Janakirani, "Comparative performance study of difference differential amplifier (DDA) using CMOS and FinFET technologies," *NeuroQuantology*, vol. 20, no. 7, pp. 770–782, 2022.

[31] M. Yasir and N. Alam, "Design of CNTFET-based CCII using gm/ID technique for low-voltage and low-power applications," *Journal of Circuits, Systems, and Computers*, vol. 29, no. 9, 2020.

Hindawi
Journal of Nanomaterials
Volume 2022, Article ID 6767941, 12 pages
https://doi.org/10.1155/2022/6767941

Research Article

Friction and Wear Response of Friction Stir Processed Cu/ZrO_2 Surface Nano-Composite

Harikishor Kumar,[1] **Rabindra Prasad**,[2] **Parshant Kumar**,[3] **and Solomon Aynalem Hailu**[4]

[1]*Department of Mechanical Engineering, MLR Institute of Technology, Hyderabad, India*
[2]*Department of Mechanical Engineering, Amity University, Gwalior, Madhya Pradesh, India*
[3]*School of Mechanical Engineering, Dr. Vishwanath Karad MIT World Peace University, Pune, India*
[4]*Department of Construction Technology and Management, University of Gondar, Ethiopia*

Correspondence should be addressed to Solomon Aynalem Hailu; solomon.ayenalem@uog.edu.et

Received 12 September 2022; Revised 20 September 2022; Accepted 27 September 2022; Published 15 October 2022

Academic Editor: Deepanraj B

The present work aims to develop Cu/ZrO_2 surface composite by friction stir processing and analyse the effect of zirconia incorporation on microstructure, mechanical, and tribological behaviour of developed copper matrix composite. Microstructural observations indicated that grains were equiaxed and fine in the stir zone of the composite and zirconia particles were uniformly dispersed in the copper matrix with excellent bonding. The test results for mechanical and wear behaviour showed increment in hardness and wear resistance as compared to copper which may be because of the effect of zirconia presence and grain refinement. The fabricated composite displayed higher value of average friction coefficient in comparison to as received copper. The worn surface observed by SEM revealed the predominance of adhesion and delamination wear mechanism in base copper.

1. Introduction

Copper has been prime material for applications in industries where electrical and thermal conductivity is a major concern [1]. This is due to satisfactory electrical and thermal conductivity, workability [2], and high oxidation and corrosion resistance [3] of copper. However, poor mechanical and wear properties limit its applications [3]. Therefore, ceramic particles are usually introduced in copper and their alloys to improve their strength and wear resistance [4–6]. Although ceramic particle reinforcement causes enhancement in mechanical and wear properties but by virtue of the occupation of hard (non-deformable) ceramic particles, metal matrix composites (MMCs) face problems in terms of loss in ductility and toughness [7]. It is observed that in various applications, only surface needs to make harden and wear resistant without disturbing the bulk configuration and structure and hence retaining the ductility and toughness [8, 9].

At present, liquid phase methods like stir casting, squeeze casting, and infiltration are being used for MMCs fabrication [9, 10]. As these are melt-based processes, temperature during processing is very high which leads to initiation of interfacial interaction between the reinforcements and the matrix and hence generation of some disturbing phases that finally hamper the performance of the composites [11, 12]. The ill effects encountered during melt-based processes may be eradicated by using solid-based processing techniques where temperature rise is not fair to be considered a threat for initiation of interfacial reactions. Recently, FSP, a variant of FSW, is in trend for manufacturing of MMCs due to its solid-state nature [13]. For example, S. Sarvankumar et al. [5] used FSP for the synthesis of Cu/AlN surface composite and investigated the effect of volume fraction on microhardness and wear behaviour. The results showed that increased volume fraction resulted in improved hardness and wear properties of the fabricated composite.

Friction stir processing is considered solid-state process as temperature rise does not melt the materials during processing and work on the same principle as friction stir welding which was first introduced by The Welding Institute (TWI) of UK in 1991 for microstructural modification [7, 14]. As mentioned earlier, its capability is not only limited to grain refinement but it has also gathered attention globally for surface/bulk composite fabrication. In the case, a given dimension plate with machined grooves/holes on the surface generally in the middle along the length with carefully packed ceramic particles is used. Then, a hard tool, generally non-consumable with distinctively developed shoulder and pin, is inserted in the plate. The material underneath the shoulder get plasticised due to heat generated due to plastic deformation and friction at the contacting point. After sufficient plasticization, it starts moving from advancing side to retreating side because of the rotational motion of the tool. Because of the synergetic effect of material flow and its mixing during the process, it becomes possible to incorporate reinforcements and hence fabricate composites [7, 15].

Particulates like AlN, SiC, TiC, and TiB_2 have been used as particulates for the manufacturing of copper matrix composites. ZrO_2 is also a ceramic material and has been used as filler in the copper matrix through various processing techniques [16–19]. It possesses high hardness, melting temperature, elastic modulus, and low adhesion friction along with very low reactivity with metals [20, 21]. As far as the available literature is concerned, there is nothing related to processing of Cu/ZrO_2 by FSP. Therefore, the present work is focused to fabricate Cu/ZrO_2 surface composite via FSP and to investigate the associated microstructure, hardness, and dry sliding wear behaviour.

2. Materials and Method

2.1. Manufacturing of the Composite. A plate of dimension 150 x100 x 6 mm^3 was considered for the present investigation. The chemical composition of the copper was as follows: elements (Wt.%) P: 0.0003, As: 0.0005, Sb: 0.0004, Te: 0.0002, and remaining copper. To fill the powder of the reinforcement, a groove of dimension 1.5 mm wide and 3.5 mm deep with rectangular cross-section was machined on the surface of the plate. To maintain the accuracy, CNC end mill cutter was utilised for machining of grooves. Grooves were in the centre of the plate along the length.

The grooves were fully packed with zirconia powder. To ensure it was fully packed, multiple times, plates were lightly hit in the side region of the plate. Before processing, groove opening was closed by a tool having no pin so that during processing, loss of powder can be minimised.

Then, it was processed for the composite fabrication with the equivalent tool which had pin.

The tool material was super alloy IN718 in peak aged form [22]. The tool shoulder was 18 mm in diameter. For smooth flow of material during processing, cylindrical pin contour with thread was used. Keeping plate and groove dimensions in mind, the length and diameter of pin were kept 6 mm and 4 mm, respectively. The entire fabrication was carried out on a modified vertical milling machine. After rigorous trials and exhaustive literature survey, the processing parameters were decided which were kept constant for the entire experimentations. The processing parameters were as follows: 920 RPM, 40 mm/min, and 2.5°, rotational speed, bed movement, and tilt angle, respectively.

A schematic of the experimental steps is presented in Figure 1.

2.2. Sample Extraction and Characterisation. Figure 2 depicts schematically how specimens were extracted for characterisation.

For microstructure characterisation, specimens were machined perpendicular to the length of the processed plate. The machined specimens were ground and polished carefully as per standard metallographic practice. An etchant with composition 10 g chromic acid, 1 g sodium sulphate, 0.85 ml hydrochloric acid, and 50 ml distilled water was prepared. The polished specimens were etched and detected beneath optical microscopy for microstructural features. The microstructural features were also observed under scanning electron microscope (SEM) (ZEISS EVO 18 RESEARCH, 20KV) but with un-etched samples. The polished samples were also analysed by electron back scattered diffraction (EBSD) analysis. The samples were electro-polished in a solution prepared by phosphoric acid and methanol at -12°C and 11 V. To observe the hardness at the various sections of the processed plate, Vickers microhardness tester was used. The processed plates were machined by 1 mm from the top for hardness indentation and indented cross-sectionally. Between every indentation, a gap of 0.5 mm was maintained. 300 gram load was used for 10 seconds during indentation for all the specimens. The chemical analysis of the plate before experimentation and after investigation was done by X-ray diffraction technique.

Friction coefficients and wear properties of plates before investigation and after experimentation were evaluated by a pin on disk tribometer at room temperature. Cylindrical specimens of size 4 mm in diameter and 30 mm in length were machined from the centre of SZ of the fabricated composite. A hardened steel which was in disc form, used as counter face. The EN-32 steel used had hardness of 65 HRC. Before experimentation, specimens were polished with various grades of emery papers. To ensure the maximum conformity, disc was also polished with surface grinder. The test parameters were kept constant during the experimentations. A normal load of 20 N and velocity of 1 m/s were maintained for all the specimens. The sliding distance (1000 m) was also kept constant for all the specimens. The friction coefficients of the specimens were determined by the machine automatically. Wear rate of the specimens was calculated by cumulative weight loss method. Before the commencement of test, samples were weighted. After the test for 100 m of sliding distance, again it was weighted. This was repeated ten times so that 1000 m of sliding distance could be completed. Then, the cumulative weight loss was plotted on the vertical axis and distance on horizontal axis to calculate wear rate. The wear out surfaces post-test was

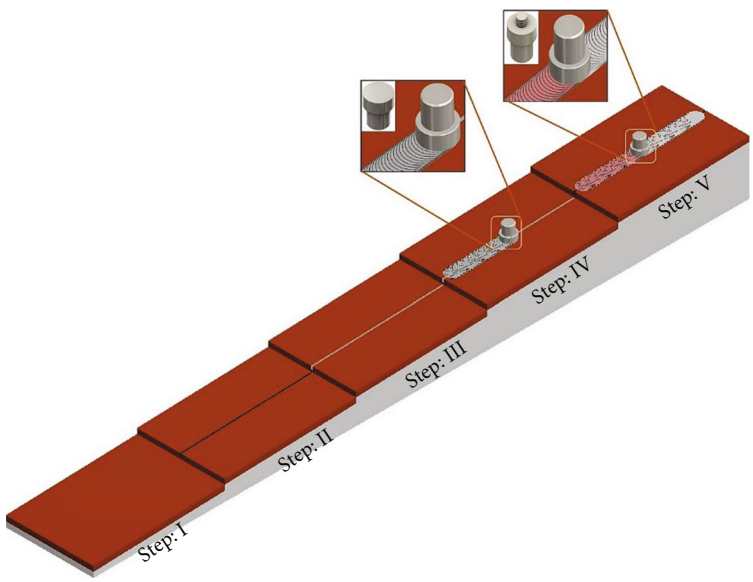

Figure 1: Illustrative view of the process (a) plate without groove. (b) Plate with groove. (c) Plate filled with powder. (d) Groove closing. (e) Final processed plate.

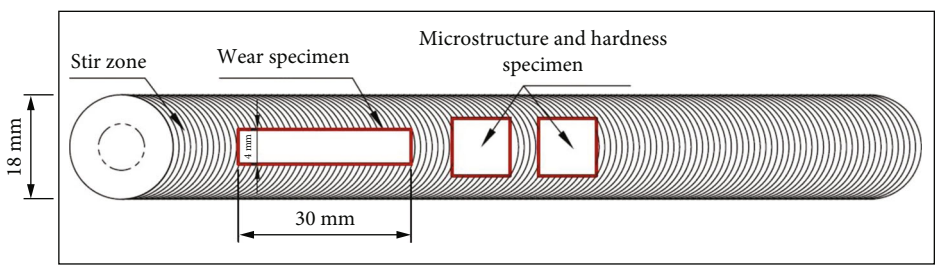

Figure 2: Diagrammatic view for specimens extraction from the plate.

detected by SEM for confirmation of wear mechanism involved. The size of the reinforced zirconia and matrix before and after processing was measured by Image J software.

3. Results and Discussion

3.1. Surface Appearance. Figure 3 displays the macroscopic top view of the fabricated Cu/ZrO_2 surface composite.

The macrograph resembles the typical ring-like patterns which is the characteristic of FSP. There are no defects like depressions or discontinuities visible on the surface of processed plate. Ring-like patterns without defects obviously justify the effectiveness of the chosen process parameters for the experimentation. Such type of surface appearance in the case of FSPed plate is required for defect-free SZ. Defects on the surface of processed plates accompany corresponding defects in the SZ of the composite. Frictional heat generated due to relative motion between tool shoulder and workpiece soften copper and at elevated temperature and copper suffered severe plastic deformation. The severely plastically deformed copper moves from one side of the tool pin to other side of the tool pin which is also known as advancing and retreating side, respectively. The simultaneous movement of materials in translation and rotation led to formation of ring-type pattern on the processed plate.

3.2. Macrostructure. The cross-sectional macrostructure of fabricated Cu/ZrO_2 surface composite is depicted in Figure 4.

The SZ region in which particles have been incorporated is quite clearly visible from the macrograph. It can be observed that the groove machined for particle compaction has completely disappeared from the copper plate which indicates that the composite formation process has been completed and material flow during composite fabrication was continuous. The figure also indicates that defects like tunnels and worm holes are not there. The macroscopic image shows that SZ is free from the irregularities.

The absence of defects in macrostructure may be because of ample flow of plasticised copper from one side of the pin to other, leads grooves to crash and mixed the filled zirconia with plasticised copper and eventually resulted into defect free SZ of FSPed Cu/ZrO_2 surface composite. The macrostructure of SZ of the composite is alike basin. That means the shape is not uniform. Its width is larger at the top and lesser at the bottom. This is believed to be varied nature of material flow during FSP. The tool being varied shape and size at different positions affects materials differently during

Figure 3: Surface appearance of fabricated Cu/ZrO_2 surface composite.

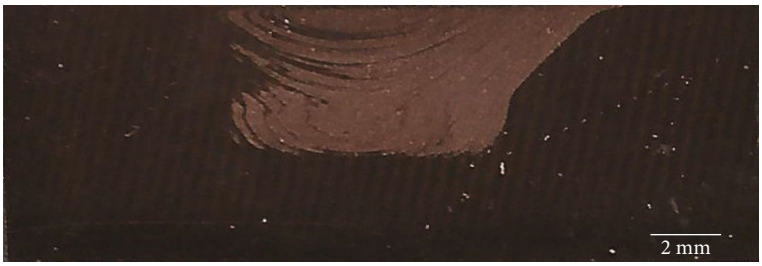

Figure 4: Cross-sectional macrostructure of fabricated Cu/ZrO_2 surface composite.

processing. The top material is affected by shoulder having larger diameter and the bottom by pin with lesser diameter and hence width changes from top to bottom.

3.3. Microstructure. Figure 5 presents SEM image of zirconia particles and corresponding size distribution.

The average particle size of zirconia was estimated to be 1.21 μm. The particles are small in size having smooth surfaces with no sharp corners.

Figure 6 depicts optical image of SZ of the composite at various area.

The microstructural features of the fabricated composite can be separated into two distinct zones (Figure 6(f)) comprising SZ and base metal (BM).

SZ is the region characterised by an exceedingly deformed structure with fine grains and evenly sputtered particles (Figures 6(b)–6(e)). Figure 6(f) shows the interface between SZ and BM. Thermally mechanically affected zone (TMAZ) and heat affected zone (HAZ) are not visible in the micrograph (Figure 6(f)). TMAZ is the region developed adjacent to SZ and is characterised by a highly deformed structure. TMAZ also gone through heat and deformation during FSP but owing to inadequate strain rate, recrystallization could not complete in this region. However, in the case of heat-affected zone (HAZ), plastic deformation did not occur during FSP, but due to annealing, grain growth is favoured. The obscene of TMAZ and HAZ in the present investigation may be thought of due to more heat flow along the depth of the plate in comparison to side of the plate. The heat flow/dissipation is favoured with high thermal conductivity of the materials. As in the present case, the backing plate used was copper and hence it might have promoted more heat dissipation along the depth of the plate in comparison to transverse section of the plate. Onion rings were not visible in the composite (Figures 6(b)–6(e)). M. Sabbagian et al. [23] observed onion rings in the fabrication of Cu/TiC composite through FSP. The reason for the same they have given was different temperature and flow nature of material moving and coming together from the shoulder to pin zone at the bottom.

Electron back scattered diffraction technique was utilised for grain structure analysis. The outcome of the analysis, i.e., IPF and grain boundaries map, is represented in Figure 7.

The effect of FSP and zirconia incorporation on grain structure of the composite is visible from the micrograph. The structural feature of grain for base copper was coarse and elongated (Figure 7(a)). Before processing, the size of grain was estimated to be 107.4 μm for base copper. The size of grain for the composite changed drastically and reduced up to nano-scale. The grain size reduction in the SZ of the fabricated composite may be because of pinning effect of reinforced zirconia particles which curb the grain growth by covering grain boundaries sliding. Moreover, heat and extremely high deformation due to tool movement promoted dynamic recrystallization which creates new nucleating sites and resulted in grain reduction.

Figures 8(a)–8(c) represent the SEM image for the composite captured at varied magnifications.

The whole SZ is comprised of zirconia particles. The zirconia particles are reasonably apart from each other.

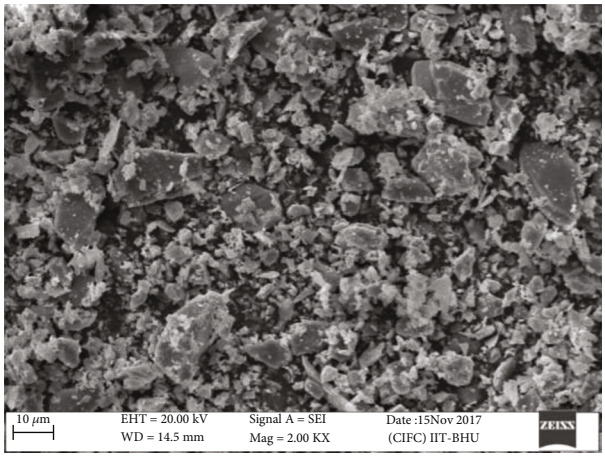

(a)

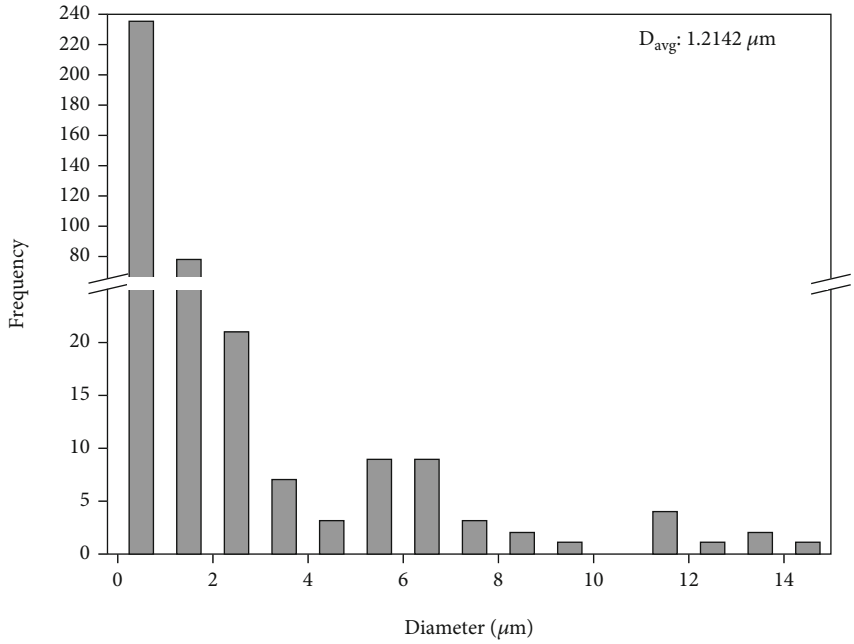

(b)

Figure 5: (a) SEM image of the particles. (b) Size distribution.

Particle-free zones are not visible in the micrographs. Hence, safely it may be assumed that sputtering of reinforcements was fairly even in SZ. This was due to the fact that high stirring rate of tool mixed the compacted zirconia and heavily deformed copper together and led to uniform dispersion of ZrO_2. Contrary to this, some results have been reported in which un-even scattering of reinforcements in the matrix was reported due to no-suitable variables chosen during processing [13, 24]. The variation in zirconia particle dispersion in SZ was not observed (Figures 8(a)–8(c)). It might have been because of non-melting feature of the process.

The reinforced zirconia particles could not move freely due to high viscosity of plasticised copper matrix. Figure 8(c) depicts SEM image of the composite captured at high magnification. The interface of zirconia and copper is continuous without any interruption. Tiny size and continuous surface of reinforcement (Figure 5(a)) allowed smooth flow of plasticised copper all over the zirconia particles. There was no appreciable change in morphology of the reinforcement during processing (Figures 5(a) and 8(c)). Literatures are available which shows appreciable changes in the morphology of the reinforcement before and after processing. [24–26]. During FSP, materials experience high strain rates owing to frictional heating and high rotational speed of the tool. Ceramic reinforcements are having brittle nature so they cannot store potential energy like metals and hence whenever experience force gets fractured directly.

Zirconia did not break in the present investigation which may be due to the following reasons. Firstly, due to tiny size, they could not provide much resistance to the flowing copper matrix.

Secondly, due to the absence of sharp edges in the reinforced zirconia, stress concentration did not happen. Lastly,

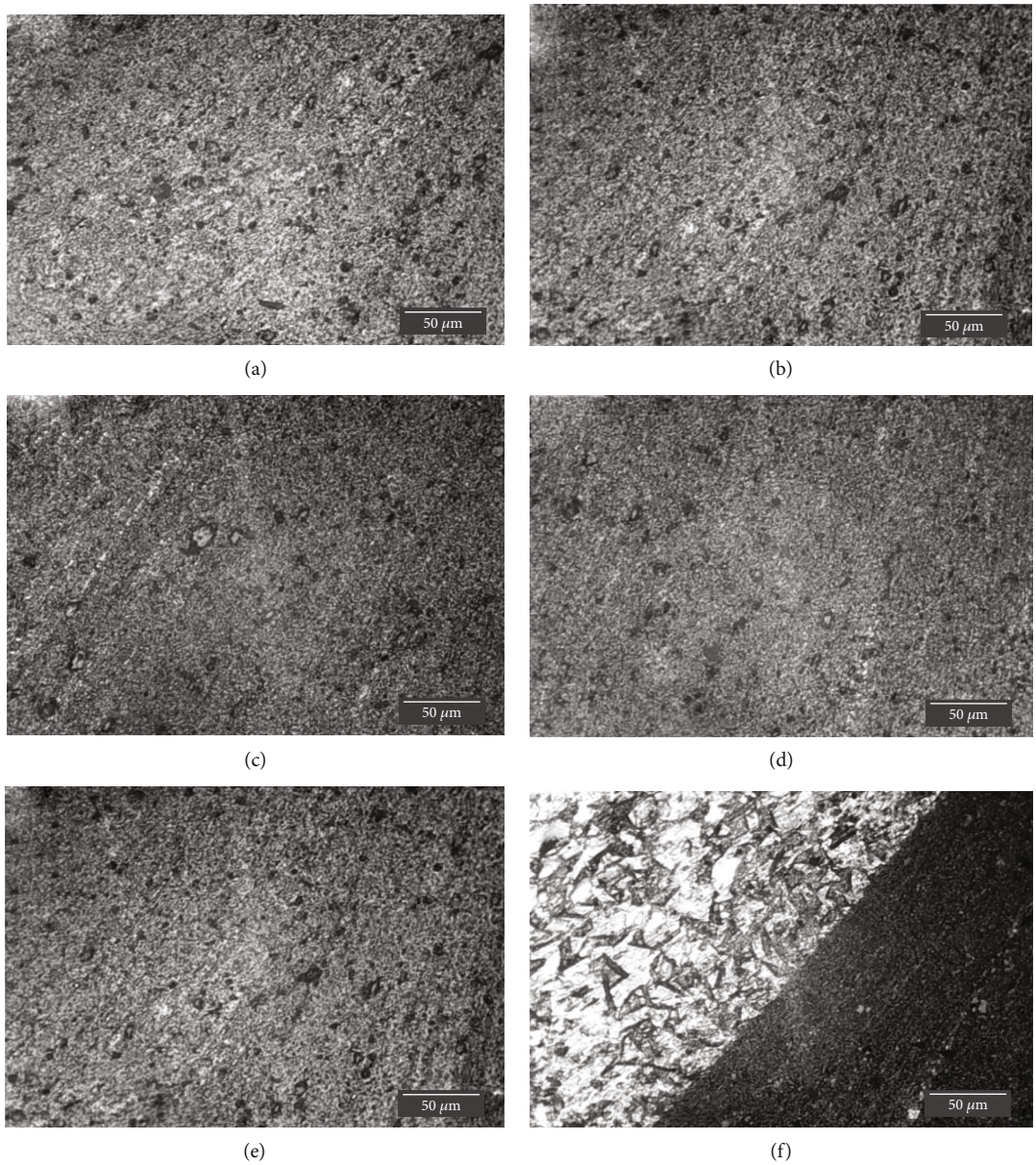

Figure 6: Optical micrograph at various locations within SZ of the composite (a) towards advancing side at the top, (b) towards retreating side on the top, (c) at the centre towards advancing side, (d) at the centre towards retreating side, and (e) towards advancing side at the bottom (f) interface.

the surface of the reinforced zirconia particulates was smooth, so plasticised copper matrix flowed smoothly without any hindrance.

3.4. Chemical Composition. The X-ray diffraction peaks (Figure 9) of the fabricated Cu/ZrO_2 surface composite displayed only copper and zirconia peaks.

No other peaks related to discernible reactional products were detected in the pattern. It clearly shows that no zirconia particle/copper matrix confluence reactions occurred during processing. Temperature rise during FSW is affected by process parameters especially the ratio of tool RPM to bed movement. In the present case, the selected parameters were sufficient for fairly even scattering of particulates.

The highest temperature reported during FSP of copper that could reach with such parameters has been reported to be 0.8 T_m of copper [27] which was not adequate for initiation of reaction between copper and zirconia. Further, low reactivity of zirconia with metals and short exposure duration during FSP may be another reason behind the denial of in-situ products in the composite.

3.5. Microhardness. The hardness distribution of the fabricated Cu/ZrO_2 composite is illustrated in Figure 10.

The average hardness of base copper was estimated to be 64 ± 2.7 HV whereas it was 116 ± 4.6 HV for the composite. The side region of the plate has lower hardness than the processed one. This may be because of the higher heat input

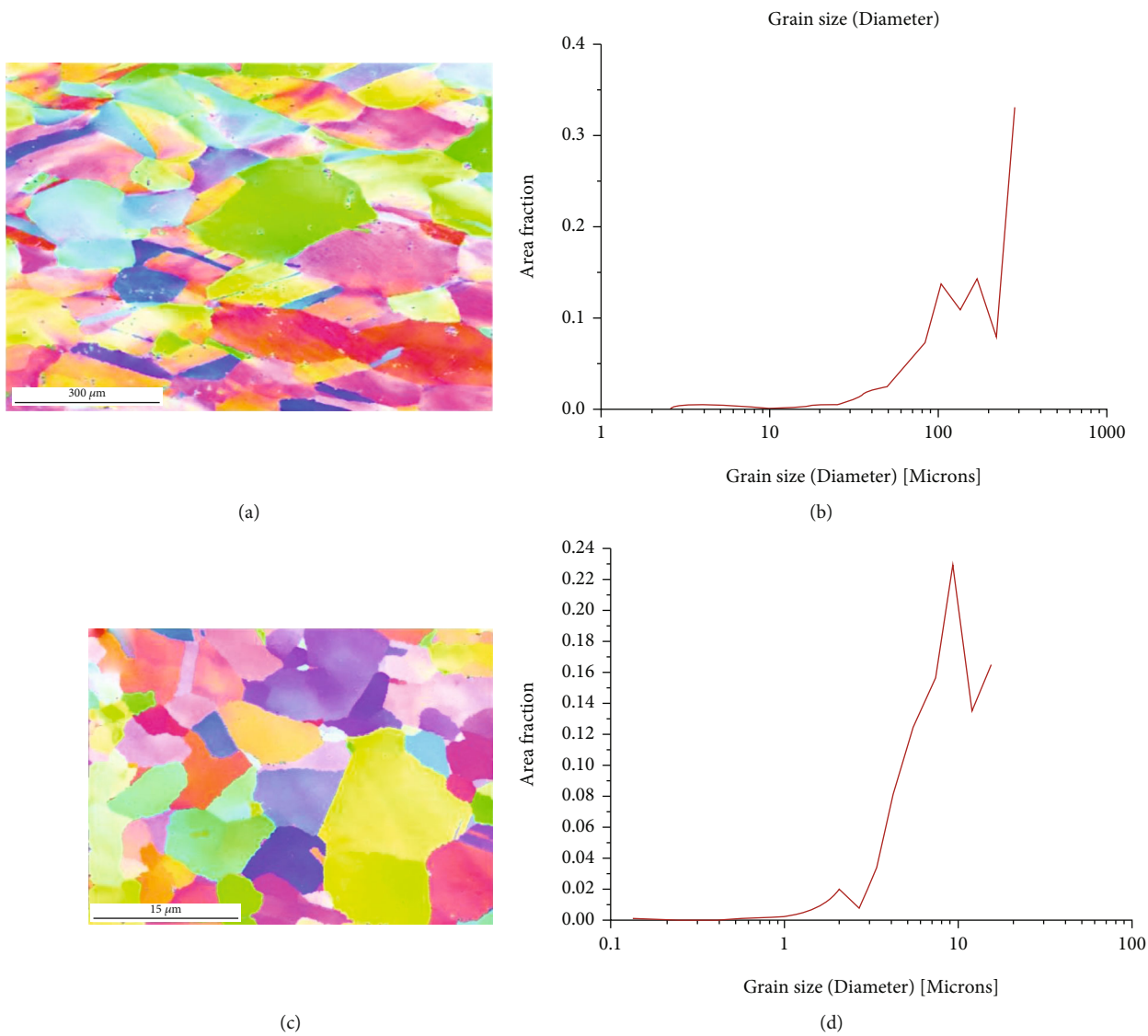

Figure 7: EBSD image of (a) base copper and (c) composite and (b) and (d) grain size.

in the region which reduces dislocation density and compressive residual stress. The improved hardness of the composite may be thought of because of the presence of hard zirconia particles. Being a hard phase, it not only increased the hardness but also impede the grain growth and hence reduction in grain size which further contributed in increased hardness.

As per the Hall-Petch relation, grain size is inversely proportional to hardness. Additionally, generated dislocations due to thermal mismatch between copper and zirconia also contributed to enhancement in hardness by hindering the motion of dislocations [28]. Moreover, the Orowan mechanism may also be responsible for higher hardness [29]. As reported by this mechanism, zirconia particles acted as a barrier to dislocation movement and hence causing improvement in hardness.

3.6. Tribological Behaviour. Figure 11 depicts the plot for friction coefficient V/S time graph.

From the figure, it is obvious that the average value of friction coefficient in the case composite is slightly more in comparison to un-processed copper. Also, the fluctuation is more for the composite compared to base copper.

As mentioned earlier, incorporation of zirconia in copper matrix and grain refinement due to FSP caused enhancement in hardness of the composites significantly. The increased hardness improved the abrasion resistance of the composite. Hence, we can say that the presence of zirconia led to gain in sliding resistance; therefore, the average value of friction coefficient elevated for the composite. The thin tribolo-layer pounded on the surface of specimens and counter disc because of deprecation of wear debris reduced the fluctuation in friction coefficient for base copper. However, this development of tribolo-layer was not favoured in the case of the composites because of the presence of hard zirconia particles which abraded the layer.

Figure 12 shows the results of wear test.

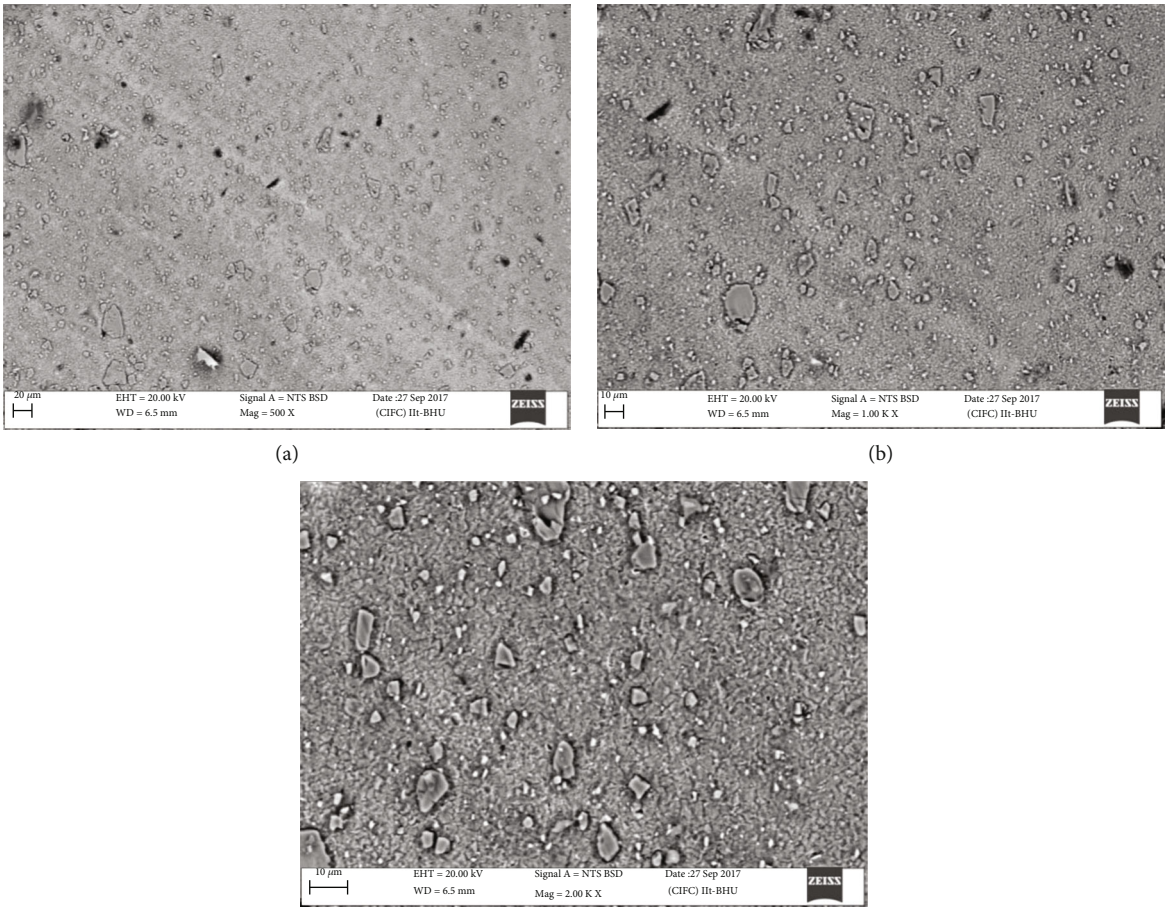

Figure 8: SEM image for composite at varied magnifications within SZ.

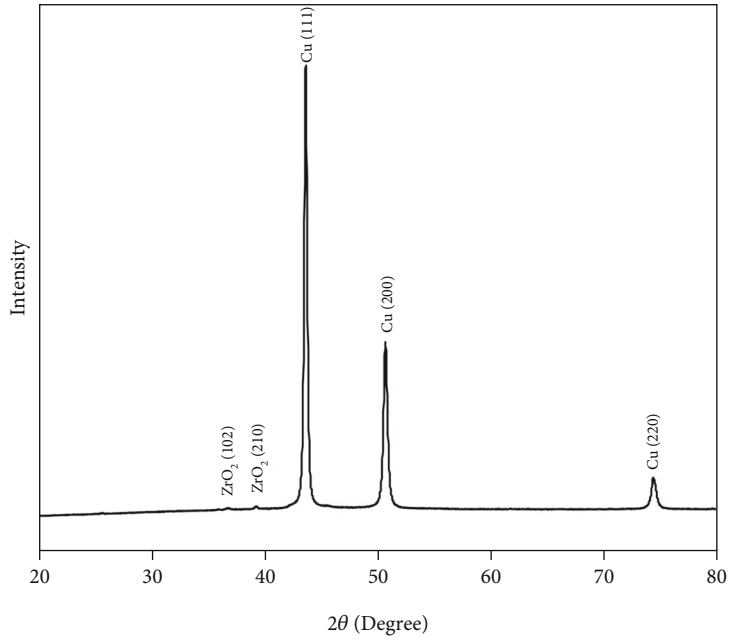

Figure 9: XRD pattern of the fabricated composite.

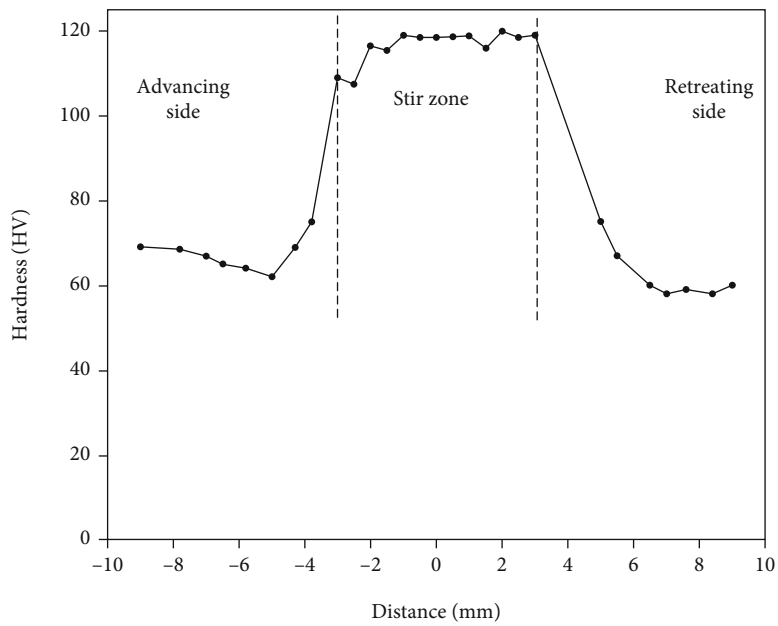

Figure 10: Microhardness distributions across cross-section of SZ of Cu/ZrO_2 composite.

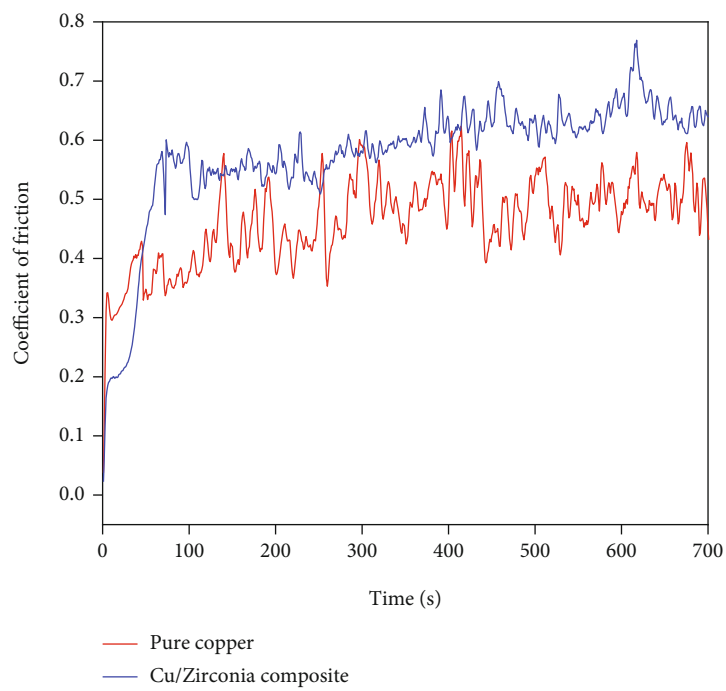

Figure 11: Friction coefficient V/S time plot for base copper and composite.

It can be observed that the weight loss in the case of the fabricated composite (Cu/ZrO_2) is less in comparison of as received copper. It is also worthy to note that as the distance of sliding is increasing, the weight loss for the composite is increasing almost linearly. However, this is not the case with matrix. Figures 13(a) and 13(b) present SEM image of wear out surfaces for base copper and composite, respectively.

It can be seen from the micrographs that adhesion is dominant in the case of base copper in comparison to the fabricated composite. Delamination and grooves due to ploughing effect are quite clearly visible in the micrograph (Figure 13(a)). Due to the dominance of adhesion, delamination pits formed in as received copper which caused relentless material eviction from copper surface. However, the presence of hard zirconia particles in fabricated composite enervated the outcome of adhesion. That's why the loss due to adhesion was less in the case of composite. Further, due to higher hardness of the composite as compared to as

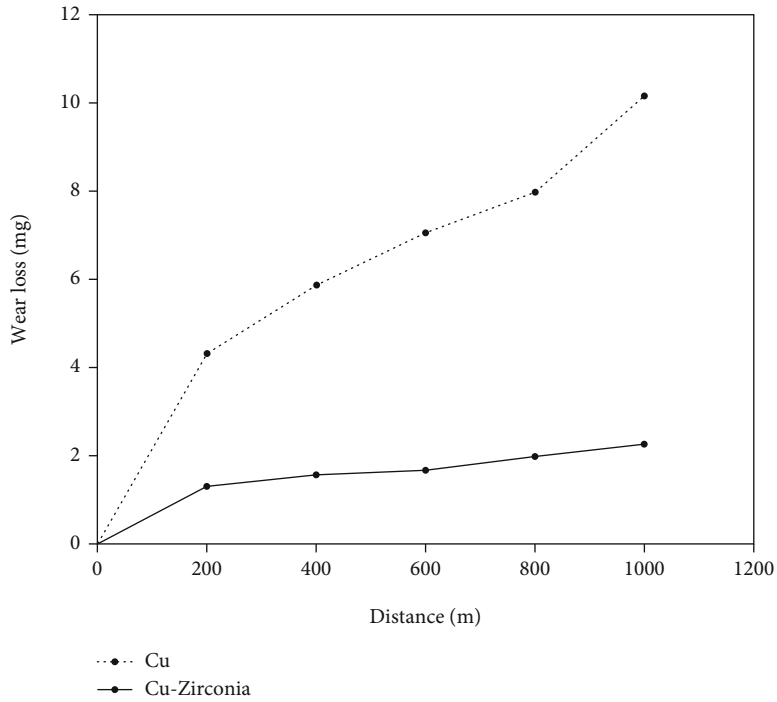

Figure 12: Wear test results for as received copper and composite.

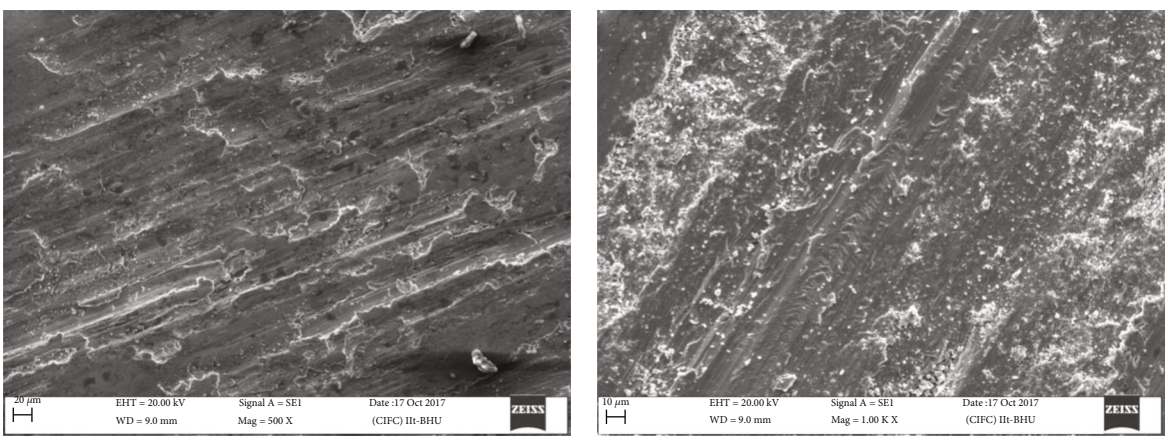

(a) (b)

Figure 13: SEM image of the surfaces after wear tests of (a) base copper and (b) composite.

received composite, resistance towards abrasive wear was also higher. The elevated value of abrasion resistance farther reduces the wear loss of the composite.

4. Conclusions

In this work, copper-ZrO2 composite was manufactured via FSP. Also, the effect of ZrO_2 reinforcement on microstructure, mechanical, and wear behaviour was adjudged. Outcomes of the investigation are summarised below:

(i) The dispersion of zirconia particles was fairly even with no obvious defects. The grain structure in the case of composite was fine comparatively

(ii) The size and shape of the particulate have not changed during processing. Also, there is no interruption at the interface of the composite which shows excellent bonding between copper and zirconia

(iii) The hardness for the composite was observed more in comparison to base copper. Also, the hardness value in vicinity of processed section was found less than that of base copper

(iv) The value of friction coefficient was more for the composite with respect to base copper

(v) Wear loss for the composite was less in comparison to copper

Data Availability

The datasets generated during and/or analysed during the current study are available from the corresponding author on reasonable request.

Conflicts of Interest

The authors declare that they have no conflicts of interest.

Acknowledgments

The authors wish to extend their sincere gratitude to OIM and texture lab, IIT-Bombay for their support for EBSD. We would also like to thank CIF, IIT (BHU), Varanasi for their support for optical microscopy, scanning electron microscopy, and X-ray diffraction.

References

[1] G. E. Dieter and D. J. Bacon, *Mechanical Metallurgy*, McGraw-hill New York, 1986.

[2] M. Barmouz, P. Asadi, M. B. Givi, and M. Taherishargh, "Investigation of mechanical properties of Cu/SiC composite fabricated by FSP: effect of SiC particles' size and volume fraction," *Materials Science and Engineering: A*, vol. 528, no. 3, pp. 1740–1749, 2011.

[3] A. Sanaty-Zadeh, "Comparison between current models for the strength of particulate-reinforced metal matrix nanocomposites with emphasis on consideration of Hall-Petch effect," *Materials Science and Engineering: A*, vol. 531, pp. 112–118, 2012.

[4] T. Thankachan and K. S. Prakash, "Microstructural, mechanical and tribological behavior of aluminum nitride reinforced copper surface composites fabricated through friction stir processing route," *Materials Science and Engineering: A*, vol. 688, pp. 301–308, 2017.

[5] V. Chithambaram, T. S. F. Rajesh, G. Palani, E. Ilango, B. Deepanraj, and S. Santhanakrishnan, "Growth and investigation of novel nonlinear optical single crystal of urea potassium dichromate by solution growth technique for photonic application," *Journal of Optics*, vol. 49, no. 2, pp. 181–186, 2020.

[6] C. Zou, Z. Chen, H. Kang et al., "Study of enhanced dry sliding wear behavior and mechanical properties of Cu- TiB_2 composites fabricated by in situ casting process," *Wear*, vol. 392-393, pp. 118–125, 2017.

[7] R. S. Mishra, Z. Ma, and I. Charit, "Friction stir processing: a novel technique for fabrication of surface composite," *Materials Science and Engineering: A*, vol. 341, no. 1-2, pp. 307–310, 2003.

[8] Y. Meng, Y. Shen, C. Chen, Y. Li, and X. Feng, "Microstructures and formation mechanism of W-Cu composite coatings on copper substrate prepared by mechanical alloying method," *Applied Surface Science*, vol. 282, pp. 757–764, 2013.

[9] H. Maharana and A. Basu, "Surface-mechanical and oxidation behavior of electro-co-deposited Cu- Y_2O_3 composite coating," *Surface and Coatings Technology*, vol. 304, pp. 348–358, 2016.

[10] J. Hashim, L. Looney, and M. Hashmi, "Metal matrix composites: production by the stir casting method," *Journal of Materials Processing Technology*, vol. 92-93, pp. 1–7, 1999.

[11] J. Qu, H. Xu, Z. Feng, D. A. Frederick, L. An, and H. Heinrich, "Improving the tribological characteristics of aluminum 6061 alloy by surface compositing with sub-micro-size ceramic particles via friction stir processing," *Wear*, vol. 271, no. 9-10, pp. 1940–1945, 2011.

[12] E. Mahmoud, M. Takahashi, T. Shibayanagi, and K. Ikeuchi, "Effect of friction stir processing tool probe on fabrication of SiC particle reinforced composite on aluminium surface," *Science and Technology of Welding and Joining*, vol. 14, no. 5, pp. 413–425, 2009.

[13] S. Shanmugan, N. Saravanan, V. Chithambaram, B. Deepanraj, and G. Palani, "Investigation on single crystal by tartaric acid–barium chloride: growth and characterization of novel NLO materials," *Bulletin of Materials Science*, vol. 43, no. 1, p. 202, 2020.

[14] R. S. Mishra and Z. Ma, "Friction stir welding and processing," *Materials science and engineering: R: reports*, vol. 50, no. 1-2, pp. 1–78, 2005.

[15] T. Peat, A. Galloway, T. Marrocco, and N. Iqbal, "*Microstructural evaluation of cold spray deposited WC with subsequent friction stir processing*," in *Friction Stir Welding and Processing VIII*, pp. 207–216, Springer, 2015.

[16] J. Gao, J. Zheng, Q.-Y. Li, and C.-K. Hou, "Nano zirconia reinforced Cu-matrix composites," *Heat Treatment of Metals(-China)*, vol. 31, no. 1, pp. 40–42, 2006.

[17] J. Ding, N. Zhao, C. Shi, X. Du, and J. Li, "In situ formation of Cu-ZrO_2 composites by chemical routes," *Journal of Alloys and Compounds*, vol. 425, no. 1-2, pp. 390–394, 2006.

[18] A. Lebedev, S. Pulnev, Y. A. Burenkov, V. Vetrov, V. Kopylov, and O. Vylegzhanin, "Thermal stability of submicrocrystalline copper and Cu: ZrO {sub 2} composite," *Scripta Materialia*, vol. 35, no. 9, 1996.

[19] B. R. Kang, J. K. Yoon, K. T. Hong, and I. J. Shon, "Mechanical properties and rapid low-temperature consolidation of nanocrystalline Cu-ZrO2 composites by pulsed current activated heating," *Metals and Materials International*, vol. 21, no. 4, pp. 698–703, 2015.

[20] B. Deepanraj, L. A. Raman, N. Senthilkumar, and J. Shivasankar, "Investigation and optimization of machining parameters influence on surface roughness in turning AISI 4340 steel," *FME Transactions*, vol. 48, no. 2, pp. 383–390, 2020.

[21] M. Khaloobagheri, B. Janipour, and N. Askari, "Electrical and mechanical properties of Cu matrix nanocomposites reinforced with yttria-stabilized zirconia particles fabricated by powder metallurgy," *Advances in Materials Research*, vol. 829, pp. 610–615, 2013.

[22] D. Pradhan, G. S. Mahobia, K. Chattopadhyay, and V. Singh, "Effect of surface roughness on corrosion behavior of the superalloy IN718 in simulated marine environment," *Journal of Alloys and Compounds*, vol. 740, pp. 250–263, 2018.

[23] M. Sabbaghian, M. Shamanian, H. Akramifard, and M. Esmailzadeh, "Effect of friction stir processing on the microstructure and mechanical properties of Cu-TiC composite," *Ceramics International*, vol. 40, no. 8, pp. 12969–12976, 2014.

[24] V. Sharma, U. Prakash, and B. M. Kumar, "Surface composites by friction stir processing: a review," *Journal of Materials Processing Technology*, vol. 224, pp. 117–134, 2015.

[25] O. S. Salih, H. Ou, W. Sun, and D. G. McCartney, "A review of friction stir welding of aluminium matrix composites," *Materials & Design*, vol. 86, pp. 61–71, 2015.

[26] M.-N. Avettand-Fènoël and A. Simar, "A review about Friction Stir Welding of metal matrix composites," *Materials Characterization*, vol. 120, pp. 1–17, 2016.

[27] I. Dinaharan, K. Kalaiselvan, E. Akinlabi, and J. P. Davim, "Microstructure and wear characterization of rice husk ash reinforced copper matrix composites prepared using friction stir processing," *Journal of Alloys and Compounds*, vol. 718, pp. 150–160, 2017.

[28] R. Bauri, D. Yadav, and G. Suhas, "Effect of friction stir processing (FSP) on microstructure and properties of Al-TiC in situ composite," *Materials Science and Engineering: A*, vol. 528, no. 13-14, pp. 4732–4739, 2011.

[29] P. Asadi, M. B. Givi, K. Abrinia, M. Taherishargh, and R. Salekrostam, "Effects of SiC particle size and process parameters on the microstructure and hardness of AZ91/SiC composite layer fabricated by FSP," *Journal of Materials Engineering and Performance*, vol. 20, no. 9, pp. 1554–1562, 2011.

Hindawi
Journal of Nanomaterials
Volume 2022, Article ID 4934926, 8 pages
https://doi.org/10.1155/2022/4934926

Research Article

Optimization of Dual Coating Using Electroless Ni-P-Nano-TiO_2 and Plasma Yttria-Stabilized Zirconia on Piston Crown and Cylinder Liner in CI Engine

V. S. Shaisundaram,[1] V. Balambica,[2] D. Sendil Kumar,[3] S. Nithish,[2] M. Chandrasekaran,[4] Mohanraj Shanmugam,[5] and Dabala Misgana Likassa[6]

[1]*Department of Automobile Engineering, Vels Institute of Science Technology and Advanced Studies, 600117, India*
[2]*Department of Mechanical Engineering, Bharath Institute of Higher Education and Research, 600073, India*
[3]*Senthil College of Education, 605110, India*
[4]*Department of Mechanical Engineering, Vels Institute of Science Technology and Advanced Studies, 600117, India*
[5]*Department of Materials Engineering and Nanotechnlogy, Politechnico di Milano, Milan, Italy 20133*
[6]*College of Engineering and Technology, Wollega University, Nekemte, Ethiopia*

Correspondence should be addressed to Dabala Misgana Likassa; dabalam@wollegauniversity.edu.et

Received 29 August 2022; Revised 25 September 2022; Accepted 27 September 2022; Published 13 October 2022

Academic Editor: Deepanraj B

Most of the automobile engine components are made up of cast iron because of its low cost, damping characteristics, castability, and commercial considerations. In modern days, the blended biodiesels are introduced into the CI engine to reduce the usage of petroleum fuels. The following problems are identified in utilizing the biodiesels, they are lower efficiency, power, wear in the engine cylinder and piston crowns, more emission from the exhaust, and performance. To overcome the wear problem in cylinder liner and piston crown, the dual coating is developed using electroless coating and plasma spray coating, and this deposit acts as a thermal barrier to the engine. The electroless Ni-P-TiO_2 composite coating process parameters are optimized using the Taguchi technique with multiresponse grey relational analysis. The plasma spray coating is developed over electroless Ni-P coating using Yttria-stabilized Zirconia for the total thickness of 2 mm. The coated components are installed in the CI engine for further testing and analysis. The morphology of the coated surfaces is tested using the scanning electron microscope. The optimization process used to improve the Ni-P coating thickness, surface roughness, and thermal resistance of the engine components. Also, the performance and emissions in the engine are reduced significantly. The emission from the CI engine such as NOx, COx, and HC are reduced significantly. The emissions of CI engine such as NOx, CO_2, CO, and HC of the noncoated engine shows higher, and EPSCE engine condition shows less pollution. The percentage of improvement in terms of emissions are 27%, 70%, 6.4%, and 21%, respectively. The performance is improved to 3% and 27.8%, respectively, for specific fuel consumption and brake thermal efficiency.

1. Introduction

Once the automotive engines are discovered, the efficiency of human beings has increased significantly. Friction is the key parameter to influence the performance of the IC engines. Piston ring and cylinder liner are considered as the most important parameters because it takes up to 50% energy loss due to friction. In terms of consumption of fuel, 1/3 of the produced energy from the fuel was consumed by friction. Due to the gradual depletion of fossil fuels, biodiesel are deliberated as the best substitute for petroleum-based fuels [1]. The common way to produce biodiesels by traditional chemical reactions called transesterification from vegetable oils and animal fats. Biodiesel are more suitable for house hold applications, and same amount of power can be developed. In the pursuit of performance and emission, biodiesel

shows superior characheristics than petroleum fuel [2]. Thus, many academician and scientist are focused to reduce the friction and wear of engine components, through it the fuel consumption and energy can be enhanced. Even with so many positive things and high consumption rate throughout the world, some challenges need to be faced to use the biodiesel in any applications. Biodiesel have oxidation instability delinquent which results in promoting the acidic nature of the fuel and cause corrosion over the engine cylinder liner and piston. Through corrosion, the free particles evolved and increased the rate of wear and friction inside the engine cylinder [3]. The prospective method to increase the wear, friction, and corrosion resistance of the components such as piston ring and cylinder liner materials is protective surface coatings. There are many surface coating techniques that have been utilized for the past five decades to improve the tribological properties. Among them, the coating of automotive components using electroless Ni-P coating has been widely used because of its high corrosion and wear resistance, high hardness of the deposits, and irregular shape can be coated easily; no electricity is utilized during the process etc. [4]. Another method to improve the wear resistance is plasma spraying; the Yttria-stabilized Zirconia (YSZ) is commercially the applied material composition to enchance the wear resistance [5].

Selvam et al. performed coating on piston ring, and reported that the BTE and fuel consumption is improved. When compared to uncoated piston, the plasma spray coated piston reduce the HC and CO emissions. The NOx is inceased however it can be reduced by varying the different parameters of the CI engine [6]. Similarly, Powell et al. [7] reported that the emission and performance of the HCCI engine are improved significantly after the YSZ coating on cylinder liner and piston head of the engine. The YSZ coating on the components of the engine not only improve the performance and emission charchteristics but also increase the wear and friction behaviour of the engine [8]. The use of biodiesel in CI engine is reported as highly corrosive in nature and affect the materials in the engine cylinder. The existence of H_2O and O in the biofuel stimulating the evolution of corrosive chemical reactions [9]. To enchance the corrosion resistance of the material, electroless Ni-P deposited are incorporated. On the other hand, the electroless coating on engine cylinder liner and piston head are never done before. So the optimization of process parameters is required to choose the best parameters to obtain the required thickness. Taguchi technique is a robust design to optimize the process parameters of any system with minimum number of experimental trials. It reduces both the time, money, and resources of the system. The L9 orthogonal array is used to optimize the single objective functions [10]. The grey analysis is used to solve the multiobjective system using Taguchi technique in many industrial applications. The hybrid Taguchi-grey-AHP method is employed by Hoang and Pham [11] to optimize the parameters in casting process and reported the best optimized condition obtained with high level of accuracy. The variable parameters in the electroless coating to obtain the high quality deposits are nickel source, reducing agent, complexing agent, stabilizing agent, wetting agent, and percentage of hydrogen. Among these variables, the highly influencing factor to control and improve the quality of the deposits is the percentage of hydrogen, wetting agent, and stabilizer according to the survey [12–16].

In this research work, the biodiesel powered CI engine piston head and cylinder liner are dual coated with Ni-P and YSZ using electroless and plasma spraying techniques, respectively. The process parameters of the electroless coating with multiresponse objectives are optimized using Taguchi-grey approach. The factors selected for optimization are pH of the electrolyte, stabilizer in the bath, and surfactant concentration in the solution. The variable responses are thickness of the deposit, thermal resistance of the coated material, and surface roughness of the deposit. The optimized combination obtained from the optimization is verified by confirmation test. Based on the obtained results, the performance characteristics such as break thermal efficiency, specific fuel consumption, and emission characteristics such as carbon monoxide, oxides of nitrogen, hydrocarbon, and carbon dioxide are measured and reported.

2. Experimental Details and Procedure

2.1. Engine Experimental Setup. Kirloskar CI engine model Tv1 is used in this study; it can generate the power of 5.2 kW at 1500 rpm. The engine output shaft is coupled with eddy current dynamometer for applying the load from the engine. Figure 1 shows the experimental setup. It is a single cylinder four stroke engine having a bore diameter and stroke length of 87.5 and 110 mm, respectively, and the compression ratio of 17.5 : 1. The schematic diagram of the engine is provided in our previous study [17]. AVL Digas 444 and AVL437 are used to determine the emission and temperature from the engine. The performance characteristics and combustion properties are investigated in a 5 HP direct injection CI engine. The consumption of fuel and air was measured using mass flow sensor and burette technique, respectively. Eddy current dynamometer is used to apply the variable load on the engine. The IC engine soft software is used to read and write the data from the experiment. AIR-REX HG540, 4Gas analyzer is engaged to detect the various emissions such as HC, CO, CO_2, NO_X, etc.

2.2. Preparation of Biodiesel Blends and Plasma Spray Coating. The total quantity of each sample is fixed to the blend of 1000 ml in which 700 ml of diesel, 300 ml of Momordica charantia seed biodiesel, and 45 PPM of cerium oxide are added into biodiesel. The properties of diesel and prepared biodiesel are given in Table 1.

Yttria-stabilized Zirconia is chosen as the primary material for coating the piston crown because of its desirable physical properties such as high coefficient of low thermal conductivity, high Poisson's ratio, thermal expansion, and stable phase structure at higher temperature conditions. A composition of the coating powder is Yttria-stabilized Zirconia 94%, alumina 2%, and Ceria 4%.

Figure 1: Experimental setup.

2.3. Electroless Ni-P-TiO_2 Coating on Cylinder Liner and Piston Head. The cylinder liner and piston head is used to coat electroless Ni-P deposit for various conditions. Initial weight of the substrate is weighed using digital weighing machine with 1 mg accuracy. The chemical required for preparing the electrolyte is purchased from Sigma Aldrich scientific grade 99% purity. The nano titanium dioxide is also purchased with the size of 50 nm size. The salts obtained are nickel chloride as a source of nickel, sodium hypophosphite as reducing agent, sodium chloride as complexing agent, and tri sodium citrate as stabilizer. To regulate the pH during the process, ammonium chloride is added and adjusted the value as needed. Prior to coating, substrate must be cleaned using acetone and ethonal, and surface must be prepared using concentrated sulfuric acid. The coated surface of the component is shown in Figure 2. The nickel, phosphorus, and titanium dioxide particles are seen in the image.

2.4. Optimization of Process Parameters. The selected responses are optimized using Taguchi and GRA theory because traditional Taguchi cannot handle multiobjective function. During the experiment, variable parameters are identified and controlled to reduce the errors in the system that reflect as noise factor. In the year 1982, Ju-long introduced a theory called GRA created with the aid of grey set by connecting the ideas with numerous philosophy such as control, space, and system theory [18]. Taguchi Grey relational analysis is a globally recognized methodology to optimize the multiobjective response system in voluminous of the industrial applications predominantly in the area of engine performance analysis and research [19–21]. Based on the knowledge obtained from the literature review, the factors selected are pH, stabilizer, and surfactant. Table 2 shows the factors and its levels for optimization, and based on Taguchi design, the L9 orthagonal array is shown in Table 3. The orthogonal arrays are generated, and Taguchi techniques are analysed using Minitab software.

2.4.1. Calculation of Signal to Noise Ratio. According to the responses, signal to noise ratio can be calculated in three ways; they are maximize, nominal the better, and minimize. In this research work, larger the better condition is used for brake thermal efficiency; smaller the better is used for emissions (NOx and CO), and brake specific fuel consumption are selected to find the values of S/N ratio using the following Equations (1) and (2), respectively.

$$x_k^o(i) = -10\log_{10}\left(\frac{1}{n}\sum_{k=1}^{n}\frac{1}{y_k^2(i)}\right), \quad (1)$$

$$x_k^o(i) = -10\log_{10}\left(\frac{1}{n}\sum_{k=1}^{n}y_k^2(i)\right), \quad (2)$$

where n is the no. of trials; $Y_k(i)$ is the obtained data of variable (i) from the trails (k).

2.4.2. Normalizing the Obtained Data. Next step is to normalize the obtained value from S/N ratio to acquire the dimensionless value, and it is needed to integrate the values into one value, and comparison is simple. The normalization can be performed using the Equations (3) and (4).

$$x_k^*(i) = \frac{x_k^o(i) - \min\ x_k^o(i)}{\max\ x_k^o(i) - \min\ x_k^o(i)}, \quad (3)$$

$$x_k^*(i) = \frac{\max\ x_k^o(i) - x_k^o(i)}{\max\ x_k^o(i) - \min\ x_k^o(i)}, \quad (4)$$

where max $x_k^o(i)$ and min $x_k^o(i)$ are the maximum and minimum responses of i in L9 experiment.

2.4.3. Calculate Grey Relational Coefficient. GRC helps to express the association among normalized value with the ideal value, and the same is given in Equation (5).

$$\gamma_k(i) = \frac{\Delta_{\min} + \zeta\Delta_{\max}}{\Delta_k(i) + \zeta\Delta_{\max}}, \quad (5)$$

where ζ is the distinguishing coefficient of range 0-1 (0.5 prefered); $\Delta_k(i)$ is the difference of normalized value and reference sequence for ith response; Δ max is the maximum value of $\Delta\_k(i)$, respectively; Δ min is the minimum value of $\Delta\_k(i)$, respectively.

$$\Delta_k(i) = |x_o^*(i) - x_k^*(i)|, \quad (6)$$

where $x_o^*(i)$ is the maximum value of $x_i^*(k)$.

2.4.4. Calculate Grey Relational Grade. Grey relational grade can be calculated by taking the mean value of grey relational coefficient and add the value with the value of weight decided for all the response variables. The simple equation for calculating GRG is given in Equation (7).

$$\delta_k = \sum_{i=1}^{h} w_i\,\gamma_k(i). \quad (7)$$

2.5. Plasma Coating over Optimized Electroless Ni-P Deposit. A polishing of substrate is done on the piston and cylinder liner before the plasma thermal spray coating. The substrate prepared for coating are blasted with known composition of powder materials (YSZ 94%, alumina 2%, and Ceria 4%) for the interlocking for sprayed particles [17]. The parameters

Table 1: Fuel properties.

Fuel property	Instrument	Diesel	Biodiesel
Density at 15°C (kg/m3)	Hydrometer	836	910
Viscosity at 40°C (mm2/s)	Rotational viscometer	2.9	5.04
Calorific value (MJ/kg)	Bomb calorimeter	42.3	72.15
Flashpoint (°C)	Flashpoint apparatus	54	224
Fire point (°C)	Pour point apparatus	62	229

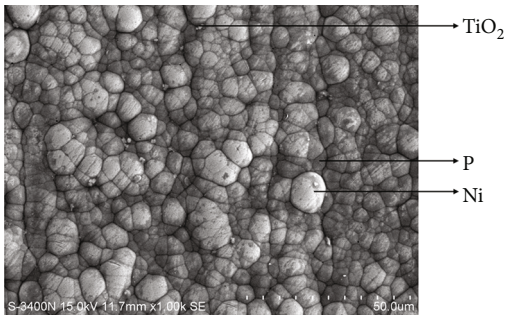

Figure 2: Coated surface of the engine component using electroless Ni-P coating.

Table 2: Factors and its level for optimization.

Description	Factors	Levels		
		1	2	3
A	pH (%)	5	7	9
B	Stabilizer (g/L)	20	25	30
C	Surfactant (g/L)	1	1.2	1.4

Table 3: Taguchi L9 orthagonal array.

S. no	pH (%)	Stabilizer (g/L)	Surfactant (g/L)
1	5	20	1
2	5	25	1.2
3	5	30	1.4
4	7	20	1.2
5	7	25	1.4
6	7	30	1
7	9	20	1.4
8	9	25	1
9	9	30	1.2

adopted for performing the coating on engine components are the following: applied voltage is 65-70 V; maximum power is 40; primary gas flow -Ar (SCfh) is 80; secondary gas flow -H_2(SCfh) is 15; spraying distance is 2. The yttrium-stabilized zirconium is coated for 2 mm in each sample after electroless Ni-P coating process.

2.6. Measurement of Coating Thickness, Thermal Resistance, and Surface Roughness. The coating thickness (T) of the deposit is measured as per the standard using weight gain method, and it is given in Equation (8). Initial and final value of the substrate is measured using weighing machine for five times, and average is taken as the final reading.

$$T = \frac{(S_2 - S_1) \times 10^4}{dA}, \tag{8}$$

where S is the initial and final reading of the substrate in g; d is the density of the substrate in g/cm^3; A is the area of the substrate in cm^2. The portable surface roughness tester connected with computer to record the evaluation profile (model SJ-210) is used for analysis. A probe is made to move through a straight line for the known distance. The peak and valleys of the substrate are detected and recorded in the storage device. Then, the average surface roughness of the substrate is determined by digital computer. The thermal conductivity of the coated component is measured using laser flash method (LFA427 and NETZSCH). The experiment is conducted at vacuum environment from room temperature to 1150 degree Celsius. The average of three readings from the evaluation is taken as thermal conductity.

3. Results and Discussions

3.1. Optimization of Electroless Ni-P Coating. The experiments are conducted in electroless Ni-P coating setup by varying the process parameters and obtained the responses such as thickness, thermal resistance, and surface roughness of the substrate as given in Table 4. From the obtained responses, the values of S/N ratio are obtained from Equations (1) and (2). The conditions selected are smaller the better and larger the better. The values are normalized using Equations (3) and (4) to stabilize the values for comparison. Now, the value of 0.5 is multiplied to each data obtained, which means providing equal weightage to all the obtained values. Table 5 shows the S/N ratio and the normalization value of each experiment. From the normalization data, grey relational coefficient is developed. The numerical values of normalization value after conversion and the GRC are given in Table 6.

In the next step, the GRC values of each experiment are incorporated with the weights assigned to each responses, and then GRG value is estimated. The GRG and the rank of each experiments are finalized, and it is given in Table 7. It is observed from the results that based on GRG rank the optimized combination is pH of 9, stabilizer of 25 g/L, and surfactant of 1 g/L. The optimized trail is denoted by A3-B2-C1.

Table 4: Responses value for DOE based on orthogonal array.

S. no	pH (%)	Stabilizer (g/L)	Surfactant (g/L)	Thickness (μm)	Thermal resistance (K/W)	Surface roughness (μm)
1	5	20	1	22	13.4	0.26
2	5	25	1.2	24	13.6	0.28
3	5	30	1.4	26	13.5	0.3
4	7	20	1.2	35	14.3	0.38
5	7	25	1.4	34	14.7	0.35
6	7	30	1	36	14.5	0.3
7	9	20	1.4	42	15	0.46
8	9	25	1	41	15.5	0.45
9	9	30	1.2	40	15.3	0.43

Table 5: Signal to noise ratio and normalization values of the experiment.

	S/N ratio			Normalization	
Thickness	Thermal resistance	Surface roughness	Thickness	Thermal resistance	Surface roughness
26.848	22.542	11.700	0.000	0.000	-1.000
27.604	22.670	11.056	0.135	0.102	-0.870
28.299	22.606	10.457	0.258	0.051	-0.749
30.881	23.106	8.404	0.718	0.447	-0.335
30.629	23.346	9.118	0.673	0.636	-0.479
31.126	23.227	10.457	0.762	0.542	-0.749
32.464	23.521	6.744	1.000	0.775	0.000
32.255	23.806	6.935	0.963	1.000	-0.039
32.041	23.693	7.330	0.925	0.911	-0.118

Table 6: Calculating the grey relational coefficient.

Converting normalized value into Δklm			Calculating Grey relational coefficient Gklm		
Thickness	Thermal resistance	Surface roughness	Thickness	Thermal resistance	Surface roughness
1.000	1.000	2.000	0.333	0.333	0.200
0.865	0.898	1.870	0.366	0.358	0.211
0.742	0.949	1.749	0.403	0.345	0.222
0.282	0.553	1.335	0.639	0.475	0.272
0.327	0.364	1.479	0.605	0.579	0.253
0.238	0.458	1.749	0.677	0.522	0.222
0.000	0.225	1.000	1.000	0.689	0.333
0.037	0.000	1.039	0.931	1.000	0.325
0.075	0.089	1.118	0.869	0.849	0.309

3.2. Confirmation Test. The confirmation test is mandatory to check the accuracy of data obtained through Taguchi optimization techniques. From Table 7, grey relational grade values are needed to predict the GRG, and it is calculated using Equation (9).

$$\delta_{pre} = \delta_{tot} + \sum_{i=1}^{n} \left(\delta_{opt} - \delta_{tot}\right), \tag{9}$$

where δ_{tot} is the total mean of GRG. δ_{opt} is the mean of GRG at the optimum level.

From the above equation, the predicted GRG value is obtained as 0.315. Table 8 depicts the values generated from confirmation test using the best combination. Based on the results, it is clearly understood that GRG is improved from 0.259 to 0.27, i.e., improvement 4.24%.

3.3. Engine Performance in Optimized Condition. The performance of engine is compared with noncoated engine (NCE), electroless coated engine (ECE), and optimised condition; electroless plasma spray coated engine (EPSCE) are shown in Figure 3. The optimised condition shows the significant improvement in performance of the CI engine.

Table 7: Calculation of GRG and GRG rank.

Thickness	Weight Thermal resistance	Surface roughness	GRG	GRG rank
0.100	0.133	0.060	0.098	9
0.110	0.143	0.063	0.105	8
0.121	0.138	0.067	0.109	7
0.192	0.190	0.082	0.154	6
0.181	0.231	0.076	0.163	4
0.203	0.209	0.067	0.160	5
0.300	0.276	0.100	0.225	3
0.279	0.400	0.097	0.259	1
0.261	0.339	0.093	0.231	2

Table 8: Confirmation test.

Setting level	Initial setting	Prediction	Experimental	Improvement %
A	41	—	42	
B	15.5	—	15.75	
C	0.45	—	0.4	
GRG	0.259	0.315	0.27	4.24

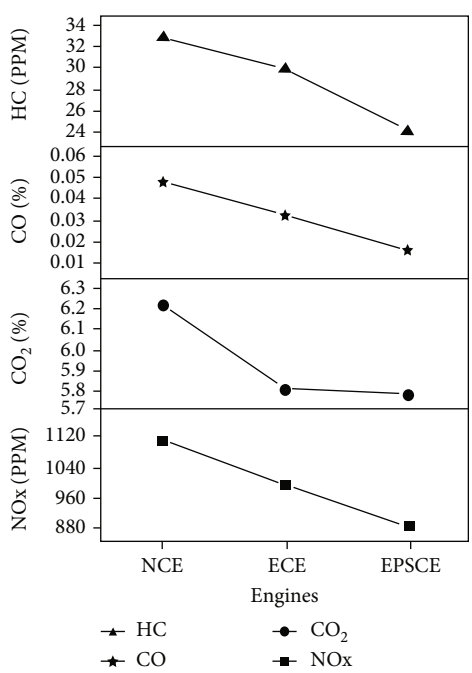

Figure 3: The performance of various categories of CI engines.

The emissions of CI engine such as NOx, CO_2, CO, and HC of the noncoated engine show higher among other conditions, whereas the EPSCE condition produces very less pollution when compared to other conditions. The main reason is that the coating provides the insulation effect on the walls of combustion chamber, thus, the combustion temperature increases gradually. Therefore, the emissions in the coated engine reduced by improving the combustion, and the intake oxygen is utilized effectively. Hence, the CO emission is reduced [22].

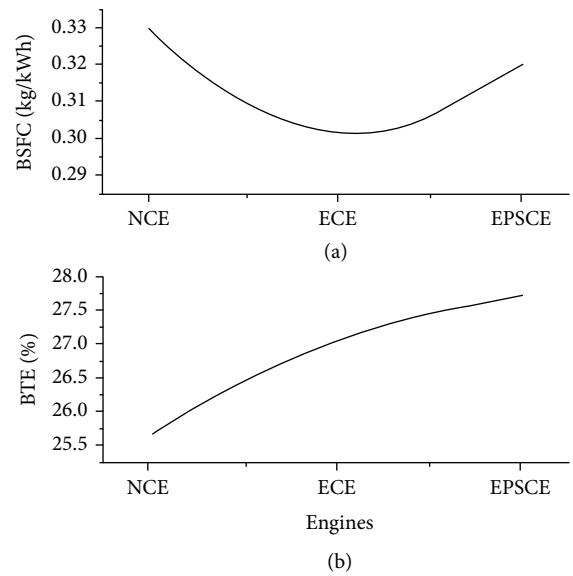

Figure 4: The efficiency of CI engines, (a) specific fuel consumption; (b) brake thermal efficiency.

The performance of the CI engine is improved; owing to the combustion, chamber wall heat transfer is reduced. Due to this effect, the incylinder temperature is increased and produce more temperature and pressure to the combustion. Thereby, the mean effective pressure is increased which leads to improve in high power and torque of the CI engine [23]. Figure 4 shows the brake thermal efficiency and specific fuel consumption of CI engine.

The possible reason for obtaining the improved efficiency of the CI engine is alumina inclusion in yittria-stabilized zirconia in plasma coating. Also, nickel coating has good wear resistance of the material and improve the oxidation and thermal resistance of the engine components, where the coatings are made. When the alumina is coated alone, it does not show superior results but when the alumina is added with yittria-stabilized zirconia, the performance and efficiency of the engine is significantly improved.

4. Conclusions

The CI engine is coated with zirconia using plasma spray technique, and Ni-P coating using electroless plating is prepared, and fuel is added with nanoadditives. Based on the research carried out using the experimental setup, the following conclusions are derived.

(i) based on GRG rank, the optimized combination is pH of 9, stabilizer of 25 g/L, and surfactant of 1 g/L. The optimized trail is denoted by A3-B2-C1.

The GRG value is improved from 0.259 to 0.27, i.e., 4.24% improved

(ii) the performance of engine is compared with non-coated engine (NCE), electroless coated engine (ECE), and optimised condition, i.e., electroless plasma spray coated engine (EPSCE).

(iii) the emissions of CI engine such as NOx, CO_2, CO, and HC of the noncoated engine shows higher and EPSCE engine condition shows less pollution. The percentage of improvement interms of emissions are 27%, 70%, 6.4%, and 21%, respectively

(iv) the performance of the CI engine, i.e., specific fuel consumption and brake thermal efficiency is improved to 3% and 27.8%, respectively

Three diverse engines are selected to study the performance and emissions in the CI engine. The life of the engine components is improved by the thermal barrier coating incorporated in the CI engine. The hybrid vehicle is the future of transportation by the integration of electric and commercial engines. Therefore, the biodiesel can be used efficiently to reduce the emissions through engine modifications.

Data Availability

The datasets generated during and/or analysed during the current study are available from the corresponding author on reasonable request.

Conflicts of Interest

The authors declare that they have no conflicts of interest.

References

[1] Y. Xu, Q. Zheng, J. Geng et al., "Synergistic effects of electroless piston ring coatings and nano-additives in oil on the friction and wear of a piston ring/cylinder liner pair," *Wear*, vol. 422-423, pp. 201–211, 2019.

[2] G. R. Srinivasan, V. Shankar, C. Sreekanth et al., "Influence of fatty acid composition on process optimization and characteristics assessment of biodiesel produced from waste animal fat," *Energy Sources, Part A: Recovery, Utilization, and Environmental Effects*, vol. 42, 2020.

[3] M. Manzoor, A. Hussain, Q. A. Ahmad et al., "Biodiesel quality assessment of microalgae cultivated mixotrophically on sugarcane bagasse," *Sustainable Energy Technologies and Assessments*, vol. 53, article 102359, 2022.

[4] R. Muraliraja and R. Elansezhian, "Effect of zwitterionic surfactant on tribological behaviour of electroless plating," *Surface Engineering*, vol. 30, no. 10, pp. 752–757, 2014.

[5] P. Lawrence, P. Koshy Mathews, and B. Deepanraj, "Experimental investigation on zirconia coated high compression spark ignition engine with ethanol as fuel," *Journal of Scientific and Industrial Research*, vol. 70, pp. 789–794, 2011.

[6] M. Selvam, S. Shanmugan, and S. Palani, "Performance analysis of IC engine with ceramic-coated piston," *Environmental Science and Pollution Research*, vol. 25, no. 35, pp. 35210–35220, 2018.

[7] T. Powell, R. O'Donnell, M. Hoffman, and Z. Filipi, "Impact of a yttria-stabilized zirconia thermal barrier coating on HCCI engine combustion, emissions, and efficiency," *Journal of Engineering for Gas Turbines and Power*, vol. 139, no. 11, 2017.

[8] J. F. Li, H. Liao, X. Y. Wang et al., "Improvement in wear resistance of plasma sprayed yttria stabilized zirconia coating using nanostructured powder," *Tribology International*, vol. 37, no. 1, pp. 77–84, 2004.

[9] A. T. Hoang, M. Tabatabaei, and M. Aghbashlo, "A review of the effect of biodiesel on the corrosion behavior of metals/alloys in diesel engines," *Energy Sources, Part A: Recovery, Utilization, and Environmental Effects*, vol. 42, no. 23, pp. 2923–2943, 2020.

[10] R. Muraliraja and R. Elansezhian, "Influence of nickel recovery efficiency on crystallinity and microhardness of electroless Ni–P coatings and optimisation using Taguchi technique," *Transactions of the IMF*, vol. 93, no. 3, pp. 126–132, 2015.

[11] A. T. Hoang and V. V. Pham, "2-methylfuran (MF) as a potential biofuel: a thorough review on the production pathway from biomass, combustion progress, and application in engines," *Renewable and Sustainable Energy Reviews*, vol. 148, article 111265, 2021.

[12] A. Hung, "Effects of thiourea and guanidine hydrochloride on electroless copper plating," *Journal of the Electrochemical Society*, vol. 132, no. 5, p. 1047, 1985.

[13] J. Sudagar, J. Lian, and W. Sha, "Electroless nickel, alloy, composite and nano coatings - a critical review," *Journal of Alloys and Compounds*, vol. 571, pp. 183–204, 2013.

[14] R. Sharma, R. C. Agarwala, and V. Agarwala, "Development of copper coatings on ceramic powder by electroless technique," *Applied Surface Science*, vol. 252, no. 24, pp. 8487–8493, 2006.

[15] A. T. Hoang, M. Tabatabaei, M. Aghbashlo et al., "Rice bran oil-based biodiesel as a promising renewable fuel alternative to petrodiesel: a review," *Renewable and Sustainable Energy Reviews*, vol. 135, article 110204, 2021.

[16] B. Bhav Singh and M. Balasubramanian, "Processing and properties of copper-coated carbon fibre reinforced aluminium alloy composites," *Journal of Materials Processing Technology*, vol. 209, no. 4, pp. 2104–2110, 2009.

[17] A. Ashok, S. K. Gugulothu, R. V. Reddy, A. E. Gurel, and B. Deepanraj, "Prediction-optimization of the influence of 1-pentanol/jatropha oil blends on RCCI engine characteristics using multi-objective response surface methodology," *Renewable Energy Focus*, vol. 42, pp. 8–23, 2022.

[18] D. Ju-long, "Control problems of grey systems," *Systems & Control Letters*, vol. 1, no. 5, pp. 288–294, 1982.

[19] G. Pohit and D. Misra, "Optimization of performance and emission characteristics of diesel engine with biodiesel using grey-taguchi method," *Journal of Engineering*, vol. 2013, Article ID 915357, 8 pages, 2013.

[20] A. Karnwal, M. M. Hasan, N. Kumar, A. N. Siddiquee, and Z. A. Khan, "Multi-response optimization of diesel engine performance parameters using thumba biodiesel-diesel blends by applying the Taguchi method and grey relational analysis," *International Journal of Automotive Technology*, vol. 12, no. 4, pp. 599–610, 2011.

[21] S. D. Jadhav and M. S. Tandale, "Multi-objective performance optimization of compression ignition engine operated on Mangifera Indica biodiesel by applying Taguchi Grey relational analysis," *Waste and Biomass Valorization*, vol. 7, no. 5, pp. 1309–1325, 2016.

[22] S. P. Jena, S. K. Acharya, H. C. Das, P. P. Patnaik, and S. Bajpai, "Investigation of the effect of $FeCl_3$ on combustion and emission of diesel engine with thermal barrier coating," *Sustainable Environment Research*, vol. 28, no. 2, pp. 72–78, 2018.

[23] H. Aydin, "Combined effects of thermal barrier coating and blending with diesel fuel on usability of vegetable oils in diesel engines," *Applied Thermal Engineering*, vol. 51, no. 1-2, pp. 623–629, 2013.

Hindawi
Journal of Nanomaterials
Volume 2022, Article ID 4056551, 15 pages
https://doi.org/10.1155/2022/4056551

Research Article

Characterization Analysis of Silver Nanoparticles Synthesized from *Chaetoceros calcitrans*

R. Anith Jose,[1] **D. Devina Merin**,[2] **T. S. Arulananth**,[3] **and Nagaraju Shaik**[4]

[1]*Department of Electronics and Communication Engineering, Ponjesly College of Engineering, Nagercoil, Kanyakumari District, India*
[2]*Department of Biotechnology, Udaya School of Engineering, Vellamodi, Kanyakumari District, India*
[3]*Department of Electronics and Communication Engineering, MLR Institute of Technology, 500043, Hyderabad, Telangana, India*
[4]*College of Engineering and Technology, Wollega University, Nekemte, Ethiopia*

Correspondence should be addressed to Nagaraju Shaik; sknagaraju@wollegauniversity.edu.et

Received 6 August 2022; Revised 22 August 2022; Accepted 29 August 2022; Published 22 September 2022

Academic Editor: Deepanraj B

The marine microalgae *Chaetoceros calcitrans* were used in the synthesis of silver or argentum nanoparticles. The reduction of silver nitrate to silver nanoparticles is observed in marine microalgae. The silver nanoparticles have a good imperative role in technological fields. The synthesis of silver nanoparticles from marine microalgae is a green nanotechnological method. The silver nanoparticle characterization is then carried out. The presence of silver nanoparticles is confirmed by UV-Vis spectroscopy. Fourier transform infrared spectroscopy, atomic force microscopy, photoluminescence, and X-ray diffractometry were used for the characterization analysis of synthesized silver nanoparticles. The research on the antimicrobial activity of silver nanoparticles is made to analyze the antagonistic nature against pathogenic organisms.

1. Introduction

Nanotechnology is a contemporary technology where it allows the engineering of materials by altering their sizes, and this has increased the application of nanomaterial in vast areas. The optical properties and thermal and physicochemical properties exhibited by nanomaterials are unusual. The reduction of the size of particles from bulk material to nanosized particles leads to pronounced modifications in the physical properties of the particular material. Reduction in imperfections, spatial confinement, and an increase in surface energy are the characteristics that lead to varied physical properties of nanomaterial [1]. The application of nanomaterials, when combined with other substances, can be increased in manufacturing devices which reduce pollution and also in the production of alternate energy [2].

Biological methods employed the microorganism or the plant extract in the synthesis of nanoparticles, which is a simple and nontoxic method [3]. Before the introduction of the biological method, the synthesis of nanomaterials involves the use of noxious chemicals and some hazardous by-products produced as well. Hence, the search for a new biological method is made, and the term "green nanotechnology" is coined. The "green" method of particle synthesis is highly demanding [2]. The size, shape, and equal distribution of nanoparticles in a solution are affected by thermal energy [4]. The nanomaterials can be used as coatings and as intercalation material during the manufacture of electrical batteries [5] and also used as optical receptors [6]. Nanomaterials can be used as catalysts [7]. These vast applications made researchers turn to the biological method of nanoparticle synthesis [8]. The antimicrobial activities exhibited by metal nanoparticles are high against pathogenic organisms [9]. Nanocrystallites are produced from magnetotactic bacteria [10]. The diatoms or the algae are proven to synthesize nanomaterials [11]. The green technology of synthesizing silver nanoparticles evolved from these observations and inferences. The silver nanomaterial produced by marine

microalgae is green nanotechnology. Silver nanoparticles are broadly used in the nanotechnology field in various applications [12].

2. Materials and Methods

2.1. Parameters Monitored and Controlled in Algal Growth. The devices used for the culturing of algae are usually built with Pyrex or Corning glasses. The algal culture absorbs the inorganic carbon and converts it into organic matter by the photosynthesis mechanism. The source used in the photosynthesis mechanism is light energy, and it drives the full mechanism. The intensity of light has an imperative role in the growth of the culture. The light intensity is low in the algal culture when the density of algae is increased and also in depth, where the light penetration is very low. Eighteen hours of illumination is provided for the culture grown on a laboratory scale. Fluorescent lamps are used for illumination in laboratory-scale algal culture, and for a large scale, culture done in tanks got illuminated by sunlight.

Temperature is the next parameter which has an influence on the growth of algae. The temperature of 20°C to 27°C is maintained in laboratories. The pH of the culture is one of the important parameters to be monitored and controlled. The optimum pH for algal culture is 8.1 to 8.8, but it can tolerate a pH of 7 to 9.1. When a slight variation is there in pH, complete disturbance happens in the culture and everything gets collapsed. Hence, great care is taken to maintain the pH of culture.

The sedimentation of culture that happens during algal culture is avoided by mixing. Mixing also helps the cells to get equally exposed to nutrients and illuminations and avoid stress on it. The mixing of algal culture is done by stirring the culture devices with hands, using aerators, using paddle wheels, and using an incubator shaker. The carbon source is made available in media, but also the fixation increases when the carbon source is supplied as carbon dioxide. This increases the growth of algae quickly. The air provided is sterilized by passing through a filter. The contaminating particles entering the culture media are avoided by using this technique.

Seawater is used for the culture to maintain the salinity of culture. The algae that are grown in salinity slightly less than their natural habitat grow well compared to the native one. Hence, a very little amount of normal water is mixed with seawater and diluted. This water is used for culture.

2.2. Algal Culture. The algal culture *Chaetoceros calcitrans* was brought from the Central Marine Fisheries Research Institute, Tuticorin, Tamil Nadu, India. The stock cultures were maintained and cultivated by using Walne's culture media. 20°C of temperature and 8.5 pH were provided to maintain the stocks. The algal cultures were illuminated for 24 hrs with fluorescent lamps. Every day, the growth of algal culture is checked and diluted appropriately when it was needed. Haffkine flasks were used for the mass culturing of algae. The media used in the mass cultivation of algae were Walne's media. Convenient aerations, low-level light intensity, 20°C of temperature, and 8.5 pH were made available for the mass production of algae. The cells are harvested when the required cell density was reached. 100 ml of each algal culture is grown separately to study the growth pattern of algae. Each alga's maximum absorbance is analyzed. The optical density of each alga is observed every 24 hrs. The analysis of the variation method was done to find the significant variation between the algal growths. Table 1 explains Walne's media.

The algal culture done on the laboratory scale is given in Figure 1.

2.3. Microscopical Identification. The algae *Chaetoceros calcitrans* maintained in the stock solution are then viewed microscopically. The nomenclature of *Chaetoceros calcitrans* is given below.

2.4. Nomenclature of Chaetoceros calcitrans. Chaetoceros is the most diverse genus of marine planktonic diatoms, with over 400 species described. In girdle view, cells are roughly rectangular. In valve view, cells are typically elliptical. Near their origin, opposing sets of adjacent cells touch.

(i) Kingdom: *Chromalveolata*

(ii) Phylum: *Heterokontophyta*

(iii) Class: *Bacillariophyceae*

(iv) Order: *Centrales*

(v) Family: Chaetocerotacae

(vi) Genus: *Chaetoceros*

(a) Specific descriptor: *calcitrans*

(b) Scientific name: *Chaetoceros calcitrans*

2.5. Synthesis of Silver Nanoparticles. Silver nanoparticles are synthesized from marine microalgae using two methods: normal marine microalgae and microwave irradiated marine microalgae.

2.5.1. Normal Marine Microalgae

(1) Synthesis of Silver Nanoparticles from Normal Marine Microalgae. The algal cultures from the midexponential phase of their growth are collected for the synthesis of nanoparticles, and the experiments are carried out in six methods. Control experiments have been carried out for all methods to determine the responsibility of algae in the production of silver nanoparticles.

(2) Synthesis of Silver Nanoparticles from Normal Marine Microalgal Culture along with 1 mM $AgNO_3$ Solution. The algae are grown in this method with 1 mM $AgNO_3$ solution. Initially, a 10% inoculum of *C. calcitrans* was being added to flasks containing seawater with normal Walne's media, followed by an equal amount of 1 mM silver nitrate solution. It was then shaken for two weeks to continue the synthesis by placing the solutions in a shaker.

(3) Synthesis of Silver Nanoparticles from the Microalgal Supernatant and Pellet. The algal cultures collected in the middle of the exponential phase are centrifuged for 5 minutes at 1000 rpm [26]. Then, the supernatants of 10 ml

Table 1: Composition of Walne's media.

Solution	Walne's media		The volume of solutions used for the algal cultivation of 100 ml
A	Potassium nitrate Sodium Orthophosphate EDTA (Na) Boric acid Ferric chloride Manganese chloride Distilled water	100 g 20 g 45 g 33.4 g 1.3 g 0.36 g 1 l	55 μl
B	Zinc chloride Cobalt chloride Copper sulfate Ammonium molybdate Distilled water	4.2 g 4.0 g 4.0 g 1.8 g 1 l	50 μl
C	Vitamin B_1 (thiamine) VitaminB_{12} (cyanocobalamine) Distilled water	200 mg 10 mg 100 ml	25 μl

Figure 1: Algal culture done in Walne's media.

Table 2: The rate of growth of *C. calcitrans* at 470 nm.

Day	*C. calcitrans* (optical density at 470 nm)
1	0.02
2	0.06
3	0.10
4	0.13
5	0.19
6	0.25
7	0.32
8	0.34
9	0.36
10	0.37
11	0.39
12	0.41
13	0.45
14	0.46
15	0.50
16	0.50
17	0.49
18	0.48
19	0.47
20	0.40
21	0.36
22	0.31
23	0.29
24	0.29
25	0.25
26	0.21
27	0.17
28	0.12
29	0.09
30	0.03

of each algal culture are transferred to test tubes and the pellets are collected in separate test tubes, and then add 10 ml of $AgNO_3$ solution to each algal supernatant and the respective pellets and retain them in a shaking machine for two weeks to carry out synthesis and develop the color change.

(4) Synthesis of Silver Nanoparticles from Ultrasonicated Marine Microalgal Culture. About 10 ml of each algal culture collected in the middle of the exponential phase is ultrasonicated for about 5 mins at 600 rpm. Then, to each ultrasonicated algal culture, add 10 ml of $AgNO_3$ solution and keep it in a shaker for two weeks for synthesis [27].

(5) Synthesis of Silver Nanoparticles from the Ultrasonicated Microalgal Supernatant and Pellet. The algal culture collected in the middle of the exponential phase is ultrasonicated for about 5 mins and centrifuged at 1000 rpm for 5 mins. Then, the supernatants of 10 ml of each algal culture and the respective pellets are transferred to test tubes, and then add 10 ml of $AgNO_3$ solution to each algal supernatant and pellet. The tubes are kept in a shaker for two weeks to develop the color change.

2.5.2. Microwave Irradiated Algal Culture

(1) Synthesis of Silver Nanoparticles from Microwave Irradiated Marine Microalgae. For the synthesis of nanoparticles, an algal culture in its midexponential phase was collected and microwave irradiated for 5 seconds on and 15 seconds off 5 times. Furthermore, the experiments were carried out using six different methods. Control experiments were carried out for all methods to determine the role of algae in the production of silver nanoparticles.

(2) Synthesis of Silver Nanoparticles from Microwave Irradiated Microalgal Culture along with 1 mM $AgNO_3$ Solution. In this method, the microwave irradiated algae are cultivated along with 1 mM $AgNO_3$ solution. A microwave irradiated algal inoculum of 10% is added to respective flasks

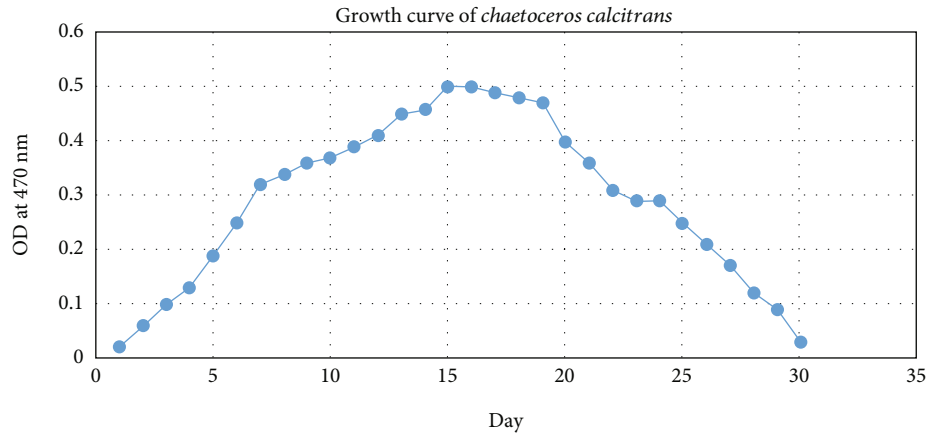

Figure 2: Growth curve of *C. calcitrans*.

Figure 3: Synthesis of silver nanoparticles from microalgae.

containing seawater with media, and then 10 ml of 1 mM silver nitrate solution was added and kept in a shaking machine for two weeks.

(3) Synthesis of Silver Nanoparticles from the Microwave Irradiated Microalgal Supernatant and Pellet. The microwave irradiated algal cultures collected in the middle of the exponential phase are centrifuged at 1000 rpm for 5 mins. The supernatant and pellet of each alga are taken in separate test tubes and added 10 ml of 1 mM silver nitrate solution and then kept in a shaker for two weeks.

(4) Synthesis of Silver Nanoparticles from Microwave Irradiated and Ultrasonicated Microalgal Culture. The microwave irradiated algal culture collected in the middle of the exponential phase is ultrasonicated for about 5 mins at 600 rpm. Then, to each ultrasonicated algal culture, add 10 ml of $AgNO_3$ solution and keep it in a shaker for two weeks.

(5) Synthesis of Silver Nanoparticles from the Microwave Irradiated and Ultrasonicated Microalgal Supernatant and Pellet. The microwave irradiated algal culture collected in the middle of the exponential phase is ultrasonicated for about 5 mins at 600 rpm and centrifuged at 5000 rpm for 5 mins. The supernatant and pellet of each algal culture are transferred to separate test tubes, and 10 ml of 1 mM silver nitrate solution is added and kept in a shaker for two weeks to identify and analyze the color changes.

2.6. Characterization of Silver Nanoparticles. The characterization study of silver nanoparticles is done to confirm the presence of silver nanoparticles and to analyze their size, shape, and other characteristic features.

2.6.1. UV-Vis Spectroscopy. UV-Vis spectroscopy is used to characterize and confirm the presence of reduced silver ions as silver nanoparticles in the algal culture. The wavelength range used for taking absorbance is from 200 nm to 700 nm. Both the UV range and the visible range are present in UV-Vis spectroscopy.

2.6.2. Scanning Electron Microscopy. The size details regarding the nanoparticle are obtained using scanning electron microscopy. The magnifications that can be done in scanning electron microscopy range from 20x to 30,000x. The area that ranges from 1 cm to 5 μm can be imaged. The colloidal solutions containing the silver nanoparticles are centrifuged at 5000 rpm for 12 minutes, and the supernatant is again centrifuged at 20,000 rpm to get pellets. These pellets are dissolved in an ionic solution and then photographed.

2.6.3. Transmission Electron Microscopy. The particle distribution and the size profile of distributed particles are analyzed using TEM. The TEM uses an electron beam to make a photograph of the image kept for identification. The silver nanoparticles obtained by the reduction process are prepared in such a way that they withstand the electron beam passing through them to make an image. The image obtained from TEM helps to make data regarding the silver nanoparticles.

2.6.4. Fourier Transform Infrared Spectroscopy. The chemical architecture of silver nanoparticles is studied using the FTIR spectrometer. The solution of nanoparticles is dried at 75°C, and the powder obtained is characterized in the range 4000 to 500 cm^{-1}.

2.6.5. Atomic Force Microscopy. Atomic force microscopy is used to investigate the presence of atoms on the surface of nanoparticles. The surface chemistry of nanoparticles can be analyzed thoroughly using AFM.

2.6.6. X-Ray Diffractometry. The size and nature of silver nanoparticles are studied by the graphical data obtained from XRD. Scherrer's formulas are used in XRD to interpret the

Figure 4: Synthesis of silver nanoparticles after microwave irradiation.

Table 3: Amount of silver nanoparticles synthesized from normal marine microalgae.

Sl. no.	Algae	Normal algae			Ultrasonicated algal culture		
		Algal culture (mg)	Algal supernatant (mg)	Algal pellet (mg)	Algal culture (mg)	Algal supernatant (mg)	Algal pellet (mg)
1	*C. calcitrans*	6.000	1.011	3.123	8.231	3.201	2.587

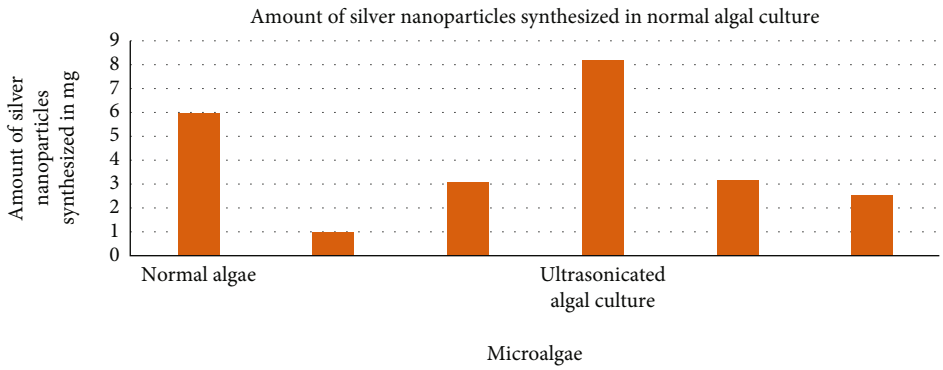

Figure 5: Amount of silver nanoparticles synthesized in normal algal culture.

Table 4: Amount of silver nanoparticles synthesized from microwave irradiated marine microalgae.

Sl. no.	Algae	Microwave irradiated algae			Microwave irradiated and ultrasonicated algal culture		
		Algal culture (mg)	Algal supernatant (mg)	Algal pellet (mg)	Algal culture (mg)	Algal supernatant (mg)	Algal pellet (mg)
1	*C. calcitrans*	9.154	2.315	3.545	12.335	4.257	2.978

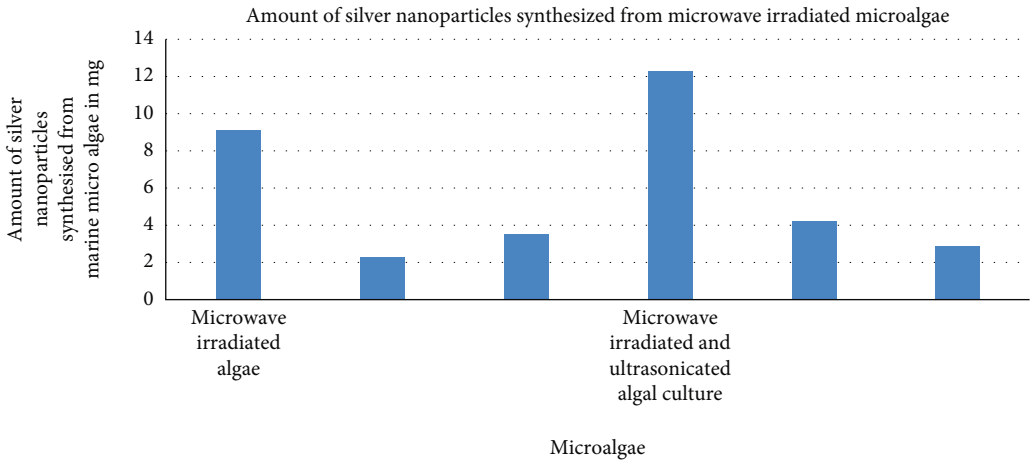

Figure 6: Amount of silver nanoparticles synthesized from microwave irradiated microalgae.

Figure 7: Silver nanoparticles in powdered form.

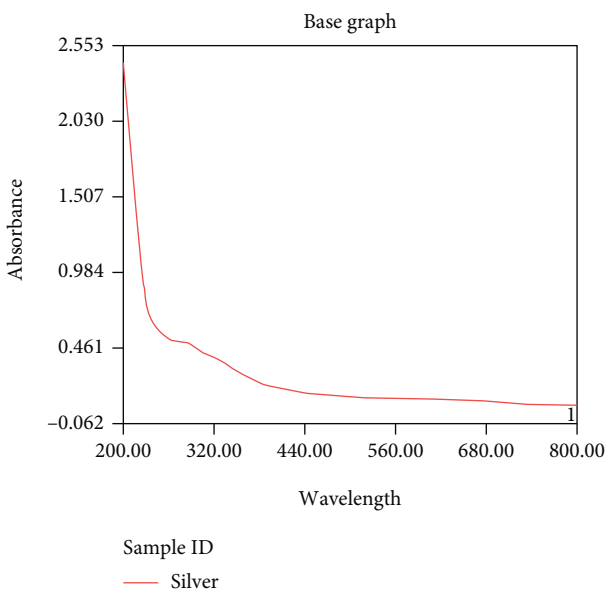

Figure 8: UV-Vis spectroscopy of silver nanoparticles.

results of XRD. The silver nanoparticles are ground to obtain a fine powder and then used in the XRD experiment.

2.6.7. Photoluminescence. The photoluminescence study is done to know the photon excitations of silver nanoparticles. A powdered sample of nanoparticles is used for the experimental data interpretation.

2.7. Antimicrobial Activity of Silver Nanoparticles. The antagonistic nature of silver nanoparticles against human pathogenic organisms is studied. The data are collected regarding the zone of inhibition obtained by silver nanoparticles against each human pathogenic organism. *A. niger*, *Enterobacter spp.*, *E. coli*, *Klebsiella spp.*, *P. vulgaricus*, *P. aeruginosa*, and *S. aureus* are human pathogenic organisms used to evaluate the opposing nature of silver nanoparticles.

3. Results and Discussion

The algal species *Chaetoceros calcitrans* are collected from the Central Marine Fisheries Research Institute (CMFRI), Tuticorin, Tamil Nadu, India. The stock is maintained in Walne's media. Walne's media are specially designed for the growth of marine microalgae by Walne in 1970. The algae were microscopically identified as *Chaetoceros calcitrans*. The mass cultivation of algae is done in Haffkine flasks. Each alga's growth was studied by measuring absorbance values at their respective maximum values. For the first 15 days, algal cells are in the exponential phase. After 15 days of growth, algal cells reach the stationary phase and begin to decline.

The λmax values for the microalgae are found using the Beer-Lambert law. The maximum absorbance for the marine microalgae *C. calcitrans* is 470 nm.

3.1. Dynamics of Algal Growth. An axenic culture of microalgae grows in five stages. Growth is usually associated with culture changes instead of just changes in an individual organism. The term "growth" refers to an increase in number beyond what was present in the original inoculums. In algal multiplication, there are five distinct stages of growth. The period after adding inoculums to a culture medium, when the population remains temporarily unchanged, is known as the lag phase. The size of algae grows beyond the normal dimensions. They are very active physiologically and are synthesizing new protoplasm. Although the organisms are metabolizing, cell division is slow. The cells divide at a constant rate during the next logarithmic or exponential phase. At this stage, the growth rate is at its peak under optimal culture conditions. When nutrients, light, pH, carbon dioxide, or other physical and chemical factors begin to limit growth, cell division starts to slow. The logarithmic phase of growth begins to taper off gradually after several hours or days in the stationary phase. For a time, the population remains relatively constant, possibly as a result of the complete withdrawal of division or the stabilizing of the regenerative capacity by an equivalent death rate. The final phase is the phase of decline or death, in which the rate at which some cells die exceeds the process at which new cells reproduce. The number of viable cells decreases in a straight line.

3.2. Data Analysis of Growth Dynamics of Algae. The growth dynamics of marine microalgae are analyzed for 30 days. The absorbance of each alga is noted at their λmax on a daily basis. The cells first undergo a lag phase where the multiplication of cells is not found, but the unicellular alga finds its adaptability to the new environment and then shows multiplication in its next phase. The exponential phase is the active phase of the alga, where it is multiplied and the cell number increases. Due to an increase in the cell number in the culture, the density, turbidity, and viscous nature of culture increase. The dense nature of culture gives an elevated absorbance for the exponential phase of algae.

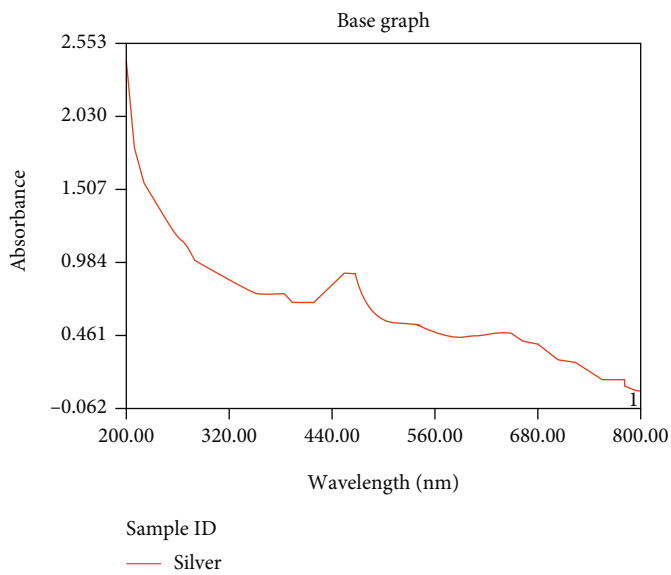

Figure 9: UV-Vis spectroscopy analysis of silver nanoparticles synthesized from microalgae *C. calcitrans*.

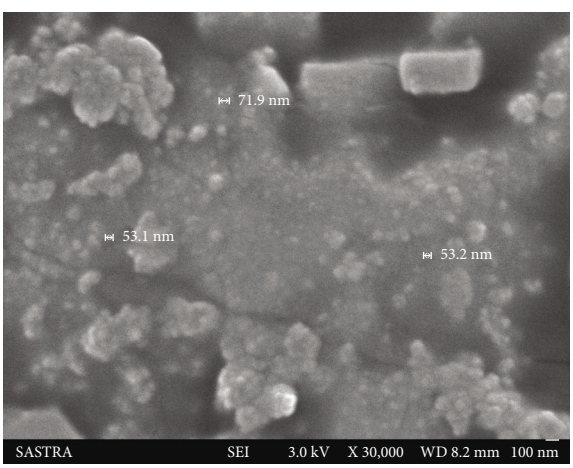

Figure 10: SEM image of nanoparticles with sizes 53 nm and 72 nm.

The microalgae reached the end of the exponential phase nearer to the 15th day, and the next phase, the stationary phase, starts. In the stationary phase, the cells remain stagnant without any multiplication due to the lack of availability of nutrients. The start of the stationary phase varied between species from 14 to 16 days. About 860×10^4 cells/ml of *C. calcitrans* are counted at the near end of an exponential phase in the marine microalgae. The algal culture at the near end of the exponential phase is used as a stock culture for the preparation of other pure cultures. The presence of marine microalgae is necessary for the balance nature of the environment since the photosynthesis process occurs at a higher rate during the exponential phase of growth, therefore reducing the carbon dioxide concentration in the environment [13]. The absorbance of algae observed for 30 days is given in Table 2.

The growth curve of *C. calcitrans* in normal nitrogen content in Walne's media is shown in Figure 2. The multiplication of *C. calcitrans* in normal nitrogen content in Walne's media showed a steep increase for 15 days and remained there in the stationary phase for 2 days and then declined. During the decline phase, cell death is not in a regular fashion but showed again a stationary phase and then declined.

3.3. Synthesis of Silver Nanoparticles. The presence of reddish brown-black color in the solution indicated the synthesis of silver nanoparticles. Due to the excitation of surface plasmon resonance and SPR bands, the solution with silver nanoparticles changes its color to brown color. The silver nanoparticles demonstrated high absorbance at 420 nm, which is the maximum absorbance demonstrated by silver particles. The color of synthesized nanoparticles was due to the surface plasmon excitation phenomenon. The size of nanoparticles also has an impact on color formation. When nanoparticles are of very small size and not aggregated, the color was yellow and turns to dark brown by the formation of larger molecules and the aggregation process that happens in the solution. The metabolites excreted by the silver-exposed culture could reduce silver ions, indicating that the reduction of the ions occurs via electron shuttles or through reducing agents released into the solution in the algal culture. These reactions took place only in the presence of light, and nanoparticles are not formed in the absence of light. The reduction process of bulk silver material to nanomaterial was analyzed [14]. The change in color acts as the primary confirmation test in silver nanoparticle synthesis [15–17]. Among the green metallic nanoparticles, silver nanoparticles were more preferable for the analysis of antimicrobials [18]. It has an oligodynamic action that allows it to bond to biomolecule membranes and aggregate the cell wall of bacteria [19]. The controls were maintained to carry out the experiment. The presence of flavonoids, alkaloids, saponins, tannins, quinones, and reducing sugars present in the alga itself acts as a capping and reducing agent. Hence, the addition of any other

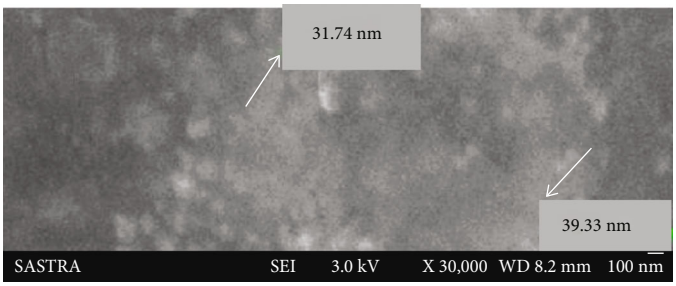

Figure 11: SEM image of nanoparticles with sizes 33 nm and 39 nm.

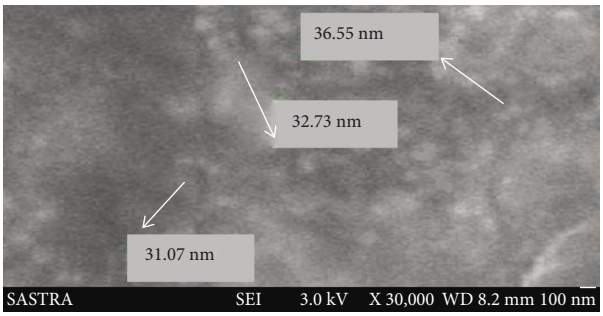

Figure 12: SEM image of nanoparticles with sizes 31 nm, 32 nm, and 36 nm.

chemicals is not needed which made the experiment eco-friendly. The silver nanoparticles synthesized from *C. calcitrans* by eco-friendly methodology remained stable for more than six months when stored at room temperature. The durability increases when preserved at a cool temperature.

The amount of silver nanoparticles synthesized in ultrasonicated algal culture is high compared to others since due to disturbance produced in the cell wall of microalgae (Figure 3), the reducing particles are released in the culture environment, and hence, many silver particles get reduced to silver nanoparticles. A trace amount of silver nanoparticles can be found in the supernatant and pellet due to the occurrence of reducing ions present. The temperatures have a great impact on the synthesis of silver nanoparticles. The temperature significantly affects the synthesis, formation, size, and shape of nanoparticles. By varying the temperature, the silver nanoparticles of the required shape and size can be obtained.

The occurrence of silver nanoparticles is given in Figure 4.

The amount of silver nanoparticles produced from normal marine microalgae is given in Table 3. The amount of silver nanoparticles synthesized by *C. calcitrans* in normal algal culture is 6 mg, and when ultrasonicated, it increases to 8.231 mg.

The amount of silver nanoparticles synthesized by *C. calcitrans* in normal algae and in ultrasonicated algal culture is graphically given in Figure 5.

The marine microalgae, when exposed to microwave irradiation, get stimulated to synthesize more silver nanoparticles than the normal microalgae, and it is given in Table 4. This is due to the reducing ions that get induced, and their release outside the cell is higher, and hence, more silver nanoparticles get synthesized. The quantity of synthesizing silver nanoparticles of microalgae can be improved by microwave irradiation for 5 sec on and 15 sec off 5 times. The amount of silver nanoparticles synthesized by *C. calcitrans* is 6.000 mg in normal which is improved to 9.154 mg by microwave irradiation.

The amount of silver nanoparticles synthesized from microwave irradiated marine microalgae is given in Figure 6.

The silver nanoparticles synthesized from microalgae can be dried and made into powder. The synthesized nanoparticles were collected after centrifugation as pellets and air-dried for 1 hour. Then, it was exposed to 100°C until the water content from the nanoparticles gets removed. The agglomerated particles were mechanically crushed to bring them to a fine powdered form. The nanoparticle powders are separated in Eppendorf tubes according to their different sizes after taking an SEM image. The powdered sample of nanoparticles is shown in Figure 7. The powdered form of silver nanoparticles is used in experiments.

3.4. UV-Visible Spectroscopy. The synthesis of silver nanoparticles in the algal culture is confirmed by taking its absorbance value using UV-Vis spectroscopy since silver nanoparticles exhibit their maximum absorbance in the UV range. The absorption and scattering efficiency of silver nanoparticles are very great. Their strong interaction with light occurs because when excited by light at specific wavelengths, the conduction electrons on the metal surface undergo a collective oscillation. Silver nanomaterial optical properties such as absorption, transmission, reflection, and light emission are dynamic and may differ significantly from bulk material properties.

The UV absorption spectra of the silver nanoparticle solution show the absorption peak in the visible range of 335.9 nm, as shown in Figure 8. In the graph, it shows that the sample silver nanoparticles have a strong absorption peak.

The UV-Vis spectroscopy is taken for all the silver nanoparticles synthesized from marine microalgae. The peak is obtained in the range of 400 nm to 460 nm which confirms the presence of silver nanoparticles. Figure 9 shows the peak of silver nanoparticles synthesized from marine algae *C. calcitrans*. The absorption spectra obtained by UV-Vis spectroscopy are accurate in confirming the presence of silver nanoparticles since these silver nanoparticles, due to surface plasmon excitation phenomenon in the UV range, show an intense absorption peak. The absorption band of 420 nm is typical for silver nanoparticles. To generate and synthesize nanoparticles with the desired size, shape, and functions, a thorough examination of a component's chemical, physical, and biological properties is needed [20]. The silver nanoparticles were purified, and the

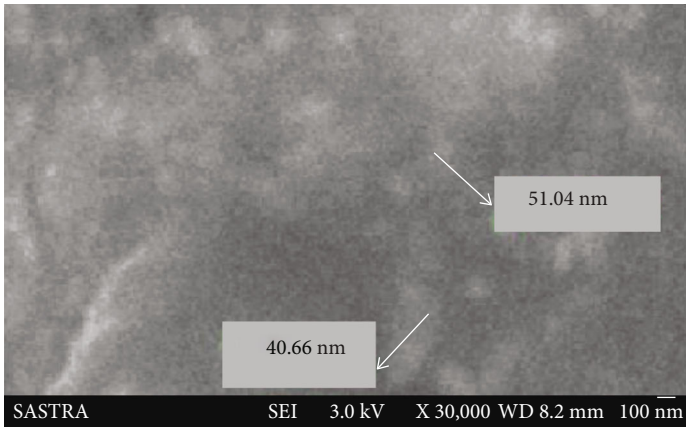

Figure 13: SEM image of nanoparticles with sizes 40 nm and 51 nm.

Figure 14: Silver nanoparticles of sizes from 25 nm to 35 nm, 55 nm to 65 nm, and 85 nm to 95 nm.

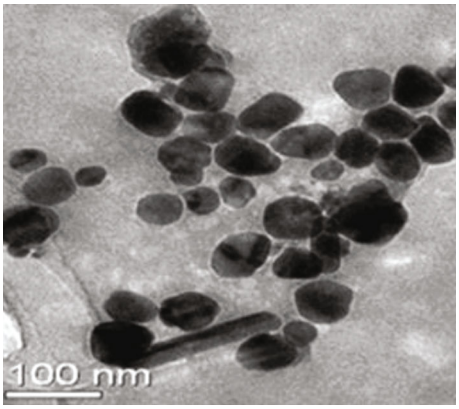

Figure 15: TEM image of silver nanoparticles.

algal cells are removed before the characterization process. If there were any algal cells, they could interfere with the results but were negligible.

The smaller nanoparticles make the band to be around 400 to 450 nm, whereas when the size of silver nanoparticles increases, it could be around 450 nm to 495 nm. The size of nanoparticles has a great impact on the excitation of photons and on the formation of bands. The color change of silver nanoparticles was also greatly influenced by the varied sizes of silver nanoparticles synthesized.

3.5. Scanning Electron Microscopy. The size of the silver nanoparticles synthesized from marine microalgae is examined with the help of a scanning electron microscope (SEM). It is found that the silver nanoparticles synthesized from marine microalgae have a size of 30–80 nm. Figure 10 shows the SEM image of silver nanoparticles with a size of 53.1 nm to 71.9 nm.

The scanning electron microscopy photographs are further taken with various sizes of nanoparticles. Various shapes of silver nanoparticles are found. A number of silver nanoparticles are found with a spherical shape. Cubic, oval, elliptical, and rectangular shapes are some other shapes found in the nanoparticles synthesized from marine microalgae. Figure 11 shows the presence of silver nanoparticles with sizes 33 nm and 39 nm.

Figure 12 shows the nanoparticles with sizes 31 nm, 32 nm, and 36 nm. The different-sized nanoparticles can then be collected separately to carry out various other experiments.

The effect of nanoparticle size on the thermal conductivity of nanoparticles is analyzed by isolating the different sizes of nanoparticles in separate Eppendorf tubes, and then the nanofluids are prepared with various concentrations. The scale used to compare the size of nanoparticles in the SEM image is 100 nm. The magnification of 30,000x is used to capture the different sizes of nanoparticles. 40 nm to 51 nm sized silver nanoparticles are shown in Figure 13.

After taking photographs of silver nanoparticles, it is found to have different ranges of silver nanoparticles. Among the various ranges of sizes in nanoparticles, the separation is done in three categories as 25 nm to 35 nm, 55 nm

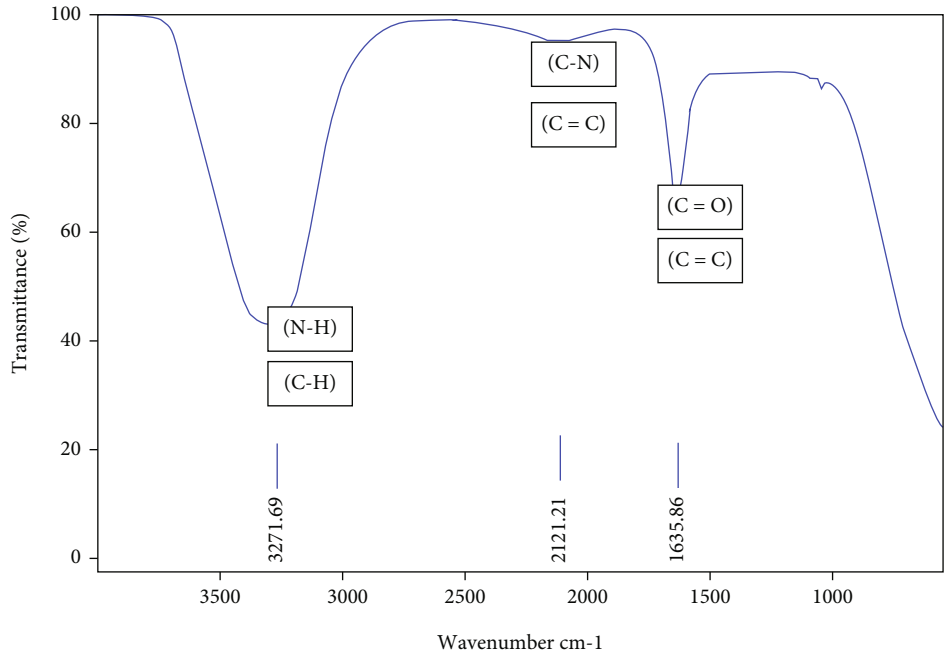

Figure 16: Fourier transform infrared spectroscopy.

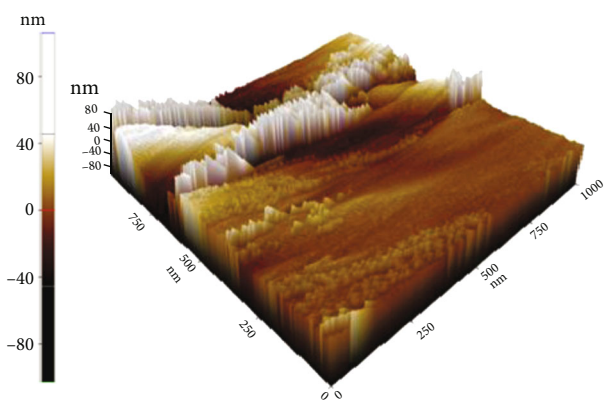

File name	190318Topography006
Head mode	NCAFM
Source	Topography
Data width	256
Data height	256
X scan size	1 um
Y scan size	1 um
Scan rate	0.5 Hz
Z servo gain	1
Set point	13.84 nm
Amplitude	17.74 nm
Set frequency	304.66E3Hz

Figure 17: 3D image of silver nanoparticles by AFM.

to 65 nm, and 85 nm to 95 nm. The powdered samples of different-sized nanoparticles are shown in Figure 14.

3.6. Transmission Electron Microscopy. Transmission electron microscopy analysis gives the data about the size of the particle, the size distribution, and the nanoparticle's morphology. The microscopical method is the only method that is used for measuring the nanoparticle size, where the specific nanoparticles are precisely detected and measured. The data regarding the dispersion of nanoparticles and agglomeration of nanoparticles are obtained using TEM images. Figure 15 illustrates the TEM image of synthesized silver nanoparticles from marine microalgae. The nanoparticles in the range of 20 nm to 99 nm are obtained. The synthesized nanoparticles are well distributed, as obtained from the TEM image taken at high resolution.

3.7. Fourier Transform Infrared Spectroscopy. FTIR analysis of silver nanoparticles was performed in the wavenumber range of 1000-3500 cm^{-1}. The graphs indicate the presence of various chemical groups, and FTIR signals are silver NPs obtained corresponding to C=O vibrations of oxygen, C=C stretching of alkenes (1635 cm^{-1}), then C=C stretching of alkenes (2121 cm^{-1}), N-H stretching of nitrogen groups (3271 cm^{-1}), and N-H stretching of aliphatic groups. These groups suggest the presence of silver NPs. The presence of amino acids is confirmed by the presence of signature peaks which supports the presence of proteins. The bands at positions 1382 and 1035 cm^{-1} are referred to as the vibrations of the C-N stretching of the aromatic and aliphatic amines, respectively. The observations obtained all give the existence and protein binding with that of silver nanoparticles which

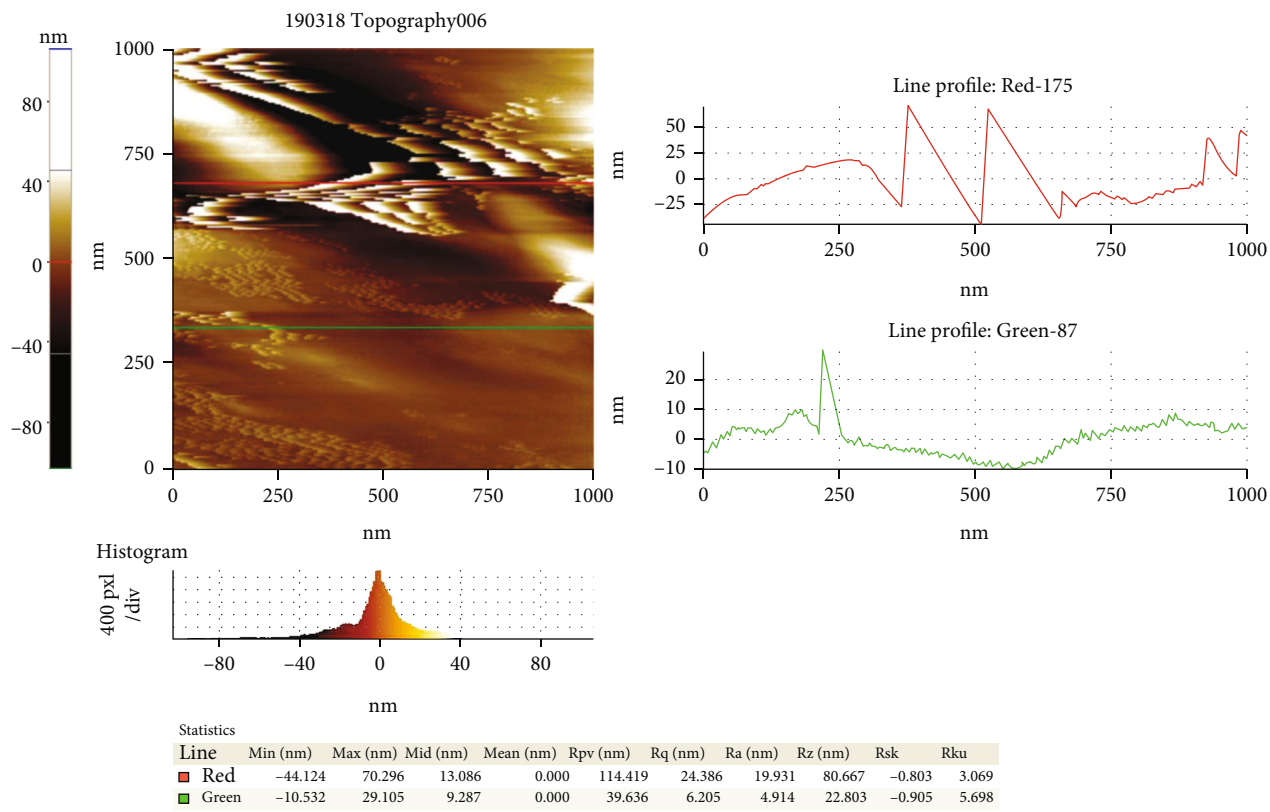

Figure 18: Atomic force microscopy 2D image of silver nanoparticles.

Table 5: Scan details of XRD.

Name	Silver.brml (smooth) #1
Type of scan	Coupled two theta/theta
Mode of scan	Continuous PSD fast
Start	10.002°
End	80.010°
Step size	0.020°
Total time/step	80.00 s
Sample rotation	15.000 1/min
Anode	Cu
Focus orientation	Line focus
Kα1	1.54060 Å
Kα2	1.54439 Å
Kα2 ratio	0.50000
Kβ	1.39222Å
Wavelength for display	1.54060 Å
Generator kV	30.0 kV
Generator mA	10.0 mA
Detector opening	4.850°
Application type	Powder diffraction

leads to stabilization. Also, the FTIR results show that the secondary protein structure did not get disturbed due to the reduction of silver ions to silver nanoparticles. The presence of –OH, C=O, and –CN groups acts as reducing agents in the eco-friendly mode of silver nanoparticle synthesis [21, 22]. Figure 16 shows the FTIR results.

3.8. Atomic Force Microscopy. Atomic force microscopy (AFM) images show the surface topology and size distribution of silver nanoparticles in the solution and also the height and amplitude of the material, as well as the three-dimensional (3D) and two-dimensional (2D) reconstructed images of the general particle. AFM analysis evaluated the presence and size distribution of the generated silver nanoparticles. The scanning area was $1 \times 1\,\mu$m in a tapping mode, and both the three-dimensional (3D) image and the two-dimensional (2D) image are generated in Figures 17 and 18, respectively. The image confirms the uniform distribution of silver nanoparticles. Most of the particles were approximately 40-80 nm in diameter in the sphere topology. The agglomeration of particles to each other can be seen. The average height of the silver nanoparticles is approximately 0-25 nm.

3.9. X-Ray Diffractometry. XRD analysis of prepared silver nanoparticles was done by a powder X-ray diffractometer. The silver nanoparticles synthesized from marine microalgae are powdered for XRD analysis.

The scan details are given in Table 5. The coupled two theta and the continuous PSD fast mode of scan are used in XRD analysis. It started at the range of 10.002° and completed at 80.010°. The type of diffraction carried out in X-ray diffractometry is powder diffraction.

Table 6: Peak details obtained from XRD analysis.

DB compound name	Angle	*d* value	Net intensity	Gross intensity	Relative intensity	Intensity	FWHM	Width (low)
Peak 1	26.078°	3.41424 Å	201.877	1753.54	18.8%	201.877	0.180	0.090
Peak 2	27.222°	3.27325 Å	95.4102	1671.44	8.9%	95.4102	0.179	0.089
Peak 3	31.710°	2.81947 Å	117.758	1711.09	11.0%	117.758	0.192	0.096
Peak 4	37.583°	2.39128 Å	1072.16	2593.43	100.0%	1072.16	0.295	0.147
Peak 5	43.708°	2.06937 Å	294.951	1562.40	27.5%	294.951	0.325	0.162
Peak 6	63.960°	1.45442 Å	259.275	878.476	24.2%	259.275	0.279	0.140
Peak 7	76.974°	1.23775 Å	231.249	766.864	21.6%	231.249	0.296	0.148

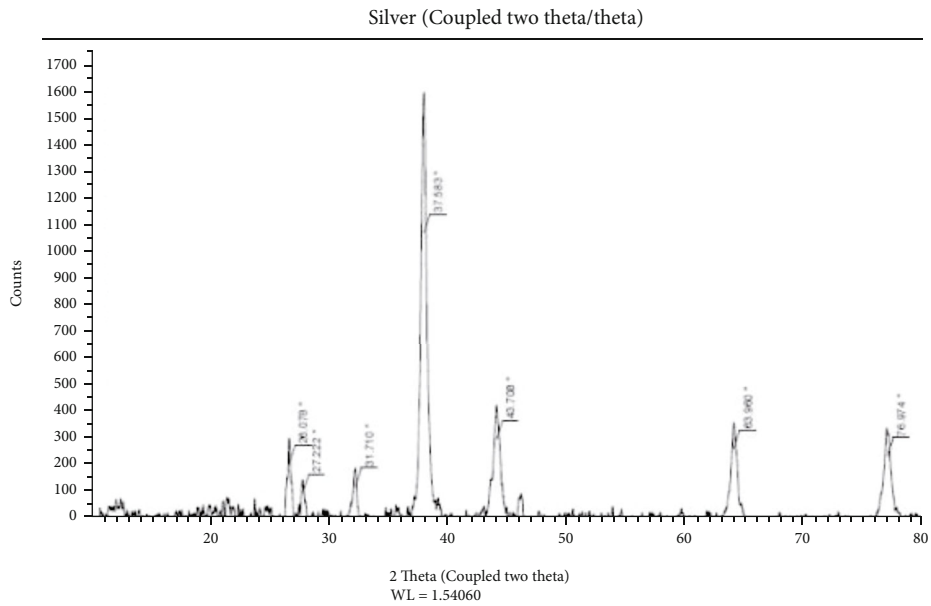

Figure 19: XRD analysis.

The complete peak details of XRD are given in Table 6. The peaks obtained at positions 26.078°, 27.222°, 37.583°, 43.708°, 63.960°, and 75.974° when analyzed confirm the presence of silver nanoparticles. The *d* value, net intensity, gross intensity, and relative intensity of each peak are obtained and tabulated. The full width at half maximum of peaks is found to be 0.180, 0.179, 0.192, 0.295, 0.325, 0.279, and 0.296 for the seven peaks obtained, respectively. The Bragg reflections obtained indicate the presence of nanoparticles in face-centered cubic form that are crystalline in nature. The peaks that correspond to (111), (121), (200), and (221) correspondingly indicate the presence of silver nanoparticles by XRD analysis.

XRD peaks observed at 26.0, 27.2, 31.7, 37.5, 43.7, 63.9, and 76.9 were related to their corresponding planes. The prepared silver nanoparticle is matched with the ICDD card NO-04-0783. XRD results reveal that the prepared sample is the silver nanoparticles. Silver nanoparticles are formed due to the reduction of $AgNO_3$ into Ag. Bragg's equation was used to calculate the reflection angles in interatomic space [23]. The acquired Bragg reflections revealed that the produced silver nanoparticles are in nanocrystal form and face-centered cubic form and are crystalline in nature when compared to the standard [24]. The excited peaks interpreted by XRD are given in Figure 19.

3.10. Photoluminescence. The photoluminescence of silver nanoparticles is studied to know about the photon excitations. The excitations are done at 350 nm and 400 nm. The peaks obtained due to the photoluminescence of silver nanoparticles are given in Figure 20.

Surface areas of nanoscale materials are far greater than those of comparable masses of larger-scale materials. As a material's surface area per mass increases, more of the material can come into contact with surrounding materials, affecting reactivity. Smaller silver nanoparticles have more reaction sites (where the sites can receive electrons) on their surfaces and are more sensitive to oxygen, a natural electron donor, than larger particles because they have a larger specific surface area.

3.11. Antimicrobial Activity of Silver Nanoparticles against Human Pathogens. The silver nanoparticles synthesized from marine microalgae that are checked for their antimicrobial activity are shown in Table 7. *A. niger*, *Enterobacter spp.*, *E. coli*, *Klebsiella spp.*, *P. vulgaricus*, *P. aeruginosa*, and *S. aureus* are human pathogens used to analyze the antimicrobial activity of silver nanoparticles. Silver nanoparticles synthesized from *C. calcitrans* showed a high zone of inhibition against *P. aeruginosa* and *S. aureus*.

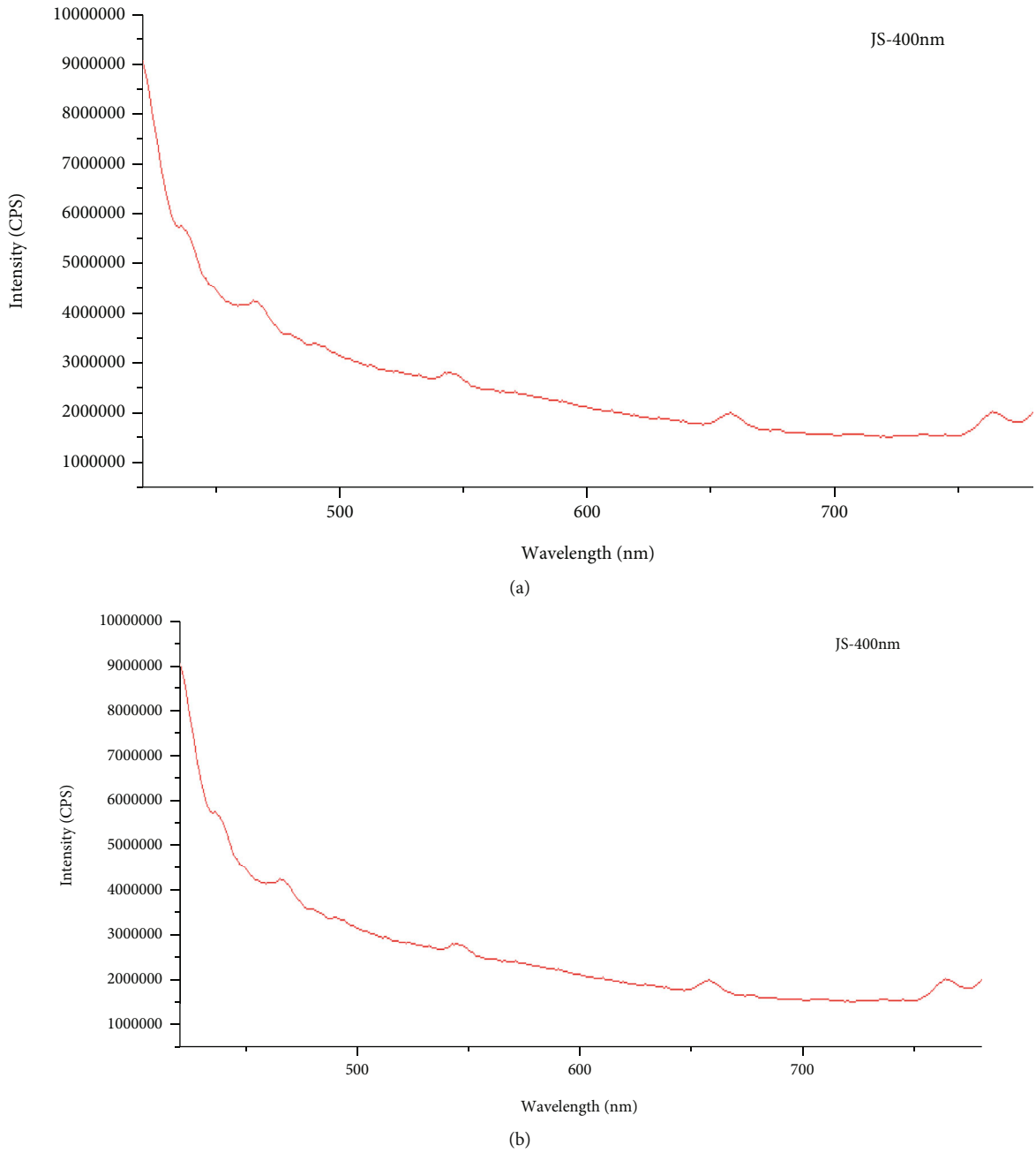

Figure 20: (a) Photoluminescence of silver nanoparticles A at 350 nm. (b) Photoluminescence of silver nanoparticles B at 400 nm.

Table 7: Zone of inhibition of silver nanoparticles against human pathogens.

Organisms	*C. calcitrans*
A. niger	17 mm
Enterobacter spp.	9 mm
E. coli	7 mm
Klebsiella spp.	19 mm
P. vulgaricus	12 mm
P. aeruginosa	18 mm
S. aureus	18 mm

The zone of inhibition shown by silver nanoparticles synthesized from marine microalgae against human pathogens is shown in Figure 21. The silver nanoparticles synthesized from marine microalgae have a high antagonistic character against human pathogens, and hence, these particles can be used in medical applications. Sudha et al. in 2013 investigated the antagonistic nature of algae against human pathogens and analyzed the zone of inhibition [25].

Silver nanoparticles have been imposed as an excellent antimicrobial agent capable of combating bacteria that cause infections in vitro and in vivo. Silver nanoparticles have antibacterial activity against both Gram-negative bacteria and

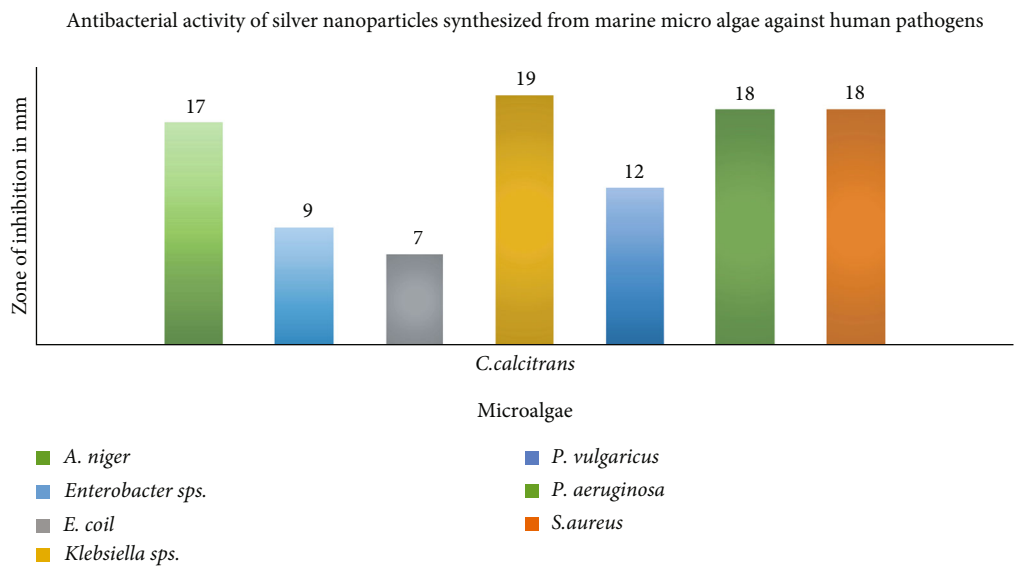

Figure 21: Antimicrobial activity of silver nanoparticles synthesized from marine microalgae against human pathogens.

Gram-positive bacteria, including multidrug-resistant strains. The antimicrobial effect is attributed to positively charged silver ions (Ag+). Silver ions kill microorganisms through a variety of mechanisms. Three major toxicity mechanisms for silver nanoparticles have been suggested: oxidative stress, DNA damage, and cytokine induction. In vivo studies have revealed that exposure to silver nanoparticles can cause effects in a variety of major organs.

The silver nanoparticles' antibacterial activity was compared with commonly available antibiotics gentamicin and streptomycin. It was analyzed that silver nanoparticles have greater potency against bacteria compared with antibiotics. The fold increase in the zone of inhibition was found in discs when silver nanoparticles were impregnated with antibiotics. The mode of action and efficiency were much greater for the wells filled with equal amounts of both silver nanoparticles and antibiotics.

4. Conclusion

Engineering combined with technology made the possibility to achieve a product "silver nanoparticle" in an eco-friendly manner. The marine microalgae are made to grow in Walne's media, and their growth patterns were checked. Value-added silver nanoparticles are synthesized from microalgae at their exponential phase. The characterization of silver nanoparticles with UV-Vis spectroscopy, SEM, TEM, FTIR, XRD, AFM, and PL is done. The antimicrobial activity of silver nanoparticles was analyzed. The silver nanoparticles exhibit high antibacterial activity against human pathogenic organisms.

Data Availability

The datasets generated during and/or analyzed during the current study are available from the corresponding author upon reasonable request.

Conflicts of Interest

The authors declare that they have no conflicts of interest.

References

[1] N. Saifuddin, C. W. Wong, and A. A. Nur Yasumira, "Rapid biosynthesis of silver nanoparticles using culture supernatant of bacteria with microwave irradiation," *E-journal of Chemistry*, vol. 6, no. 1, p. 61, 2009.

[2] H. Huang and X. Yang, "Synthesis of polysaccharide-stabilized gold and silver nanoparticles: a green method," *Journal Carbohydrates Research*, vol. 339, no. 15, pp. 2627–2631, 2004.

[3] A. Ahmad, P. Mukherjee, S. Senapati et al., "*Extracellular biosynthesis of silver nanoparticles using the fungus _Fusarium oxysporum_*," *Colloids and Surfaces B: Biointerfaces*, vol. 28, no. 4, pp. 313–318, 2003.

[4] Y. Zhou, H. Itoh, T. Uemura, K. Naka, and Y. Chujo, "Synthesis of novel stable nanometer-sized metal (M = Pd, Au, Pt) colloids protected by a π-conjugated polymer," *Nanoscience and Nanotechnology Research, Langmuir*, vol. 18, no. 1, pp. 277–283, 2002.

[5] T. Klaus-Joerger, R. Joerger, E. Olsson, and C. G. Granqvist, "Bacteria as workers in the living factory: metal-accumulating bacteria and their potential for materials science," *Trends in Biotechnology*, vol. 19, no. 1, pp. 15–20, 2001.

[6] S. Schultz, D. R. Smith, J. J. Mock, and D. A. Schultz, "Single-target molecule detection with nonbleaching multicolor optical immunolabels," *Proceedings of the National Academy of Sciences*, vol. 97, no. 3, pp. 996–1001, 2000.

[7] M. A. Hayat, *Colloidal Gold: Principles, Methods and Applications*, vol. 1, Academic Press, San Diego, USA, 1989.

[8] K. Simkiss and K. Wilbur, Eds., *Biominerlisation*, Academic press, Elsevier, Availble from: Elsevier books, 2012.

[9] P. K. Stoimenov, R. L. Klinger, G. L. Marchinand, and K. J. Khabude, "Metal oxide nanoparticles as bactericidal agents," *Langmuir*, vol. 18, no. 17, pp. 6679–6686, 2002.

[10] R. Blakemore and P. Ann, "Magnetotactic bacteria," *Annual Review of Microbiology*, vol. 36, no. 1, pp. 217–238, 1982.

[11] N. Kroger, R. Deutzmann, and M. Sumper, "Polycationic peptides from diatom biosilica that direct silica nanosphere formation," *Journal Science*, vol. 286, no. 5442, pp. 1129–1132, 1999.

[12] L. Cepoi, I. Zinicovscaia, R. Ludmila et al., "Effects of PEG-coated silver and gold nanoparticles on Spirulina platensis biomass during its growth in a closed system," *Coatings*, vol. 10, no. 8, pp. 717–732, 2020.

[13] A. V. Miguel, F. Antonio, C. M. Jose, and L. G. Pires Ana, "CO_2 capture using microalgae," in *Advances in Carbon Capture*, Woodhead Publishing, 2020.

[14] D. Devina Merin, S. Praksh, and B. Valentine Bhimba, "Antibacterial screening of silver nanoparticles synthesized by marine micro algae," *Asian Pacific Journal of Tropical Medicine*, vol. 3, no. 10, pp. 797–799, 2010.

[15] R. Nishanthi, S. Malathi, S. John Paul, and P. Palani, "Green synthesis and characterization of bioinspired silver, gold and platinum nanoparticles and evaluation of their synergistic antibacterial activity after combining with different classes of antibiotics," *Materials Science & Engineering C*, vol. 96, pp. 693–707, 2019.

[16] A. K. Genevieve, M. W. Laura, J. F. Sarah, H. Michael, L. P. Amy, and E. O. Janel, "Microwave – assisted green synthesis of silver nanoparticles using orange peel extract," *ACS Sustainable Chemistry & Engineering*, vol. 2, no. 3, pp. 367–376, 2014.

[17] M. Ndikau, N. M. Noah, D. M. Andala, and E. Masika, "Green synthesis and characterization of silver nanoparticles using Citrullus lanatus fruit rind extract," *International Journal of Analytical Chemistry*, vol. 2017, Article ID 8108504, 9 pages, 2017.

[18] H. Safafar, J. Van Wagenen, P. Moller, and C. Jacobsen, "Carotenoids, phenolic compounds and tocopherols contribute to the antioxidative properties of some microalgae species grown on industrial wastewater," *Marine Drugs*, vol. 13, no. 12, pp. 7339–7356, 2015.

[19] R. Anith Jose and P. Jagatheeswari, "Neutroscopic data synthesis of biodegradable polymer for industrial bio robots," *Cognitive Systems Research*, vol. 56, pp. 72–81, 2019.

[20] P. Boomi, R. M. Ganesan, G. Poorani, H. G. Prabu, S. Ravikumar, and J. Jeyakanthan, "Biological synergy of greener gold nanoparticles by using _Coleus aromaticus_ leaf extract," *Materials Science and Engineering*, vol. 99, pp. 202–210, 2019.

[21] K. Gopinath, S. Kumaraguru, K. Bhakyaraj et al., "Green synthesis of silver, gold and silver/gold bimetallic nanoparticles using the _Gloriosa superba_ leaf extract and their antibacterial and antibiofilm activities," *Microbial Pathogenesis*, vol. 101, no. 1, pp. 1–11, 2016.

[22] M. M. J. Gonzalez, M. A. Rodriguez, S. Luque, and J. R. Alvarez, "Recovery of heavy metals from metal industry waste waters by chemical precipitation and nanofiltration," *Desalination*, vol. 200, no. 1-3, pp. 742–744, 2006.

[23] K. Pramila and K. S. Sushil, "Mycogenic nanoparticles and their bio-prospective applications: current status and future challenges," *Journal of Nanostructure in Chemistry*, vol. 8, no. 4, pp. 369–391, 2018.

[24] A. O. Gloria and J. A. Anthony, "*In vitro* antibacterial, antioxidant, and toxicity profile of silver nanoparticles green – synthesized and characterized from aqueous extract of a spice blend formulation," *Biotechnology & Biotechnological Equipment*, vol. 32, no. 3, pp. 724–733, 2018.

[25] S. S. Sudha, K. Rajamanickam, and J. Rengaramanujam, "Microalgae mediated synthesis of silver nanoparticles and their antibacterial activity against pathogenic bacteria," *Indian Journal of Experimental Biology*, vol. 52, pp. 393–399, 2013.

[26] P. Pradeepkumar, R. Naresh Kumar, A. A. Alarfaj, M. A. Murugan, and M. Rajan, "Deep eutectic solvent-mediated FA-g-β-alanine-co-PCL drug carrier for sustainable and site-specific drug delivery," *ACS Applied Bio Materials*, vol. 1, no. 6, pp. 2094–2109, 2018.

[27] A. M. Pradeepkumar, A. H. Elgorban, and M. Rajan, "Natural solvent-assisted synthesis of amphiphilic co-polymeric nanomicelles for prolonged release of camptothecin delivery," *New Journal of Chemistry*, vol. 42, no. 12, pp. 10366–10375, 2018.

Hindawi
Journal of Nanomaterials
Volume 2022, Article ID 1454037, 7 pages
https://doi.org/10.1155/2022/1454037

Research Article

Influence of Future Material Nano-ZrO_2 and Graphene on the Mechanical Properties of Al Composites

MD. Umar,[1] R. Muraliraja,[1] V. S. Shaisundaram,[2] and Shiferaw Garoma Wayessa[3]

[1]*Department of Mechanical Engineering, Vels Institute of Science, Technology and Advanced Studies, 600117, Chennai, India*
[2]*Department of Automobile Engineering, Vels Institute of Science, Technology and Advanced Studies, 600117, Chennai, India*
[3]*College of Engineering and Technology, Wollega University, Nekemte, Ethiopia*

Correspondence should be addressed to R. Muraliraja; muralimechraja@gmail.com
and Shiferaw Garoma Wayessa; shiferawg@wollegauniversity.edu.et

Received 6 August 2022; Revised 27 August 2022; Accepted 5 September 2022; Published 22 September 2022

Academic Editor: Deepanraj B

Recent developments in mechanical applications have led to the development of metal matrix composites, which represent the future of composite structures. Al7010 aluminium alloy matrix with nano-ZrO_2 and graphene particle reinforced composite is created in this experiment. By adopting the stir casting procedure in two different casting, 2 percent reinforcement of zirconium dioxide and 1 percent of graphene is included in the composite materials. The composite's metallurgical and mechanical characteristics are studied. The SEM image demonstrates uniform dispersion of the particles in the alloy matrix. The manufactured material's ability to gather particulate matter is clearly found in SEM and EDS. The addition of zirconia particles works together to prevent the alloy matrix from dislocating, which increases the base material's hardness as well as its tensile resistance. Similar results are also found in graphene-casting material. Results from tensile tests reveal that adding nano-zirconium dioxide particle (ZrO_2) and graphene boosts the material's tensile and hardness strength. In terms of the ultimate tensile strength (UTS), the Al7010/2% ZrO_2 composite had a 6% increase and Al7010/1% graphene had a 5.5% increase above the Al7010 alloy. Compared to Al7010 alloy, the microhardness of Al7010/ZrO_2 is 17.64% greater and Al7010/1% graphene is 14% greater.

1. Introduction

High-strength, lightweight, and low-cost metal matrix composites are becoming more common in the industry [1]. Aluminium alloys are often used in aircraft and automobiles due to their outstanding strength-to-weight ratio and corrosion resistance. The metal matrix composite (MMC) made from aluminium alloys may be improved by using the right reinforcements [2]. The commercially available 7010 grade aluminium alloy is one of the most widely used general-purpose materials. The chemical composition of the Al7010 alloy is shown in Table 1.

Because of its outstanding mechanical and corrosion resistance, it is widely used in a wide range of industries. This precipitate-hardening aluminium alloy has outstanding weld ability [3]. The most difficult aspect of implementing MMC components has been manufacturing them; nevertheless, mass production techniques using several heat treatments are becoming increasingly realistic. As this technology improves, a greater number of aircraft engines will be able to employ these lighter, more durable components [4]. When compared to an engine made of standard nickel-based superalloys, a jet engine using MMC components has been demonstrated to save between 10% and 15% in fuel. This fuel savings not only saves corporations money but also reduces air travel's severe carbon imprint, making MMCs both economically and ecologically viable. Aircraft now account for roughly 11% of all carbon dioxide emissions in the United States, with estimates that this will quadruple by the midcentury [5]. The immediate advantages of using MMC in aviation engines are evident, but examining the less obvious outcomes is also important. Currently, there are few possibilities for recycling MMCs, but future research may change that. The introduction of MMCs into the aviation sector is a hopeful step toward a more

Table 1: Chemical composition of the Al7010 alloy.

Element	Content (%)
Aluminium, Al	87.8–90.6
Zinc, Zn	5.70–6.70
Magnesium, Mg	2.10–2.60
Copper, Cu	1.50–2.0
Iron, Fe	0.15
Zirconium, Zr	0.10–0.16
Silicon, Si	0.12
Manganese, Mn	0.1
Titanium, Ti	0.06
Chromium, Cr	0.05
Nickel, Ni	0.05
Other, total	0.15

environmentally friendly future. Hard ceramic particles such as SiC, TiB_2, ZrO_2, Gr, TiC, B_4C, and others are used to reinforce the characteristics of the traditional base metal. These ceramic particles may range in size from micro to nano [6]. The inclusion of microsize reinforcing particles, on the other hand, reduces AMMC ductility and fracture toughness [7]. The use of nanosized particles in aluminium metal matrix composites improves fracture toughness and ductility [8]. Madeva Nagaral et al. examined the mechanical and wear characteristics of ultrasonic cavitation stir cast aluminium-boron carbide nanocomposites [9] . Increases in B_4C nanoparticles boosted hardness and tensile strength, as well as wear resistance, as compared to the base alloy. The addition of nanosized B_4C and BN to an aluminium alloy made by ultrasonic aided stir casting raised the tensile strength by 67%. According to Gurushantha et al., the fracture toughness and hardness of Al 2024/Gr composites declined as the Gr wt. % in the composites increased [10]. Rashad Muhammad et al. documented the mechanical and wear characteristics of metal matrix composites [11]. The zircon particles are evenly distributed throughout the aluminium matrix. The mechanical characteristics of aluminium-zircon composites are excellent, including ultimate tensile strength, compression strength, and impact strength. As the proportion of zircon rises, these characteristics improve. The wear resistance of the aluminium-zircon composite is excellent. The hardness qualities of the aluminium-zircon composite are excellent. To optimise the wear processing parameters, the Taguchi approach may be applied. Abdizadeh et al. stated that the researchers looked at how powder metallurgy may enhance the physical and mechanical characteristics of Al/Zircon composites [12]. In powder metallurgy settings, the microstructures of these composites revealed distinct size distributions of zircon when present in varying quantities in the composite. Green specimens were sintered at two temperatures of 600° and 650°C after being created by the isostatic pressing of prepared powders with varying zircon percentages. These samples were then subjected to a variety of physical and mechanical tests to determine which circumstances yielded the best results. The sample with 5% zircon sintered at 650°C had the best pressure quality. With a high unequivocal surface zone and a high Young's modulus, graphene possesses extraordinary characteristics. Because of its good thermal conductivity, graphene is a good rival for Al matrices when it comes to redesigning thermal conductivity. When compared to other reinforcement particles' interfacial exposure areas, graphene particulates' expansion into the Al alloy matrix affects the composite's tribological as well as mechanical behaviour [13–16]. Stir casting procedures are one of the most extensively utilized manufacturing processes for aluminium-based composites, according to the literature. Reinforcement may be disseminated evenly in the alloy matrix and creates superior strength by maintaining the stirring speed and duration. The inclusion of an unequal amount of reinforcements, such as silicon carbide or graphite, increases hardness while decreasing ductility. It was also noted that research on zirconium dioxide-based composites was restricted and that the potential of such composites had yet to be discovered. The inclusion of ceramic particles such as zirconium dioxide into this grade of aluminium alloy enhances stiffness and corrosion resistance while also lowering weight. The decreased thermal expansion also increases the material's dimensional stability, making it suited for high-precision applications. To improve material behaviour, the potential of zirconium dioxide and particle reinforced metal matrix composites must be investigated. The behaviour of a zirconium dioxide particle reinforced aluminium alloy metal matrix composite was investigated in this study employing stir casting techniques. Friction stir casting, powder metallurgy, mechanical alloying, stir casting, and squeeze casting are some of the procedures used to make metal matrix nanocomposites (MMNCs) [17–21].

Metal matrix composites that are high-strength, light-weight, and inexpensive are becoming increasingly popular in the market. Due to its exceptional strength-to-weight ratio and resistance to corrosion, aluminium alloys are often employed in vehicles and aeroplanes. By employing the appropriate reinforcements, such as ZrO2 and graphene, the metal matrix composite (MMC) manufactured of aluminium alloys may be enhanced. Metal matrix composites that are high-strength, light-weight, and inexpensive are becoming increasingly popular in the market. Due to its exceptional strength-to-weight ratio and resistance to corrosion, aluminium alloys are often employed in vehicles and aeroplanes. By employing the appropriate reinforcements, such as ZrO2 and graphene, the metal matrix composite (MMC) manufactured of aluminium alloys may be enhanced. The approach introduced warmed reinforcing particles into a vortex of molten alloy generated by a revolving impeller; because of the density difference between matrix and reinforcement during the melting and casting processes, the procedure resulted in microstructural inhomogeneities, particle agglomeration, and sedimentation. Casting by mechanical stirring, ceramic reinforcing particles are incorporated into the matrix alloy. This technique combines the advantages of both liquid and solid ceramic production. The uniform dispersion of reinforcement particles is made possible by the matrix phase's high viscosity. There is a stronger influence on the distribution of reinforcement and mechanical characteristics, as well as porosity if the right

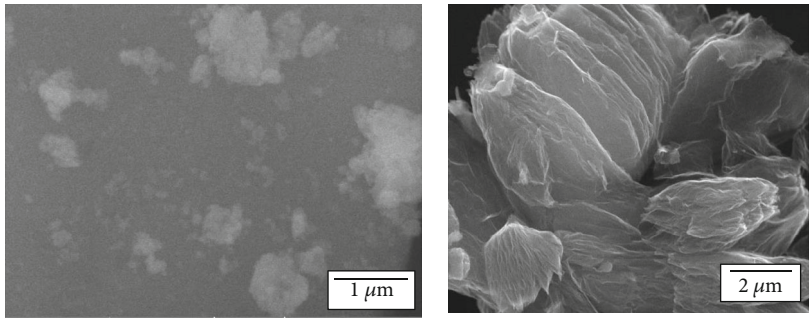

(a) (b)

Figure 1: SEM images of (a) ZrO_2 and (b) graphene.

parameters are used. The combination of zirconium and graphene with Al7070 is not attempted by previous researchers. Based on literature survey, the proposed combination of material will deliver enhancement in the strength and wear resistance because of the hard particle and lubricant property. A stir casting procedure is used in this study to produce Al7070, ZrO_2, and graphene composite, as well as to study the microstructure and mechanical properties of Al7010 alloy reinforced with ZrO_2 ceramic and graphene reinforcements.

2. Materials and Methods

Because of its broad range of applications in the automotive and avionics sectors, Al7010 was chosen as the matrix material. As reinforcements, ZrO_2 particles (2 wt. %) and graphene (1 wt. %) were employed in three distinct casting methods: (1) Al7010 in its pure form, (2) Al7010 with ZrO_2 particles weighing 2%, and (3) for composites, Al7010 with 1% graphene particles.

Fenfee Metallurgical Private Limited in Bengaluru, Karnataka, India, provided the Al7010 composite billets. BT Corp, Hoskote, Bangalore, Karnataka, India, provided the graphene. Minco metal in Bangalore, Karnataka, India, was used to get ZrO_2. Al7010 is used as the matrix material with nanosize (100 nm) ZrO_2 and graphene is used as a reinforcement material. The SEM images of the particles are shown in Figure 1. Initially, the Al7010 was preheated at 450°C in a muffle furnace to remove the surface oxides. The furnace temperature was raised above the liquid temperature of aluminium alloy (750°C) to melt the aluminium alloy completely. Figure 2 shows that the molten metal is stirred in the furnace. The proper stirring produced the best mixing results in a uniform microstructure compared to a conventional stirring. Preheating of the moulds was performed at 250–350°C before pouring the melt. After the removal of slag, the composite melt was transferred to the preheated mould.

The MMC manufacturing process metal matrix composite samples were manufactured utilizing the stir casting procedure in this investigation. The metal matrix was a 7010-grade aluminium alloy, with zirconium dioxide and graphene particles as reinforcement. Samples were made using a reinforcement ratio of 2 wt. %, respectively. Later, two distinct castings of 2 wt. % zirconium dioxide and 1 wt. % graphene particles were introduced to molten aluminium alloy.

Figure 2: Molten metal is stirred in the furnace.

To achieve a homogeneous dispersion of particles, the semiliquid mixture was agitated for around 10 minutes at a 450 rpm constant speed. After that, the semi-liquid mixture was put into a cylindrical casting mould.

3. Results and Discussion

The SEM is used to check for correct reinforcing particle distribution. The SEM of Al 7010 alloy, ZrO_2, and graphene is shown in Figure 2. The consistent homogeneous circulation of ZrO_2 and graphene particles in the Al 7010 alloy may be seen using SEM. It is also clear that there is a strong interfacial interaction between ZrO_2 and graphene and Al7010 alloy, which enhances the alloy's characteristics even more. Al7010's 2 wt. % ZrO_2 and 1 wt. % graphene composites demonstrate Al7010 castability in conjunction with aesthetic fortifications [15].

The EDS allows experts to see what those specific components and quantities are. EDS is one of the most amazing and beneficial sorts of elemental research. The EDS investigation of Al7010 alloy combinations, as well as Al7010-ZrO_2 and graphene, is shown graphically. The EDS spectrograph of Al7010 aluminium amalgam is shown in Figure 3. EDS examinations of Al7010 2 wt % ZrO_2 and 1 wt% graphene composites in the range are shown in Figures 4(a)–4(c) demonstrating the presence of Z and C inside the aluminium alloy Al7010.

3.1. SEM Micrograph. Scanning electron microscope was utilized to inspect the internal structure of the composite and spreading of the reinforcement particles in the produced MMC. The illustrations were refined by means of numerous results of emery sheets reaching from 220 to 1200 grid size

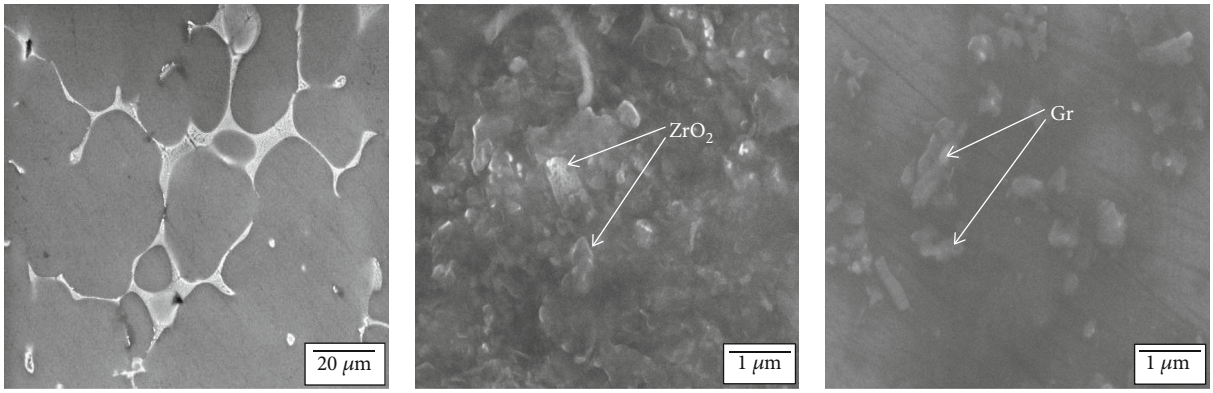

(a) (b) (c)

Figure 3: SEM images of (a) Al7010, (b) Al7010 + 2% ZrO_2, and (c) Al7010 + 1% Gr.

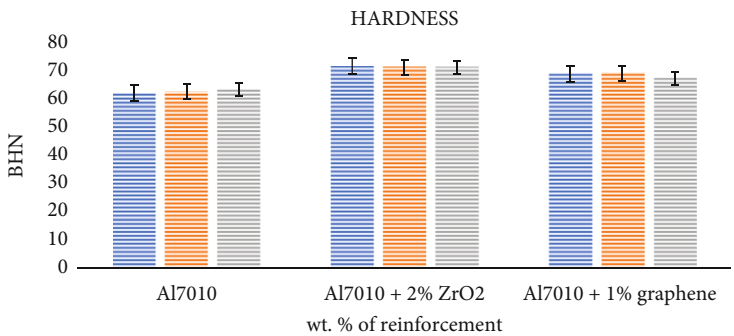

Figure 4: Hardness of Al7010, Al7010 + 2% ZrO_2, and Al7010 + 1% Gr.

and then elegant through an alumina answer to realize a mirror excellence. Keller's agent is used to etch the practiced samples according to conventional methods [16].

Figure 3 shows a scanning electron micrograph of all of the samples. In the 7010 alloy with reinforcement, it demonstrates homogeneous dispersion of ZrO_2 and graphene particles, respectively. The amount of particle aggregation has significantly decreased. It ensures that appropriate stirring was used during MMC manufacturing as cast material has consistent strength due to the random orientation of particles.

3.2. EDS. Figure 5 shows the EDS patterns of base Al7010, Al7010 + 2%ZrO_2, and Al7010 + 1% graphene nanocomposites (a–c). The presence of matrix, ZrO_2, and graphene phases is seen in the result. The intensity diffraction peaks of aluminium in aluminium nanocomposites are high owing to the large quantity of matrix material, but the intensity diffraction peaks of ZrO_2 and graphene nanoparticles are low due to their presence being less than the matrix material. Furthermore, the intensity peaks of aluminium are steadily diminishing as the number of particles reinforced increases. The nanoparticles were found to be evenly dispersed throughout the Al matrix.

3.3. Hardness. The hardness of manufactured MMC with reinforcing weight percentage was measured. Because MMC is made up of a soft matrix alloy and a hard ceramic reinforcement, the position of the hardness measurement is critical. On pure matrix alloy or reinforcement agglomeration zones, measurement should be avoided. The hardness test was carried out according to the ASTM E10 standards using a 10 mm steel ball indenter of 500 Kgf load for a dwell time of 10 seconds. Hardness measurements were made at different locations throughout the material, and the mean results are displayed in Figure 5 with an error bar. It has been observed that as reinforcement increases, hardness improves. MMC's hardness is increased by the inclusion of ZrO2 and graphene particles.

The Brinell hardness number of the sample with 2% ZrO_2 and 1% Gr inclusion is high, as shown in Figure 4, and the values have been shown to rise owing to the addition of particles in the composites. Changes in BHN values from one level to the next are compared and depicted in Figure 4 to analyse the influence of ZrO_2 and graphene inclusion in weight percentage. In contrast, there has been a significant improvement in the microhardness value. The average hardness value for ZrO_2 and graphene is 74.66 BHN and 72.36 BHN. As a result of the inclusion of ZrO_2 particles, the resistance behaviour of the Al7010/ZrO_2 composites to indentation has been dramatically improved.

3.4. Ultimate Tensile Strength and Yield Strength. The mechanical strength of produced MMC samples, including yield and ultimate tensile strength, was determined using the ASTM-E8 tensile test. Figure 4 depicts the major role

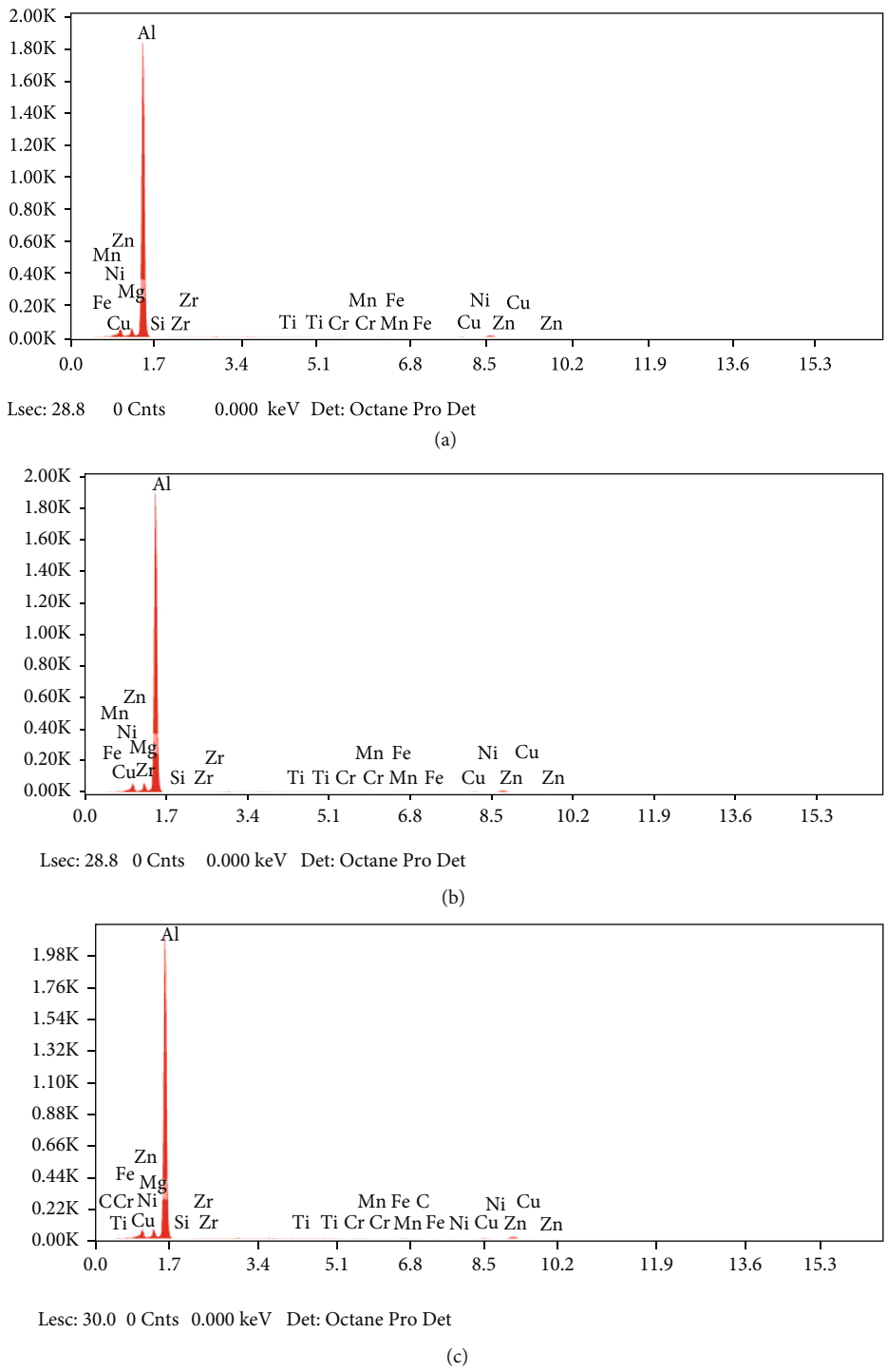

Figure 5: EDS images of (a) Al7010, (b) Al7010 + 2%, ZrO_2, and (c) Al7010 + 1% Gr.

of reinforcement in the MMC, the experimental results of the basic metal, and the alloy with 2% reinforcement, respectively. It has been shown that as the reinforcement of MMC increases, so does the variance in load-bearing capability. The maximum breaking load of MMC is increased by lowering the reinforcing weight %. With more reinforcement, MMC's maximum displacement and breaking load-displacement decrease. Because of the reinforcement, it loses strength quickly during plastic deformation. The effect of graphene and ZrO_2 nanoparticles on the ultimate and yield strength of Al7010 alloy is shown in Figures 6 and 7, respectively.

The inclusion of nanographene and ZrO_2 particles to the Al7010 alloy increased its tensile strength. Al7010 alloy has ultimate and yield strengths of 215.1 and 178.5 MPa, respectively. The presence of nanographene and ZrO_2 dual particles leads to the basic Al7010 alloy's increased strength [17]. The specimens with 2 percent ZrO_2 inclusions showed

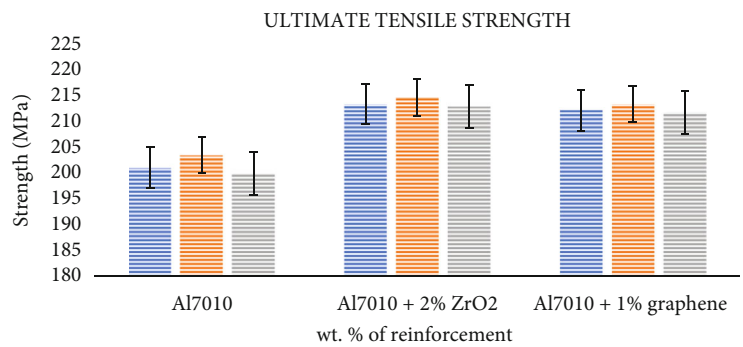

Figure 6: Ultimate tensile strength of Al7010, Al7010 + 2% ZrO_2, and Al7010 + 1% Gr.

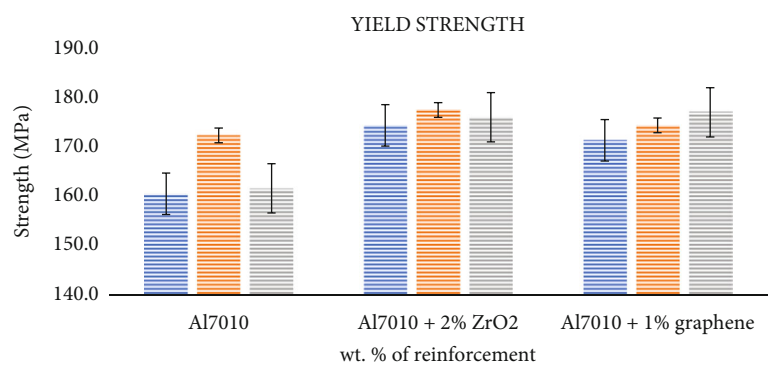

Figure 7: Yield strength of Al7010, Al7010 + 2% ZrO_2, and Al7010 + 1% Gr.

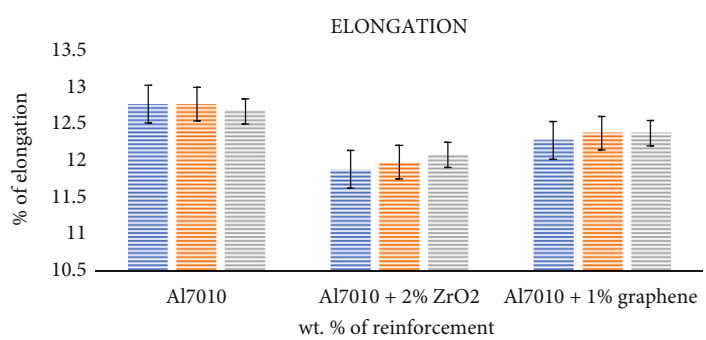

Figure 8: Percentage of elongation of Al7010, Al7010 + 2% ZrO_2, and Al7010 + 1% Gr.

a larger improvement in tensile strength. The average tensile strength for ZrO_2 and graphene is 214.06 MPa and 212.86 MPa. When comparing the ZrO_2 and graphene inclusion specimens, it was shown that graphene has a lower rise in tensile strength due to its solid lubrication, followed by a fall in strength, and the strength at reduced.

3.5. Percentage of Elongation. Figure 8 depicts the influence of nanographene and ZrO_2 particles on the ductility of the Al7010 alloy [22]. The Al7010 alloy's ductility was reduced due to the combined influence of nanographene and ZrO_2 particles. In most cases, graphene particles increase the elongation of the Al matrix; however, in this study, graphene and ZrO_2 composites had lower ductility than the base. The inclusion of hard nano-ZrO_2 particles causes the ductility to be reduced. These ZrO_2 particles outnumber the base Al7010 particles, resulting in a reduction in elongation [17]. These particles function as a limit on the Al7010 alloy matrix's deformation.

4. Conclusion

The following conclusions may be derived based on synthesis and material characterization:

(i) ZrO_2 and graphene particle reinforced aluminium alloy MMC were made in various ratios. The reinforcement is spread evenly within the alloy matrix, according to SEM micrographs. Particle agglomeration in the matrix alloy is minimized by swirling for a long time

(ii) According to hardness testing, the introduction of ceramic particles increases the hardness by 62.8 BHN to 72.6 BHN in reinforcing content. This is because the ceramic particles limited the matrix alloy's dislocation, resulting in improved hardness

(iii) The addition of zirconium dioxide particle reinforcement raises tensile strength from 200.2 MPa to 215.1 MPa, improving the strength

(iv) The prepared material can be used in brake pad application in motorcycles because of its improved strength and hardness

Data Availability

The datasets generated during and/or analysed during the current study are available from the corresponding author on reasonable request.

Conflicts of Interest

The authors declare that they have no conflicts of interest.

References

[1] R. Pandiyarajan, P. Maran, S. Marimuthu, and K. C. Ganesh, "Mechanical and tribological behavior of the metal matrix composite AA6061/ZrO2/C," *Journal of Mechanical Science and Technology*, vol. 31, no. 10, pp. 4711–4717, 2017.

[2] M. Nagaral, V. Hiremath, V. Auradi, and S. A. Kori, "Influence of two-stage stir casting process on mechanical characterization and wear behavior of AA2014-ZrO2 Nano-composites," *Transactions of the Indian Institute of Metals*, vol. 71, no. 11, pp. 2845–2850, 2018.

[3] S. Pandey, N. Son, S. Kim, D. Balakrishnan, and M. Kang, "Locust bean gum-based hydrogels embedded magnetic iron oxide nanoparticles nanocomposite: advanced materials for environmental and energy applications," *Environmental Research*, vol. 214, Part 3, article 114000, 2022.

[4] P. H. Nayak, H. K. Srinivas, M. Nagaral, and V. Auradi, "Characterization and tensile fractography of nano ZrO2 reinforced Copper-Zinc alloy composites," *Frattura ed Integrità Strutturale*, vol. 13, no. 48, pp. 370–376, 2019.

[5] M. Nagaral, V. Auradi, S. A. Kori, and V. Hiremath, "Investigations on mechanical and wear behavior of nano Al2O3 particulates reinforced AA7475 alloy composites," *Journal of Mechanical Engineering and Sciences*, vol. 13, no. 1, pp. 4623–4635, 2019.

[6] S. Shanmugan, N. Saravanan, V. Chithambaram, B. Deepanraj, and G. Palani, "Investigation on single crystal by tartaric acid–barium chloride: growth and characterization of novel NLO materials," *Bulletin of Materials Science*, vol. 43, no. 1, p. 202, 2020.

[7] P. Parthiban, S. Kar, A. K. Mondal, S. Gunasekar, and V. S. Shaisundaram, "Stress-strain behaviour of (hpfrc) high-performance fibre reinforced concrete: an experimental study," *Materials Today: Proceedings.*, 2021.

[8] G. P. Prasad, H. C. Chittappa, M. Nagaral, and V. Auradi, "Effect of the reinforcement particle size on the compressive strength and impact toughness of LM29 alloy-B_4C composites," *Structural Integrity and Life*, vol. 19, no. 3, pp. 231–236, 2019.

[9] M. Nagaral, B. K. Shivananda, V. Auradi, and S. A. Kori, "Development and mechanical-wear characterization of Al2024-nano B4C composites for aerospace applications," *Strength, Fracture and Complexity*, vol. 13, no. 1, pp. 1–13, 2020.

[10] D. M. Patoliya and S. Sharma, "Preparation and characterization of zirconium dioxide reinforced aluminium metal matrix composites," *Engineering and Technology*, vol. 4, pp. 3315–3321, 2015.

[11] S. Malhotra, R. Narayan, and R. D. Gupta, "Synthesis and characterization of aluminium 6061 alloy-flyash & zirconia metal matrix composite," *International Journal of Current Engineering and Technology*, vol. 3, no. 5, pp. 1716–1719, 2013.

[12] S. Saravanakumar, N. K. Chandramohan, S. T. Prabakaran, M. Muniyappan, M. Shanmugam, and V. S. Shaisundaram, "The static structural analysis of torque converter material for better performance by changing the stator angle," *Materials Today: Proceedings*, vol. 37, pp. 1963–1972, 2021.

[13] M. Rashad, F. Pan, A. Tang, and M. Asif, "Effect of graphene nanoplatelets addition on mechanical properties of pure aluminum using a semi-powder method," *Progress in Natural Science: Materials International*, vol. 24, no. 2, pp. 101–108, 2014.

[14] V. S. Shaisundaram, S. Saravanakumar, V. Balambica et al., "Effects of thermal barrier coating using various dosing levels of aluminium oxide nanoadditive fuel on diesel in compressed ignition engine," *Journal of Nanomaterials*, vol. 2022, Article ID 8355098, 10 pages, 2022.

[15] S. E. Shin, H. J. Choi, J. H. Shin, and D. H. Bae, "Strengthening behavior of few-layered graphene/aluminum composites," *Carbon*, vol. 82, pp. 143–151, 2015.

[16] S. F. Bartolucci, J. Paras, M. A. Rafiee et al., "Graphene-aluminum nanocomposites," *Materials Science and Engineering: A*, vol. 528, no. 27, pp. 7933–7937, 2011.

[17] V. Chithambaram, T. S. Franklin Rajesh, G. Palani, E. Ilango, B. Deepanraj, and S. Santhanakrishnan, "Growth and investigation of novel nonlinear optical single crystal of urea potassium dichromate by solution growth technique for photonic application," *Journal of Optics*, vol. 49, no. 2, pp. 181–186, 2020.

[18] R. Muraliraja, R. Elansezhian, and K. Patterson, "Optimization of reducing agent and key parameters effect on the efficiency of electroless ni-p plating by Taguchi method," *Procedia Materials Science*, vol. 5, pp. 2478–2486, 2014.

[19] B. R. Singh, M. Shoeb, W. Khan, and A. H. Naqvi, "Synthesis of graphene/zirconium oxide nanocomposite photocatalyst for the removal of rhodamineB dye from aqueous environment," *Journal of Alloys & Compounds*, vol. 651, pp. 598–607, 2015.

[20] Y. Zhan and G. Zhang, "Graphite and SiC hybrid particles reinforced copper composite and its tribological characteristic," *Journal of Materials Science Letters*, vol. 22, no. 15, pp. 1087–1089, 2003.

[21] D. G. Mallesh, H. S. Manjunatha, V. G. Pradeep Kumar, and D. R. Rakesh, "Mechanical and tribological properties of aluminium Al6061 alloy reinforced with SiC," *International Journal of Emerging Technology and Advanced Engineering*, vol. 5, no. 3, pp. 111–117, 2016.

[22] D. Veeman, S. Palaniyappan, G. J. Surendhar, and R. Shanmugam, "Process optimization of compressive property and dimensional error on wood polylactic acid gyroid-structured polymer composite," *Journal of Reinforced Plastics and Composites*, vol. 7, 2022.

Hindawi
Journal of Nanomaterials
Volume 2022, Article ID 4611251, 8 pages
https://doi.org/10.1155/2022/4611251

Research Article

Glass Fibre Reinforced Epoxy Composites Modified with Graphene Nanofillers: Electrical Characterization

Lokasani Bhanuprakash,[1,2] **Soney Varghese**,[2] **and Sitesh Kumar Singh**[3]

[1]*Department of Mechanical Engineering, MLR Institute of Technology, Hyderabad 500043, India*
[2]*Nanomaterials and Devices Research Laboratory, School of Nano Science and Technology, National Institute of Technology Calicut, Kerala 673601, India*
[3]*College of Engineering and Technology, Wollega University, Nekemte, Ethiopia*

Correspondence should be addressed to Lokasani Bhanuprakash; lokasanibhanu@gmail.com and Sitesh Kumar Singh; sitesh@wollegauniversity.edu.et

Received 5 August 2022; Revised 24 August 2022; Accepted 1 September 2022; Published 20 September 2022

Academic Editor: Senthilkumar N

Composites with improved electrical properties created new pathways in electrical engineering industries. In this work, electrical studies conducted on continuous unidirectional E-glass fibre-reinforced epoxy composites modified with three different graphite oxide fillers are discussed. The three different fillers are (i) graphite oxide (GO), (ii) exfoliated graphite oxide (EGO), and (iii) reduced exfoliated graphite oxide (rEGO). Incorporation of GO fillers exhibited significant improvement in the dielectric characteristics of the composites, where it showed 42% enhancement in breakdown strength values. Dielectric constant measurements of GO-filled composites have also demonstrated considerable enhancement in the values where the fillers promoted interfacial and dipolar polarization phenomena in the material. On the other hand, in the case of EGO and rEGO fillers, conducting nature induced from graphitic structure had significantly reduced the dielectric properties of their composites.

1. Introduction

Due to their versatile properties, glass fibre-reinforced epoxy composites are found extensively used in many engineering sectors such as aerospace, automobile, and civil. In the last two decades, composites with improved electrical properties have created new pathways in electrical engineering industries. For example, a joint venture undertaken by ABB Plast and ABB Components have developed glass fibre-reinforced composites with improved dielectric and mechanical properties for meeting the design specifications of a cylinder used in transformer tap changers [1]. Other potential applications for these composites are high-voltage switchgear, composite cylinders as an alternative to porcelain insulators, electrical insulation for superconducting magnets or magnetic components, etc. [2–5]. Recently, Volvo Car Corporation partnering with researchers from Imperial College London have developed a multifunctional structural composite material by combining carbon fibres, fibreglass, and a polymer resin for primarily using it as a car body structure and secondarily as a battery [6, 7]. Aerospace industries are obviously more interested in employing such composites to gain the extra mileage by increasing fuel efficiency and for storing the electrical energies. In general, these industries often demand for materials which are highly reliable and highly durable (damage-tolerant) in nature. When an electrical equipment is in operation, the insulating materials (mostly epoxy resin) used in the equipment often subject to varieties of electrical discharges. The constant bombardment of electrons and ions generated by discharges produces heat and deteriorates the properties of insulating materials, in turn causing degradation of the material. Thus, the durability of insulating materials is dependent on trapped electrical charges [8], and hence, it is recommended that the insulating materials which are employed in the electrical environments should possess significantly high electrical breakdown strength values.

Glass fibre-reinforced epoxy composites are used for making radar domes (radomes), which is a protective

dielectric housing for a microwave antenna that transmits selective electromagnetic waves [9]. One of the attractive characteristics of these composites is that it possess high damage tolerances because of their ability to resist micro-damage development events such as matrix cracking, delamination, and fibre cracking. Thus, glass fibre-reinforced composites have found a place in the electrical industry as an important class of low dielectric material since they are good electrical insulators possessing low dielectric loss and excellent mechanical properties [10].

The role of fibre-matrix interface and fibre orientation on the dielectric properties of glass fibre-reinforced epoxy composites were studied by Kechaou et al. using the scanning electron microscope mirror effect (SEMME) technique [11]. The SEMME method can be applied to any insulating material, and their ability to trap or diffuse electric charges can be known. In general, epoxy matrix being an insulating material can trap a high amount of charges and long fibres can allow the diffusion of trapped charges along the interface [12]; however, Kchaou and their team's studies on the role of the fibre-matrix interface demonstrated that the interfacial zone is also playing a considerable role in trapping the charges. Hence, a high interface strength medium which can diffuse the trapped charges and is linked to localized polarization energies is recommended for obtaining high dielectric properties to the materials. Dielectric properties of woven glass fibre-reinforced polymer composites were studied in the THz frequency by Kimiyoshi et al., where they identified that the real part of the complex dielectric constant was frequency independent in the 0.2 to 1 THz range and the imaginary part of the dielectric constant was linearly increasing with increasing frequencies in the range of 0.1 to 0.33 THz [10]. Investigations on the dielectric properties of high-performance bishphthalonitrile/polyarylene ether nitrile/glass fibre composite laminates had shown little dependence on frequency [13]. Glass fibre/epoxy composites loaded with plasma-synthesized aluminium nitride powder (10 wt.%) showed enhanced dielectric breakdown strength of 30.26 kV/mm [14]. The addition of three additives, i.e., thiokol, epoxidized natural rubber, and epoxidized linseed oil to the glass fibre-reinforced epoxy composites, had found no significant effect on the dielectric properties [15].

Studies on the dielectric properties of composite materials were often used for evaluating the damage phenomenon occurring in the composites [6]. Fazzino and his group have used electrochemical impedance spectroscopy to characterize the damage initiation and progression in woven glass fibre-reinforced epoxy composites [16]. In measuring the damage developed, they obtained larger, more consistent, and clearer distinctions compared to common methods which work based on physical properties or visual assessments. The effect of electric stress on glass fibre-reinforced epoxy composites under a wet environment has been examined by Gao et al., where they studied morphological changes in the composite surfaces and development trend of current for assessing the degradation process of composites [3].

In recent years, interest on natural fibre-reinforced polymer composites has been growing wider, which is mainly due to the features of natural fibres, i.e., low cost, low density, ease in its processing, and being renewable and biodegradable in nature [17–20]. Elammaran and coworkers have conducted a comparative study on the dielectric properties of synthetic (glass) and natural (bamboo) fibre-reinforced epoxy composites [19]. They noticed all the composites showing improved dielectric properties compared to pure epoxy resin in which only instantaneous atomic and ionic polarizations are possible. With the concentration of fibres increasing in the matrix, the dielectric properties of composites were also improved; however, at higher concentrations (20 wt.%), the amount of free charges accumulating at the interface was found to be increased, leading to higher interfacial polarization resulting in lower dielectric properties. Incorporating glass fibres in chopped form in the epoxy composites demonstrated higher dielectric properties compared to bamboo fibres. In general, natural fibres show lower modulus, lower strength, and higher moisture absorption; to overcome these limitations, natural fibres are combined with synthetic fibres at an optimized ratio in fabricating their hybrid composites [20]. Dielectric properties of Roystonea regia fibres combined with glass fibres/epoxy composites were studied by Goud and Rao, where they identified an increase in glass fibre content in the hybrid composites which resulted in a decrease in dielectric constant values at all the frequencies [20]. The addition of more

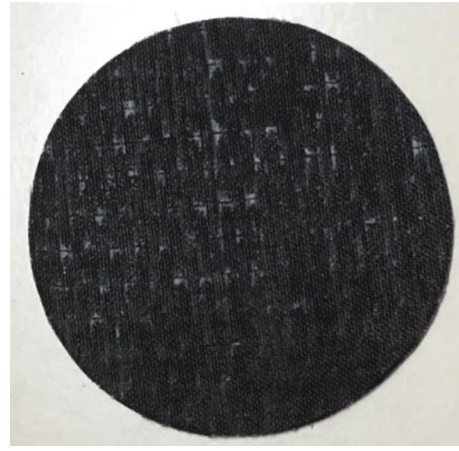

Figure 1: Photograph of composite test specimen (circular disc) for electrical characterization.

(a) (b)

Figure 2: Photographs of the Impedance analyser test setup (a) for dielectric characterization of samples; sample holder (b).

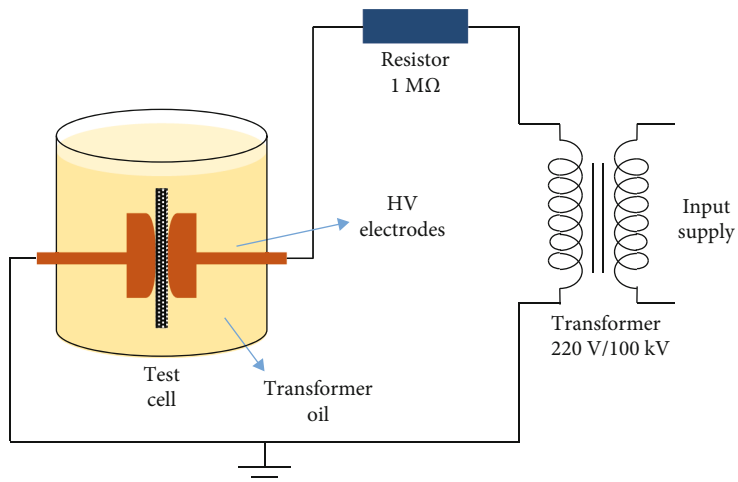

Figure 3: Schematic diagram of the experimental setup for AC dielectric breakdown voltage measurements.

amounts of glass fibres in the hybrid system caused a reduction in availability of polar groups; as a result, a decrease in dielectric constant values is observed.

In the present investigation, the dielectric properties of glass fibre-reinforced epoxy composites modified with three different graphene fillers are studied. The three different forms of graphene fillers incorporated are graphite oxide (GO), exfoliated GO (EGO), and reduced EGO (rEGO). The measurements of dielectric constant, loss factors, and dielectric breakdown strength are obtained according to the corresponding ASTM standards.

2. Experimental

2.1. Materials. Bisphenol-based epoxy resin (epofine 1564) and polyetheramine-based hardener (finehard 3486) procured from Fine Finish Organics Pvt. Ltd., India, are used as the matrix system. An E-glass fabric of 500 gsm purchased from Urja Products Pvt., Ltd., India, is used as reinforcement system for the composite. Different variants of graphene prepared in the laboratory are used for the work. All the materials used in this work are the same as mentioned in our earlier published work [21, 22]. The materials and the method description partly reproduces the wording [21, 22].

2.2. Preparation of Composites. Hybrid glass fibre-reinforced epoxy composites were fabricated by varying concentrations of GO, EGO, and rEGO fillers at 0.5, 1, and 2.5 wt.%, respectively, through a simple hand layup method using the vacuum bagging technique. The fabrication methodology of composite laminates is the same as discussed in our earlier work [21, 22]. The composites prepared for different electrical tests have used 4 fabric plies to produce laminate thicknesses in the range of 1–1.3 mm. Test specimens were cut into 75 mm diameter circular discs (Figure 1).

2.3. Characterization. The dielectric characteristics of composites are measured using an Impedance analyser (Wayne Kerr Electronics) using an in-house-developed sample holder by scanning at a frequency range of 20 Hz to 1 MHz with a bias voltage of 1 V. The sample holder employed is a spring-controlled one so that a good contact between the sample and electrodes is achieved. The samples of diameter 75 mm and thickness about 1 mm were used for testing. Photographs of the Impedance analyser instrument and the sample holder are shown in Figure 2. Breakdown

Figure 4: Photographs of the AC dielectric breakdown test setup and sample holder (inset picture).

Table 1: Dielectric breakdown strength measurements of all the composites.

	Breakdown strength (kV/mm)		% change
	Mean	S.D.	
Baseline	21.59	0.54	
EP-GO (0.5)	22.94	2.11	6.25
EP-GO (1)	30.69	2.19	42.14
EP-GO (2.5)	29.43	1.77	36.31
EP-EGO (0.5)	18.18	1.00	−15.79
EP-EGO (1)	10.17	3.03	−52.89
EP-EGO (2.5)	8.15	2.20	−62.25
EP-rEGO (0.5)	13.33	0.64	−38.25
EP-rEGO (1)	8.7	2.34	−59.7
EP-rEGO (2.5)	7.46	1.26	−65.44

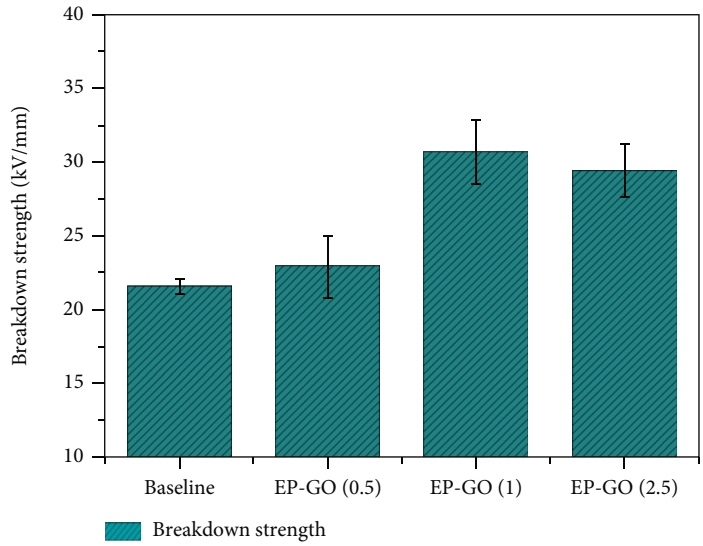

Figure 5: Dielectric breakdown strength measurements of glass fibre-reinforced composites filled with GOs.

voltage measurements are obtained from an experimental setup (Figure 3) designed according to ASTM D149 [23].

Photographs of the breakdown voltage instrument setup and the sample holder are shown in Figure 4. Here, 25 mm diameter high-voltage (HV) electrodes with an edge radius of 3.2 mm were chosen for conducting the experiments. To avoid surface flashover, the complete electrode assembly was submerged in transformer oil. By applying an AC voltage to the HV electrodes, breakdown strength experiments were performed at a rate of 0.5 kV/sec until the sample got punctured. As the voltage increased, bubbling in the oil was observed near the end of the electrodes at the curved region. Most of the samples have noticed puncturing at the regions close to the electrode contact points, and the corresponding voltage was recorded for calculating the breakdown strength. The dielectric breakdown strength was calculated according to the equation: $E = V/d$, where V is the breakdown voltage and d is the thickness of the sample close to the point at which the puncture took place. At least five specimens were tested in each configuration, and the average values were plotted.

3. Results and Discussion

3.1. Dielectric Breakdown Strength Measurements. Dielectric breakdown strength is defined as the maximum voltage at which material gets punctured to the thickness of the material near the point of puncture. Breakdown in polymer-based insulators occurs at a point close to the electrodes, which is a catastrophic failure that generally is an irreversible and destructive process. In solid materials, breakdown occurs due to long-interval partial discharges which generate heat and cause degradation of the material near the area of electrodes. The continued discharges eventually char the material and allow the current to conduct through a passage of carbonized material. The AC dielectric breakdown studies of glass fibre-reinforced epoxy composites modified with three different graphene fillers were carried out according to ASTM standard D149, and the values of corresponding composites are summarized in Table 1.

The dielectric breakdown strength measurements of GO-filled epoxy composites are shown in Figure 5. The breakdown strength of the baseline glass fibre/epoxy composite system is measured as 21.6 kV/mm. It can be observed from the results that the breakdown strength measurements of GO-filled glass fibre-reinforced composites have noticed a significant improvement in their values, where the maximum enhancement of 42% was noted with 1 wt.% of GO fillers. The improvement in breakdown values for 0.5 wt.% GO-filled composites is found to be marginal compared to baseline ones. As the concentration of GOs increased in the composite system, the strength values reached a maximum value at 1 wt.% and then values started decreasing by showing an enhancement of 36% at 2.5 wt.%. At a lower concentration of fillers, the availability of fillers in the matrix resin will be small and the interlayer distances between them will become more. Consequently, the volume fraction of the pure polymer will become more. In this scenario, when a high amount of electric stress is applied, the mobility of charges between the electrodes becomes easier through the loose polymer [24].

The above results can be explained with the understanding of the key differences possessed by these three filler materials, GO, EGO, and rEGO. The critical characterization of the GO, EGO, and rEGO fillers was conducted, and the results were discussed in our earlier works [21]. In brief, GO fillers are observed with oxygen-containing functional groups such as hydroxyl, epoxide, carbonyl, and carboxyl groups with disordered morphology. The exfoliation and chemical reduction of GO resulted in EGO and rEGO fillers, which have removed these functional groups in both cases and restored the graphitic structure with expanded sheets with wrinkles at the edges and thin and fluffy morphology, respectively.

Graphite oxide being in oxide form acts as an insulating material, the insulating behaviour of which is purely

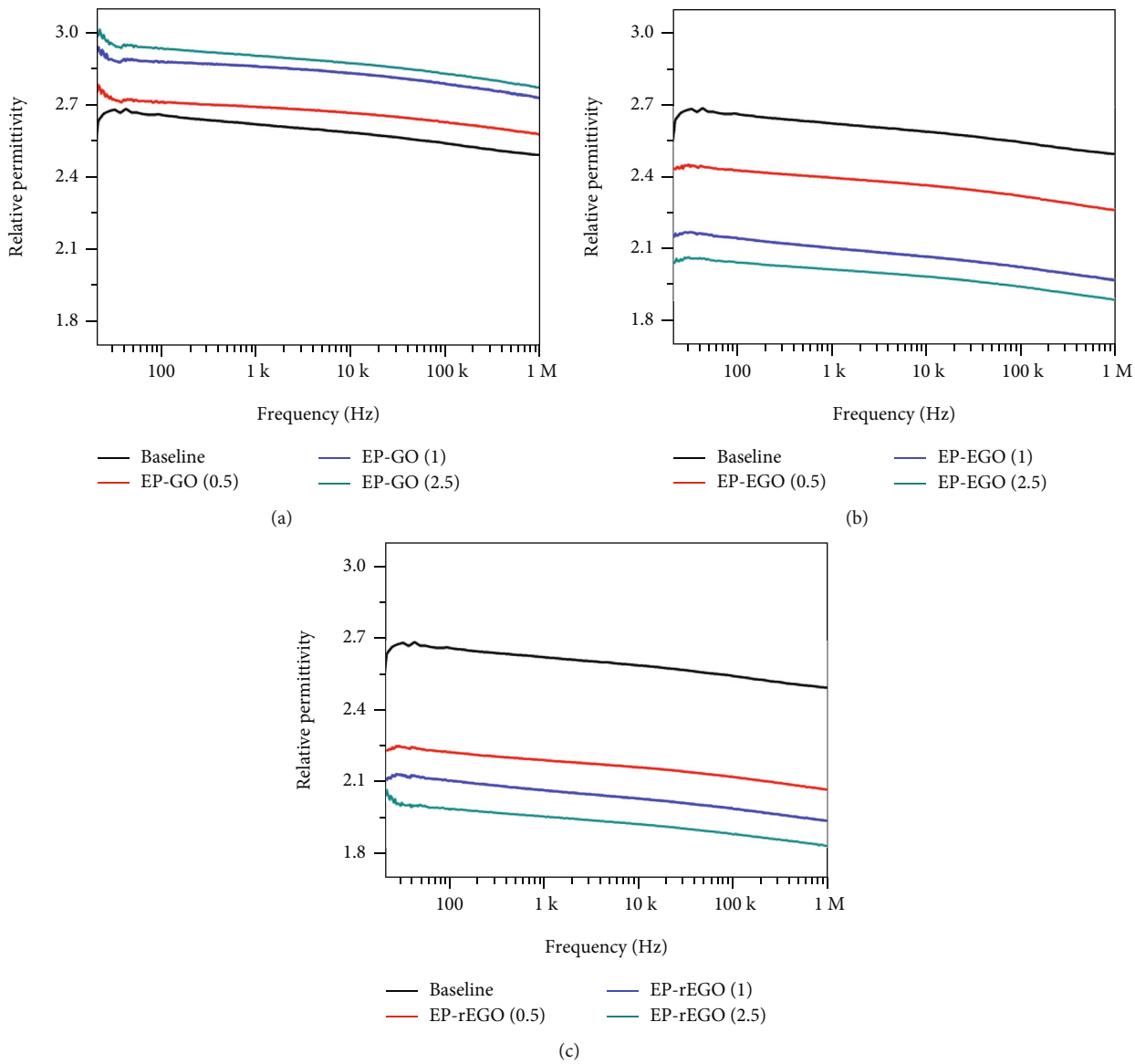

Figure 6: Dielectric constant measurements of glass fibre/epoxy composites modified with graphite oxide derivatives.

dependent on the degree of oxidation. The difference in permittivity values between matrix resin and filler material causes field enhancement near the particles leading to partial discharges. However, it is probable that the field enhancement can occur due to the presence of voids; hence, it cannot provide sufficient explanations for breakdown phenomena [25]. The synergetic effect of surface discharges, the localized partial discharges at particle sites, and the ease in mobility of charges through loose polymers will dictate the final breakdown of the material [8]. In the case of GO fillers, the functional groups present on their surfaces can form hydrogen bonds with the matrix resin and they can form secondary bonds with the reinforcement fibres as well. When the loading of GO increased in the matrix resin, GO fillers tightly bind with the matrix resin; as a result, the packing density and interfacial polarization predominantly get improved in the composite system. In addition, the mobility of charges through dense matrix resin will become tough and space charge distribution will be altered. All these factors contribute to oppose the flow current between the electrodes, which leads to enhanced dielectric breakdown values for the materials. On the other hand, composites modified with EGO and rEGO fillers have observed a deterioration in breakdown strength values. As the concentration of EGO and rEGO fillers increases, the dielectric breakdown strength values of composites were found to be decreased. It is mainly attributed to the conducting nature of the fillers. In the case of EGO, thermal exfoliation of GO caused defunctionalization and partial restoration of the graphitic structure. In case of rEGO, the chemical reduction treatment involved in its production has removed most of the functional groups and restored the graphene structure. The conducting behaviour of EGO and rEGO fillers has dramatically tailored the composite charge storage and dissipation capabilities, and they promoted the flow of current between the electrodes.

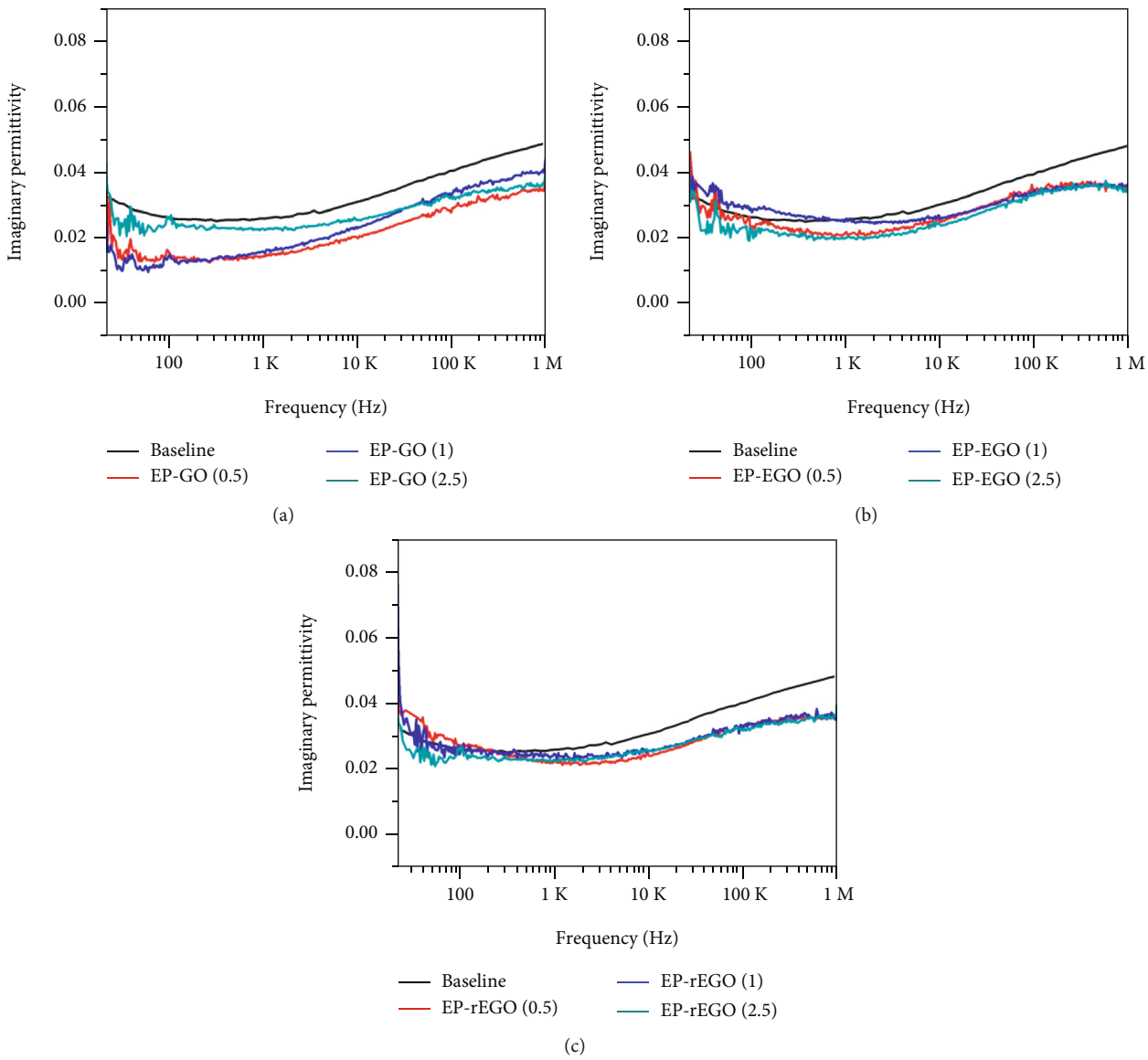

Figure 7: Imaginary permittivity measurements of glass fibre/epoxy composites modified with graphite oxide derivatives.

3.2. Dielectric Constant and Dielectric Loss Measurements. When an electric field is applied to a dielectric material, induced electric charges shift from its equilibrium positions causing dielectric polarization. The measure of polarizability of a material is known as dielectric property. It is an important property which provides information regarding storage and dissipation of electric and magnetic energies in the material. The permittivity (ε) is also commonly referred to as the dielectric constant of material, which represents the material's ability to store electrical energy with the applied electric field. Dielectric constant is the measure of relative permittivity (ε_r) of a material, which is defined as the permittivity of a material relative to the permittivity of a vacuum. The real part of relative permittivity (ε') indicates the ability of material to store the electric energies, whereas the imaginary part (ε'') gives the measure of energy loss. Figure 6 presents the relative permittivity measurements of nanofiller-incorporated glass fibre-reinforced epoxy composites. These measurements were carried out in the frequency range from 20 to 1 MHz using an Impedance analyser. It can be observed from the graphs that the real permittivity values increased with the decrease in frequencies, which is mainly due to the space charge polarization as well as dipolar polarization [26]. When an alternating electric field is applied, the dipolar groups present in the material will orient at lower frequencies in the direction of flow of current. At higher frequencies, the dipoles which are big in size will not get sufficient time to orient in the direction of flow of current and thus it notices a decrease in permittivity values.

GO-filled composites have shown improved dielectric properties compared to the unmodified composites, where the relative permittivity values were found to be increased with the increase in loading concentration of GOs. Typically, in the baseline glass fibre/epoxy composite system, polar groups such as $-NH_2$ and $-NH$ from curing agents, epoxide,

hydroxyl groups, and a few secondary bonds were available for dipole polarization. Through the addition of GO fillers, a new bond formation takes place between the matrix and the fillers and between the reinforcement and the fillers. These additional bonding groups provide the extra dipoles to orient in the direction of flow of current which leads to an increase in permittivity values [27]. Graphite oxide being an insulating material, it can trap significant amount of charges within and at the interfaces, which eventually increases the space charge accumulation at the electrodes. The synergic effect of all these factors contributes in improving the permittivity of values of GO-filled glass fibre composites [28]. On the other side, EGO and rEGO fillers being conductive in nature, they allow the flow of current through them without the accumulation of charges leading to deterioration of the permittivity values. The same was confirmed in the results which shows the decrease in permittivity values is reciprocal to the increase in loading concentrations of EGO and rEGO fillers (Figure 6).

The imaginary part of permittivity illustrates the losses involved in a dielectric material due to the storage and dissipation of electrical charges. Figure 7 shows the imaginary permittivity measurements of glass fibre-reinforced epoxy composites modified with graphite oxide derivatives as a function of frequency. The loss factor in all the composites was found to be decreased with the incorporation of graphene-based fillers. Particularly, GO-filled composites demonstrated significantly lower values compared to the baseline system. It indicates that with the incorporation of GO fillers, composites have improved the storage capabilities of the charges and minimized the occurring losses. On the other hand, at lower frequencies, EGO- and rEGO-filled composites showed imaginary permittivity values close to the baseline composite. With the increase in frequency, these composites showed lower dielectric loss values which may be attributed to the conductive nature of the EGO and rEGO fillers.

4. Conclusions

Dielectric characteristics of E-glass fibre-reinforced epoxy composites modified with graphite oxide derivatives were studied according to relevant ASTM standards, where graphite oxide-filled composites have shown enhancement in dielectric breakdown strength and dielectric constant values. At 1 wt.% of GOs, glass fibre composites have noticed the highest improvement in breakdown strength values gaining by 42%. With the increase in concentration of GOs, dielectric constant measurements also showed significant enhancements in their values. Oxygen-containing functional groups present on the surfaces of GOs were found involved in covalent bonds such as hydrogen with the epoxide matrix, which created new interface regions. The newly formed interface regions participated in polarization upon the application of an external electric field. In addition, the dipoles created during the covalent bonds are also involved in dipolar polarization. The synergetic effect of this phenomenon contributed in improving the dielectric properties of GO-filled glass fibre/epoxy composites. On the other hand, the conducting nature of EGO and rEGO fillers was found to be reducing the dielectric breakdown strength and dielectric constant values by allowing the flow of current between the electrodes. Imaginary permittivity measurements of all the composites modified with fillers have shown considerable reduction in dielectric losses occurring during the storage and dissipation of electric charges.

Data Availability

The datasets generated during and/or analysed during the current study are available from the corresponding author on reasonable request.

Additional Points

Supporting Information. The materials used, preparation of graphene nanofillers, fabrication of composites and characterization of nanofillers are clearly discussed in our earlier publications [21, 22]. The hyperlinks for the same is as followed: 21. doi:10.1002/pc.24809 22. doi:10.1016/j.compscitech.2019.04.034

Conflicts of Interest

The authors declares that there is no conflict of interest regarding the publication of this article.

References

[1] A. Strombeck and T. Larsson, "Fiber-reinforced composites-extra mechanical and electrical strength for transformer tap-changers," *Composite Materials*, vol. 42, pp. 38–42, 1999.

[2] S. Li, H. Tsang, Y. Cheng, and Z. Lu, "Seismic testing and modeling of cylindrical electrical equipment with GFRP composite insulators," *Composite Structures*, vol. 194, pp. 454–467, 2018.

[3] Y. Gao, X. Liang, Y. Liu, W. Bao, S. Li, and C. Wu, "Effect of electrical stress on glass fiber reinforced polymer used in high voltage composite insulator under wet environment," *Composites Science and Technology*, vol. 155, pp. 151–159, 2018.

[4] S. Rajiv, V. L. Tanna, C. V. S. Rao et al., "Development of indigenous insulation material for superconducting magnets and study of its characteristics under influence of intense neutron irradiation," in *IOP Conference Series: Materials Science and Engineering, Volume 171, 26th International Cryogenic Engineering Conference & International Cryogenic Materials Conference*, New Delhi, India, 2017.

[5] K. P. Weiss, S. Westenfelder, A. Jung, N. Bagrets, and W. Fietz, "Determination of mechanical and thermal properties of electrical insulation material at 4.2 K," *AIP Conference Proceedings*, vol. 1435, pp. 148–155, 2012.

[6] M. R. Raihan, "Dielectric properties of composite materials during damage accumulation and fracture. Doctor of philosophy PhD dissertation," in *Mechanical Engineering*, University of South Carolina, Columbia, USA, 2014.

[7] "Volvo develops body panels that serve as batteries," April 2021, http://www.carbodydesign.com/2013/10/volvo-develops-body-panels-that-serve-as-batteries/.

[8] P. Preetha and M. J. Thomas, "AC breakdown characteristics of epoxy nanocomposites," *IEEE Transactions on Dielectrics and Electrical Insulation*, vol. 18, no. 5, pp. 1526–1534, 2011.

[9] P. C. Kim, D. G. Lee, W.-G. Lim, and I. S. Seo, "Polarization characteristics of a composite stealth radome with a frequency selective surface composed of dipole elements," *Composite Structures*, vol. 90, no. 2, pp. 242–246, 2009.

[10] K. Naito, Y. Kagawa, S. Utsuno, T. Naganuma, and K. Kurihara, "Dielectric properties of woven fabric glass fiber reinforced polymer-matrix composites in the THz frequency range," *Composites Science and Technology*, vol. 69, no. 11-12, pp. 2027–2029, 2009.

[11] B. Kechaou, M. Salvia, K. Benzarti, C. Turki, Z. Fakhfakh, and D. Tréheux, "Role of fiber/matrix interphases on dielectric, friction, and mechanical properties of glass fiber-reinforced epoxy composites," *Journal of Composite Materials*, vol. 46, no. 2, pp. 131–144, 2012.

[12] B. Kchaou, C. Turki, M. Salvia, Z. Fakhfakh, and D. Tréheux, "Role of fibre–matrix interface and fibre direction on dielectric behaviour of epoxy composites," *Composites Science and Technology*, vol. 64, no. 10-11, pp. 1467–1475, 2004.

[13] Z. Chen, Y. Lei, H. Tang, J. Wei, and X. Liu, "Mechanical, thermal, electrical, and interfacial properties of high-performance bisphthalonitrile/polyarylene ether nitrile/glass fiber composite laminates," *Polymer Composites*, vol. 34, no. 12, pp. 2160–2168, 2013.

[14] P. Panda, G. Mishra, S. Mantry, S. K. Singh, and S. P. Sinha, "A study on mechanical, thermal, and electrical properties of glass fiber-reinforced epoxy hybrid composites filled with plasma-synthesized AlN," *Journal of Composite Materials*, vol. 48, no. 25, pp. 3073–3082, 2014.

[15] C. M. Vu, L. T. Nguyen, T. V. Nguyen, and H. J. Choi, "Effect of additive-added epoxy on mechanical and dielectric characteristics of glass fiber reinforced epoxy composites," *Polymer Korea*, vol. 38, no. 6, pp. 726–734, 2014.

[16] P. D. Fazzino, K. L. Reifsnider, and P. Majumdar, "Impedance spectroscopy for progressive damage analysis in woven composites," *Composites Science and Technology*, vol. 69, no. 11-12, pp. 2008–2014, 2009.

[17] P. A. Sreekumar, J. M. Saiter, K. Joseph, G. Unnikrishnan, and S. Thomas, "Electrical properties of short sisal fiber reinforced polyester composites fabricated by resin transfer molding," *Composites. Part A, Applied Science and Manufacturing*, vol. 43, no. 3, pp. 507–511, 2012.

[18] Z. Ghallabi, H. Rekik, S. Boufi, M. Arous, and A. Kallel, "Effect of the interface treatment on the dielectric behavior of composite materials of unsaturated polyester reinforced by alfa fiber," *Journal of Non-Crystalline Solids*, vol. 356, no. 11-17, pp. 684–687, 2010.

[19] J. Elammaran, T. C. Peng, B. M. K. Bin, and K. Akshay, "Comparative analysis on dielectric properties of polymer composites reinforced with synthetic and natural fibers," *Journal of Vinyl & Additive Technology*, vol. 24, pp. E201–E216, 2018.

[20] G. Goud and R. N. Rao, "Mechanical and electrical performance of Roystonea regia/glass fibre reinforced epoxy hybrid composites," *Bulletin of Materials Science*, vol. 35, no. 4, pp. 595–599, 2012.

[21] L. Bhanuprakash, A. Ali, R. Mokkoth, and S. Varghese, "Mode I and mode II interlaminar fracture behavior of E-glass fiber reinforced epoxy composites modified with reduced exfoliated graphite oxide," *Polymer Composites*, vol. 39, no. S4, pp. E2506–E2518, 2018.

[22] L. Bhanuprakash, S. Parasuram, and S. Varghese, "Experimental investigation on graphene oxides coated carbon fibre/epoxy hybrid composites: mechanical and electrical properties," *Composites Science and Technology*, vol. 179, pp. 134–144, 2019.

[23] American Society for Testing and Materials, *Standard Test Method for Dielectric Breakdown Voltage and Dielectric Strength of Solid Electrical Insulating Materials at Commercial Power Frequencies*, ASTM International, 2013.

[24] T. Tanaka, "Dielectric nanocomposites with insulating properties," *IEEE Transactions on Dielectrics and Electrical Insulation*, vol. 12, no. 5, pp. 914–928, 2005.

[25] R. Lovell, "The effect of specimen size on the electric breakdown of unfilled and filled epoxy polymers," *IEEE Transactions on Electrical Insulation*, vol. EI-11, no. 4, pp. 110–114, 1976.

[26] P. Preetha, M. J. Thomas, and R. Ranjan, "Electrothermal ageing of epoxy nanocomposites," *IEEE Transactions on Dielectrics and Electrical Insulation*, vol. 19, no. 6, pp. 2081–2089, 2012.

[27] K. C. Kao, *Dielectric Phenomena in Solids: With Emphasis on Physical Concepts of Electronic Processes*, Elsevier, USA, 1st edition, 2004.

[28] P. Preetha and M. J. Thomas, "Partial discharge resistant characteristics of epoxy nanocomposites," *IEEE Transactions on Dielectrics and Electrical Insulation*, vol. 18, no. 1, pp. 264–274, 2011.

Hindawi
Journal of Nanomaterials
Volume 2023, Article ID 9825217, 1 page
https://doi.org/10.1155/2023/9825217

Retraction

Retracted: Spatial-Temporal Variation Characteristics of Soil Moisture and Nutrients Based on Nanomaterials in the Root Zone of Haloxylon ammodendron Seedlings

Journal of Nanomaterials

Received 20 June 2023; Accepted 20 June 2023; Published 21 June 2023

This article has been retracted by Hindawi following an investigation undertaken by the publisher [1]. This investigation has uncovered evidence of one or more of the following indicators of systematic manipulation of the publication process:

1. Discrepancies in scope
2. Discrepancies in the description of the research reported
3. Discrepancies between the availability of data and the research described
4. Inappropriate citations
5. Incoherent, meaningless and/or irrelevant content included in the article
6. Peer-review manipulation

The presence of these indicators undermines our confidence in the integrity of the article's content and we cannot, therefore, vouch for its reliability. Please note that this notice is intended solely to alert readers that the content of this article is unreliable. We have not investigated whether authors were aware of or involved in the systematic manipulation of the publication process.

Wiley and Hindawi regrets that the usual quality checks did not identify these issues before publication and have since put additional measures in place to safeguard research integrity.

We wish to credit our own Research Integrity and Research Publishing teams and anonymous and named external researchers and research integrity experts for contributing to this investigation.

The corresponding author, as the representative of all authors, has been given the opportunity to register their agreement or disagreement to this retraction. We have kept a record of any response received.

References

[1] Z. Wang, H. Gu, A. Yan et al., "Spatial-Temporal Variation Characteristics of Soil Moisture and Nutrients Based on Nanomaterials in the Root Zone of Haloxylon ammodendron Seedlings," *Journal of Nanomaterials*, vol. 2022, Article ID 9202493, 15 pages, 2022.

Hindawi
Journal of Nanomaterials
Volume 2022, Article ID 9202493, 15 pages
https://doi.org/10.1155/2022/9202493

Research Article

Spatial-Temporal Variation Characteristics of Soil Moisture and Nutrients Based on Nanomaterials in the Root Zone of Haloxylon ammodendron Seedlings

Ze Wang, Haibin Gu, An Yan, Pingan Jiang, Hao Ma, Jiandong Sheng, and Wentai Zhang

College of Resources and Environment & Xinjiang Key Laboratory of Soil and Plant Ecological Processes, Xinjiang Agricultural University, Urumqi, 830052, China

Correspondence should be addressed to Pingan Jiang; 19402075@masu.edu.cn

Received 14 July 2022; Revised 1 August 2022; Accepted 6 August 2022; Published 22 August 2022

Academic Editor: Ao Xia

Haloxylon ammodendron is the main constituent species in the desert area of Junggar Basin, which plays a key role in biodiversity protection and regional ecological balance. Replenishment and settling capacity of seedlings determine population regeneration and community stability, and soil moisture and nutrients are the main limiting factors of natural regeneration. In view of the serious degradation and low seedling survival rate of Haloxylon ammodendron forest in Junggar, typical degraded Haloxylon ammodendron population was selected in Gurbantunggut Desert. The effects of soil moisture on soil nutrients were explored, and the temporal and geographical fluctuations of soil moisture and nutrients in the root zone of Haloxylon ammodendron seedlings were clarified. The results showed that soil moisture and nutrient content in the root zone of seedlings had obvious temporal and spatial variation characteristics. With the advance of the growth period, it decreased at first and then increased, reaching the maximum in April and the minimum in August. In the soil horizontal space (0~40 cm), with the extension of the horizontal distance, the soil moisture content has an obvious "wet island" effect, and the soil moisture content at the 10 cm level is 1.99 times that at the 40 cm level in August, when the growth period is the driest. The nutrients available in the soil were clearly "poor on the inside and high on the outside." The degrees of soil natural matter, soluble hydrolyzable nitrogen, accessible phosphorus, and accessible potassium in August were 57.97%, 44.37%, 75.46%, 19, and 55% higher at the 40 cm level of the sapling spine, 10 cm level each. The soil moisture content increased first, then declined, and the soil nutrient content gradually fell in the vertical (0.50 cm) space of soil as soil depth increased. The soil moisture content in the 20~30 cm layer is the highest, reaching 11.04%, 7.90%, 2.92%, and 4.29%, respectively, in each period. Soil water content in 0~30 cm was significantly affected by habitat rainfall ($P < 0.05$), and soil water had a higher effect on soil organic matter, alkali-hydrolyzable nitrogen, and available potassium ($P < 0.05$).

1. Introduction

Vegetation degradation under climate change has become a hot issue in international research, especially focusing on the relationship between vegetation and its environment (soil moisture and nutrients). Seedling settlement is a key link in the process of Haloxylon ammodendron population renewal, and its ecological adaptation mechanism is a research hotspot in the field of ecology. The desert ecological environment is extremely bad, with the problems of serious degradation of Haloxylon ammodendron population and low survival rate of natural seedlings, resulting in the continuous reduction of the area of natural Haloxylon ammodendron forest, which has been listed as a national class III endangered plant [1], and the continuous reduction of the area of Haloxylon ammodendron forest has caused the disintegration of the ecological balance in the region [2], It not only seriously affects the process of Haloxylon ammodendron population renewal but also hinders the process of desert ecological control.

Haloxylon ammodendron (C.A. Mey.) Bunge (also known as Haloxylon Bunge) is a perennial shrub of

Haloxylon Bunge in Chenopodiaceae. It is a constructive species and dominant species in Gurbantunggut Desert. It has the characteristics of drought resistance, barren, saline alkali resistance, and wind sand resistance. It is known as the "desert guard" ([3–6]); the parasitic Cistanche deserticola in its roots is known as "desert ginseng". The desert community formed by Haloxylon ammodendron as the dominant species provides habitat and breeding habitat for nearly 200 species of animals and plants. It is an important place for biodiversity protection in desert areas and plays an irreplaceable role in sand prevention and fixation, mitigating desertification, maintaining regional ecological balance, and promoting national economic development [6–10].

The physiological and ecological adaptability of Haloxylon ammodendron seedlings determines its survival ability and plays a key role in the recruitment, maintenance, expansion, and recovery of the Haloxylon ammodendron population [11]. Under the condition of natural precipitation in the desert, the survival, growth, and development of Haloxylon ammodendron seedlings mainly depend on the shallow soil water and nutrients. The theory of the change characteristics of water and nutrient content in the horizontal and vertical space of shallow soil in the root zone, which is most closely related to the survival of seedlings, is not clear, and there is no ready-made and systematic conclusion on the impact of habitat soil water change on soil nutrients. The research of Haloxylon ammodendron young seedlings' temporal and geographic variation features, as well as the effects of soil moisture and nutrients in the root zone, is useful in mastering the adaptive link between seedling growth and environment.

1.1. Research Progress of Desert Soil Moisture Characteristics. The spatial dispersion aspects of soil dampness and supplements represent the relationship between soil dampness, supplements, and ecological situations. The development, improvement, and circulation of vegetation in the over the ground vegetation framework are totally impacted by the spatial fluctuation of soil dampness and supplements [12]. Previous studies have shown that the desert area on the southeast edge of Junggar has poor environmental conditions (lack of soil moisture and nutrients) which is the main factor limiting plant growth, and it is also a key ecological problem for desert vegetation restoration and renewal [13]. Haloxylon ammodendron, as the main sand fixing plant in the desert, has a close relationship between the normal growth and development of Haloxylon ammodendron and the soil water conditions of the habitat. Plant morphology, on the other hand, has feedback on the dynamic changes in soil water [14].

The spatial variation characteristics of soil water and its interaction with vegetation are the key contents of water cycle research in the northwest desert area. Li Yan et al. [15] studied the carbon and water balance of Haloxylon ammodendron individuals and communities. Studies show that there is a significant relationship between flat groundwater content, evaporation, and precipitation. Under the condition of tending by precipitation alone and limited by the spatial distribution of Haloxylon ammodendron roots, the survival of seedlings mainly depends on shallow soil water. When the density of Haloxylon ammodendron exceeds 1333 plants per hectare, it will decline due to water balance problems. Li Jun et al. studied the soil moisture characteristics of Haloxylon ammodendron forest land on the southern edge of Gurbantunggut Desert. It showed that the soil moisture content of adult Haloxylon ammodendron from the trunk to the edge of the shrub showed a decreasing trend. Yang Yanfeng et al. [16] found that the soil spatial range of the root zone of adult Haloxylon ammodendron has an obvious "wet island" effect, and the "wet island" effect in summer is more prominent than that in spring. Zhang Kehai et al. compared and analyzed the soil moisture content of different sand dunes in the desert area. The topographic difference has a prominent effect on the spatial differentiation of soil moisture, and there are areas with relatively rich soil moisture in the soil space of adult shrubs. Zhu Hai et al. study on soil water characteristics of Haloxylon ammodendron root area at different tree ages; the younger the Haloxylon ammodendron tree age, the higher the utilization rate of shallow soil water (0~50 cm layer) and the stronger the dependence. The shallow soil water content is greatly affected by precipitation, snowmelt water infiltration supply, and evaporation.

1.2. Research Progress on Nutrient Characteristics of Desert Soil. The growth physiological activities of desert plants are affected not only by water deficit but also by the barren soil nutrients in the desert area [17]. Nutrient content and its dynamic balance in habitat soils directly affect the uptake and utilization of various nutrients by plants, indirectly affect plant productivity levels and the composition of community structures and ecosystem health, and have a significant impact [18]. There are many examinations of soil supplements in plant territories at home and abroad, yet the vast majority of them center around wetland, woods, and meadow biological systems [19–21]. Liu Yunhua et al. [11] showed that adult Haloxylon ammodendron has obvious "fat island" effect in the study on the change characteristics of soil nutrients in desert Haloxylon ammodendron forest land, and the older the tree age is, the more significant the fat island effect is. Chen Jing et al. found in the study of soil nutrient space of artificial Haloxylon ammodendron at different tree ages that the hierarchical changes of soil nutrients were obvious, and the nutrient content of surface soil was significantly higher than that of deep soil.

The distribution characteristics of soil nutrients surrounding the roots of adult Haloxylon ammodendron were researched by Li Congjuan et al. [22], and it was discovered that the content of soil nitrogen and phosphorus nutrients in desert areas was low, significantly lower than the national average level. The content of soil nutrients gradually decreased as the depth of the soil profile increased, the rate of soil decomposition in desert areas was low due to a lack of precipitation, and the rate of soil weathering and the ability of soil to store nutrients were low, resulting in low nutrient availability. Previous research has demonstrated that soil nitrogen and phosphorus are the material foundation for

plant life and the primary nutrient limiting variables impacting Haloxylon ammodendron growth and development [2]. Therefore, control the components of complement dispersion of seedlings exposed to various changes in soil moisture and over time Haloxylon ammodendron seedling root soil moisture and complement temporary and spatial. It is necessary to consider the diversity attribute. It is important to understand.

To sum up, the current research on Haloxylon ammodendron degradation is mainly concentrated in Inner Mongolia and Gansu, while there are few studies on Haloxylon ammodendron degradation and seedling regeneration in Gurbantunggut Desert, Xinjiang, which has the largest distribution area of Haloxylon ammodendron forest. Many studies have been conducted in the past on the evolution law of water and nutrients in the deep soil space of adult Haloxylon ammodendron at the regional scale, but few studies have been conducted on the temporal and spatial variation characteristics of soil water and nutrients in the shallow root zone, which is most closely related to Haloxylon ammodendron seedling survival. As a result, the characteristics of temporal and geographical variation, as well as the interaction relationship between shallow soil water and nutrients in the root zone of a deteriorated Haloxylon ammodendron population, were thoroughly investigated [23–25]. It is of great significance to reveal the survival strategy and adaptive mechanism of Haloxylon ammodendron seedlings in response to adverse environmental changes.

With the aim of investigating the problems of severe deterioration and poor survival of Junggar's Haloxylon ammodendron seedlings, this article discusses the typical degraded Haloxylon ammodendron population in the Gurbantunggut Desert. Select and study the soil of the seedling habitat and study temporal and spatial variability. In the root area of immature Haloxylon ammodendron seedlings, there is a relationship between soil moisture and nutritional properties. In the regeneration seedling habitat area of the degraded Haloxylon ammodendron population, the water and nutrient content in the horizontal and vertical space of the shallow soil in the root area most closely related to the survival of seedlings was dynamically monitored during the growth period, the influence of soil water change on soil nutrient content was analyzed, and the worldly and spatial variety attributes and impact relationship of soil water and supplement in the root area of Haloxylon ammodendron youthful seedlings were uncovered.

2. Materials and Research Methods

2.1. Overview of the Study Area. The study region is in Xinjiang, China, in the Gurbantunggut Desert, on the southeast margin of the Junggar Basin. The geographical location is 44°23′39.98″~44°46′59.99″N, 88°40′15.39″~89°07′57.34″E. The terrain is high in the south and low in the north, with an altitude of 500~700 m. It belongs to a mesotemperate continental semidesert arid climate. It has greater precipitation in the spring; enough water, high temperatures, and hot weather in the summer; drought and little rain in the summer; big evaporation, a lack of water, and a steep temperature rise and fall in the autumn; and dry and cold weather in the winter. The average annual temperature is about 6.7 degrees Celsius, the average annual precipitation is 165-180 mm, the annual evaporation is 2100-2300 mm, the average annual relative humidity is about 60%, and the overall temperature is 3500-3550°C. The annual sunshine hours are 3100-3200 hours, the frost-free period is 150-170 days, and the groundwater level is 23 m.

Haloxylon persicum is the dominant species in the plant community, accompanied by Haloxylon persicum, krascheninnikovia ewersmannia, Tamarix ramosissima, Reaumuria soongorica, Calligonum leucocladum, Ceratocarpus arenarius, Eremosparton songoricum, Horaninovia ulicina, etc. The soil is mainly fixed and semifixed aeolian sandy soil. The pH of the soil is 8.20, and the total salt content is 1.552.50 $g{\cdot}kg^{-1}$, organic matter is 1.173.06 $g{\cdot}kg^{-1}$, total nitrogen is 0.250.56 $g{\cdot}kg^{-1}$, total phosphorus is 0.321.65 $g{\cdot}kg^{-1}$, and total potassium is 10.1018.25 $g{\cdot}kg^{-1}$.

2.2. Test Design and Sample Collection

2.2.1. Test Design. From March to October 2018, three typical degraded natural Haloxylon ammodendron forest sample plots were selected in the desert area in the southeast of Gurbantunggut Desert, with a sample plot spacing of 20 km and a sample plot area of 100 m × 100 m (see Figure 1). Five test plots (30 m × 30 m) are randomly set in each sample plot, with a total of 15 test plots. In each experimental plot, three seedlings with relatively consistent growth, no diseases and insect pests, and normal growth and development were randomly selected as markers, and a total of 45 seedlings were labeled.

2.2.2. Soil Sample Collection and Analysis. In April, June, August, and October of the growth period, take the basal stem of the marked seedling trunk as the center, horizontal distance sampling points; soil augers were placed 10 cm, 20 cm, 30 cm, and 40 cm horizontally from the seedling trunk; and soil samples of 0 to 10 cm, 10 to 20 cm, 20 to 30 cm, 30 to 40 cm, and 40 were collected. Layers of ~50 cm were used at various horizontal distances in the vertical direction of the floor. A total of 45 soil samples (see Figure 2) were collected from each layer of soil in the root zone of young seedlings in each growth period. Measuring factors include soil moisture, organic matter, alkaline hydrolyzable nitrogen, available phosphorus, and available potassium. Soil pesticide analysis is the method of measurement [26]. The soil organic matter content was measured by the potassium dichromate sulfate external heating method, and the soil water content was measured by the dry weighing method. The accessible phosphorus content was determined by sodium bicarbonate extraction, molybdenum antimony antichromolytic analysis, and ammonium acetate flame photometric extraction, and the alkaline hydrolyzable nitrogen content was determined by the alkaline hydrolyzable diffusion method. Calculate the amount of potassium that can be accessed.

2.3. Data Statistical Analysis. The rainfall data in the study area comes from the meteorological station of desert

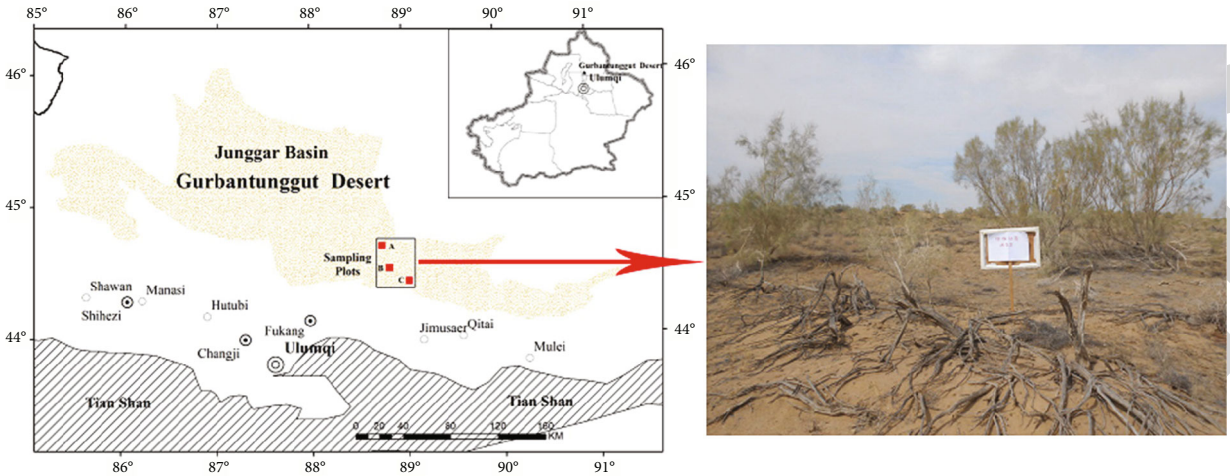

Figure 1: Geographical location and typical degraded population of H. ammodendron in the study area.

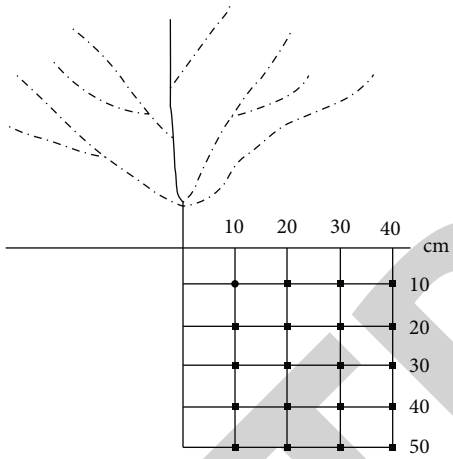

Figure 2: Schematic diagram of soil sampling.

management and Protection Station of Jimusar County Natural Resources Bureau, Changji Prefecture, Xinjiang. The statistical periods for precipitation data are early March to mid-April, mid-April to mid-June, mid-June to mid-August, and mid-August to mid-October.

I used Excel 2010 to sort the soil moisture and nutrient data. Experimental data was analyzed using SPSS 19.0 software (SPSS Inc, Chicago, Illinois, USA) including one-way ANOVA, LSD, and Duncan's new complex pole difference test. A two-sided Pearson test was used for the correlation analysis. The data was presented as mean standard error, and the significance level was set to $a = 0.05$.

3. Results and Analysis

3.1. Analysis of Rainfall in Haloxylon Ammodendron Seedling Habitat during Growth Period. From Figure 3, during the growth period from March to mid-October, the rainfall in the Haloxylon ammodendron habitat area is mainly light rain, and the daily rainfall is less than 5 mm. Among them, the rainfall frequency from early March to mid-April is 13, the cumulative rainfall can reach 28.20 mm, and the daily average rainfall is 0.71 mm. The frequency of rainfall from mid-April to mid-June is 14, with cumulative rainfall of 49.40 mm and daily average rainfall of 0.80 mm. The frequency of rainfall from mid-June to mid-August is 10, with cumulative rainfall of 25.00 mm and daily average rainfall of 0.41 mm. The rainfall frequency from mid-August to mid-October is 12, the cumulative rainfall can reach 36.50 mm, and the daily average rainfall is 0.64 mm. In different growth stages, the rainfall frequency and cumulative rainfall from mid-April to mid-June are the largest, followed by from mid-August to mid-October and from early March to mid-April. The rainfall frequency and rainfall from mid-June to mid-August are the smallest.

3.2. Temporal and Spatial Variation Characteristics of Soil Moisture in Young Seedling Root Area

3.2.1. Temporal Variation Characteristics of Soil Water Content in Young Seedling Root Zone

(1) Statistical Characteristics of Soil Moisture Content in April of Growth Period. It can be seen from Table 1 that the extreme difference in soil moisture content in the 0~10 cm layer, 10~20 cm layer, 20~30 cm layer, 30~40 cm layer, and 40~50 cm layer in the root zone of young seedlings in April of the growth period is 3.87%, 4.69%, 8.04%, 5.43%, and 3.63%, respectively. The soil moisture content increased first, then declined as soil depth climbed. The 20-30 cm layer had the highest average soil moisture content, up to 11.04 percent, which was much greater than the other levels. The coefficient of variation of soil water content in each stratum ranges from 0.20 to 0.47, indicating a medium amount of variance. The following are the attributes of the soil water content trend factor for different soil layers. 30-40 cm layer > 40-50 cm layer > 20-30 cm layer > 0-10 cm layer > 10-20 cm layer > 30-40 cm layer > 40-50 cm layer > 20-30 cm layer. The skewness coefficient of soil water content varies between 0.15 and 1.02 percent in each soil layer, the kurtosis coefficient between -1.62 and 0.43 percent, and the K-S test result between 0.19 and 0.87 percent.

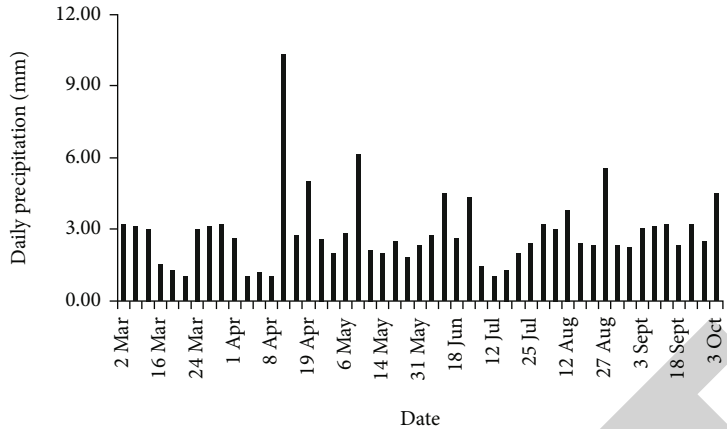

Figure 3: Daily rainfall of H. ammodendron habitat in 2018.

Table 1: Statistical characteristics of soil moisture content in different layers in April.

Soil depth (cm)	Min	Max	Mean	STDE	CV (%)	Skewness	Kurtosis	K-S test
0~10	1.21	5.08	2.48[d]	1.16	0.47	0.82	-0.32	0.64
10~20	4.30	8.99	5.73[c]	1.37	0.24	1.02	0.43	0.61
20~30	8.25	16.29	11.04[a]	2.23	0.20	0.75	-0.23	0.87
30~40	4.48	9.91	6.81[b]	1.79	0.26	0.15	-1.62	0.19
40~50	3.94	7.57	5.19[c]	1.07	0.21	0.94	0.40	0.57

Note: test of K-S representing normal distribution. Different lowercase letters showed that the soil moisture content had significant differences in different layers ($P < 0.05$), $n = 45$.

According to the skewness coefficient, kurtosis coefficient, and K-S test, the change in soil moisture content of each soil layer in the root region of young seedlings in April conforms with the normal distribution at the test level of 5%.

(2) Statistical Characteristics of Soil Moisture Content in June of Growth Period. It very well may be seen from Table 2 that the attributes of the mean worth of water content in various soil layers of the dirt vertical profile in the seedling root zone are as per the following: layer 20-30 cm > layer 30-40 cm > layer 10-20 cm > layer 40-50 cm > layer 0-10 cm. Among them, the mean value of soil water content in the 20~30 cm layer is 7.90%, which is significantly higher than that in other layers. The extreme value difference of each soil layer is 1.56%, 2.13%, 3.50%, 2.88%, and 1.63%, respectively. The coefficient of variation of soil water content in each layer is between 0.13 and 0.55, which belongs to the medium variation level, and the coefficient of variation in the 0~10 cm layer is the largest, which is 0.55. The skewness coefficient of soil water content in each soil layer is between 0.28% and 0.50%, the kurtosis coefficient is between -1.68% and 0.88%, and the K-S test result is between 0.03 and 0.63. The skewness coefficient, kurtosis coefficient, and K-S test show that the change of water content in each soil layer in the root area of young seedlings in June accords with the normal distribution at the test level of 5%.

(3) Statistical Characteristics of Soil Moisture Content in August of Growth Period. It very well may be seen from Table 3 that with the increment of soil profundity, the dirt dampness content expands first and afterward diminishes. The typical worth of soil dampness content in the 20~30 cm layer is the biggest, up to 2.92%, which is altogether higher than that in other soil layers. The extreme difference of soil moisture content in each soil layer was 0.64%, 0.90%, 3.60%, 1.83%, and 0.82%, respectively. The coefficient of the variety of soil water content in each dirt layer is somewhere in the range of 0.18 and 0.56, which has a place with the medium variety level. The variety coefficients of soil water content in various soil layers are 0 ~ 10 cm layer > 20 ~ 30 cm layer > 30 ~ 40 cm layer > 10 ~ 20 cm layer > 40 ~ 50 cm layer. The skewness coefficient of soil dampness content in each dirt layer is between 0.07% and 0.78%, and the kurtosis coefficient is between -1.47% and 1.18%. The analysis of skewness coefficient, kurtosis coefficient, and K-S test shows that the change of soil moisture content in the young seedling root zone in August of the growth period conforms to normal distribution at the test level of 5%.

(4) Statistical Characteristics of Soil Moisture Content in October of Growth Period. It very well may be seen from Table 4 that the qualities of soil dampness content in the upward profile of soil in the root zone of seedlings are 20 ~ 30 cm layer > 30 ~ 40 cm layer > 10 ~ 20 cm layer > 40 ~ 50 cm layer > 0 ~ 10 cm layer. Among them, the typical worth of soil dampness content in the 20~30 cm layer is 4.29%, which is altogether higher than that in other soil layers. The extreme value difference of each soil layer is 1.24%, 1.86%, 3.69%, 2.01%, and 1.91%, respectively. The coefficient of variation of soil water content is between 0.25 and 0.55,

Table 2: Statistical characteristics of soil moisture content in different layers in June.

Soil depth (cm)	Min	Max	Mean	STDE	CV (%)	Skewness	Kurtosis	K-S test
0~10	0.32	1.88	0.93d	0.51	0.55	0.40	-1.25	0.42
10~20	2.09	4.22	2.90c	0.70	0.24	0.50	-1.08	0.38
20~30	6.52	10.02	7.90a	1.05	0.13	0.47	-0.88	0.63
30~40	2.43	5.31	3.69b	1.03	0.28	0.28	-1.56	0.37
40~50	2.02	3.65	2.62c	0.58	0.22	0.40	-1.68	0.03

Note: test of K-S representing normal distribution. Different lowercase letters showed that the soil moisture content had significant differences in different layers ($P < 0.05$), $n = 45$.

Table 3: Statistical characteristics of soil moisture content in different layers in August.

Soil depth (cm)	Min	Max	Mean	STDE	CV (%)	Skewness	Kurtosis	K-S test
0~10	0.11	0.75	0.33^{d}	0.19	0.56	0.71	-0.55	0.32
10~20	0.92	1.82	1.24^{c}	0.28	0.22	0.49	-1.03	0.53
20~30	1.69	5.29	2.92^{a}	1.07	0.37	0.78	-0.23	0.97
30~40	1.03	2.86	1.86^{b}	0.59	0.31	0.07	-1.47	0.45
40~50	0.71	1.53	1.02^{c}	0.18	0.18	0.52	1.18	0.63

Note: test of K-S representing normal distribution. Different lowercase letters showed that the soil moisture content had significant differences in different layers ($P < 0.05$), $n = 45$.

Table 4: Statistical characteristics of soil moisture content in different layers in October.

Soil depth (cm)	Min	Max	Mean	STDE	CV (%)	Skewness	Kurtosis	K-S test
0~10	0.25	1.49	0.68^{d}	0.37	0.55	0.52	-0.85	0.62
10~20	1.42	3.28	2.08^{b}	0.59	0.28	0.83	-0.19	0.65
20~30	2.49	6.18	4.29^{a}	1.19	0.28	0.05	-1.34	0.94
30~40	1.85	3.86	2.72^{b}	0.71	0.26	0.16	-1.54	0.20
40~50	0.95	2.86	1.75^{c}	0.43	0.25	0.49	0.80	0.73

Note: test of K-S representing normal distribution. Different lowercase letters showed that the soil moisture content had significant differences in different layers ($P < 0.05$), $n = 45$.

which belongs to the medium variation level, and the coefficient of variation of the 0~10 cm layer is the largest, which is 0.55. The skewness coefficient of soil water content in each soil layer is between 0.05% and 0.83%, the kurtosis coefficient is between -1.54% and 0.80%, and the K-S test result is between 0.0 and 0.94. The analysis of the skewness coefficient, kurtosis coefficient, and K-S test shows that the change of water content in each soil layer in the root area of young seedlings in October of the growth period conforms to the normal distribution at the test level of 5%.

(5) Variation Characteristics of Soil Moisture in the Root Zone of Young Seedlings during the Whole Growth Period. As can be seen in Figure 4, the mud water content in the 0-50 cm layer at seedling heights of 10 cm, 20 cm, 30 cm, and 40 cm after April of the developmental period decreases first and then increases as the time frame develops. The average value of soil moisture content in the 0~50 cm layer at each horizontal distance decreased from 6.25% in April to 3.61% in June, with a decrease of 73.27%, then decreased to 1.48% in August, with a decrease of 144.42%, and then increased to 2.30% in October, with an increase of 55.90%. The characteristics of soil water content in the root zone of young seedlings in the growth period are April > June > October > August. In April, the soil moisture content of each layer at 10 cm, 20 cm, 30 cm, and 40 cm of the seedling level reached the maximum, which were 8.20%, 6.79%, 5.20%, and 4.80%, respectively, which were 4.06, 4.03, 4.56, and 4.54 times higher than that in August.

3.2.2. Spatial Variation Characteristics of Soil Water Content in Young Seedling Root Zone

(1) Spatial Variation Characteristics of Soil Water Content in April of Growth Period. The progressions of soil dampness at various level distances of seedlings are unique. It tends to be seen from Figure 5 that in April of the development time frame, the dirt dampness content of each layer at 10 cm and 20 cm is fundamentally higher than that at 30 cm and 40 cm. Among them, the dampness content of the 0~10 cm layer, 10~20 cm layer, 20~30 cm layer, 30~40 cm layer, and 40~50 cm layer at the 10 cm level arrives at the most extreme, 140.59% higher than that of a similar layer at 30 cm level 57.40%, 42.78%, 72.33%, and 43.21%, which are 165.73%, 67.54%, 60.77%, 76.110%, and 55.73% higher than a similar layer at the flat 40 cm, respectively. The water content of each soil layer at the 20 cm level is 73.14%, 27.04%, 19.77%, 53.44%, and 15.94% higher than that at the 30 cm level and 91.24%, 35.24%, 34.86%, 56.81%, and 26.07% higher than that at the 40 cm level.

The change in soil moisture content in different soil layers was amazing. Soil moisture in vertical sections 10 cm, 20 cm, 30 cm, and 40 cm from the seedling bottom showed up at the greatest in the 20~30 cm layer, which was 13.97%, 11.72%, 9.79%, and 8.69%, respectively, which were 3.55 times, 4.13 times, 5.97 times, and 5.86 seasons of the least 0~10 cm layer. Contrasted and the past soil layer, the upward 10~20 cm layer and 20~30 cm layer of the dirt profile show an increment. The increase of 20~30 cm layer at each horizontal distance is the largest, up to 85.40%, 82.68%, 104.39%, and 93.22%, respectively. The 30~40 cm layer and 40~50 cm layer show a decrease. The decrease of 30~40 cm layer at each horizontal distance is the largest, up to 35.81%, 31.86%, 46.82%, and 41.40%, respectively.

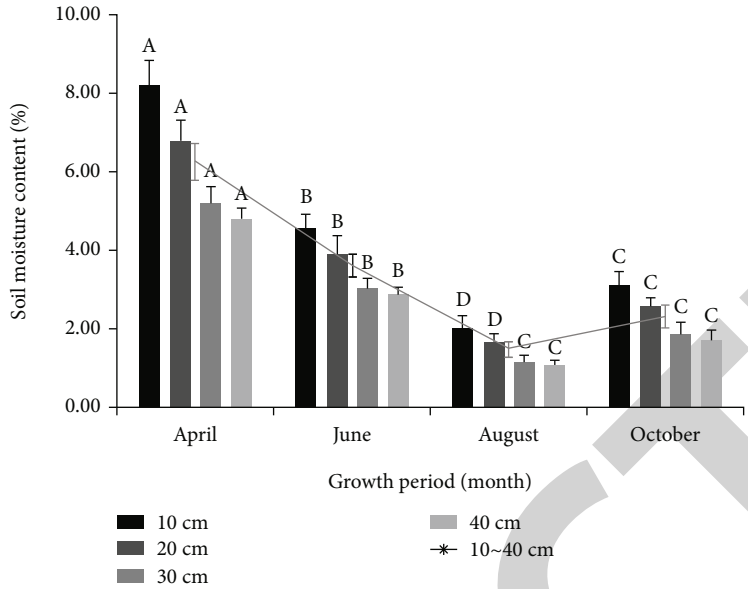

Figure 4: Variations of soil moisture characteristics at the roots of 0-50 cm seedlings. Note: other lowercase letters refer to soil moisture in the same layer. Significant differences in different growth periods ($P < 0.05$).

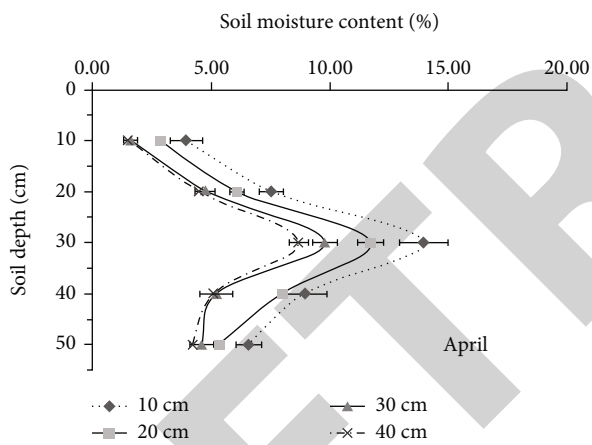

Figure 5: Spatial variation characteristics of soil moisture content in root zone of seedlings in April.

(2) Spatial Variation Characteristics of Soil Water Content in June of Growth Period. It very well may be seen from Figure 6 that in June of the development time frame, the water content of each layer at various flat distances of the seedlings is altogether higher than that at 30 cm and 40 cm at the degree of 10 cm and 20 cm. Among them, the water content of each soil layer at the level of 10 cm is the maximum, which is 201.56%, 51.87%, 29.90%, 75.39%, and 47.05% higher than that at the same layer at the level of 30 cm, 276.95% and 60.78% higher than that at the same layer at the level of 40 cm 33.73%, 88.17%, and 56.28%, with a significant difference. The water content of each soil layer at the 20 cm level is 112.19%, 35.04%, 17.67%, 45.91%, and 29.84% higher than that at the 30 cm level and 165.23%, 42.96%, 21.14%, 56.54%, and 38.00% higher than that at the 40 cm level.

The soil moisture content in the vertical profile increases from 0~10 cm layer to 20~30 cm layer. Among them, the increase of the 20~30 cm layer is the largest at each horizontal distance, up to 152.39%, 157.13%, 195.08%, and 203.45%, respectively, while the soil moisture content decreases from 20~30 cm layer to 40~50 cm layer. The decrease of the 30~40 cm layer is the largest at each horizontal distance, up to 45.40%, 49.86%, 59.56%, and 61.20%, respectively. The moisture content of a layer of 20-30 cm at a height of 10, 20, 30, and 40 cm from the bottom of the seedling is the most elevated, at 9.23 percent, 8.36 percent, 7.10 percent, and 6.90 percent, individually, which was essentially higher than the water content of different layers and was 5.74 times, 7.38 times, 13.32 times, and 16.17 times that of the least 0-10 cm layer.

(3) Spatial Variation Characteristics of Soil Water Content in August during Growth Period. It can be seen from Figure 7 that in August of the growth period, the soil moisture content of each layer at the level of 10 cm and 20 cm is significantly higher than that at the level of 30 cm and 40 cm. Among them, the moisture content of each layer at the level of 10 cm reaches the maximum, which is 221.70%, 47.16%, 103.51%, 77.63%, and 27.23% higher than that at the level of 30 cm, 184.17%, 57.05%, 120.95%, 90.63%, and 44.36% higher than that at the level of 40 cm. The difference is significant. The water content of each soil layer at the level of 20 cm is 119.81%, 16.59%, 63.16%, 63.64%, and 13.09% higher than that at the level of 30 cm and 94.17%, 24.43%, 77.14%, 75.61%, and 28.32% higher than that at the level of 40 cm.

The water content of soil vertical areas at 10 cm, 20 cm, 30 cm, and 40 cm at the foundation of seedlings arrived at the most extreme in the layer of 20~30 cm, which was

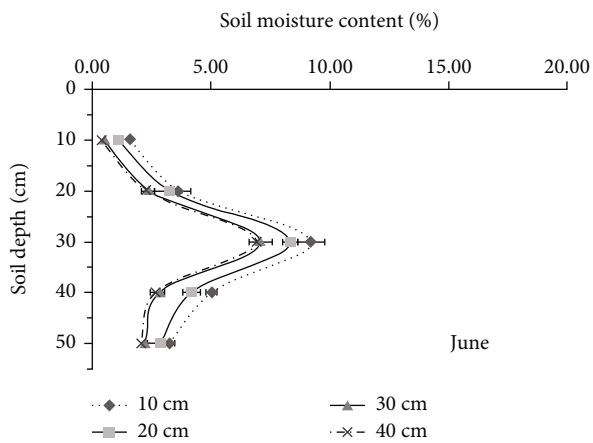

Figure 6: Spatial variation characteristics of soil moisture content in root zone of seedlings in June.

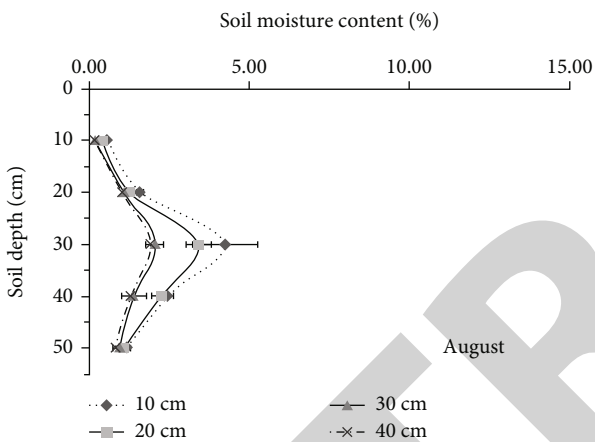

Figure 7: Spatial characteristics of soil moisture content in root zone of seedlings in August.

4.25%, 3.41%, 2.09%, and 1.93%, respectively, which were 7.48 times, 8.78 times, 11.83 times, and 9.63 seasons of the layer with the least water content of 0~10 cm. Contrasted and the past soil layer, the upward 10~20 cm layer and 20~30 cm layer of the dirt profile showed an increment, and the increment of the 20~30 cm layer at every flat distance was the biggest, up to 166.39%, 169.57%, 92.63%, and 89.34% individually. The 30~40 cm layer and 40~50 cm layer showed a decrease, and the decrease of the 30~40 cm layer at each horizontal distance was the largest, up to 41.81%, 33.14%, 33.33%, and 32.55%, respectively.

(4) Spatial Variation Characteristics of Soil Water Content in October of Growth Period. It can be seen from Figure 8 that in October of the growth period, the soil water content at 10 cm and 20 cm of the seedling level is significantly higher than that at 30 cm and 40 cm. Among them, the water content of each soil layer at 10 cm reaches the maximum, which is 192.47%, 59.35%, 71.32%, 62.71%, and 42.66% higher than the same layer at 30 cm, 251.26%, 75.43%, 85.97%, 71.84%, and 60.36% higher than that at 40 cm. The difference is significant. The water content of each soil layer at the 20 cm level is 103.35%, 11.11%, 46.26%, 52.38%, and 17.58% higher than that at the 30 cm level and 144.22%, 22.32%, 58.76%, 60.94%, and 32.17% higher than that at the 40 cm level.

From 0~10 cm layer to 40~50 cm layer, the dirt dampness content expanded first and afterward diminished. Among them, the increment of the 20~30 cm layer at every level distance was 100.99%, 146.08%, 86.94%, and 89.60%, respectively, and the abatement of the 30~40 cm layer was 39.84%, 34.00%, 36.65%, and 34.89% individually. The water content of the 20-30 cm layer of soil at 10 cm, 20 cm, 30 cm, and 40 cm of the seedling level arrived at a limit of 5.77 percent, 4.92 percent, 3.37 percent, and 3.10 percent, individually, which was fundamentally higher than the water content of different layers, which was 4.95 times, 6.08 times, 8.45 times, and 9.35 times that of the most reduced 0-10 cm layer.

3.3. Temporal and Spatial Variation Characteristics of Soil Nutrients in Young Seedling Root Area

3.3.1. Temporal and Spatial Variation Characteristics of Soil Organic Matter in Young Seedling Root Area. Figure 9 shows that the change characteristics of soil organic matter content in each soil layer at 10 cm, 20 cm, 30 cm, and 40 cm of the seedling level are as follows: with the advancement of the seedling growth period, it decreases first and then increases. The characteristics of soil organic matter content at 10 cm of the seedling level in different periods are as follows: April > June > October > August. The characteristics of soil organic matter content at 20 cm, 30 cm, and 40 cm are as follows: April > October > June > August. Among them, the substance of soil natural matter in each dirt layer at the degree of 10 cm, 20 cm, 30 cm, and 40 cm arrived at the most extreme in April, which was 62.96%, 78.10%, 64.75%, and 44.88% higher than that in August. With the augmentation of flat distance, the substance of the natural matter in each dirt layer expanded. In April, the natural matter substance in the 0~10 cm soil layer at the 40 cm level was 68.75%, 58.82%, and 29.69% higher than that in the 0~10 cm soil layer at 10 cm, 20 cm, and 30 cm. The substance of soil natural matter in the 10~20 cm layer was 66.21%, 65.07%, and 37.71% higher than that in a similar layer at different distances. The substance of soil natural matter in the 20~30 cm layer was 71.05%, 69.57%, and 45.52% higher than that in a similar layer at different distances.

With the increment of soil profundity, the substance of the natural matter in various soil layers diminished. In April, when the natural matter substance is the biggest in the development time frame, the natural matter substance of the 0~10 cm layer at various distances is the most extreme, which is 1.98 times, 1.99 times, 2.14 times, and 1.95 seasons of the base 40~50 cm layer, respectively. Contrasted and the past layer, the decline of the 10~20 cm layer is the biggest, coming to 21.38%, 28.08%, 30.86%, and 23.24% individually. In August, when the natural matter substance was the most minimal in the development time frame, the natural matter substance in the 0~10 cm layer was 1.57 times, 1.75 times,

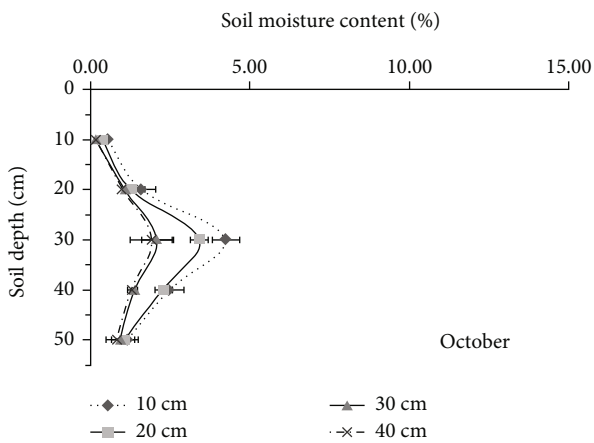

Figure 8: Spatial characteristics of soil moisture content in root zone of seedlings in October.

1.81 times, and 2.09 times that in the 40~50 cm layer, respectively. Compared with the previous soil layer, the decrease in the 10~20 cm layer was the largest, reaching 30.99%, 17.98%, 41.84%, and 41.38%, respectively.

3.3.2. Temporal and Spatial Variation Characteristics of Soil Alkali Hydrolyzable Nitrogen in Young Seedling Root Area. It can be seen from Figure 10 that the size characteristics of soil alkali hydrolyzable nitrogen content at 10 cm, 20 cm, 30 cm, and 40 cm at the seedling base level during different periods are as follows: April > June > October > August. The substance of soil antacid hydrolyzable nitrogen in each dirt layer at various level distances of seedlings arrived at the greatest in April. The substance of soil dissolvable base hydrolyzable nitrogen in the surface layer of 0-10 cm at the levels of 10 cm, 20 cm, 30 cm, and 40 cm was 113.35 $mg{\cdot}kg^{-1}$, 120.43 $mg{\cdot}kg^{-1}$, 128.86 $mg{\cdot}kg^{-1}$, and 135.38 $mg{\cdot}kg^{-1}$, respectively, which was 18.93 percent, 17.70 percent, 16.37 percent, and 26.23 percent higher than that in August with the most unjoyous. With the expansion of even distance, the substance of salt hydrolyzable nitrogen in each dirt layer expanded constantly. In April, when the soluble base hydrolyzable nitrogen content was the biggest in the development time frame, the antacid hydrolyzable nitrogen content of the 0~10 cm layer at the 40 cm level was 19.44%, 12.41%, and 5.06% higher than that of the 0~10 cm layer at 10 cm, 20 cm, and 30 cm, and the salt hydrolyzable nitrogen content of the 10~20 cm layer was 15.67%, 10.47%, and 5.51% higher than that of the similar layer at different distances. The antacid hydrolyzable nitrogen content of the 20~30 cm layer was 15.55%, 7.49%, and 4.25% higher than that of the similar layer at different distances.

The amount of soil salt hydrolyzable nitrogen decreased as the depth of the soil increased. In April, when the salt hydrolyzable nitrogen content is at its highest in the development time frame, the dirt soluble base hydrolyzable nitrogen content of the 0–10 cm soil layer which is 1.32 times, 1.31 times, 1.34 times, and 1.32 times higher than that of the base 40–50 cm soil layer at the degrees of 10 cm, 20 cm, 30 cm, and 40 cm is 1.32 times, 1.31 times, 1.34 times, and 1.32 times higher than that of the base 40. When compared to the previous soil layer, the decline in the 10-20 cm soil layer is the greatest, with 10.44 percent, 8.29 percent, 10.68 percent, and 10.20 percent, respectively. The soluble base hydrolyzable nitrogen content of the 0-10 cm soil layer was 1.29 times, 1.27 times, 1.36 times, and 1.15 times greater than that of the 40-50 cm soil layer at various distances in August, when the antacid hydrolyzable nitrogen concentration was lowest in the development time frame. With 7.50 percent, 8.99 percent, 7.63 percent, and 6.43 percent, respectively, the abatement of the 20-30 cm soil layer was the greatest as compared to the previous soil layer.

3.3.3. Temporal and Spatial Variation Characteristics of Soil Available Phosphorus in Young Seedling Root Area. It can be seen from Figure 11 that with the advance of the seedling growth period, the content of available phosphorus in each soil layer decreases first and then increases. The characteristics of soil available phosphorus content at the horizontal distance in different periods are as follows: April > October > June > August. During the growth period in April, the content of available phosphorus in the surface soil at the level of 10 cm, 20 cm, 30 cm, and 40 cm was 33.70%, 29.71%, 25.53%, and 18.89% higher than that in August, which was the lowest. With the extension of horizontal distance, the content of soil available phosphorus in each soil layer increased continuously. Available phosphorus content in the soil layer 0-10 cm at 40 cm level is 47.12 percent, 33.68 percent, and 15.67 percent more than that of the 0-10 cm soil layer at 10 cm, 20 cm, and 30 cm in April, when the available phosphorus content is at its highest throughout the growth season. The accessible phosphorus content of the 10-20 cm soil layer is 55.13 percent, 38.17 percent, and 19.53 percent greater than that of the same layer in other places, while the available phosphorus content of the 20-30 cm soil layer is 71.43 percent, 51.38 percent, and 25.00 percent higher.

The difference is significant.

With the increment of soil profundity, the substance of soil accessible phosphorus diminished. In April, when the accessible phosphorus content is the biggest in the development time frame, the accessible phosphorus content in the 0~10 cm soil layer at various level distances is the greatest, which is 2.08 times, 1.90 times, 1.77 times, and 1.59 seasons of the base 40~50 cm soil layer, respectively. Contrasted and the past soil layer, the downfall of the 20~30 cm soil layer is the biggest, coming to 29.09%, 27.98%, 22.16%, and 16.82% individually. In August, when the mobile phosphorus content was lowest, the mobile phosphorus content was 1.85, 1.68, 1.57, and 1.44 times higher in the soil layer of 0-10 cm compared to the soil layer of 40-50 cm. In the case of the previous soil layer, the 10 to 20 cm soil layer decreased the most, respectively, to 30.57%, 25.60%, 23.33%, and 18.15%.

3.3.4. Temporal and Spatial Variation Characteristics of Soil Available Potassium in Young Seedling Root Area. It can be seen from Figure 12 that with the advance of the seedling growth period, it decreases first and then increases. The size

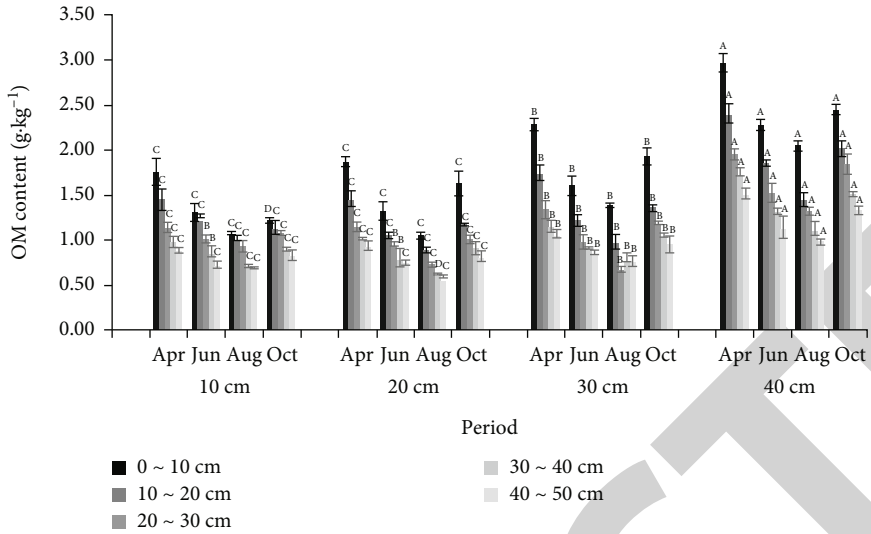

Figure 9: Content of organic matter at soil horizontal-vertical space in the root zone of seedlings in growth period. Note: different capital letters showed that the soil moisture content of the same layer in the same period has significant differences at different horizontal distances ($P < 0.05$).

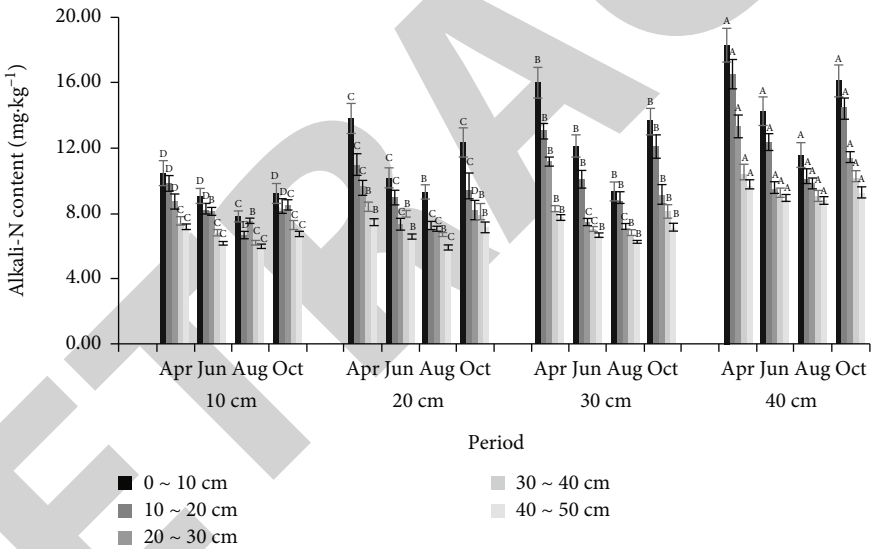

Figure 10: Content of alkali hydrolyzable nitrogen at soil horizontal-vertical space in the root zone of seedlings in growth period. Note: different capital letters showed that the soil moisture content of the same layer in the same period has significant differences at different horizontal distances ($P < 0.05$).

characteristics of soil available potassium content are April > October > June > August. The content of available potassium in each soil layer at different horizontal distances reached the maximum in April, which was 33.70%, 29.71%, 25.53%, and 18.89% higher than that in August. With the extension of horizontal distance, it shows an increasing trend. In April, when the content of available potassium was the highest in the growth period, the content of available potassium in the 0~10 cm soil layer at the 40 cm level was 47.12%, 33.68%, and 15.67% higher than that in the 0~10 cm soil layer at 10 cm, 20 cm, and 30 cm. The content of available potassium in the 10~20 cm soil layer was 55.13%, 38.17%, and 19.53% higher than that in the same layer at other distances. The content of available potassium in the 20~30 cm soil layer was 71.43%, 51.38%, and 25.00% higher than that in the same layer at other places. The difference was significant.

With the increment of soil profundity, the substance of soil accessible potassium diminished. During the April development period, the available potassium content in the 0~10 cm soil layer at 10 cm, 20 cm, 30 cm, and 40 cm was 2.08, 1.90, 1.77, and 1.59 times higher than that in the 40~50 cm soil layer, respectively. Compared to the previous soil layer, the 20-30 cm soil layer decreased the most, reaching 29.09%, 27.98%, 22.16%, and 16.82%, respectively. In August, when the available potassium content decreased the most in terms of development, the available potassium content in the 0~10 cm soil layer was 1.85 times, 1.68 times,

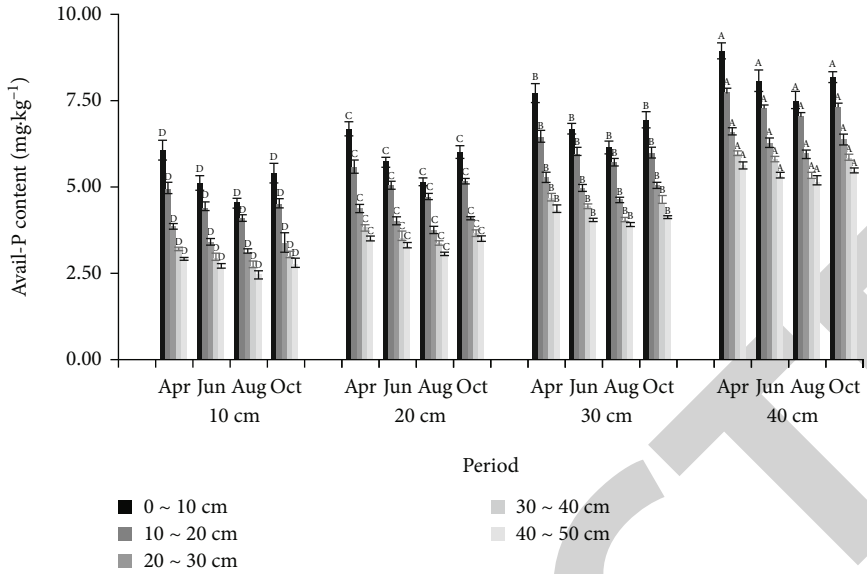

Figure 11: Content of available phosphorus at soil horizontal-vertical space in the root zone of seedlings in growth period. Note: different capital letters showed that the soil moisture content of the same layer in the same period has significant differences at different horizontal distances ($P < 0.05$).

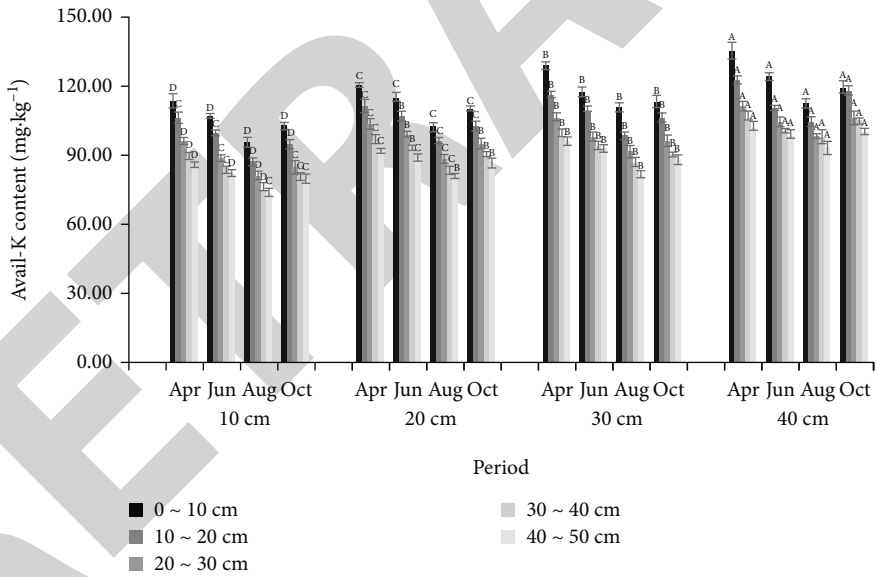

Figure 12: Content of available potassium at soil horizontal-vertical space in the root zone of seedlings in the growth period. Note: different capital letters showed that the soil moisture content of the same layer in the same period has significant differences at different horizontal distances ($P < 0.05$).

1.57 times, and 1.44 times higher than those in 40~50 years. See the soil layer. Compared with the previous soil layer, the reduction of the soil layer of 10 to 20 cm was the largest, reaching 30.57%, 25.60%, 23.33%, and 18.15%, respectively.

3.4. Analysis of the Relationship between Rainfall and Soil Moisture in Seedling Habitat. It very well may be seen from Table 5 that there is no critical relationship between precipitation in April of the development period and water content of each dirt layer ($P < 0.05$). There was a huge positive connection between precipitation in June and soil water content in the 0~10 cm layer and 10~20 cm layer, and the relationship coefficients were 0.564 and 0.473, which had a feeble connection with water content in other soil layers ($P < 0.05$). There was a critical positive relationship between precipitation in August and soil dampness content in the 0~10 cm layer, 10~20 cm layer, and 20~30 cm layer, and the connection coefficients were 0.865, 0.623, and 0.519, respectively, which had a frail relationship with soil dampness content in different layers ($P < 0.05$). There was a critical positive

Table 5: Correlation analysis between rainfall and moisture content in different soil layers in growing period.

Growth period	April	June	August	October
0~10 cm	0.374	0.564*	0.865*	0.716*
0~20 cm	0.306	0.473*	0.623*	0.524*
0~30 cm	0.275	0.312	0.519*	0.480*
0~40 cm	0.221	0.246	0.388	0.277
0~50 cm	0.109	0.225	0.362	0.219

Note: * showed significant correlation at 0.05 level.

Table 6: Correlation analysis between moisture content and nutrient content in different soil layers in growth period.

Soil depth	OM	Avail-N	Avail-P	Avail-K
0~10 cm	0.525*	0.462*	0.287	0.829**
0~20 cm	0.431*	0.381	0.212	0.731**
0~30 cm	0.368	0.304	0.185	0.665**
0~40 cm	0.184	0.257	0.163	0.572*
0~50 cm	0.153	0.213	0.147	0.556*

Note: * showed significant correlation at 0.05 level, and ** showed significant correlation at 0.01 level.

relationship between precipitation in October and soil water content in the 0~10 cm layer, 10~20 cm layer, and 20~30 cm layer, and the connection coefficients were 0.716, 0.524, and 0.480, respectively, which had a frail relationship with soil water content in different layers ($P < 0.05$). With the increment of soil profundity, the relationship coefficient among precipitation and soil dampness content declines, and the connection degree diminishes.

3.5. Analysis of the Relationship between Soil Moisture and Nutrients in Seedling Habitat. In Table 6, the relationship between the moisture content of the soil and the natural substances in the soil, soluble base hydrolyzable nitrogen, accessible phosphorus, and accessible potassium content in various soil profundities of seedling living space in the development period is unique. Among them, there was a huge positive connection between dirt water content and natural matter substance in the 0~10 cm layer and 10~20 cm layer, and the relationship coefficients were 0.525 and 0.431, respectively. The connection between dirt water content and natural matter substance in other soil layers was feeble ($P < 0.05$). There was a critical positive connection between dirt water content and soluble base hydrolyzable nitrogen content in the 0~10 cm soil layer, and the relationship coefficient was 0.462. The relationship between dirt water content and natural matter substance in other soil layers was feeble ($P < 0.05$). The connection between dirt water content and accessible phosphorus content in various soil layers was frail ($P < 0.05$). There was an exceptionally huge positive connection between dirt water content and accessible potassium content in the 0~10 cm layer, 10~20 cm layer, and 20~30 cm layer, and the relationship coefficients were 0.829, 0.731, and 0.665, respectively ($P < 0.01$). There was a critical positive connection between dirt water content and accessible potassium content in the 30~40 cm layer and 40~50 cm layer, and the relationship coefficients were 0.572 and 0.556, respectively ($P < 0.05$). With the increment of soil profundity, the connection coefficient between soil water content and soil natural matter, antacid hydrolyzable nitrogen, and accessible potassium diminished.

4. Discussion

4.1. Temporal and Spatial Variation Characteristics of Soil Moisture in Young Seedling Root Area. In 3-6 is the relationship between the moisture content of the soil and the natural substances in the soil. The change of soil water in the seedling root zone is not only affected by terrain, soil texture, groundwater, and other factors but also affected by snow melting, precipitation, evaporation, wind, and other factors [27, 28]. The dirt water content in the seedling root zone diminishes first and afterward increments with the development of the seedling development period, demonstrating that the dirt water content in the seedling root zone has clear occasional variety attributes. The explanation is that the dirt water content in the seedling root zone is unevenly dispersed during the development time frame because of the impact of precipitation and dissipation. In April, which is the growing season, the soil moisture in the root area of the seedlings is the highest compared to other growing seasons. The soil moisture content in the 0~50 cm layer of the soil is 6.25%, which is less than 7.15% of the research results of Dai Yue in the habitat of adult Haloxylon ammodendron in the same period in Fukang desert area, Xinjiang. The difference may be related to the precipitation and soil texture of the two regions and the difference in water use efficiency of Haloxylon ammodendron at different ages.

During the development time frame, the dirt dampness content of each dirt layer at various even distances in the root zone of youthful seedlings is described by a generally speaking diminishing pattern with the expansion of the flat distance. The change qualities of soil dampness content at every level distance are that it first increments and afterward diminishes with the increment of soil profundity, which is predictable with the examination finishes of Yang Yanfeng et al. [16]. The dirt space in the root zone of Haloxylon ammodendron has a self-evident "wet island" impact. The results showed that Haloxylon ammodendron seedlings had the ability to accumulate water in the process of adapting to desert and arid environments. This unique ability to accumulate water can obtain more water for seedlings to resist drought, thus reflecting the advantage of Haloxylon ammodendron as the main constructive species in Gurbantunggut Desert [29].

4.2. Temporal and Spatial Variation Characteristics of Soil Nutrients in Young Seedling Root Area. The low satisfaction of different soil supplements in the desert region is one reason for its intense pressure [30, 31]. The items in soil natural matter, soluble base hydrolyzable nitrogen, accessible phosphorus, and accessible potassium in each dirt layer of the

youthful seedling root zone diminished first and afterward expanded with the development of the seedling development period. The dirt supplement content in April of the development period was generally high. The substance of the natural matter in the 20~30 cm layer of soil was 1.14 $g \cdot kg^{-1}$, and the substance of quick accessible phosphorus was 3.85 $mg \cdot kg^{-1}$, which was not exactly that of Liu Yunhua et al. [11]. The outcomes of Haloxylon ammodendron in the desert region around Ganjiahu Haloxylon ammodendron Nature Reserve were 3.08 $g \cdot kg^{-1}$ and 7.13 $mg \cdot kg^{-1}$. The justification for the thing that matters is connected with the dirt surface, Haloxylon ammodendron age, and environment in the two regions. The soil nutrient content of the vertical soil profile is in Chen Jing et al. Consistent with the study, it shows a decreasing trend with increasing soil depth (2019): artificial Haroxylon ammodendron forest in the desert area of Inner Mongolia. The effect of fortifying nutrients on the soil surface is clear.

The variation characteristics of soil nutrient content at different horizontal distances in the root zone of Haloxylon ammodendron seedlings are as follows: with the extension of horizontal distance, the overall trend is increasing. Differences in spatial variation characteristics and soil nutrients in the root zone show that there is an obvious characteristic of "low inside and high outside" in the horizontal space of Haloxylon ammodendron seedlings, which is similar to the research results of Chen Jing et al. and Liu Yunhua et al.. On the contrary, adult Haloxylon ammodendron has a typical "fat island" effect. The reason for the difference may be related to the age and soil texture of Haloxylon ammodendron. Most of the nutrients in the surface soil are mainly obtained from the litter materials of plants. Compared with adult Haloxylon ammodendron, Haloxylon ammodendron seedlings have smaller crown width, plant height, and base diameter, resulting in less litter, less nutrient accumulation in the root zone soil, and lower ability of seedlings to accumulate nutrients. In addition, the root system of seedlings is smaller than that of adult Haloxylon ammodendron, and the controlled soil space resources are also small. Its growth continuously consumes the nutrients around its root system, making the soil nutrient content near the root system lower than that in the surrounding area, which is also one of the reasons why Haloxylon ammodendron seedlings are prone to death and low survival rate.

4.3. Effect of Rainfall on Soil Water Content in Seedling Habitat. In desert settings, soil moisture is one of the most important water sources for plants. Soil moisture deficit is one of the main causes of desert shrub forest deterioration, which has a significant impact on ecosystem nutrient cycles [14]. The supply of soil water mainly comes from snowfall, rainfall, and groundwater supplement, and the consumption of soil water mainly includes plant absorption, evaporation, and infiltration. During the growth period from March to October, there are 49 rainfall events during the growth period of Haloxylon ammodendron in the desert, with an average of once every 6 days, mainly small rainfall events and sporadic medium rainfall events, accounting for more than 88.98%, which is consistent with the research results of Yue yuemeng et al. on Haloxylon ammodendron habitat in Gurbantunggut Desert. The fluctuation range of precipitation in the desert area is small, and there is little difference between soil texture and terrain. The dynamics of soil water mainly depend on the amount absorbed by desert plants. The characteristics of rainfall frequency and average rainfall in Haloxylon ammodendron habitat in different growth periods are as follows: mid-April~mid-June>mid-August~-mid-October>early March~mid-April>mid-June~mid-August. It shows that there is seasonal variation in rainfall in the desert area of Xinjiang Uygur Autonomous Region.

The endurance of Haloxylon ammodendron seedlings for the most part relies upon the water invaded by snowmelt and precipitation and utilization of the shallow soil water content [32]. The connection between precipitation in seedling environment and soil water content in various soil layers was unique. There was no critical relationship between the precipitation in April and the dirt dampness content of each dirt layer. There was a critical positive relationship between the precipitation in June and the dirt dampness content of the 0~10 cm layer and 10~20 cm layer. There was a huge positive relationship between the precipitation in August and October and the dirt dampness content of the 0~10 cm layer, 10~20 cm layer, and 20~30 cm layer ($P < 0.05$). With the increment of soil profundity, the connection coefficient among precipitation and soil dampness content abates, and the relationship degree diminishes. It shows that the precipitation in the center and late development phase of desert seedling living space critically affect the difference in soil water content in the shallow layer of 0~30 cm. With the augmentation of soil profundity, the effect diminishes, which is reliable with the examination consequences of Xu Hao et al.. There are not many enormous precipitation occasions in the desert, which affects the dirt water content in the shallow layer; Haloxylon ammodendron for the most part utilizes the shallow soil water framed by precipitation to keep up with its endurance.

4.4. Effect of Soil Moisture Change in Young Seedling Root Zone on Soil Nutrients. Soil nutrient resources in desert areas are absorbed and utilized by plants under the action of water. Therefore, the temporal and spatial changes of soil water directly affect the changes in soil nutrient resources and then affect the nutrient circulation and utilization of ecosystems in arid areas [33]. There was a huge positive connection between dirt water content and natural matter substance in the 0~10 cm layer and 10~20 cm layer in the root zone of Haloxylon ammodendron youthful seedlings at the development stage; there was a critical positive relationship between dirt water content and salt hydrolyzable nitrogen content in the 0~10 cm layer, and the relationship between dirt water content and accessible phosphorus content in various soil layers was frail ($P < 0.05$). This relationship is like the aftereffects of Li congjuan et al. in the review region. Soil dampness essentially affects shallow soil natural matter and accessible nitrogen content, yet not on soil accessible phosphorus content. With the increment of soil profundity, the effect of soil dampness on soil natural matter and accessible nitrogen is debilitating, It shows that dirt dampness

significantly affects the conveyance example of soil supplement assets.

Due to the influence of climate, landform, vegetation, parent rock, precipitation, soil animals, and other soil forming factors and human activities, the distribution of soil nutrient content in the desert area is uneven, and the soil nutrient content is generally low. The growth of desert plants is mainly limited by carbon, nitrogen, and phosphorus nutrients [33, 34]. Most examinations show that the change attributes and corresponding relationship of soil natural matter and soil accessible supplements, which are generally straightforwardly consumed by plants, assume a significant part in the development and advancement of desert plants. In this review, the substance of accessible nitrogen in the shallow soil in the seedling living space differs from 5.96~10.96 $mg{\cdot}kg^{-1}$, and the substance of accessible phosphorus changes from 2.45~6.07 $mg{\cdot}kg^{-1}$. The typical proportion of accessible nitrogen to accessible phosphorus is 1.87. The difference in accessible nitrogen is not exactly that of Tao Ye et al. on the desert territorial size of Junggar bowl, which is 16.04~25.10 $mg{\cdot}kg^{-1}$, and the difference in accessible phosphorus is more prominent than that of 3.61~4.37 $mg{\cdot}kg^{-1}$. The available nitrogen phosphorus ratio is less than the result of 5.87, indicating that the soil available nitrogen content in the study area is low, and the available nitrogen phosphorus ratio is far lower than the desert regional scale level, which further reflects the lack of nitrogen nutrients in the soil in the study area, which is related to the scarce precipitation and low soil water content in the study area. In addition, there are fewer types and quantities of soil microorganisms, resulting in a relatively low decomposition rate of soil nutrients. The weathering rate and the ability of soil to store nutrients are low, resulting in low available soil nutrient content [35].

5. Conclusion

The soil moisture and nutrient content in the root zone of seedlings have obvious temporal and spatial variation characteristics. It shows that there is seasonal variation in rainfall in the desert area of Xinjiang Uygur Autonomous Region. In the space of soil level (0~40 cm), with the expansion of flat distance, there is a self-evident "wet island" impact in soil water content and a self-evident "low inside and high outside" trademark in soil supplement content. In the upward (0~50 cm) space of soil, with the increment of soil profundity, the dirt water content expanded first and afterward diminished, and the dirt supplement content diminished. Living space precipitation essentially affected soil water content in 0~30 cm ($P < 0.05$), and soil water highly affected the items in natural matter, soluble base hydrolyzable nitrogen, and accessible potassium in surface soil ($P < 0.05$). The natural succession of soil water and soil nutrient resources in the Haloxylon ammodendron habitat changes very slowly, with long periodicity and small variation range. Therefore, in the degraded area of Haloxylon ammodendron and the area with a low seedling survival rate, strengthening the protection and management of habitat water and nutrient resources with artificial assistance will contribute to the renewal and rejuvenation of degraded Haloxylon ammodendron population in the desert area of Junggar Basin.

Data Availability

The data used to support the findings of this study are included within the article.

Conflicts of Interest

The authors declare that they have no conflicts of interest.

Acknowledgments

The Natural Science Foundation of China provided funding for this research (No. 31800384).

References

[1] Division of protected areas and species management, Department of Nature Protection, State Environmental Protection Administration, *Protection and Research of Rare and Endangered Plants*, China Environmental Science Press, Beijing, 1991.

[2] L. Tang, "Land degradation and ecological reconstruction in oasis desert ecotone in arid area," *Study on arid area*, vol. 19, no. 3, pp. 43–47, 2002.

[3] Q. Guo, Z. Cong, and C. Wang, *Study on Ecology of Haloxylon ammodendron and Cistanche deserticola*, Science Press, Beijing, 2009.

[4] S. Hu, "Haloxylon ammodendron desert in Northwest China," *Plant ecology and geobotany series*, vol. 1, no. 2, pp. 81–108, 1963.

[5] P. Huang and Z. Lv, "Establishment of green state in Mosuo Bay and dynamics of Haloxylon ammodendron desert," *Resources and environment in arid areas*, vol. 9, no. 4, pp. 173–178, 1995.

[6] L. Zhang, "Haloxylon ammodendron and Haloxylon persicum in Xinjiang Desert (part I)," *Journal of plants*, vol. 5, no. 4, pp. 4–7, 2002.

[7] Z. Jia, Q. Lu, and B. Guo, "Research progress of Haloxylon ammodendron," *Forestry science*, vol. 17, no. 1, pp. 125–132, 2004.

[8] X. Xu, X. Ji, and W. Jin, "Nighttime water consumption and its influencing factors of typical sand fixing plants in arid area of Northwest China," *Journal of Northwest botany*, vol. 35, no. 7, pp. 1443–1450, 2015.

[9] A. A. Sher, D. E. Goldberg, and A. Novoplansky, "The effect of mean and variance in resource supply on survival of annuals from Mediterranean and desert environments," *Oecologia*, vol. 141, no. 2, pp. 353–362, 2004.

[10] Y. Qiyue, Z. Wenzhi, L. Bing, and L. Hu, "Physiological responses of Haloxylon ammodendronto rainfall pulses in temperate desert regions, Northwestern ChinaPhysiological responses of Haloxylon ammodendron to rainfall pulses in temperate desert regions, Northwestern China," *Trees*, vol. 28, no. 3, pp. 709–722, 2014.

[11] B. Liu, D. Liu, and L. Li, "Causes of large-scale degradation of Haloxylon ammodendron in the Western Gurbantunggut Desert," *Journal of Ecology*, vol. 29, no. 4, pp. 637–642, 2010.